

SMART GREEN AND INTEGRATED TRANSPORT

Integrity improvement of rotorcraft main gearbox

D2-7: Test report and conclusions



Disclaimer



Funded by the European Union. Views and opinions expressed are however those of the author(s) only and do not necessarily reflect those of the European Union or the European Union Aviation Safety Agency (EASA). Neither the European Union nor EASA can be held responsible for them.

This study has been carried out for the European Union Aviation Safety Agency by an external organization and expresses the opinion of the organization undertaking the study. It is provided for information purposes only and the views expressed in the study have not been adopted, endorsed or in any way approved by the European Union Aviation Safety Agency. Consequently it should not be relied upon as a statement, as any form of warranty, representation, undertaking, contractual, or other commitment binding in law upon the European Aviation Safety Agency.

Ownership of all copyright and other intellectual property rights in this material including any documentation, data and technical information, remains vested to the European Aviation Safety Agency. All logo, copyrights, trademarks, and registered trademarks that may be contained within are the property of their respective owners.

Reproduction of this study, in whole or in part, is permitted under the condition that the full body of this Disclaimer remains clearly and visibly affixed at all times with such reproduced part.

REPORT NUMBER: D2-7
REPORT CLASSIFICATION: UNCLASSIFIED
DATE: 21 February 2024
KNOWLEDGE AREA(S): Research, rotorcraft, MGB components, design limitations, crack prevention
DESCRIPTOR(S): Component testing, integrated raceway, crack prevention factors, RCF
CUSTOMER: simulation European Union Aviation Safety Agency
CONTRACT NUMBER: EASA.2019.C15
OWNER: European Union Aviation Safety Agency
DISTRIBUTION: Limited
CLASSIFICATION OF TITLE: UNCLASSIFIED

Author(s): Dr. Ramdane Boukellif, S. Hilleke, W. Riesen

APPROVED BY:	AUTHOR	REVIEWER	MANAGING DEPARTMENT
R. Stürzer	Dr. Ramdane Boukellif, S. Hilleke, W. Riesen	J. Litzba	AH Tech Drive Train Components

DATE: 21 February 2024

EVALUATE AND DEFINE ROTOR AND ROTOR DRIVE SYSTEM DESIGN
OPTIONS TO PREVENT SINGLE POINTS OF CATASTROPHIC FAILURE

Test report and conclusions

Airbus Helicopters Technik GmbH

Airbus Helicopters Technik GmbH is a worldwide company known for its helicopter transmission systems. With our EASA and FAA privileges we are active for design and development, manufacturing and maintenance of helicopter transmission systems and geared applications for fix wing aircrafts and engines. Our service activities are not only keeping transmission system components airworthy, also mission support for a broad range of customers are conducted. For nearly all helicopter manufacturers around the world, Airbus Helicopters Technik GmbH designs and supplies worldwide turn-key solutions for gearbox and rotor test stands.

Flugplatzstrasse | 34379 Calden, Germany | + 49 5674 701 0 | + 49 5674 701 606 | GIFT-MGB.aviation@zf.com |

SUMMARY

Problem area

The aim of this report is to describe the testing and simulation planned for stream 2 of the project between EASA and AH Tech [2] and the EASA tender [1] based on the Horizon 2020 Work Programme Societal Challenge 4 ‘Smart, green and integrated transport’.

Description of work

For D2-7, different testing and simulation activities were conducted to analyze rolling contact fatigue in more detail and gain important information for the understanding of these phenomena and potential improvements. The testing phase was split into three main parts (phase I.1, phase I.2 and phase II), while two types of bearing applications were tested. One test stand was prepared with an outer bearing ring raceway, and the other was equipped with an integrated inner race on a shaft. During the different test phases, pure rolling contact, rolling contact with variable bearing design parameters, and rolling contact with additional body stress (complex load) were tested and compared. In parallel, finite element models were built to study and evaluate the parameters that promote crack development back to the surface rather than into the core. Finally, a validation and comparison to the test results was performed to provide confidence in the accuracy of the simulations.

Based on the information gained from the test and simulation, conclusions are presented regarding the threats for which crack initiation and propagation under RCF cannot be reliably prevented, and a guideline for future developments is given.

The main focus of the work for D2-7 was on the detailed description of test and simulation activities that were done by taking into account the main objectives for tasks 3, 4, and 5 ([1],[2]). This includes an evaluation of the tested parameters with interpretation of all observations made during testing, as well as validation and correlation of the simulations performed within the test campaign. The test campaign was divided into three main phases:

- Phase I.1: Pure RCF for different load levels
- Phase I.2: Pure RCF with variations in key parameters
- Phase II: RCF with additional body stress (complex load)

These different phases were set to validate the hypothesis, which was defined and presented during D2-2, as a fundamental baseline for this research project [4]:

1. In the case of a pure rolling contact load, the initiation of a crack with a finite depth may occur.
 - Crack growth ends at a finite depth
 - A crack typically leads to spalling damage
 - Crack growth toward the surface is known for pure RCF. Crack growth into the material is known in combination with a second driver (body stress)
2. Without a complex load situation present, such as for example, in a planetary gear, there will be no further crack growth under a single load of the rolling contact
3. Only under a complex load situation (body stress), crack propagation into the material is possible and must be considered

Results and application

As an overall conclusion within the scope of the project, it is worth mentioning that no fixed limits for the given parameters, load conditions, or body stresses could be presented or carried over to other applications. Potential applications (without any guarantee of completeness) could include planetary gears, integrated or non-integrated bearings, and gears or integrated raceways on housings, liners, and shafts.

Limits that could be extracted from the test campaign and simulation (e.g. max. allowable pressure level or body stress) could be different for other applications due to geometrical effects or manufacturing factors (e.g. influence on fracture mechanics material properties). Nevertheless, it is possible to use the general approach in other applications based on the flow chart presented below (see Figure 153).

Four main pillars can be mentioned as a starting point and baseline. These are: the evaluation of the geometry, external load, material properties, and residual stress profile (see Figure 153 for more details). Moreover, additional information should be derived from available MRO data to ensure that the simulation is conservative. This could be done by additional output of MRO data, which is currently not considered as generic MRO data (e.g. max spalling depth or information on subsurface cracks).

A general body of experience on the sensitivity of initial crack depth/angle in response to key parameters is also known thanks to the current research project and could be used in conjunction with the MRO data to build the simulation model properly (e.g. max spalling depth in a range of 0.3-0.5 mm vs. critical crack depth based on residual stress profile for the tested applications). Detailed knowledge on these pillars is mandatory for further evaluation and needs to be done for any new application, which might also lead to the use of further simulation model details (e.g. 2D vs. 3D). Nevertheless, reduced complexity of the model is recommended due to simulation time and could be supported by additional testing. After some sensitivity analysis within the simulation, a statement of potential critical crack growth can be made, which could lead to recommendations for re-design. Even if critical crack propagation (i.e. across the thickness of the part) may be ruled out by simulation, additional testing would typically be required to validate the results and support certification according to CS 27.571/CS 29.571. Additional testing could be necessary for several reasons (see also the details in Figure 153).

As demonstrated by Figure 153, the simulations developed (see chapter 6) and the experience from testing (see chapter 5) are not limited to the applications of this research project. They can be transferred to support future development activities and provide recommendations for more sustainable design solutions to prevent critical crack propagation. With the information gained from this research project, it was possible to provide a guideline for any future development of components subject to RCF with catastrophic failure modes.

CONTENTS

SUMMARY.....	5
Problem area	5
Description of work.....	5
Results and application	6
CONTENTS.....	7
ABBREVIATIONS	9
1. Introduction.....	10
2. Specimens.....	11
2.1 Outer Ring	11
2.1.1 Outer ring for Phase I testing	11
2.1.2 Specific design of the outer ring for phase II of testing/test bench '1'	12
2.1.3 Manufacturing steps	14
2.2 Shaft	15
2.2.1 Shaft (solid) for Phase I of testing	15
2.2.2 Specific design of the shaft (hollow) for phase II of testing/test bench '2'	17
2.2.3 Manufacturing steps	17
2.3 Residual stress measurement	18
2.3.1 Residual stress measurement outer ring	18
2.3.2 Residual stress measurement shaft	20
2.3.3 Residual stress measurement issues in equilibrium	21
3. Test bench	22
3.1 Test bench '1' for outer ring specimen	22
3.2 Test bench '2' for shaft specimen	24
4. Test plan	26
4.1 Phase I.1	26
4.2 Phase I.2	28
4.3 Phase II	29
5. Test results	31
5.1 General explanation/description	31
5.2 Preparation of parts	33
5.2.1 Shaft	33
5.2.2 Outer ring	34
5.3 Phase I.1	34
5.3.1 Shaft	34
5.3.2 Outer ring	37

5.4	Phase I.2	41
5.4.1	Shaft	41
5.4.2	Outer ring	52
5.5	Phase II	56
5.5.1	Hollow shaft	56
5.5.2	Outer ring with notch	60
5.6	Test results – overview and conclusions	64
6.	Prediction of rolling contact fatigue crack propagation	69
6.1	Introduction	69
6.2	Description of the FE-model and simulation approach	69
6.3	Parametric study to prepare Phase I.1	71
6.3.1	Influence of initial crack length on crack paths and stress intensity factors	71
6.3.2	Influence of initial crack angle on crack paths and stress intensity factors	73
6.3.3	Influence of friction (cylinder / half-plane) on crack paths and stress intensity factors	76
6.3.4	Influence of contact pressure on crack paths and stress intensity factors	77
6.3.5	Influence of friction at crack surfaces on crack paths and stress intensity factors	79
6.3.6	Comparison of the FE- results with the literature	81
6.3.7	Discussion of the results	83
6.4	Phase I.2	83
6.4.1	Implementation of residual stresses in the FE model	84
6.4.2	Parametric study	86
6.4.3	Prediction of rolling contact fatigue crack propagation using the measured residual stresses from the shaft/16NCD13	94
6.4.4	Discussion of the results	95
6.5	Phase II	95
6.5.1	Parametric study to prepare Phase II	95
6.5.2	Hollow shaft	101
6.5.3	Outer ring with notch	108
6.6	Simulation conclusion	119
7.	Summary and conclusion	122
8.	References	126
	Bibliography	128
Annex A	Specimen	129
A.1	Outer Ring – Test campaign	129
A.2	Shaft – Test campaign	137
A.3	Complex load introduction for outer ring	140
A.4	Complex load introduction for shaft	141
A.5	White layer evaluation	142

ABBREVIATIONS

ACRONYM	DESCRIPTION
AH Tech	Airbus Helicopters Technik GmbH
CHD	Case hardening depth
CS	Certification Specification
EASA	European Union Aviation Safety Agency
LEFM	Linear elastic fracture mechanics
NHD	Nitriding hardening depth
OEI	One Engine Inoperative
RCF	Rolling contact fatigue
V	Version (e.g. 1)
ZF	ZF AG
ZFL	ZF Luftfahrttechnik GmbH

1. Introduction

The aim of this report is to report the testing and simulations of the project between EASA and AH Tech [2] and the EASA tender [1] based on the Horizon 2020 Work Programme Societal Challenge 4 ‘Smart, green and integrated transport’.

As part of Stream 2 of the project, this test report is based on test plan D2-6 [8], which details the description of the test specimen, test bench, and the type and method of testing to be performed, as well as the related inspection and acceptance criteria for verification.

The selection of key design parameters to be tested was already completed by the investigations in the D2-2 report [4]. Based on this, the residual stress, hardness, hardness depth, and contact stress were selected for Phase I of testing, and body stress for Phase II of testing, as among the main parameters.

Phase I: Crack initiation and propagation

1. Starting from a surface defect to the initiation of a crack by pure rolling contact
2. Crack network grows and propagates but only to a limited depth with variable design parameters

Phase II: Crack propagation due to additional loading by a complex load situation

For Phase I.1, the focus was on the variation of contact pressure by pure rolling contact, while the other design parameters were adjusted and fixed according to predefined baseline values. As the case hardening depth and hardness have a direct influence on the profile of residual stress and stress state, these parameters were also taken into account as variables within Phase I.2.

Moreover, two different material combinations (case carburized and nitrided raceways) were used to evaluate the possible impact of different material properties (e.g. ΔK_{th} threshold value).

For Phase II of testing, the selected parameters were also fixed. As mentioned above, body stress (complex load situation) was used and evaluated to prove the hypothesis and the statement that a complex load should be one of the main drivers for critical crack propagation.

- Chapter 2** describes the specimen used and the naming within the report, important excerpts of the manufacturing and the initial measurements in advance of the test as well as deviations to the final test plan [8], if any
- Chapter 3** describes the deviation and adaptation of the test benches used
- Chapter 4** points out the changes in testing in relation to the final test plan [8] that became necessary
- Chapter 5** presents the test and simulation results
- Chapter 6** summarizes the results, concludes the recommendation for application, and proposes a way forward based on the outcome of this report

2. Specimens

For the proposed test, it was decided to use two different specimen geometries. One of them was an outer ring of a bearing representing an integrated outer race of a bearing, which was geometrically adapted on its outside contact area for Phase II to introduce the complex load situation (body stress). The testing of this geometry was conducted at the facilities of SKF Aviation, Valance. The other specimen was a solid shaft, representing an integrated inner raceway of a bearing. The same geometry was used for Phase II testing but was manufactured as a hollow shaft to introduce the complex load situation. The testing of this geometry was conducted at the University of Hannover, department IMKT.

Before the tests, a first article inspection (FAI) was performed on each specimen reference, and an additional dimensional report for each specimen was produced. All specimens, as well as the support bearings, were crack tested (NDT) before testing to check their behavior and minimize the risk of unwanted failure during the test. Further destructive measurements were performed to analyze the stress profile at several depths before the test by residual stress measurement up to a depth of 2 mm.

The hardening processes considered for the test specimen are in line with the applications used in aviation parts. In addition, the specific properties of the hardening processes support the evaluation of the specific parameter value ranges with different hardening depths and residual stresses.

2.1 Outer Ring

2.1.1 Outer ring for Phase I testing

The purpose of this specimen is to evaluate the integrated outer races (OR). All bearings consist of an inner ring and rolling element in M50, while the outer ring material is modified. Therefore, two materials usually considered for aerospace applications were selected: M50NiL and 32NCD13. In addition, to evaluate the influence of surface hardness, residual stress profile, and case hardening depth, one baseline and one lower value of each of these parameters were selected for the outer race. All variants are presented in Table 1, and the associated detailed drawings are provided in Appendix Annex A .

In addition, for each variant, one outer ring was subjected to destructive tests to check the surface hardness, the residual stress profile (measured to a depth of 2mm), and the case hardening depth at three points evenly distributed at 120° around the OR).

Description		M50NiL	32CDV13
Treatment/Surface variant	Baseline	9	9
	Reduced surface hardness	3	3
	Reduced residual stress	3	3
	Reduced case hardening depth	3	3

Table 1: Number of Outer race specimens to be tested for Phase I per variant

For each material, four different versions were manufactured, as shown in the following table. Three parameters were actually modified with manufacturing process adaptations to evaluate their influence on the spall characteristics. The parameters modified are raceway surface hardness (impacting hardness in depth too), carburizing/nitrating hardening depth, and surface residual stress. Table 2 gives an overview of the planned and obtained specimen parameters (hardness, CHD and residual stress are presented as <target value> / <obtained value>), highlighting deviations in red if applicable. As most of the parameter variations were introduced by modification of the usual and known process steps according to adjustments of the manufacturing process (see Table 2), it was challenging to meet the previously planned values by the first

manufacturing batch. Due to the time constraints within the project, all deviations were accepted without rework or re-manufacturing with a modification of the processes. The assessment and conclusions have been adapted accordingly (see 5.6).

Pos.	Variant	Manufacturing approach	Material	Code	Hardness	CHD [mm]	Surface residual stress*
1	baseline	current aviation standard	M50NiL	B	700-800 HV1 / 760 HV1	0.7-1.3 / 0.71	-700 / -490
2	baseline	current aviation standard	32CDV13	DA	720-850 HV0.5 / 760 HV0.5	0.5-0.9 / 0.56	-700 / -490
3	hardness	heat treatment process adjustment	M50NiL	BB	650-700 HV1 / 690 HV1	0.3-0.8 / 0.56	-700 / -490
4	hardness	heat treatment process adjustment	32CDV13	DC	650-720 HV0.5 / 730 HV0.5	0.5-0.9 / 0.54	-700 / -490
5	CHD	heat treatment process adjustment	M50NiL	BA	700-800 HV1 / 689 HV1	0.7-1.3 / 0.56	-700 / -490
6	CHD	heat treatment process adjustment	32CDV13	DB	720-850 HV0.5 / 720 HV0.5	0.4-0.7 / 0.47	-700 / -490
7	Res. stress	adjustment of surface finish process	M50NiL	BC	720-850 HV1 / 739 HV1	0.5-0.9 / 0.59	-400 MPa minimum / -690 MPa
8	Res. stress	adjustment of surface finish process	32CDV13	DD	700-800 HV0.5 / 780 HV0.5	0.5-0.9 / 0.56	-440 MPa minimum / -460 MPa

*for project time restrictions, only surface residual stress was measured using the value at the surface as an indicator for confirming the complete residual stress profile (baseline profile was measured as reference)

Table 2: Overview of specimen parameter and changes in accordance with the final test plan

2.1.2 Specific design of the outer ring for phase II of testing/test bench '1'

The overall dimensions of the specific test specimens are shown in Annex A.3. To induce the complex load situation on test bench '1', the design of the specimen was adjusted by a notch/groove at the outer ring to enable the outer ring to bend under the roller load, as shown in Figure 1, Table 3, and Figure 2.

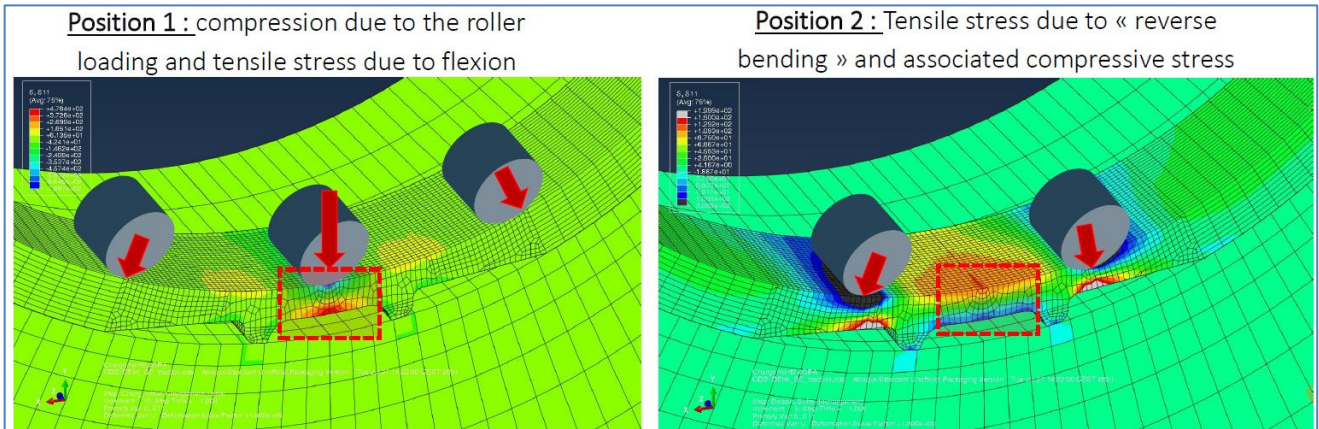


Figure 1: FE-analysis of complex load situation for test bench '1' [4]

Version T102 C		
S11 Stress range	Race surface [MPa]	Bottom Point [MPa]
Max	193	733
Min	-2400	-128
Version T104 A		
S11 Stress range	Race surface [MPa]	Bottom Point [MPa]
Max	109	465
Min	-2400	-75

Table 3: FE-analysis of complex load situation for test bench '1' [4] at 2.4 GPa

The number of tests for each specimen is shown in Table 4. Based on the results of Phase I, six specimens of the variant baseline (same hardness and hardness depth of baseline) of each material were tested. Three of the specimens were in accordance with geometry 102 (Figure 2 and A.3), and the other three specimens were in accordance with geometry 104 (higher thickness of the notch shown in Figure 2), which is less severe according to bending deformation. For a comparison of residual stress profiles see 2.3.2.3

	Description	Geometry/Code	M50NiL	32CDV13
Treatment/Surface variant	Baseline – severe design acc. body stress	102	3	3
	Baseline – less severe design acc. body stress	104	3	3

Table 4: Number of outer race specimens to be tested for Phase II per variant

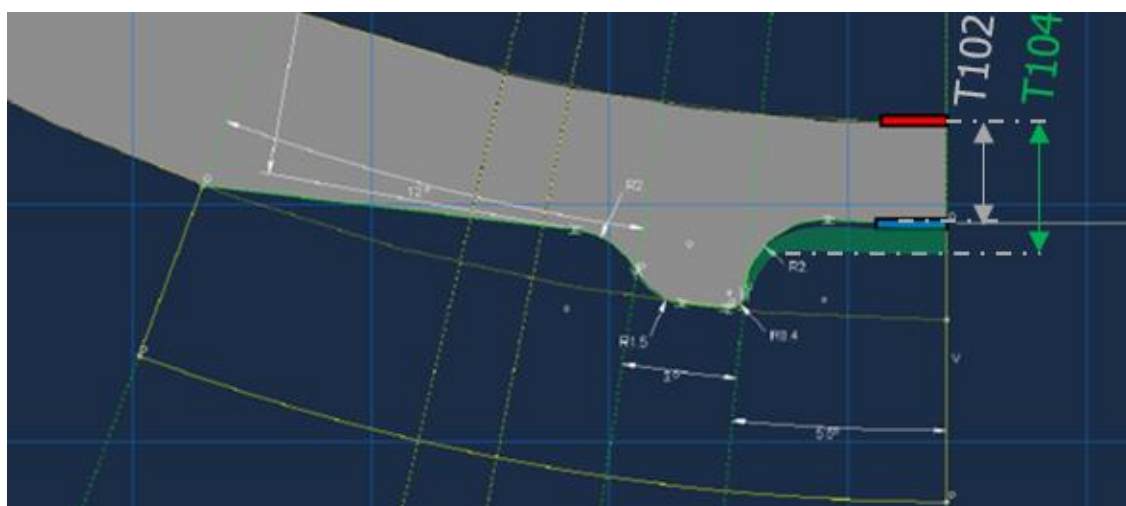


Figure 2: Specific geometry 102 for test bench '1' [4]

The specific notch for Phase II was manufactured by electrical discharge machining (EDM) and was applied and adapted after manufacturing the baseline specimen (Code B and DA). By this thermoelectric process, the material was removed from the specimen through a series of recurring rapid current discharges between electrodes, which were separated with a dielectric fluid, as shown in Figure 3. An example of the specimen is shown in Annex A.3.

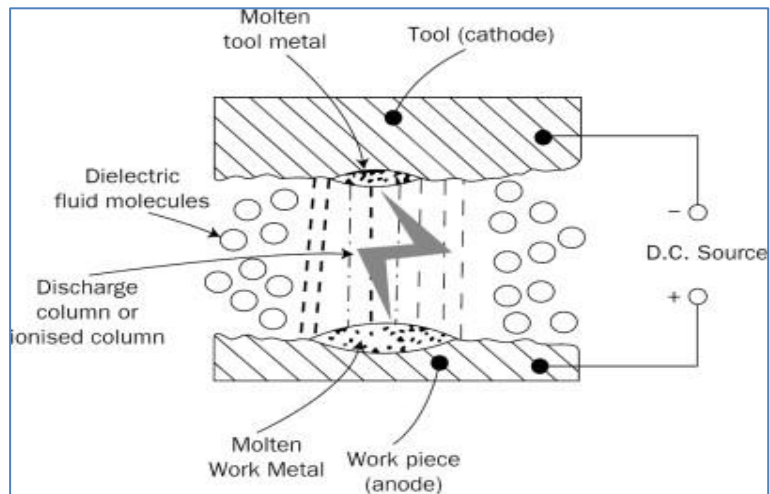


Figure 3: Basic principal of EDM procedure [8]

2.1.3 Manufacturing steps

To illustrate and highlight the different, sequential manufacturing steps of the specimens, Figure 4 is presented. The steps indicated are mandatory for the detailed properties of the specimen and need to be considered while applying any results from this research project to other applications and components and when interpreting the residual stress measurement results. The steps described below essentially represent the current state of the art for bearing manufacturing for the aviation industry (except specific changes for parameter variation and notch production for Phase I.1 and Phase II).

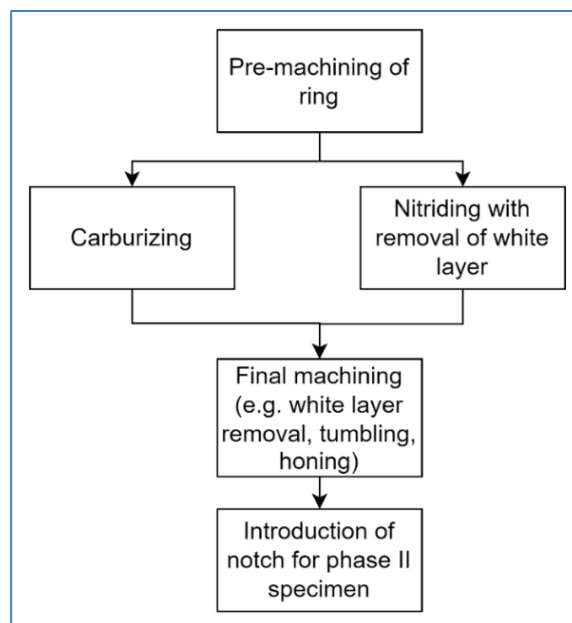


Figure 4: Manufacturing steps for ring specimens

2.2 Shaft

2.2.1 Shaft (solid) for Phase I of testing

The purpose of the test specimen used on test bench '2' was to evaluate integrated inner races.

The geometry of the test specimen was intended to validate the basic thesis in D2-2 [4] that, under pure rolling contact fatigue conditions (i.e. no body stresses), no crack propagation into the body is possible. Therefore, a solid shaft was manufactured to isolate pure rolling contact conditions from complex loading (bending of the shaft/raceway) and the impact of the residual stress profile (tensile stress), as both are anticipated to be limited by the solid geometry.

The selection of materials and surface treatments are identical to those used for bearings for bench '1', except that 16NCD13 was used instead of M50NiL, as M50NiL is not commonly used on rotorcraft gearbox shafts with integrated races, but 16NCD13 is. All variants are presented in Table 5, and the associated detailed drawings are provided in Annex A.2.

	Description	16NCD13	32CDV13
Treatment/Surface variant	Baseline	9	9
	Reduced surface hardness	3	3
	Reduced residual stress	3	3
	Reduced case hardening depth	3	3

Table 5: Number of inner race specimens to be tested for Phase I per variant

Measurements were carried out to check the initially anticipated specimen parameters (Table 6; (hardness, CHD and residual stress are presented as <target value> / <obtained value>) compared with the parameters that were reached after adjustments due to manufacturing limitations. Deviations are highlighted in red if applicable. As most of the parameter variations were introduced by modification of the usual and known process steps by modifications to the manufacturing process (see Table 6), it was challenging to meet the previously planned values by the first manufacturing batch. Due to the time constraints within the project, all deviations were accepted without rework or re-manufacturing. The assessment and conclusions have been adapted accordingly (see 5.6).

Pos.	Variant	Manufacturing approach	Material	Code	Hardness	CHD [mm]	Residual stress profile
1	baseline	current aviation standard	16NCD13	V1	58 HRC / 58-59 HRC	1 / 0.75	baseline / see Figure 5
2	baseline	current aviation standard	32CDV13	V2	>700 HV1 / 943-982 HV1	0.2...0.25 / 0.43	baseline / see Figure 5
3	hardness	adjustment of heat treatment process	16NCD13	V3	63 HRC / 58-59 HRC	1 / 1.03	baseline / see Figure 5
4	hardness	adjustment of heat treatment process	32CDV13	V4	>700 HV1 / 866-955 HV1	0.3...0.4 / 0.58	baseline / see Figure 5
5	CHD	adjustment of heat treatment process	16NCD13	V5	58 HRC / 58-59 HRC	0.15 / 0.89 --> increased by salt bath hardening	baseline / see Figure 5
6	CHD	adjustment of heat treatment process	32CDV13	V6	>700 HV1 / 962-982 HV1	0.1...0.15 / 0.41 --> increased by nitro carburizing process	baseline / see Figure 5
7	Res. stress	use of intermediate heating for stress relief	32CDV13	V10.1	>700 HV1 / 880-895 HV1	0.2...0.25 / 0.43	Modification with intermediate heating / see Figure 5
8	Res. stress	use of intermediate heating and additional surface finish (surface rolling)	16NCD13	V11	58 HRC / 65 HRC	1 / 1.11 --> increased by additional surface rolling	Modification with intermediate heating and surface rolling / see Figure 5

Table 6: Overview of specimen parameter and changes in accordance with the final test plan [8]

For the residual stress profile, it was possible to keep the profile similar for all the baseline residual stress profiles (see position 1-6 of Table 6). Nevertheless, small deviations could not be avoided, so the profiles were not fully identical.

However, adaptations of residual stress profiles within V11 and V10 (compared to the baseline variants) could be reached within a certain range (see Figure 5).

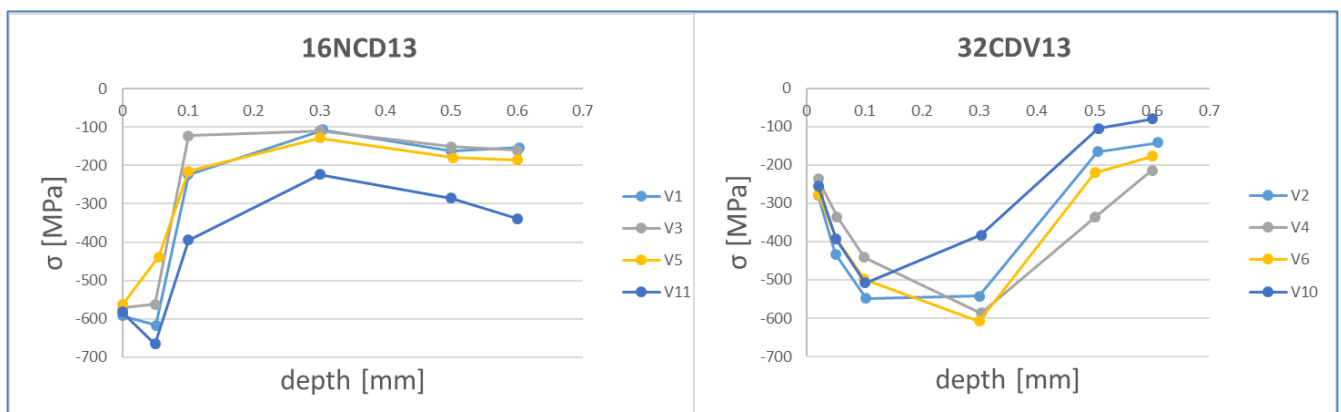


Figure 5: Residual stress profiles for specimens of phase I

2.2.2 Specific design of the shaft (hollow) for phase II of testing/test bench '2'

To introduce the complex load situation (body stress) on test bench '2', the solid shaft specimen (Annex A.4) was replaced by a hollow shaft to enable the application of a bending load and bending stress on the shaft, as shown in Figure 6. The body stress conditions alternate between 0 and 180 MPa.

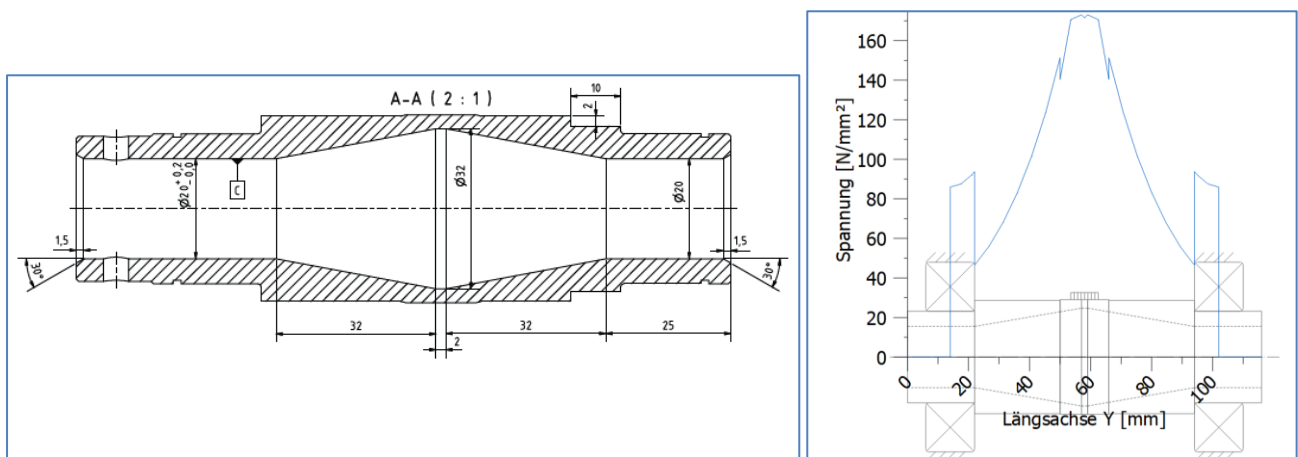


Figure 6: Bending stress profile for hollow shaft

The number of tests for each specimen is shown Table 7. Six specimens of each material were tested in two different load steps based on the results during testing.

Description		Load step	16NCD13 Code V1.2	32CDV13 Code V2.2
Treatment/Surface variant	Baseline	A	3	3
		B	3	3

Table 7: Overview of test specimen variants of the hollow shaft (Phase II)

After manufacturing, the hollow shafts were checked against the planned and achieved parameter values, with deviations highlighted in red (see Table 8). Considering the deviations for the solid shafts (Table 6), it was possible to reach almost the same parameter values for the hollow shafts.

Pos.	Variant	Material	Code	Hardness	CHD [mm]	Residual stress profile
1	Baseline - hollow	16NCD13	V1.1	58 HRC / 58-59 HRC	1 / 0.85	baseline / see Figure 11
2	Baseline - hollow	32CDV13	V2.1	>700 HV / 903-950 HV1	0.2...0.25 / 0.42	baseline / see Figure 12

Table 8: Overview of the specimen parameter and the changes according to final test plan [8]

Because most of the parameter variations were introduced by modification of the usual and known process steps, it was challenging to meet the previously planned values by the first manufacturing batch. Due to the time constraints within the project, all deviations were accepted without rework or re-manufacturing. The assessment and conclusions have been adapted accordingly (see 5.6).

2.2.3 Manufacturing steps

To illustrate and highlight the different and sequential manufacturing steps of the specimens, Figure 7 is presented. The given steps are mandatory for the detailed properties of the specimen and need to be

considered while carrying over any results from this research project to other applications and components, or when interpreting the residual stress measurements correctly. The described manufacturing steps are essentially the current state of the art in the aviation industry (mainly for shaft and gear applications), with the exception of specific changes that were made to reach parameter variations (phase I.2 and Phase II).

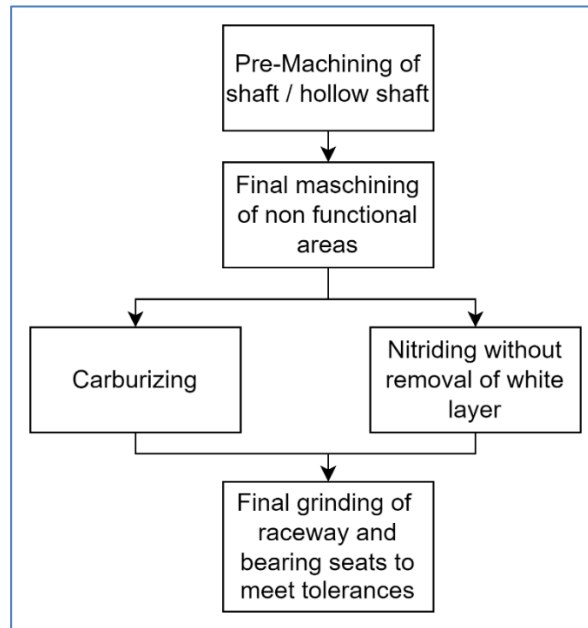


Figure 7: Manufacturing steps for shaft prototypes

2.3 Residual stress measurement

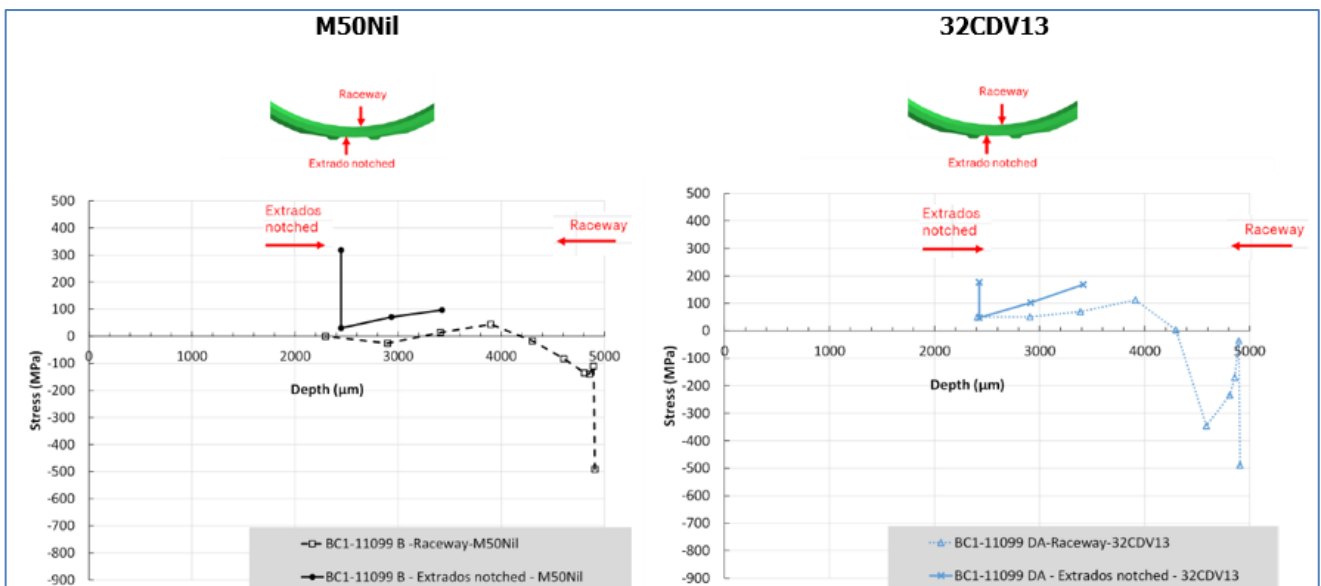
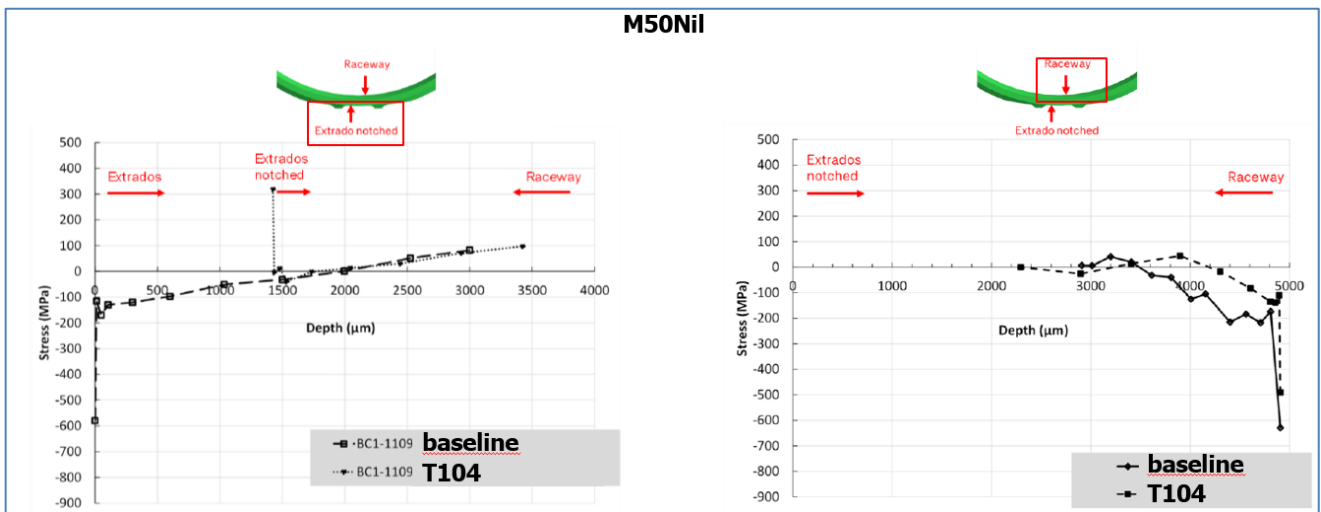
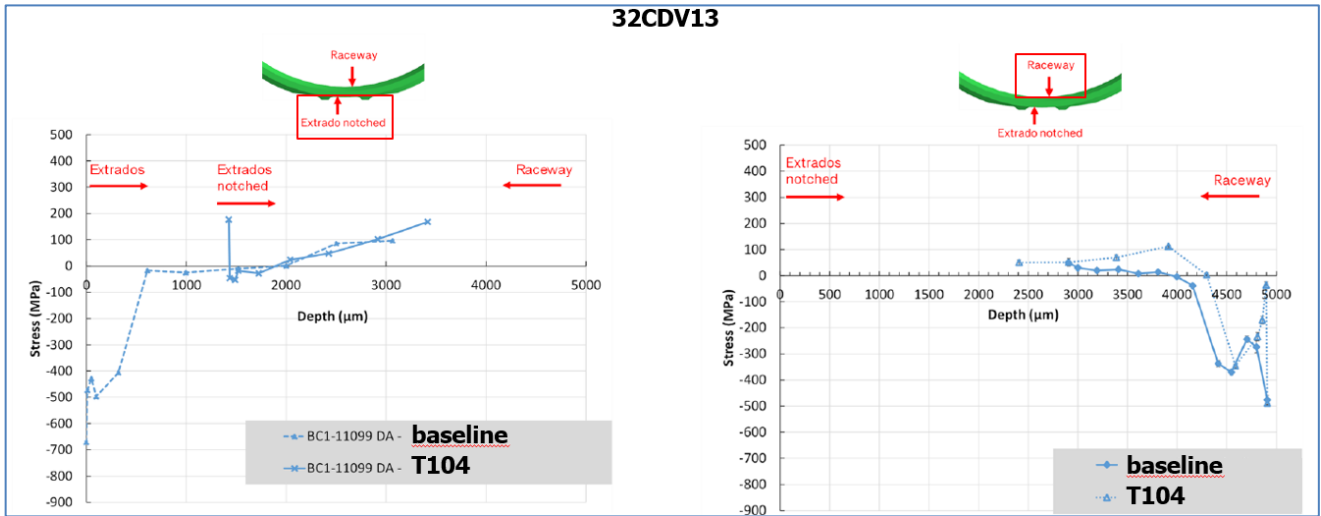
2.3.1 Residual stress measurement outer ring

For the residual specimens of Phase I, surface residual stresses were measured before testing on separate specimens by X-ray. For Phase II both notch design specimen, the circumferential residual stress were measured at the center of the notch, in addition.

The general measurement were performed first from the outer diameter side (Extrados), after which the ring was cut to allow the measurement from the raceway side (Raceway). Figure 8 to Figure 10 report the raw data measurements made for both materials and designs, including a comparison of baseline vs. notched ring T104. It can be observed that the baseline and both notched designs show similar residual stress profiles.

The x-axis origin corresponds to the surface of the outer ring without notch machining. On the raceway side, it is possible to observe the effect of the nitriding and carburizing processes; and on the outer diameter, it is possible to observe the presence of positive residual stress on the surface (Extrados) due to the EDM process. As a limitation, it is important to underline that both measurements (Extrados and Raceway) were performed on the same ring, side by side in the notch area with limited space, allowing for some possible interactions between the two measurements. In addition, the measurements were performed at an extended depth for the simulation, which is not a common depth for residual stress measurement. These two conditions mean that the data at significant depths must not be considered necessarily accurate.

Both measurement profiles are used for the simulation described in chapter 6 by taking into account some conservative assumptions. Further information on issues related to residual stress measurements can be found in 2.3.3.



2.3.2 Residual stress measurement shaft

In addition, the residual stress profile was measured before testing on separate specimens. The measurement of the residual stress depth profile by X-ray diffraction was performed in the following (nominal) depth steps: 0, 50, 100, 300, 500, 600 μm . The individual measuring depths were created by electrolytic material removal using a suitable electropolishing device, and the resulting depths were determined using a calibrated dial gauge. This process is the same as that used for the outer ring specimen. Over the length range of the depth profile, the extended measurement uncertainty of the dial indicator is 3 μm . Figure 11 and Figure 12 report the raw data measurements for both materials. The profiles of the different variants of a material are slightly different; therefore, only the baseline results are presented. In addition, it can be seen that there is only a slight difference between the solid and hollow shafts. It is worth noting that the residual stress measurements were performed up to an extended depth to gain information for the simulation (similar to measurements for the outer ring), which is not a common depth. This is driven by the fact that the deeper the measurement, the larger the error due to mechanical material removal. This and additional limitations could lead to uncertainties in the measured values, whereas conservative values were chosen for the simulation (see 6). Further information on issues related to residual stress measurements can be found in 2.3.3.

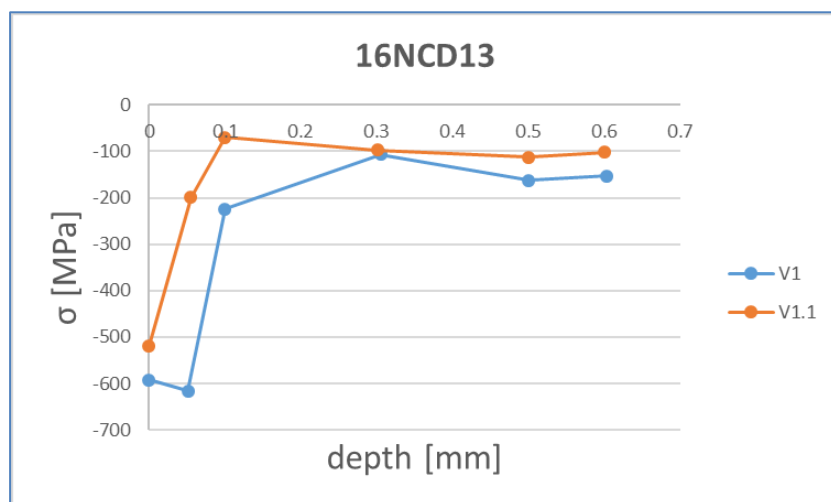


Figure 11: Residual stress measurement for solid (V1) and hollow (V1.1) shafts with 16NCD13 material

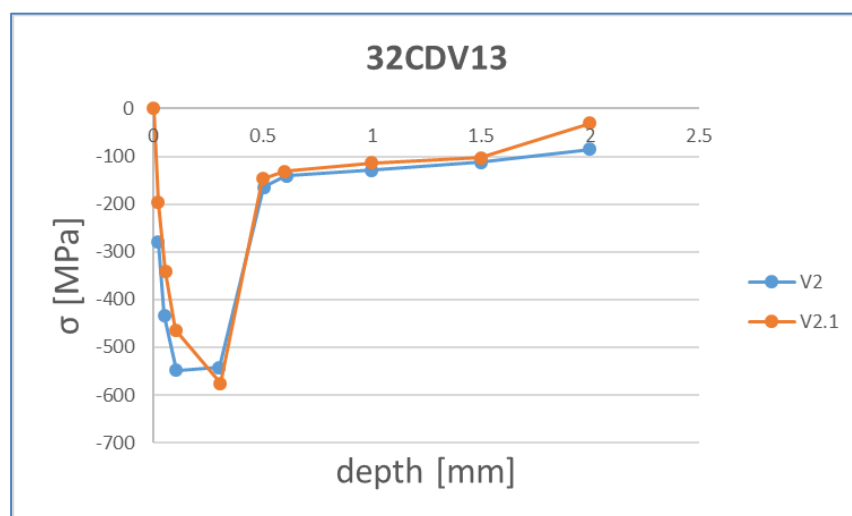


Figure 12: Residual stress measurement for solid (V2) and hollow (V2.1) shafts with 32CDV13 material

2.3.3 Residual stress measurement issues in equilibrium

Residual stress was defined as a key parameter to be evaluated during the test campaign of this research project. Therefore, investigations were conducted to change the residual stresses compared with the baseline specimens by the introduction of additional heat treatments or mechanical processing. For both applications (ring and shaft), X-ray measurements were performed to evaluate the stress state close to the surface layer, extending downward. This measurement was then performed from both sides of the raceway to clarify the stress distribution through the complete thickness of the component. In contrast to expectations, no equilibrium of compressive and tensile stresses was found for all measurements. Although there is a high compressive layer close to the surface, no significant tensile stress was found in the core of the specimens. As an explanation for these results, the following points are worth mentioning:

- For the bearing application, a final mechanical processing of the outer ring geometry (not the raceway side) is performed after heat treatment, which could have impacted the residual stress from this side. This type of manufacturing process is in accordance with the state-of-the-art technique for bearing manufacturing for the aviation industry.
- For the shaft application, a final mechanical grinding of the raceway is performed to meet the tolerances defined in the drawings, which could have impacted the residual stress distribution. This is also a common procedure in the aviation industry (e.g. final gear modification on teeth).
- Residual stress distribution is a three-dimensional problem, whereas the measurements were only performed orthogonal to the surface, extending downward. Measurements were performed only at one local area. It is possible that the area of the highest tensile stress was not covered by the measurement.
- Any measurement technique with mechanical material removal will impact the results, especially when going deeper into the material compared to the surface layer.
- To measure residual stress adequately from both sides of the raceways, both specimens were cut during measurement process. This was necessary, but could also have impacted the residual stress distribution.

As described in chapter 6, an equilibrium of residual stresses was used for the simulations as a conservative approach, considering the above-mentioned points.

3. Test bench

Two different test campaigns were conducted in parallel. The monitoring system of both benches was calibrated, and the measurement uncertainty of the measured values was identified and documented at the supplier level. Schematic measuring points (position and orientation) were also identified.

3.1 Test bench '1' for outer ring specimen

The test campaign on test bench '1' focused on the outer raceway of the test bearing in different material configurations and was performed on a simplified bearing test bench, as shown in Figure 14. It consists of a rotational shaft equipped with three bearings. Two of the bearings are support bearings, and the one in the middle is the test bearing. The rotational shaft was driven by a belt and an electric motor. The bearings were lubricated with two injectors mounted at the top of the test head. In addition, a hydraulic actuator was mounted on the test head, applying a radial force of up to 70 kN to the test bearing.

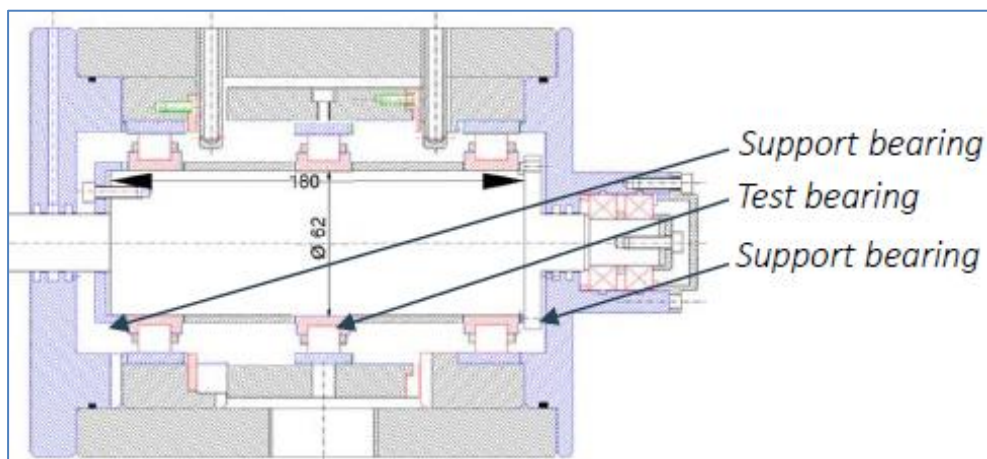


Figure 13: Test bench '1' test head

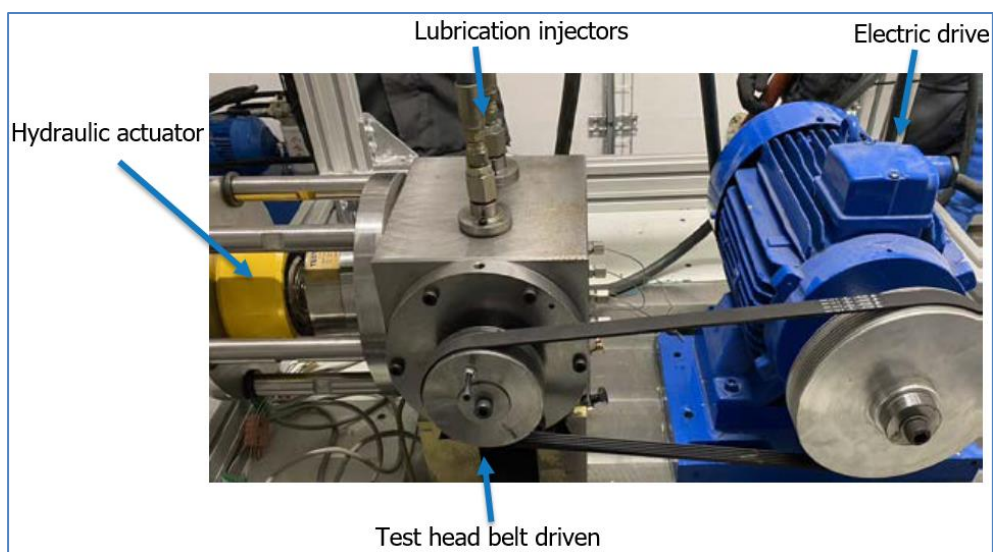


Figure 14: Test bench '1'

Figure 14 and Figure 15 show the setup of test bench '1', as well as the control application and the monitoring system. The descriptions of the different sensors and their functions are given in Table 9.

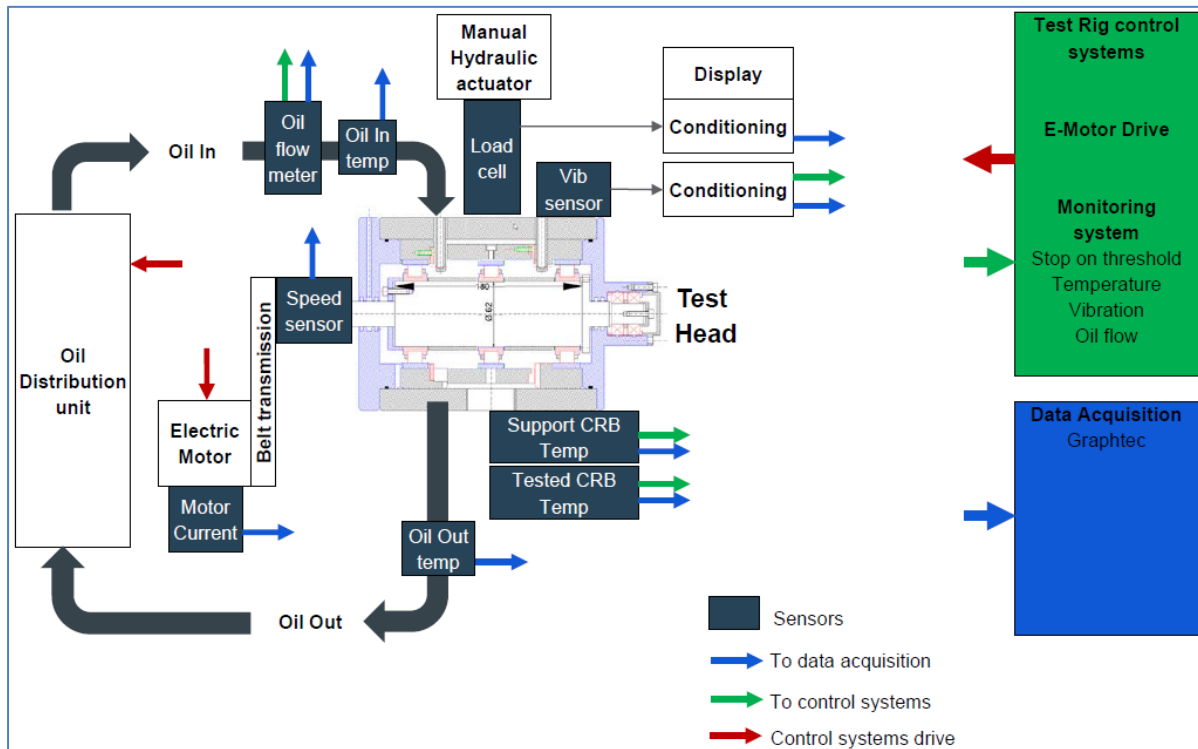


Figure 15: Test bench '1' monitoring & control system (schematic view)

Sensors	Description	Function		
		Test Rig protection	Test Operating condition verification	Test purpose (Spall detection)
Load cell	Load cell monitoring the load applied on the tested CRB bearing by the hydraulic actuator. The conditioning unit provides the display and the analog signal for data acquisition and test rig control systems. Check operating condition according to the required test case load.			
Vib sensor	Accelerometer measuring the radial vibration on the test head. The conditioning unit provides the peak-peak value of the signal. Stop the test rig in case of increase. Detect a spall which makes the Peak-Peak value increase.			
Speed sensor	Hall effect sensor measuring the rotating speed. Check the operating condition speed according to the required test case.			
Motor Current	Sensor measuring the e motor current. Stop the test rig in case of over current.			
Oil flow meter	Oil flow meter measuring the oil flow to the test head. Check operating condition oil flow according to the required test case. Stop the test rig in case of incorrect oil flow;			
Oil In Temp	Thermocouple measuring the temperature of the oil entering in the test head. Check the operating condition temperature according to the required test case.			
Oil Out Temp	Thermocouple measuring the temperature of the oil exiting the test head. Check indicatively the heat removed by the oil flow.			
Support CRB Temp	Thermocouple measuring the temperature of the outer ring of the support CRB. One sensor per support CRB. Stop the test rig in case of overheating.			
Tested bearing Temp	Thermocouple measuring the temperature of the outer ring of the tested bearing in the loaded zone. Check the operating condition temperature according to the required test case. Stop the test rig in case of overheating.			

Table 9: Sensor description

Implementation of a chip detector in the test bench setup was evaluated before the test as an additional indication tool for detecting spalling.

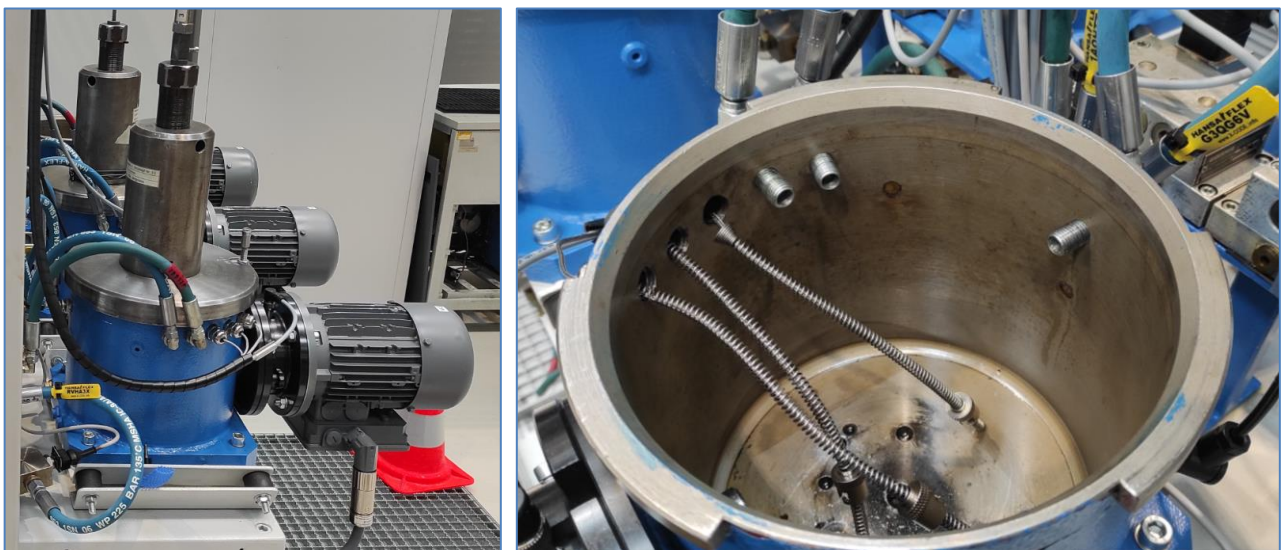
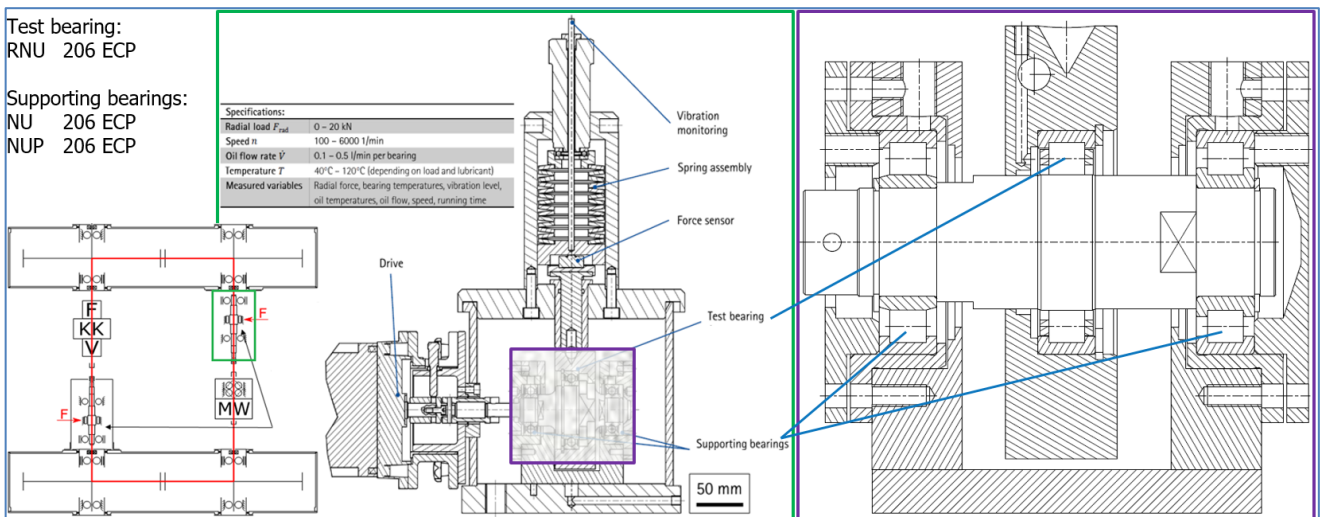
No deviations between the actual test bench setup and the planned one [8] occurred during testing.

3.2 Test bench '2' for shaft specimen

The test campaign on test bench '2' focused on the inner raceway of a bearing and material combinations and was performed on a test bench capable of a heated lubrication circuit. This circuit included a filter system which was able to monitor temperature and vibration levels as well as oil flow, oil temperature and speed.

This test bench likewise consisted of two support bearings and a test bearing in the middle (Figure 16), but with an integrated raceway on the shaft specimen. A radial force was introduced by the spring assembly pushing on the test bearing with a maximum force of 20 kN. At a maximum radial load of 20 kN and along with the bearing clearance, a maximum roller load of 7810 N was present. In total, five rollers carried the introduced load. Figure 17 also shows the existing test bench.

Implementation of a chip detector in the test bench setup was evaluated before the test as an additional indication tool for detecting spalling.



Furthermore, a monitoring system was attached to the test bench for each test position. The system recorded radial vibrations at the 'F' position and the constant time signal is transformed into the frequency spectrum via FFT, and the RMS is generated, as shown in Figure 18. If a threshold level was exceeded (e.g. an increase in the signal by 100% after the run-in Phase), the system was switched off.

The vibration signal was used to detect the potential begin of spalling and/or to protect the test bench from extreme vibrations and damage caused by abnormal running conditions.

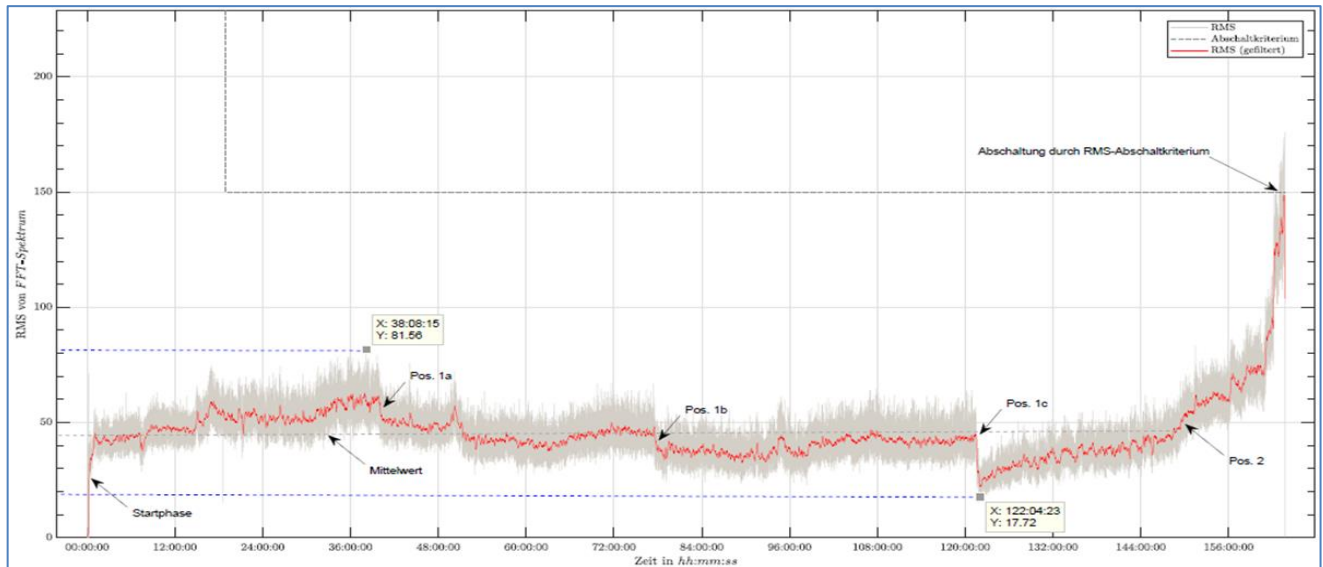


Figure 18: Test bench '2' stop criteria definition (example)

A deviation between the actual test bench setup and the planned one [8] did not occur during testing.

4. Test plan

The following test procedure considers Phase I and Phase II of testing and outlines the definition of the procedure in more detail. Deviations to the final test plan [8] are highlighted by red and “(**)” “(***)”.

4.1 Phase I.1

Phase I.1 of testing focused on the variation of contact pressure, whereas the other parameters were adjusted and fixed according to predefined baseline values. For this purpose, high, medium, and low contact pressure values were evaluated in test Phase I.1. The main procedure and general information of this test Phase are summarized in Table 10 and Figure 19.

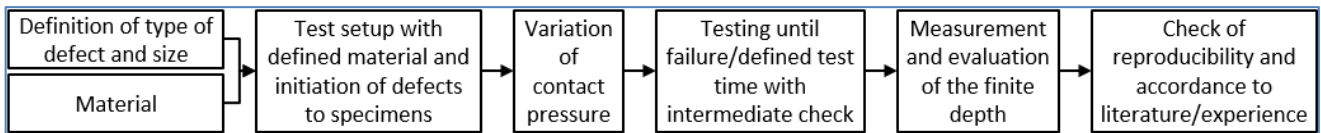


Figure 19: Definition of phase I.1 procedure

Crack initiation	From surface defect to the initiation of a crack	
Pre-damage	Predefined indent sizes: critical (quick spalling initiation) Creation of a line with several indents on the raceway	
Boundary conditions	Speed '1' / '2' [rpm]:	8000 / 5500-6000
	Temperature '1' / '2' [°C]:	70-80
	Oil type	AH Tech AirGo 3001
	Lubrication assessment '1'/'2' to minimize lubrication impact(*)	$\lambda > 2$ / $\kappa > 1.7$
Contact pressure level [MPa]	3 levels to be tested:	
	- Minimum:	1500 MPa(**)
	- Mean:	1800 MPa(**)
	- Maximum:	2400 MPa
Materials	Test bench '1':	
	Material variation only on the outer ring:	M50Nil, 32CDV13
	Inner ring, only 1 material:	M50
	Rolling element, only 1 material:	M50
	Test bench '2':	
	Rolling element material:	M50
	Shaft material:	16NCD13, 32CDV13
Surface hardness (***)	- Baseline level only	values see 2.1 and 2.2
Residual stresses (***)	- Baseline level only	values see 2.1 to 2.3
Case hardening depth (***)	- Baseline level only	values see 2.1 and 2.2

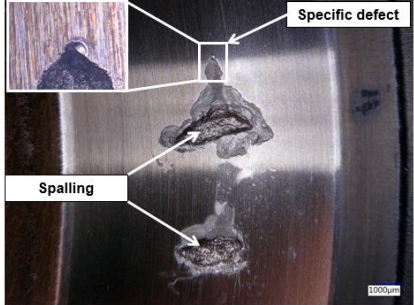
Crack initiation	From surface defect to the initiation of a crack
Repetition	Minimum repetitions to support a trend: 3
Specimen quantity per test bench	3 (contact pressure) x 2 (material) x 3 (repetitions) = 18
Max. test duration (what occurs first)	Max. crack propagation time (T2) on initial defect or 200 000 000 load cycles (**)
Test completion criteria	Detection of the first spall is important: T1 Max. crack propagation time: T2 = T1 + 60(****) minutes
Spall detection	Variation of vibration level / exceedance of threshold - pitting too small compared to Figure 20 (<15 mm ²), e.g. (micro-)pitting = relaunch of test  <i>Figure 20: Spalling example [8]</i> - No spall detection = relaunch of test until max. test duration
Inspection/Investigation	T1: Visual identification of spalling acc. to Figure 20 T2: Visual (NDT) / Measurement of crack depth (DT) (for all test specimens at the end of test): '1': Metallurgical/destructive testing (cut of specimen) '2': Laser scanning/ultrasonic microscopy/destructive testing (cut of specimen)

Table 10: Parameters of phase I.1 testing

(*) Because the running conditions are simple due to the constant load (constant rotation speed, only rotating bending load without alternating loads or shocks) and the component geometry and tolerances are well chosen to minimize eccentricity, the lubrication condition was considered to be appropriate. Nevertheless, the components were visually checked after the first tests with regard to sufficient lubrication film thickness. Because no wear marks were visible besides the normal spalling surface, the lubrication impact was considered negligible.

(**) Deviation to final test plan: Test not performed, as no damage occurred during initial testing at 1800 MPa.

(***) Different level profiles are based on the available manufacturing processes, which have already been taken into account. In addition, the specimen with independent variation of parameters stayed within the limits of certified aviation processes. The final values were checked and documented after the manufacturing process (Table 2, Table 6).

(****) This value is based on broad testing experience, e.g., similar test campaigns at SKF. The aim of this value is to give the initial spall time to slightly propagate on the raceway, without destroying the raceway or damaging the test bench due to vibrations. Finally, it was evaluated through testing by several intermediate checks, and

an appropriate value of the propagation time was determined for further testing. However, if the vibrations were too high before reaching the value, the test was stopped.

4.2 Phase I.2

Phase I.2 of the test campaign was continued on the two selected test benches with new specimens. No change was made to the boundary conditions or the introduced pre-damage. The tests were carried out for all selected material combinations, similar to Phase I.1. The focus of this Phase was on the variation of hardness, residual stress, and hardening depth to evaluate their influence on crack initiation, depth, and shape. The main procedure and general information of this test Phase are summarized in Table 11 and Figure 21.

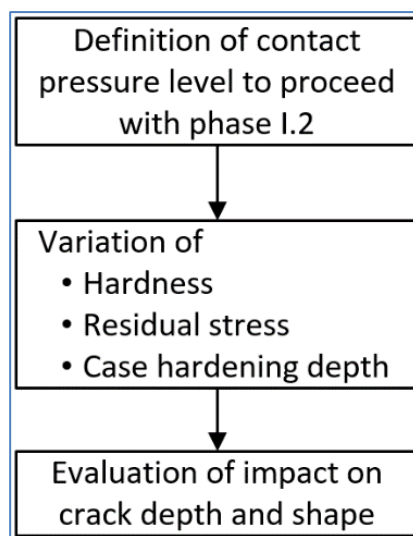


Figure 21: Definition of phase I.2 procedure

Crack initiation	Crack network grows and propagates but to a limited depth
Pre-damage	Same as Phase I.1
Boundary conditions	Same as Phase I.1
Contact pressure level [MPa]	- 2400 MPa; defined acc. to Phase I.1 results
Materials	Same as Phase I.1
Surface hardness (***)	2 levels (***) - Baseline level - Changed level For 32CDV13 shafts, no change in surface hardness was possible (>700 HV); two levels of NHD were tested instead (detailed values according to chapter 2)
Residual stresses (***)	2 levels (***) - Baseline level - Reduced compressive and tensile stress level (detailed values according to chapter 2)
Case hardening depth (***)	2 levels (***) - Baseline level - Reduced level (detailed values according to chapter 2)
Repetition	Minimum repetitions to give a trend: 3
Specimen quantity per test bench	1 x (Contact pressure baseline level) x 3 (parameter reduced level) x 2 (material) x 3 (repetitions) = 18
Max. test duration (what occurs first)	Same as Phase I.1
Test completion criteria	Same as Phase I.1
Spall detection	Same as Phase I.1
Inspection/Investigation	Same as Phase I.1

Table 11: Parameters of phase I.2 testing

(***) Different level profiles are based on the available manufacturing processes, which have already been taken into account. In addition, the specimen with independent variation of parameters stayed within the limits of certified aviation processes. The final values were checked and documented after the manufacturing process.

(****) The values presented are targets to be reached. Nevertheless, these values may not be exactly reached. The final values were evaluated following a destructive test on one sample of each combination of material/case hardening treatment/surface treatment. The values from these samples are considered to be identical for the tested specimens as variations are considered negligible, particularly as the manufacturing process was identical/frozen for all components to be tested.

4.3 Phase II

Phase II of testing focused on the introduction of a body stress (complex load) situation and the evaluation of the impact on crack propagation. The main procedure and general information of this test Phase are summarized in Table 12 and Figure 22.

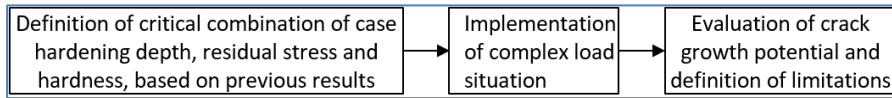


Figure 22: Definition of phase II procedure

Crack propagation	Crack propagation due to additional loading in complex load situation
Pre-damage	Same as Phase I.1/I.2
Boundary conditions	Same as Phase I.1
Contact pressure level [MPa] ^(6*)	- Maximum: 2400 MPa
Materials	Same as Phase I.1/I.2
Surface Hardness ^(7*)	Same as Phase I.1
Residual stresses ^(7*)	Same as Phase I.1
Complex load situation	2 levels - Approximate: see chapter 2 ^(8*) - Other stress level (option)
Case hardening depth ^(7*)	Same as Phase I.1
Repetition	Minimum repetitions to give a trend: 3
Repetition option	Additional repetitions of each material with other complex load level or geometry on baseline specimen: 3
Specimen quantity per test bench	1 (complex load situation) x 2 (material) x 3 (repetition) = 6 1 (complex load/geometry) x 2 (material) x 3 (rep. option) = 6
Max. test duration (what occurs first)	Same as Phase I.1/I.2
Test completion criteria	Same as Phase I.1/I.2
Spall detection	Same as Phase I.1/I.2
Inspection/Investigation	Same as Phase I.1/I.2

Table 12: Parameter of phase II testing

^(6*) The value was set on the basis of the results from Phase I, as lower contact pressure levels produce no spalling.

^(7*) The Phase II specimens were sent to manufacturing before Phase I testing was finalized and a conclusion was reached to meet the time frame of the project. Nevertheless, the surface hardness, the residual stress profile, and the case hardening depth were chosen as ‘baseline’ as no significant influence was found during the first test results of Phase I.2 and simulations (results shown in [7]), especially for the residual stress profile. The simulation results do not show a negative impact on crack propagation through the rim of the specimen. In any case, the target of Phase II was to evaluate the influence of adding a complex load situation and to compare it with the same variant without a complex load.

^(8*) In D2-5 [7], it is shown that there should be an impact with that load. According to the calculations, this load is sufficient.

Chapter 5 summarizes the tests conducted and their parameters linked to the related specimen.

5. Test results

5.1 General explanation/description

Phase I.1.1 was added to the test plan to describe the iterative approach to validate the value of '60 minutes' for $T_2=T_1+60$ minutes, which were introduced in Table 10 above during Phase I.1. This Phase is necessary to ensure that the appropriate time for T_2 is chosen and that the test would not be stopped too early and thereby cause essential results to be lost.

Therefore, the test duration for the first specimens was extended by several iterations of T_2 after the first spalling. After each T_2 iteration, the component was visually inspected and documented until 3 consecutive checks did not show a changed pattern of damage or the spalling surface reached a size of approximately 15 mm². The final size of the spalling surface stop criteria will be evaluated after the first results in accordance with the vibration signal and will be adapted if necessary.

The vibration signal was tracked in parallel to avoid inadmissible conditions for the test specimen and test bench. Going beyond a critical vibration signal would stop the test to protect the test bench.

This iterative test procedure must be repeated for each variant to ensure that changes in component and material properties are covered by an adaption of T_2 . For different repetitions, the determined T_2 could then be used without further adjustment.

A global overview of the test results is given in Table 13. The following chapters 5.2 to 5.5 describe the results and observations in more detail. The test results and measurements, including explanations and pictures, were taken from the dedicated reports of IMKT Hannover [11] and SKF aerospace [10].

Test phase	Material	Specimen	Version	Treatment/ Surface variant	Quantity	Contact Pressure	Reached cycles	Damage (visual inspected)
Phase I.1	M50Ni1	Ring	B- Version 1	Baseline	3	2400 MPa	115.1 M. 179.2 M. 55.5 M.	Surface: spalling
	M50Ni1	Ring	B- Version 1		1	1800 MPa	200 M.	n/a
	M50Ni1	Ring	B- Version 1		0	1500 MPa	Canceled	n/a
	16NCD13	Shaft	V1 V1 V1		3	2400 MPa	127.5 M. 70.1 M. 38.1 M.	Surface: spalling
	16NCD13	Shaft	V1 V1 V1		3	1800 MPa	200 M. 200 M. 200 M.	n/a
	16NCD13	Shaft	V1 V1 V1		3	1500 MPa	200 M. 200 M. 200 M.	n/a
	32CDV13	Ring	DA- Version 1		3	2400 MPa	58.6 M. 40.3 M. 36.8 M.	Surface: spalling
	32CDV13	Ring	DA- Version 1		1	1800 MPa	200 M.	n/a
	32CDV13	Ring	DA- Version 1		0	1500 MPa	Canceled	n/a

Test phase	Material	Specimen	Version	Treatment/ Surface variant	Quantity	Contact Pressure	Reached cycles	Damage (visual inspected)
	32CDV13	Shaft	V2 V2		1	2400 MPa	135.68 M.	Surface: peeling
	32CDV13	Shaft	V2 V2		2	1800 MPa	200 M. 200 M.	n/a
	32CDV13	Shaft	V2		1	1500 MPa	200 M.	n/a
Phase I.2	M50Ni1	Ring	BB- Version 4	Reduced Surface Hardness	3	2400 MPa	88.5 M. 57.1 M. 43.0 M.	Surface: spalling
	16NCD13	Shaft	V3		3	2400 MPa	32.31 M. 55.84 M. 84.31 M.	Surface: spalling
	32CDV13	Ring	DC- Version 4		2	2400 MPa	67.7 M. 48.4 M. 54.2 M.	Surface: spalling
	32CDV13	Shaft	V4		1	2400 MPa	1.1 M. 22.7 M. 14.6 M.	Surface: peeling
Phase I.2	M50Ni1	Ring	BA- Version 2	Reduced Case hardening depth	3	2400 MPa	45.5 M. 108.8 M. 106.0 M.	Surface: spalling
	16NCD13	Shaft	V5		3	2400 MPa	76.70 M. 86.71 M. 52.13 M.	Surface: spalling
	32CDV13	Ring	DB- Version 2		3	2400 MPa	47.5 M. 66.5 M. 31.0 M.	Surface: spalling
	32CDV13	Shaft	V6		0	2400 MPa	14.1 M. 97 M. 9.5 M.	Surface: peeling
Phase I.2	M50Ni1	Ring	BC- Version 3	Modified Residual Stress	3	2400 MPa	84.8 M. 43.5 M. 47.8 M.	Surface: spalling
	16NCD13	Shaft	V11		3	2400 MPa	107.8 M. 13.6 M. 67.7 M.	Surface: spalling
	32CDV13	Ring	DD- Version 3		3	2400 MPa	83.3 M. 78.3 M. 86.8 M.	Surface: spalling
	32CDV13	Shaft	V10.1		1	2400 MPa	11.5 M. 0.5 M. 41.8 M. 14.6 M.	Surface: peeling
Phase II	16NCD13	Hollow shaft	V1.1	baseline	3	2400 MPa	115.6 M. 82.9 M. 39.4 M. 32.4 M.	No spalling / no crack propagation
	16NCD13	Hollow shaft	V1.1		3	2900 MPa	9.4 M. 13.2 M. 1.2 M.	No spalling / finite crack
	32CDV13	Hollow shaft	V2.1		3	2400 MPa	35.8 M. 30.1 M. 5.4 M.	Finite crack / crack network to surface
	32CDV13	Hollow shaft	V2.1		3	2900 MPa	1.3 M. 0.6 M. 0.7 M.	Finite crack / crack network to surface
	M50Ni1	Ring with notch	T104		3	2400 MPa	2.1 M. 2.9 M. 2.2 M.	Spalling with through-crack

Test phase	Material	Specimen	Version	Treatment/ Surface variant	Quantity	Contact Pressure	Reached cycles	Damage (visual inspected)
	32CDV13	Ring with notch	T104		3	2400 MPa	113.3 M. 86.6 M. 115.6 M.	Spalling / no through-crack
	M50Ni1	Ring with notch	T102		3	1800 MPa	n/a 200 M. 200 M.	Spall with severe cracks / No spall-reaching suspension time
	32CDV13	Ring with notch	T102 Pre-test		1	2400 MPa		Spalling with through-crack
	32CDV13	Ring with notch	T102		1	1800 MPa	200 M.	No spall-reaching suspension time
	32CDV13	Ring with notch	T102		3	2400 MPa	n/a 200 M. 200 M.	Spalling without crack / No spall-reaching suspension time
Phase I.1	M50 Ni1	Ring	B- Version 1 – long duration	Baseline	1	2400 MPa	43.4 M.	Surface: spalling
	32CDV13	Ring	DA- Version 1 – long duration		1	2400 MPa	54.3 M.	Surface: spalling

Table 13: Overview table of tested specimens during GIFT project

5.2 Preparation of parts

5.2.1 Shaft

All shafts were pre-damaged according to the definitions in [8] using a diamond tip and a load of 100 N with a scratch over the entire raceway. Pre-tests were carried out to ensure that classical spalling damage would be initiated by this scratch in a short time to reduce the overall testing time. The indenter and scratch geometry are described in Figure 23 and Table 14.

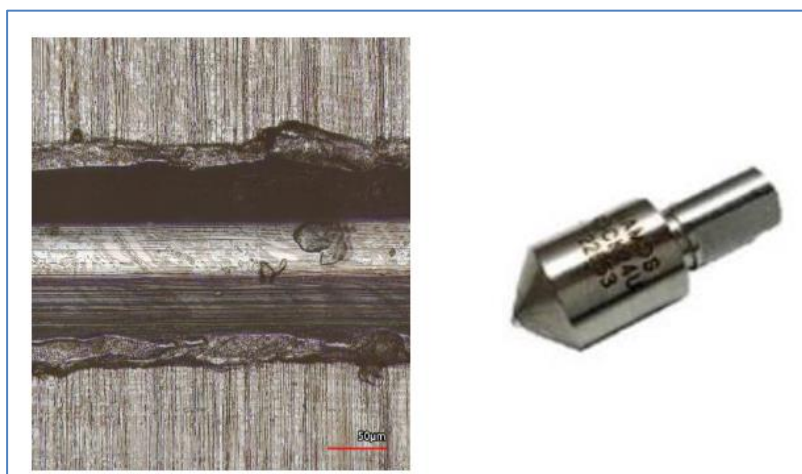


Figure 23: Indenter with scratch on the raceway

Depth	Shoulder high	Width without shoulders	Width with shoulders
23.8 μm	18.7 μm	83.6 μm	200.5 μm

Table 14: Dimensions of scratch for shaft specimens

5.2.2 Outer ring

The outer rings were pre-damaged with an identical indenter as for the shafts (see also [8]). The evaluation and selection of the right raceway damage was a key step of specimen preparation to generate quick spalling during testing. Therefore, several tests were performed in advance to validate the best performing geometry. The final scratch is introduced over the full raceway (see Figure 24) with the dimensions presented in Table 15.



Figure 24: Picture of raceway with scratch before the start of testing

Width	Depth	Shoulder height
175 \pm 18 μm	20 \pm 2 μm	3 to 12 μm

Table 15: Scratch dimensions for the outer ring

5.3 Phase I.1

As described in 1, Phase I.1 testing was performed to evaluate RCF for pure rolling contact for a case hardened and nitrided material at different load levels. The main focus for Phase I.1 is the evaluation and study of the maximum spalling depth and the tendency for crack propagation (into the core or back to the surface). The tests were performed for two types of specimens.

5.3.1 Shaft

For Phase I.1, the baseline version of the shaft specimens was tested for 16NCD13 and 32CDV13 material (V1 and V2). The case hardened shafts for V1 were first tested with the highest load level of 2.4 GPa, which all led to classical spalling damage. The vibrational stop criteria were set to the limit of the test bench so that a spalling dimension approximately equal to rolling element length was reached. The final spalling dimensions are summarized in Table 16.

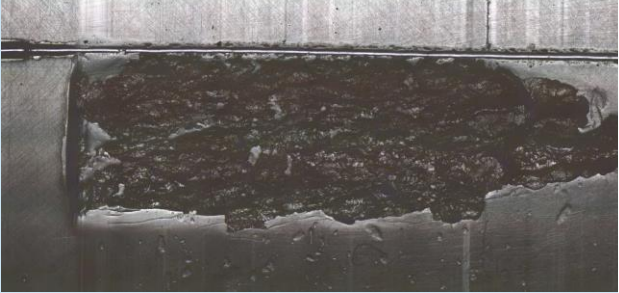
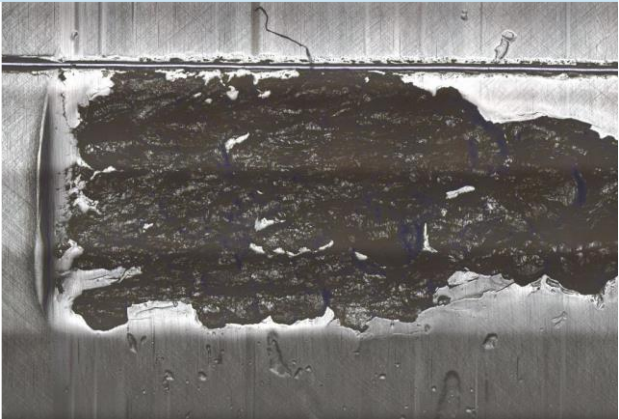
Version	Serial number	Spalling depth (max) [mm]	Width [mm]	Length [mm]	Spalling
V1	1	0.13	1.8	8	
V1	5	0.3	2.2	7.3	
V1	7	0.18	2.86	6.67	

Table 16: Overview of spall dimensions for V1 – phase I.1

A cut of specimen V1 with serial number 5 was performed to evaluate the depth of the damage and potential crack propagation into the material. No crack was found during deeper analysis of the specimen (Figure 25). There is no indication that further running time will lead to deeper spalling. It can be assumed that there will only be further breakouts.

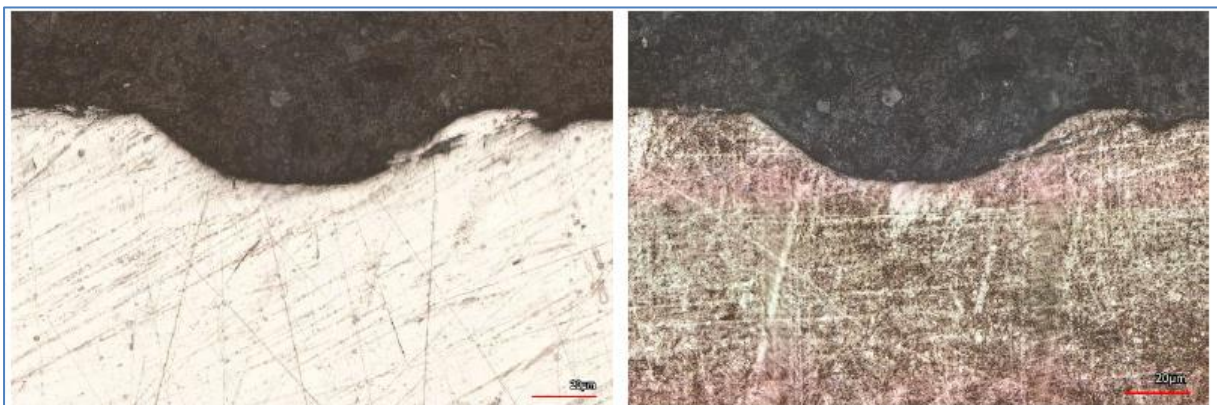


Figure 25: Example of a cut shaft for crack investigation – phase I.1

The vibration signal was tracked during the test to document the time needed for spall initiation (see Figure 26). All three shafts show similar behavior according to the vibrational signals with a constant curve for approximately 90% of the lifetime until a fast and rapid increase to the test bench limit. No specific relationship between the number of cycles and the spalling size could be determined based on the results.

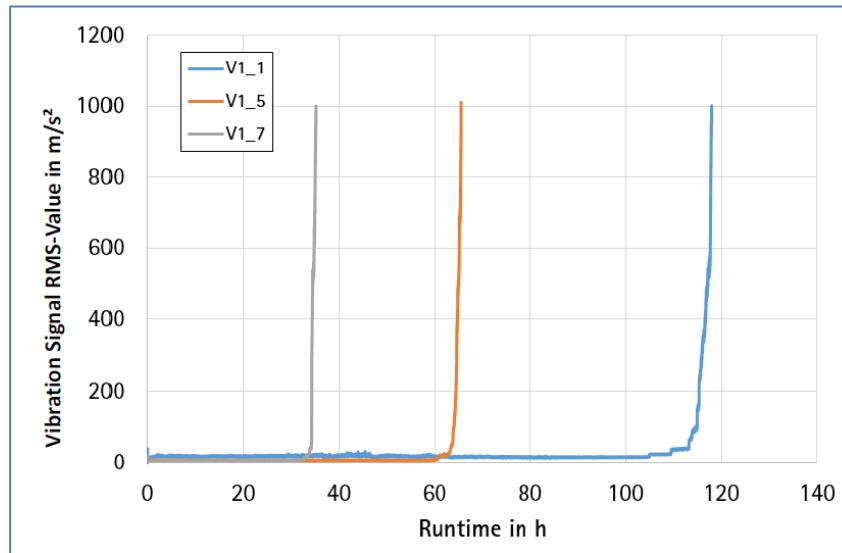


Figure 26: Vibration signal for phase I.1 at 2.4 GPa

Three additional shafts of V1 were tested at lower load levels of 1.5 and 1.8 GPa. For all bearings, the maximum running time of 200 million load cycles (185 h) was exceeded without any spall on the raceway. Except for flattening of the introduced scratch, the raceways were undamaged.

For the nitrided shafts (V2), identical tests were carried out by again starting with a high load level of 2.4 GPa. The test was stopped after 135 million cycles (about 125 h) because of an alarm on the installed chip detection sensor. The damage in this case was not classical spalling. The surface layer had peeled off and the area of damage was much larger than that of the case hardened shafts (compare Figure 27 and Table 17).

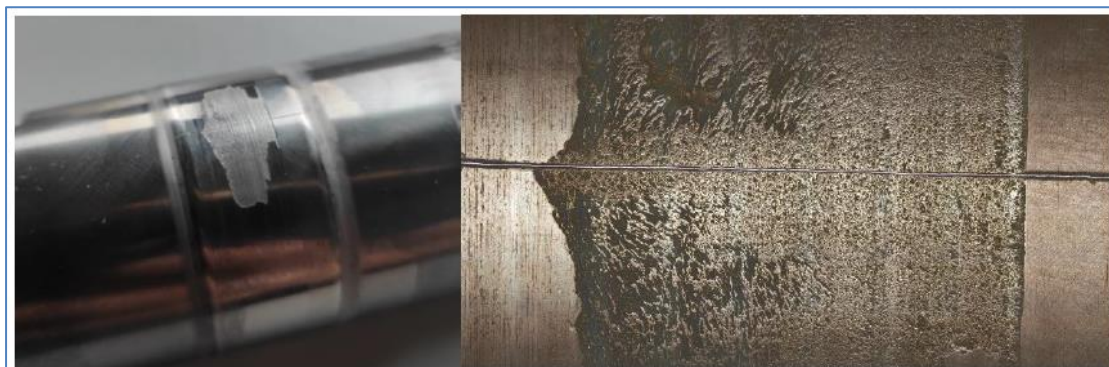


Figure 27: Peeled surface of the nitrided shaft at 2.4 GPa

Version	Serial number	Spalling depth (max) [mm]	Width [mm]	Length [mm]	Spalling
V2	1	0.096	>20 (peeling of surface)	8.62	

Table 17: Overview of spall dimensions of V2 – phase I.1

This secondary damage is induced by the white layer, which has a higher hardness (brittle) than the base material and, in combination with the pre-damage, it leads to flaking of the brittle white layer in both directions of the scratch. Moreover, severe damage was found during the inspection of the rollers due to the hard nitride particles in the contact zone.

In addition, the measured vibration signal showed an unexpected development (see Figure 28). This may also be a result of the breakout process of the white layer. Further tests at 2.4 GPa were initially interrupted for further investigations of the white layer (see A.5).

Two additional V2 shafts were tested at 1.5 GPa and 1.8 GPa to see if similar results would occur at lower load levels. All of them exceeded the maximum running time of 200 million cycles without damage.

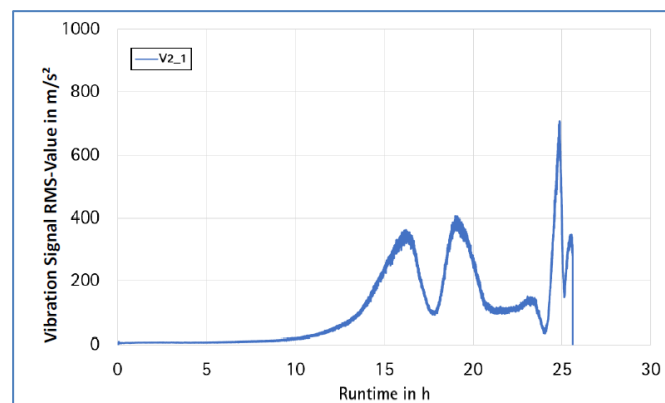


Figure 28: Vibration signal of V2 shaft at 2.4 GPa – phase I.1

5.3.2 Outer ring

For Phase I.1, two materials were tested according to the test plan described in [9]. The results for the M50Ni1 material at 2.4 GPa are summarized in Table 18. The results for 32CDV13 are presented in Table 19. For all of the rings tested at 2.4 GPa, a classical spall was observed and the test was stopped because of the vibration limit of the test bench. For most of the bearings, the evaluation of the maximum spalling depth was only done in detail for one specimen (after pre-selection for bearing with deepest spall); therefore, only one value is given. Nevertheless, using this approach, it was guaranteed that the spalling depths given in the following tables

always represent maximum values for the tested rings. The cuts were also performed only for one specimen (the one with the highest spall propagation cycles).

While the size and depth of the spalling look quite similar for both materials, some deeper cracks were found, especially for the nitrided material (see Figure 29). To validate that these cracks were finite or that they tended to propagate back to the surface, long duration tests were carried out for both materials. The goal of these tests was to confirm that a longer running time would lead to a larger spalling area but not deeper crack propagation.

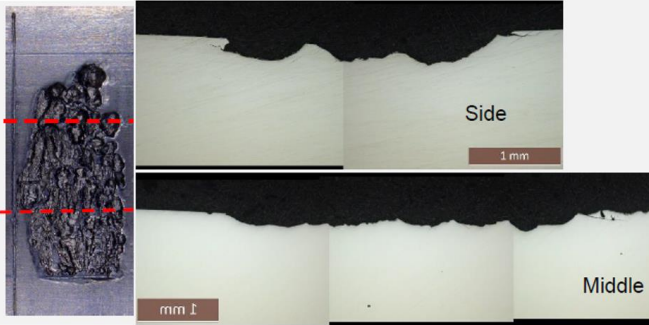
Version	Serial number	Spalling depth (max) [mm]	Width [mm]	Length [mm]	Spalling
Version 1	B-221009	not done during testing	7.65	2.87	not done during testing
Version 1	B-221008	not done during testing	11.55	5.81	
Version 1	B-221004	0.381	11.24	4.90	not done during testing

Table 18: Overview of spall dimensions for version B outer ring – phase I.1

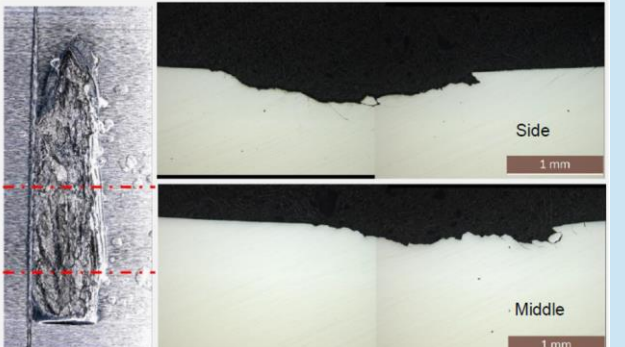
Version	Serial number	Spalling depth (max) [mm]	Width [mm]	Length [mm]	Spalling
Version 1	DA-22545	not done during testing	8.88	1.7	not done during testing
Version 1	DA-22551	not done during testing	10.72	2.71	
Version 1	DA-22537	0.399	8.11	2.63	not done during testing

Table 19: Overview of spall dimensions for the version DA outer ring – phase I.1

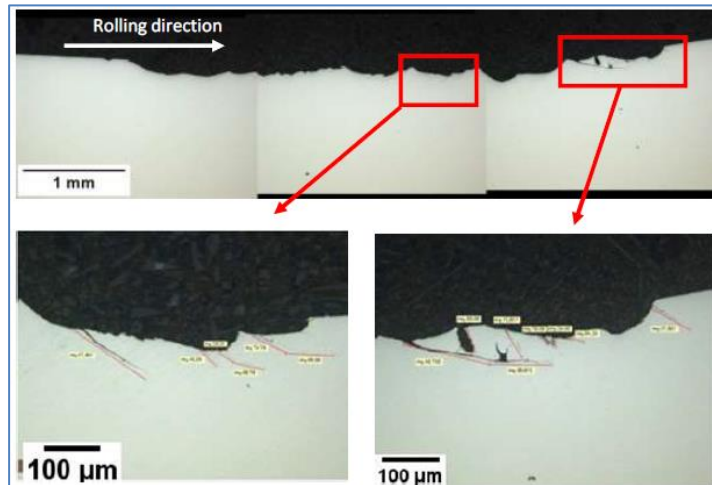


Figure 29: Cross-section of 32CDV13 ring of version 1

Figure 30 and Figure 31 summarize the results from the long duration test. It turned out that the spall topography is similar to the results of phase I.1. The longer running time did not lead to a deeper crack propagation, and the maximum spalling depth is in line with the results presented for the previous tests. The cuts demonstrate that the cracks propagated at a similar slight angle and grew back to the surface by producing larger spalling.

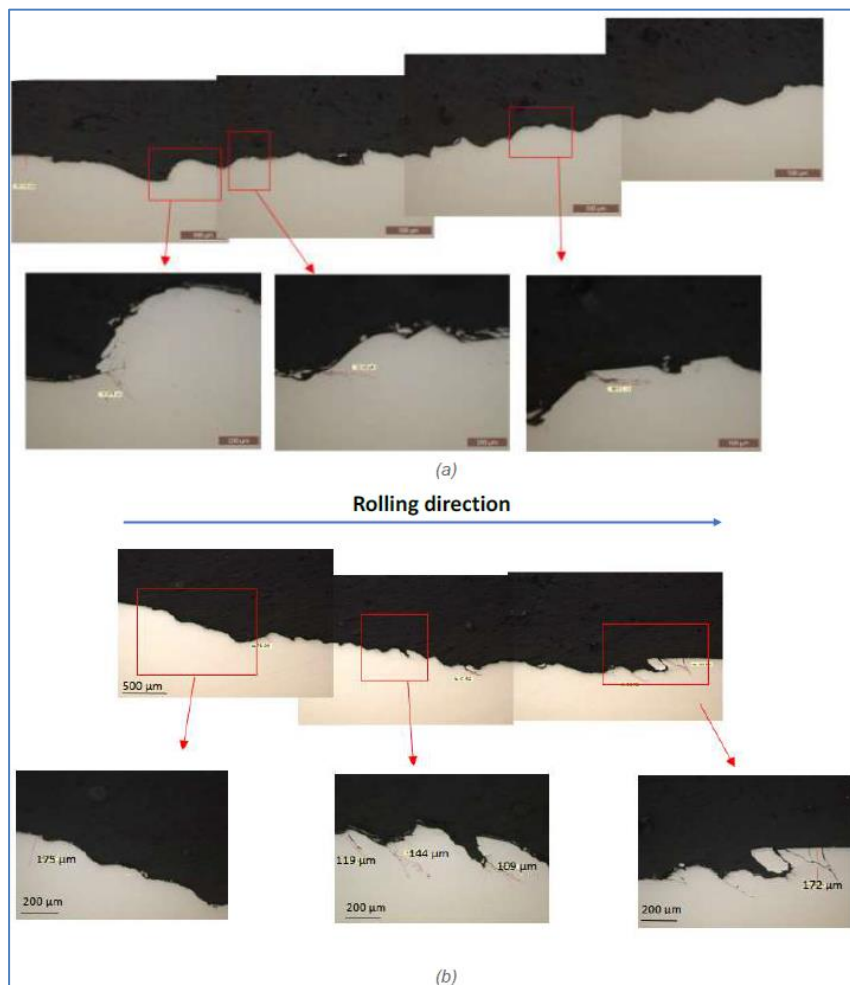


Figure 30: Cuts of long duration test for the outer ring specimen of version 1 for both material

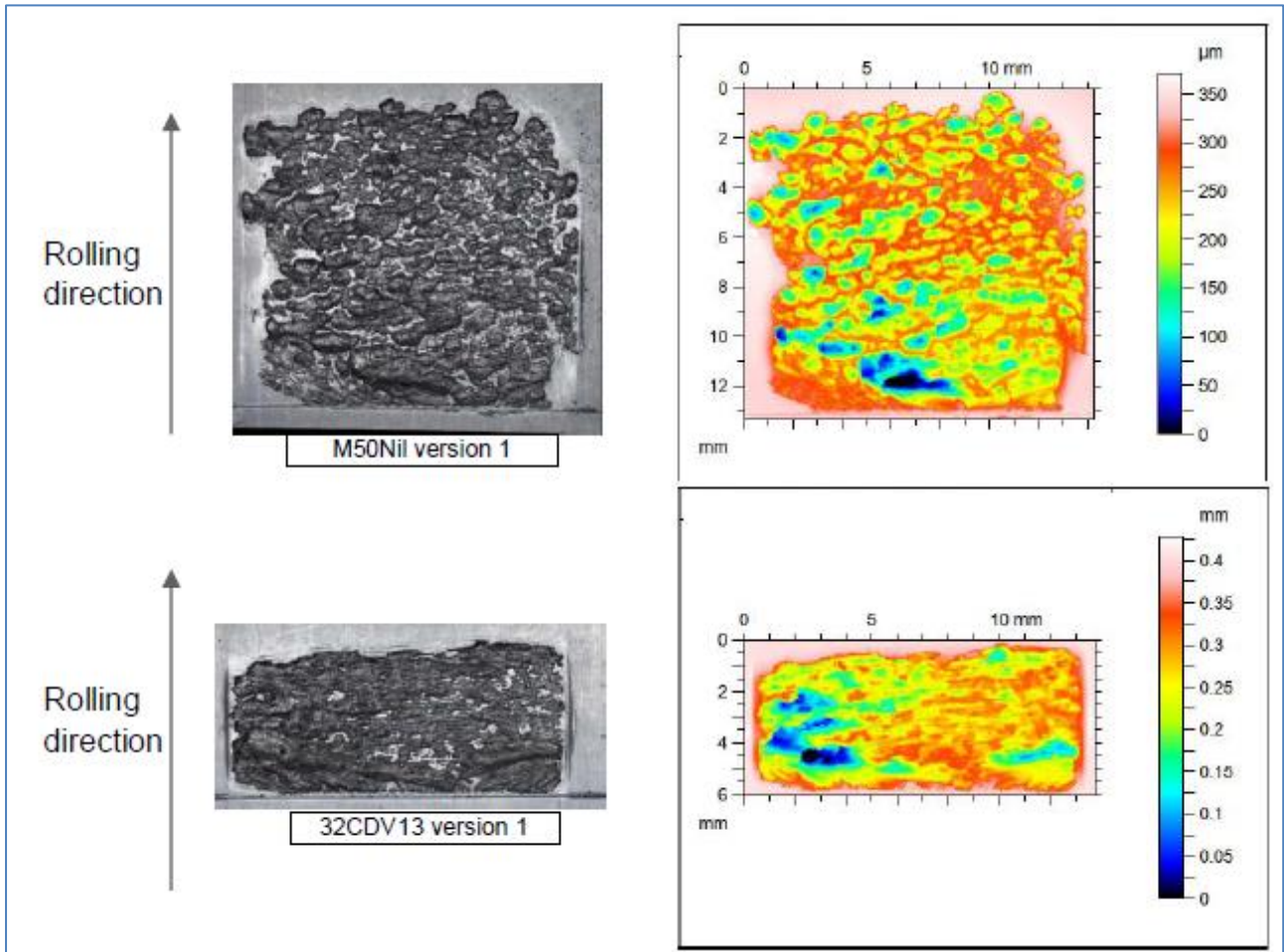


Figure 31: Results of the long duration test for outer ring specimens of version 1 for both material

Tests with the V1 specimens were also performed at a lower contact pressure level (1.8 GPa). For this load level, none of the tested bearings spalled. All of them reached the limit of the running time without any failure. Based on these results, no further testing was performed at 1.5 GPa, and it was decided to skip lower load level testing for the next Phases.

5.4 Phase I.2

As described in 1, Phase I.2 testing is performed to evaluate RCF for pure rolling contact for a case of hardened and nitride material at a fixed load level (2.4 GPa) by varying the treatment and process parameters (see chapter 2). The main focus of Phase I.2 is the evaluation and study of the maximum spalling depth and the tendency for crack propagation (into core or back to the surface) compared with the baseline variant of Phase I.1.

5.4.1 Shaft

During Phase I.2 of testing, the shafts of V3, V4, V5, V6, V10.1, and V11 were tested. As a first step, V3 shafts (with an increased CHD compared to baseline) were tested at 2.4 GPa. For all specimens, classical spalling was observed after testing with dimensions comparable to those of Phase I.1 results (see Table 16).

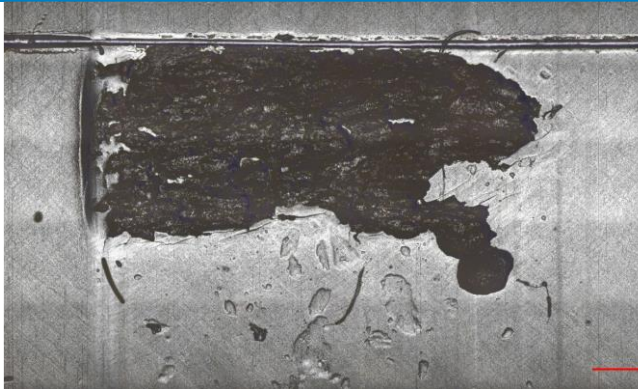
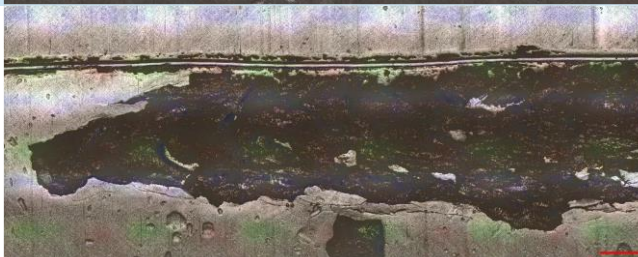
Version	Serial number	Spalling depth (max) [mm]	Width [mm]	Length [mm]	Spalling
V3	4	0.127	2.7	6.5	
V3	3	0.134	2.7	5	
V3	6	0.107	2.4	7.1	

Table 20: Overview of spall dimensions for V3 – phase I.1

A cut of specimen V3-3 was done to investigate the spalling depth and crack propagation into the core of the material (see Figure 32). There is no indication that further running time will lead to deeper spalling. It can be assumed that there will only be further breakouts.



Figure 32: Cross section of V3 - 3 shaft after test at 2.4 GPa – phase I.2

In addition, the vibration signal was checked and compared after testing (see Figure 33). All three shafts show similar behavior according to the vibrational signals with a constant curve for approximately 90% of the lifetime, until a fast and rapid increase to the test bench limit. No specific relationship between the number of cycles and the spalling size could be determined based on the results. The measured signals are comparable to those of Phase I.1 and as a result, the lifetime with increased CHD appears to be lower.

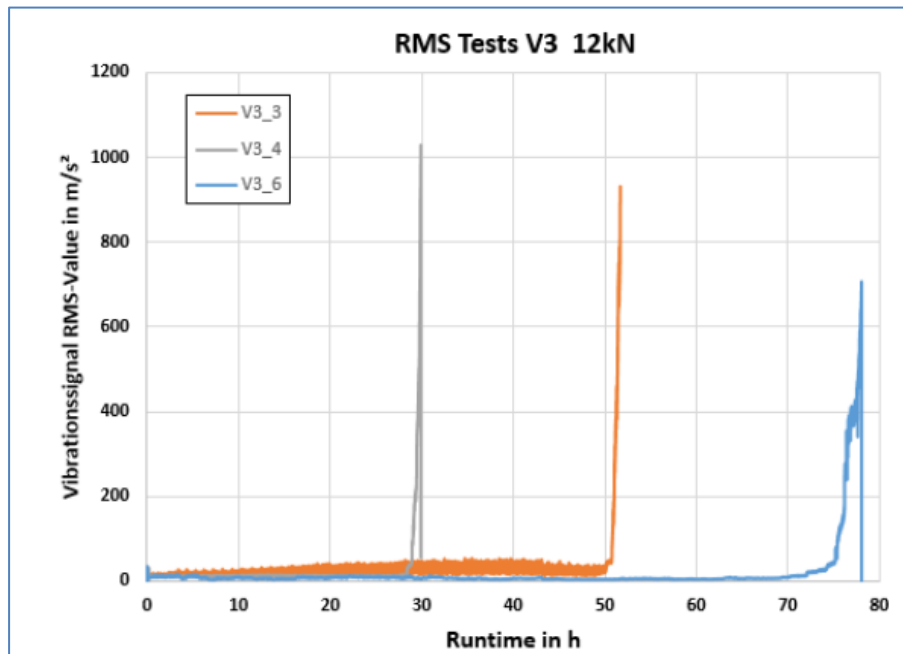


Figure 33: Vibration signal of V3 shafts at 2.4 GPa – phase I.2

Next, the nitrided shafts of V4 were tested. Compared to the baseline variant (V2), these shafts had a deeper NHD of 0.58 mm compared to 0.3–0.4 mm. At a load level of 2.4 GPa, uncommon peeling of the surface layer was detected for all shafts, similar to the baseline variant (see Table 21).

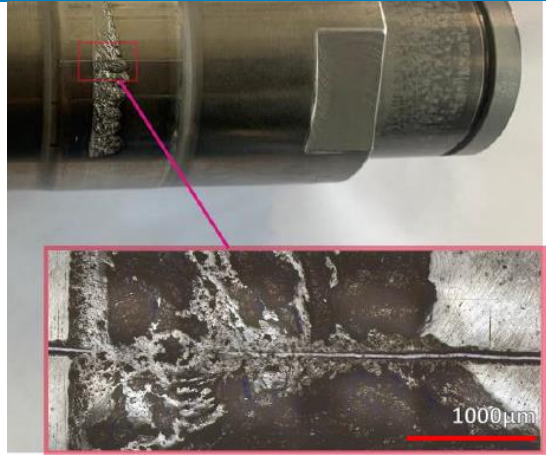
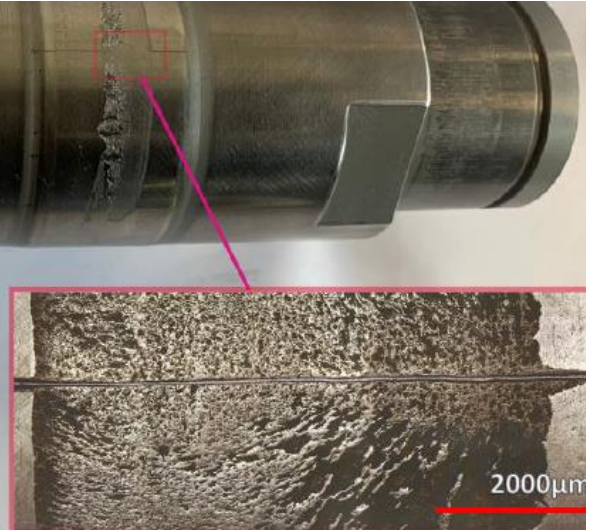
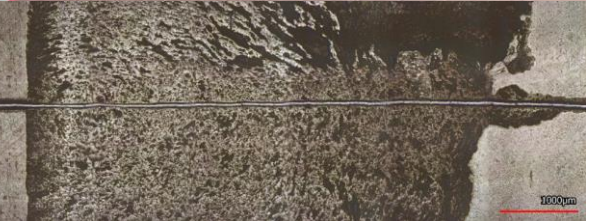
Version	Serial number	Spalling depth (max) [mm]	Width [mm]	Length [mm]	Spalling
V4	1	0.107	Less than one third of the raceway	4.933	
V4	4	0.0743	Less than one third of the raceway	5.992	
V4	5	0.1889	One third of the raceway	6.561	

Table 21: Overview of damage dimensions for V4 – phase I.2

The vibration signal (see Figure 34) obtained from the three shafts shows significant jumps in the vibration level. These variations can be attributed to the progression of surface defects. During the breakout of the raceway surface layer, the signal tends to rise until it decreases again after the release of surface flakes. The tests were either stopped because of reaching the vibration limit or triggering the chip detector. Nevertheless, compared to the V2 shaft results, the component lifetime seems to be shorter because of the deeper nitriding process.

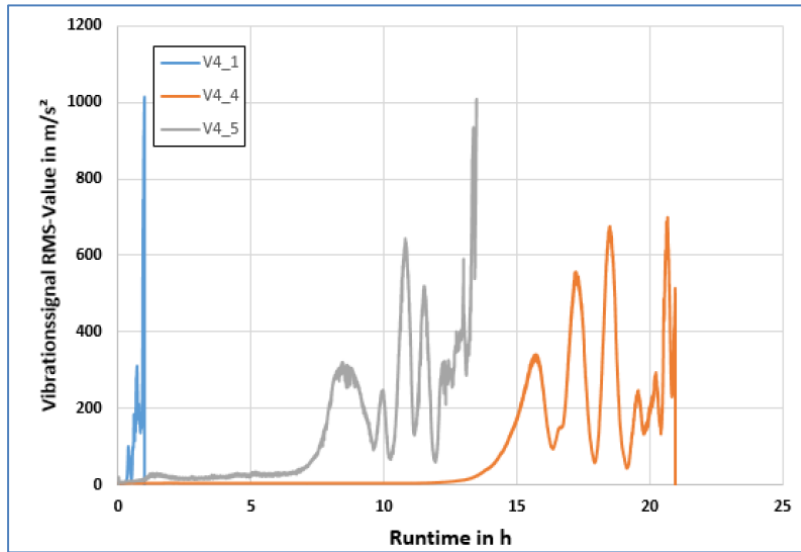


Figure 34: Vibration signal of V4 shafts at 2.4 GPa – phase I.2

Moreover, V5 shafts (with a CHD between V1 and V3) were tested. These shafts were produced with a salt bath process to reach a different CHD. Table 22 gives an overview of the damage incurred. All three tests were stopped because of the vibration signal limit. However, for V5-2 and V5-3, the vibration sensor was not properly calibrated (see Figure 35 – Y-axis), so the spall dimensions reached almost one-third of the raceway surface.

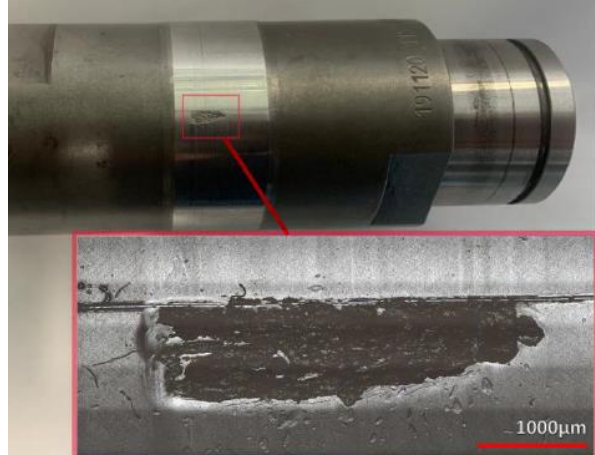
Version	Serial number	Spalling depth (max) [mm]	Width [mm]	Length [mm]	Spalling
V5	1	0.158	2.26	7.85	
V5	2	0.12	One third of the raceway surface	10.82	
V5	3	0.117	One third of the raceway surface	9.47	

Table 22: Overview of damage dimensions for V5 – phase I.2

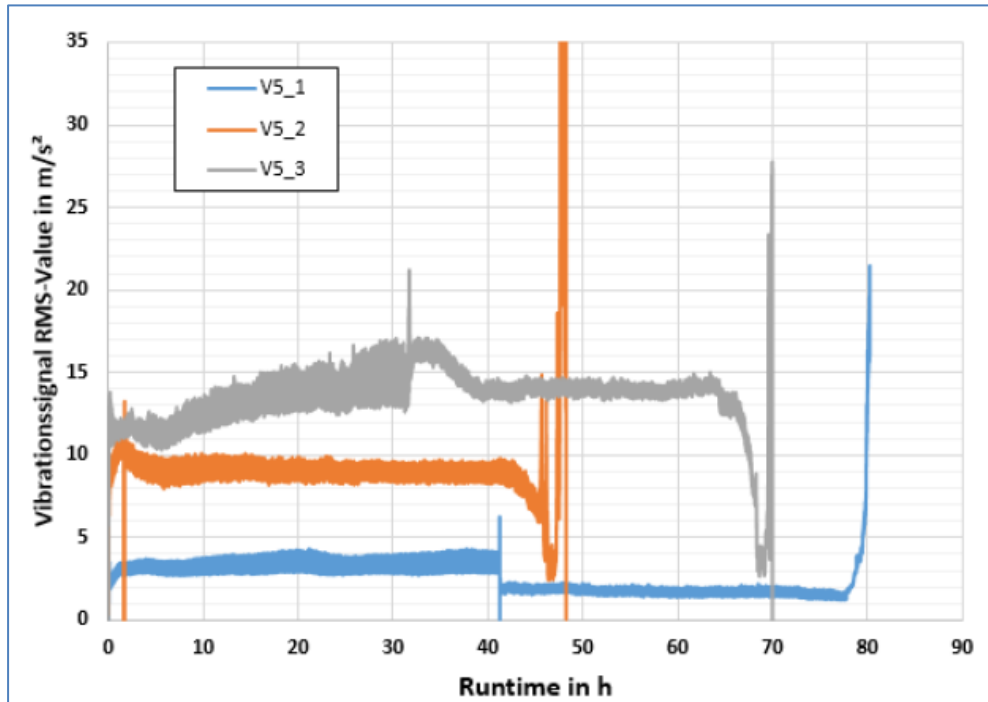


Figure 35: Vibration signal of V5 shafts at 2.4 GPa – phase I.2

V6 shafts were tested for Phase I.2 at a load level of 2.4 GPa. For all of the shafts, the results are comparable to those of the previously tested shafts with the nitrided material. Due to the presence of the white layer, peeling of the surface is observed (see Table 23).

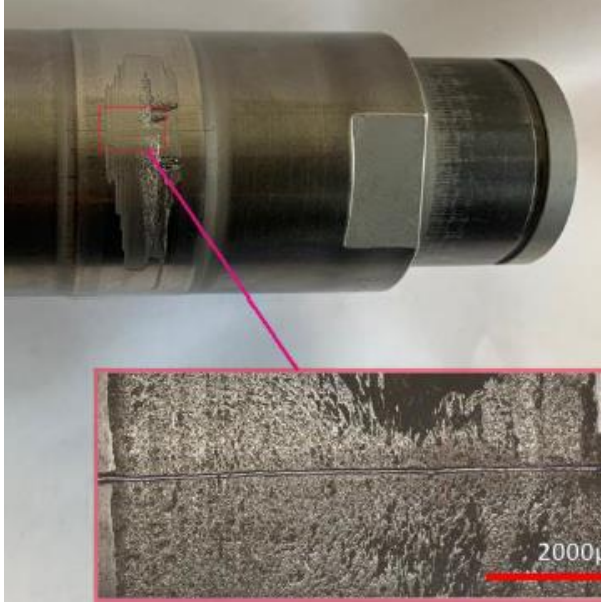
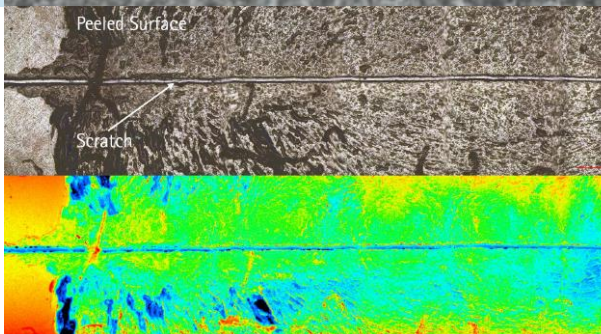
Version	Serial number	Spalling depth (max) [mm]	Width [mm]	Length [mm]	Spalling
V6	2	0.02	One third of the raceway surface	9.26	
V6	3	0.02	One third of the raceway surface	10.038	
V6	5	0.017	One third of the raceway	6.33	

Table 23: Overview of damage dimensions for V6 – phase I.2

Based on the vibration signal (see Figure 36), the V6-5 shaft evidently reached the vibration limit. The other two shafts (V6-3 and V6-5) showed a low vibration signal, while the chips produced triggered the chip

detection sensor and stopped the test. In addition, the results were similar to the previous tests of the 32CDV13 material.

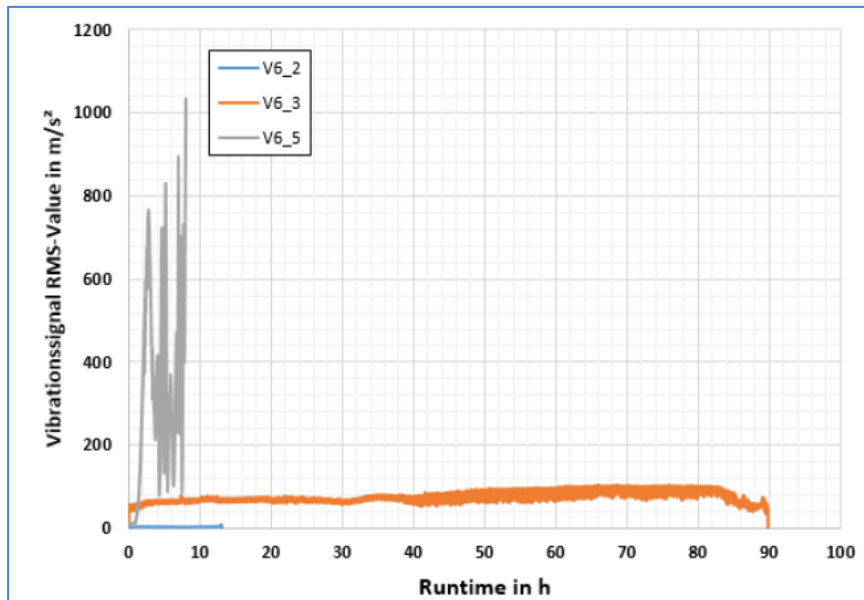


Figure 36: Vibration signal of V6 shafts at 2.4 GPa – phase I.2

For V10.1 shafts, additional intermediate heating was used during the manufacturing process to reduce the residual stresses. The maximum compressive stress was reduced slightly, and in the range of 0.1–0.3 mm in depth, there was less compressive stress left after intermediate heating (see Figure 37).

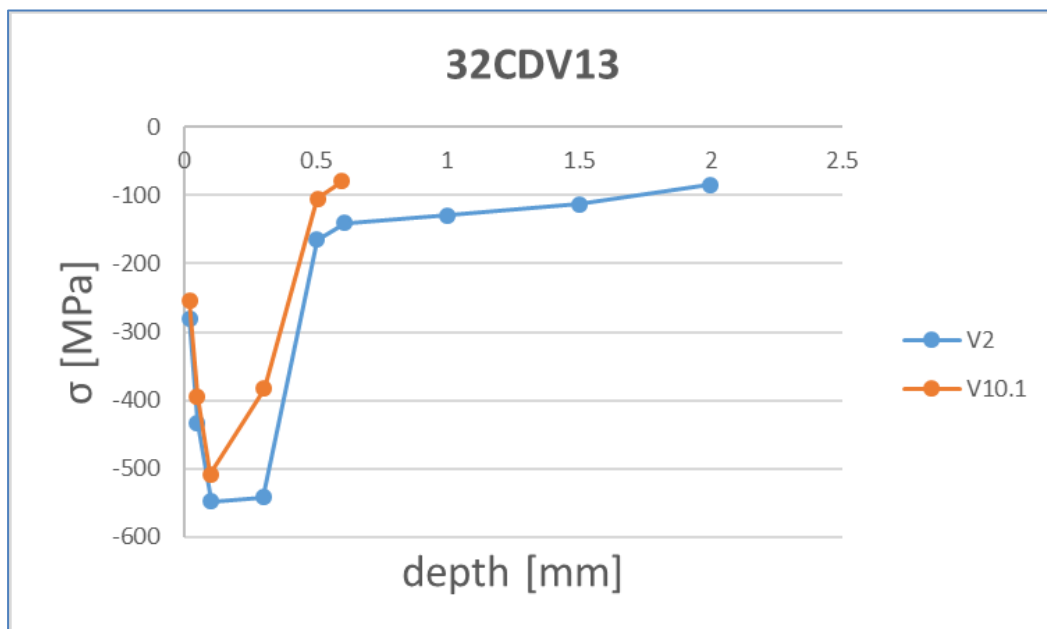


Figure 37: Residual stress adaption for V10.1 compared with V2 baseline

The test results for the V10.1 shafts are highlighted in Table 24. Nevertheless, no significant change in damage dimensions was observed compared with the baseline variant. For all shafts, peeling of the white layer occurred with a comparable maximum depth.

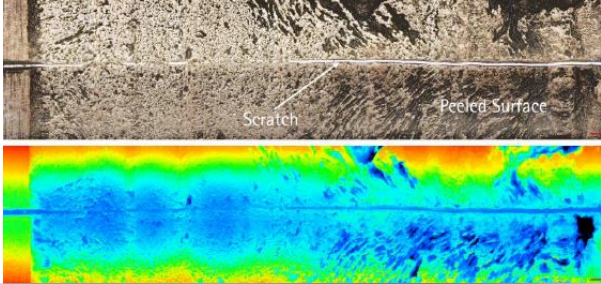
Version	Serial number	Spalling depth (max) [mm]	Width [mm]	Length [mm]	Spalling
V10.1	5	0.107	One third of the raceway surface	8.97	
V10.1	6	0.130	One third of the raceway surface	10.09	
V10.1	1	0.15	One third of the raceway	Approximately the roller length (~10 mm)	

Table 24: Overview of damage dimensions for V10.1 – phase I.2

The vibration signal (see Figure 38) shows again a high fluctuation until the chip detector is triggered. The V10.1-4 shaft was canceled due to a misalignment issue during the test.

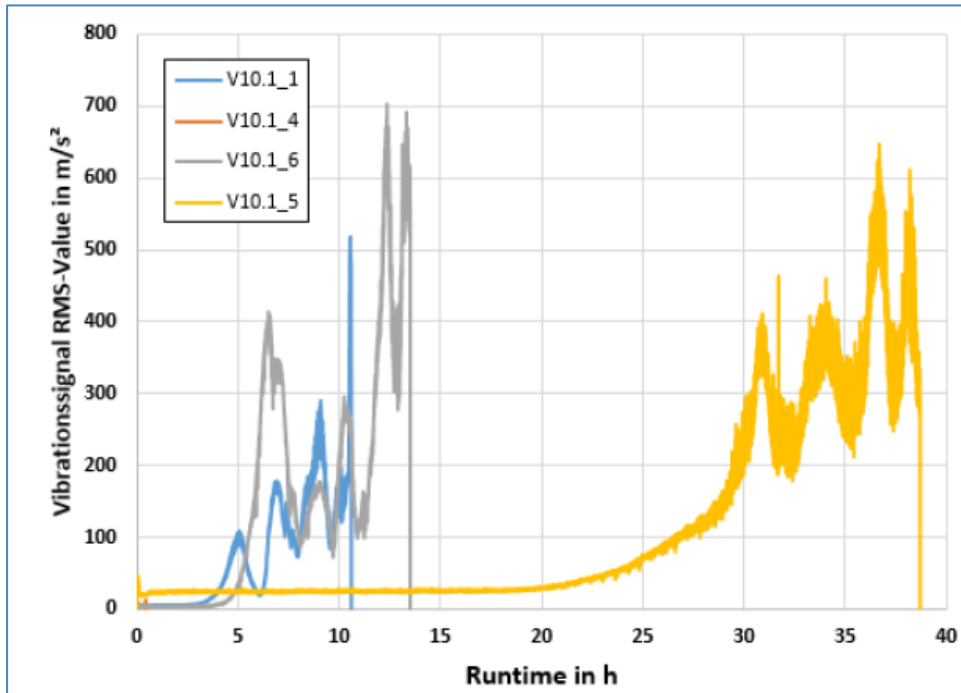


Figure 38: Vibration signal of V10.1 shafts at 2.4 GPa – phase I.2

V11 shafts were tested at the end of Phase I.2, with intermediate heating and additional rolling of the surface. Based on that, V11 shafts showed higher surface hardness (65 HRC compared to 59 HRC), and the residual stress at 0.1 mm and deeper was elevated compared to the baseline.

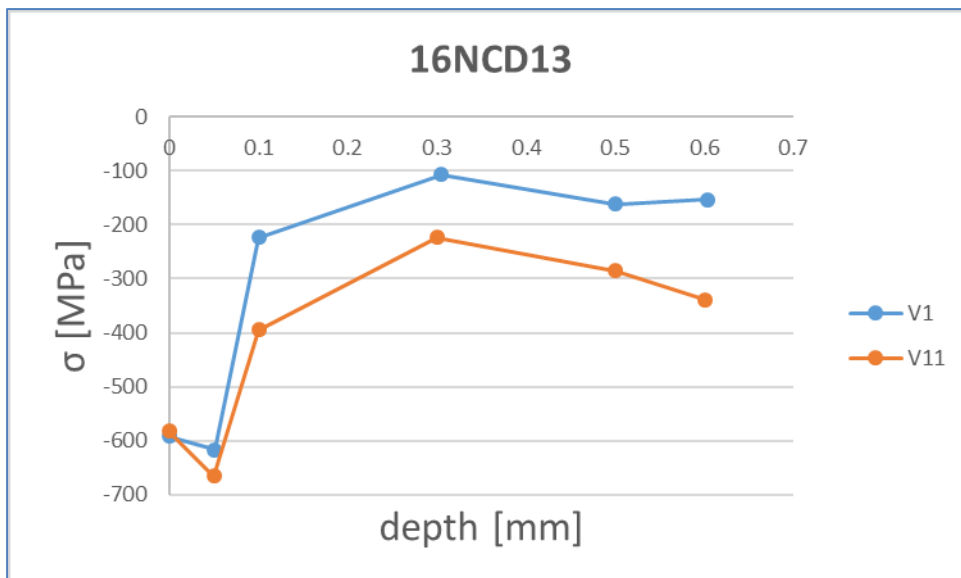


Figure 39: Residual stress profile for V11 shafts compared to baseline

Table 25 shows the damage obtained from testing at 2.4 GPa. No significant change compared with baseline was observed. Nevertheless, V11-7 shows an increased spalling size, which triggered the chip detection sensor. Based on the damage location and the quick spalling, it is assumed that there was a misalignment effect which caused the larger spalling. Therefore, V11-1 was used as a repetition of V11-7, which showed classical spalling without misalignment. It can be assumed that the misalignment was caused by poor mounting of the bearing.

Nevertheless, misalignments could be reliably detected after the test campaign by the unevenly distributed damage pattern (see V11-7 in Table 25).

V11-2 and V11-3 behaved similarly to the baseline variant (see also Figure 40) by reaching the vibration limit with comparable spalling sizes.

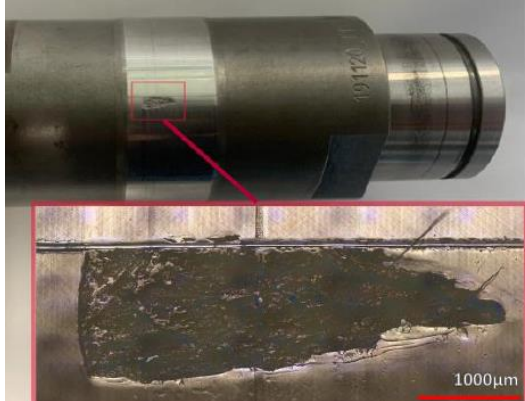
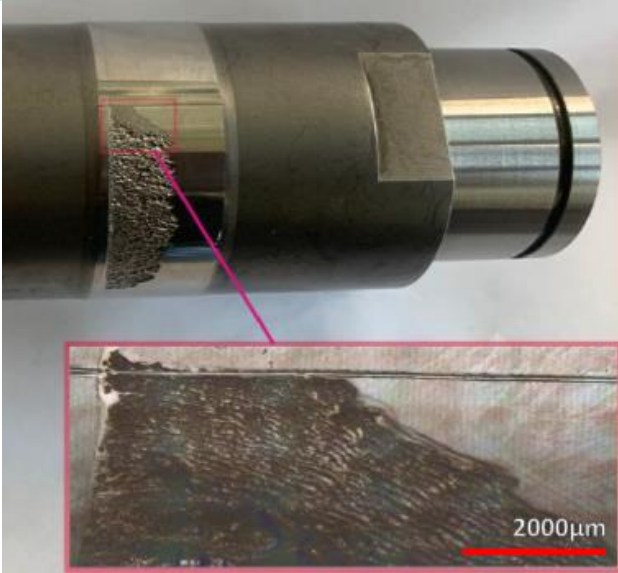
Version	Serial number	Spalling depth (max) [mm]	Width [mm]	Length [mm]	Spalling
V11	2	0.127	2.076	5.68	
V11	3	0.107	2.76	7.4	
V11	7	0.095	One third of the raceway surface	6.35	
V11	1	0.16	1.5	Not done during testing	Not done during testing

Table 25: Overview of damage dimensions for V11 – phase I.2

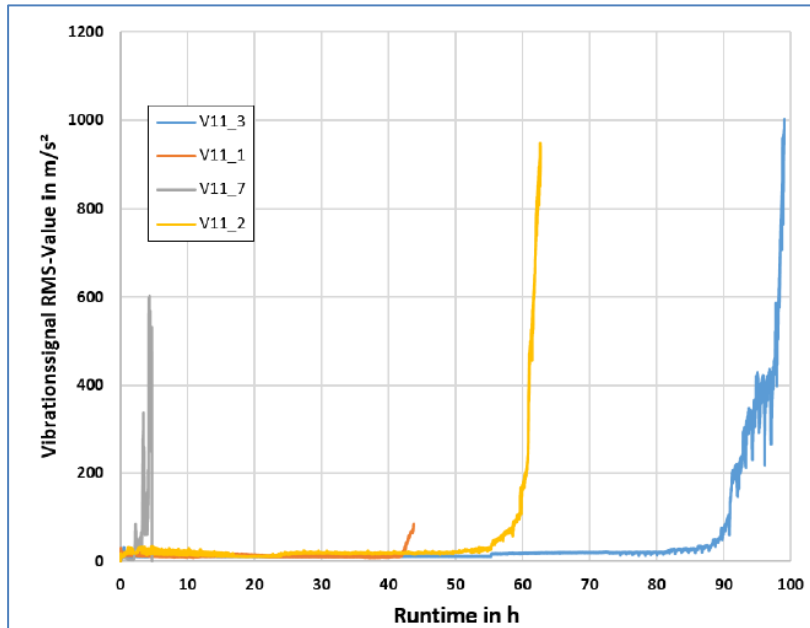


Figure 40: Vibration signal of V11 shafts at 2.4 GPa – phase I.2

5.4.2 Outer ring

The focus of Phase I.2 testing for the outer ring was the evaluation of surface hardness, hardness depth, and surface residual stress by varying these parameters. A summary of the specimen parameters (planned vs. reached) is highlighted in chapter 2.1. Although the variation in hardness and hardness depth turned out to be manageable, the change in surface residual stress was difficult. For M50NiL, the surface hardness was reduced, but the hardness depth was also reduced. For the 32CDV13 material, only a slight reduction was achieved, so that version 3 was almost identical to the baseline variant. The hardness profiles for both materials are highlighted in Figure 41 and Figure 42.

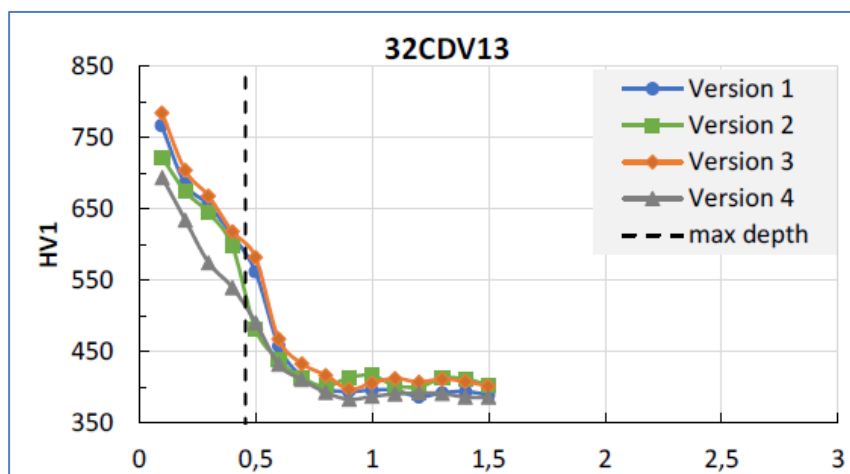


Figure 41: Comparison of hardness profile for 32CDV13 material

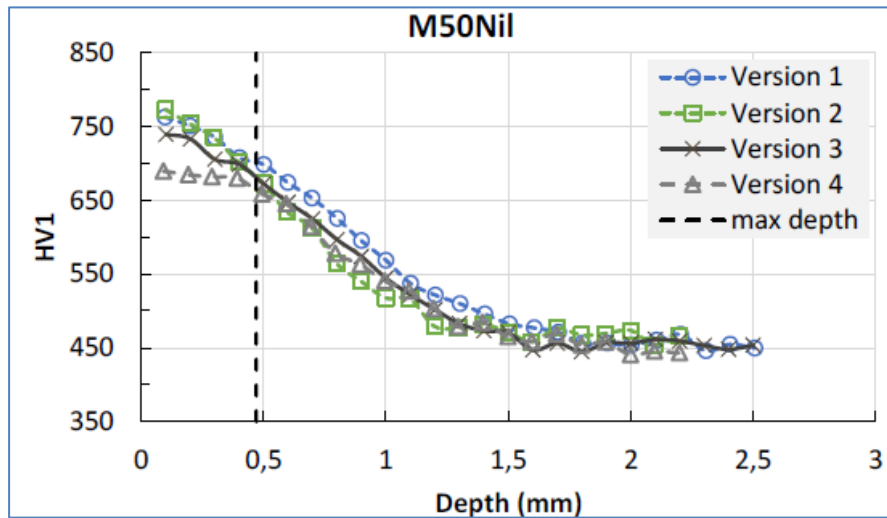


Figure 42: Comparison of hardness profile for M50Ni1 material

The test results for the specimens of both materials are summarized in Table 26 to Table 31. For all of the specimen, a classical spalling was observed, whereas the topography of the spalled area and its size was comparable to the results of phase I.1. All tests were stopped by the limit of the vibration signal.

Version	Serial number	Spalling depth (max) [mm]	Width [mm]	Length [mm]	Spalling
Version 2	BA-22203	0.398	11.23	4.21	Not done during testing
Version 2	BA-22202	0.348	11.82	2.47	Not done during testing
Version 2	BA-22201	not done during testing	11.36	6.93	

Table 26: Summary of results for outer ring version 2 – M50Ni1

Version	Serial number	Spalling depth (max) [mm]	Width [mm]	Length [mm]	Spalling
Version 3	BC-22401	Not done during testing	10.99	2.86	
Version 3	BC-22404	0.496	12.85	10.12	Not done during testing
Version 3	BC-22402	0.324	11.47	3.42	Not done during testing

Table 27: Summary of results for outer ring version 3 – M50Ni1

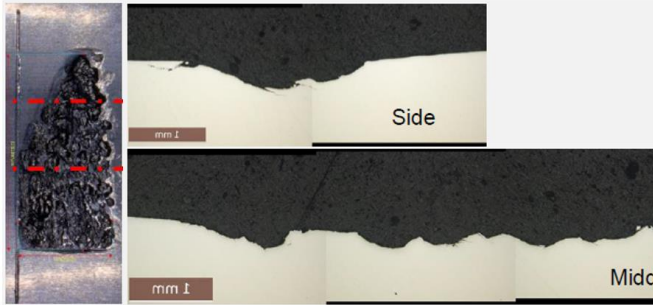
Version	Serial number	Spalling depth (max) [mm]	Width [mm]	Length [mm]	Spalling
Version 4	BB-22301	0.418	8.95	4.65	Not done during testing
Version 4	BB-22302	0.492	12.46	8.51	Not done during testing
Version 4	BB-22303	Not done during testing	11.40	5.53	

Table 28: Summary of results for outer ring version 4 – M50Nil

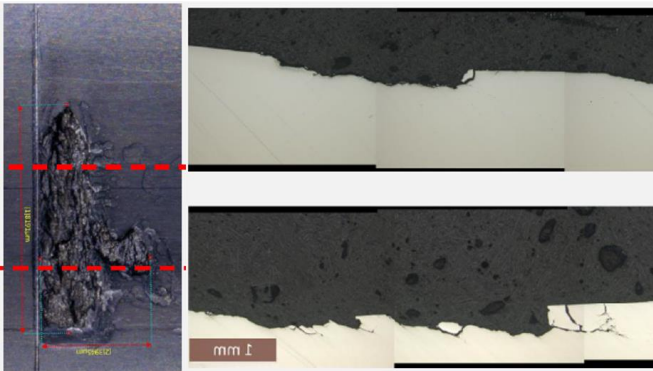
Version	Serial number	Spalling depth (max) [mm]	Width [mm]	Length [mm]	Spalling
Version 2	DB-22701	0.421	11.8 7	5.26	Not done during testing
Version 2	DB-22703	0.346	10.0 5	2.03	Not done during testing
Version 2	DB-22704	Not done during testing	8.19	3.95	

Table 29: Summary of results for outer ring version 2 – 32CDV13

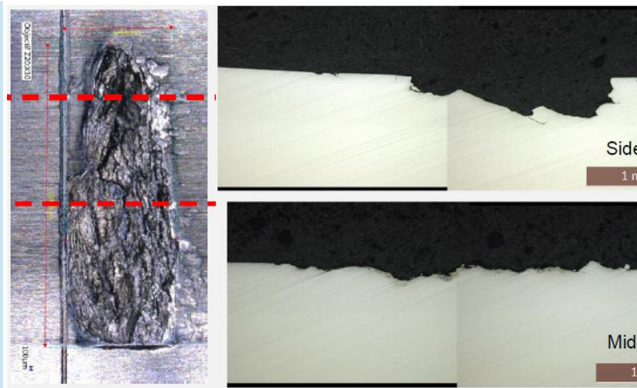
Version	Serial number	Spalling depth (max) [mm]	Width [mm]	Length [mm]	Spalling
Version 3	DD-22904	0.355	9.31	3.23	Not done during testing
Version 3	DD-22903	Not done during testing	9.69	3.55	
Version 3	DD-22902	0.440	10.49	2.07	Not done during testing

Table 30: Summary of results for outer ring version 3 – 32CDV13

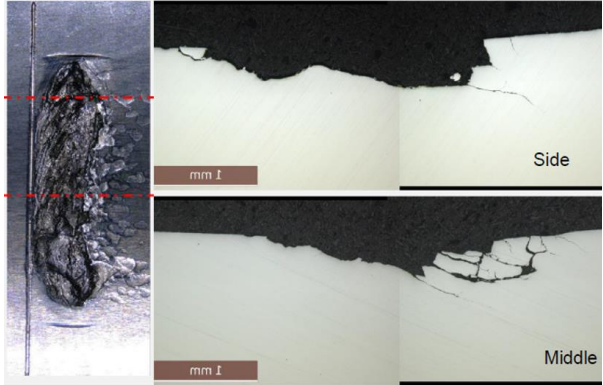
Version	Serial number	Spalling depth (max) [mm]	Width [mm]	Length [mm]	Spalling
Version 4	DC-22803	0.456	10.02	2.20	Not done during testing
Version 4	DC-22804	0.483	8.29	2.98	Not done during testing
Version 4	DC-22801	Not done during testing	11.64	3.10	

Table 31: Summary of results for outer ring version 4 – 32CDV13

For all the tested outer rings, a detailed analysis using several cuts was performed to evaluate and compare the maximum spalling depth and maximum crack depth observed after testing. Figure 43 provides an overview of the relationship between these two parameters. As an outcome, it is obvious that specimens with less surface hardness and lower hardness depth tend to spall more deeply and with deeper cracks (e.g. V4). Moreover, it appears that the M50NiI baseline version (V1) achieved the lowest spalling and crack depth. Besides that, no specific correlation was found between the maximum spalling depth and the maximum crack depth (note: values were measured on different samples).

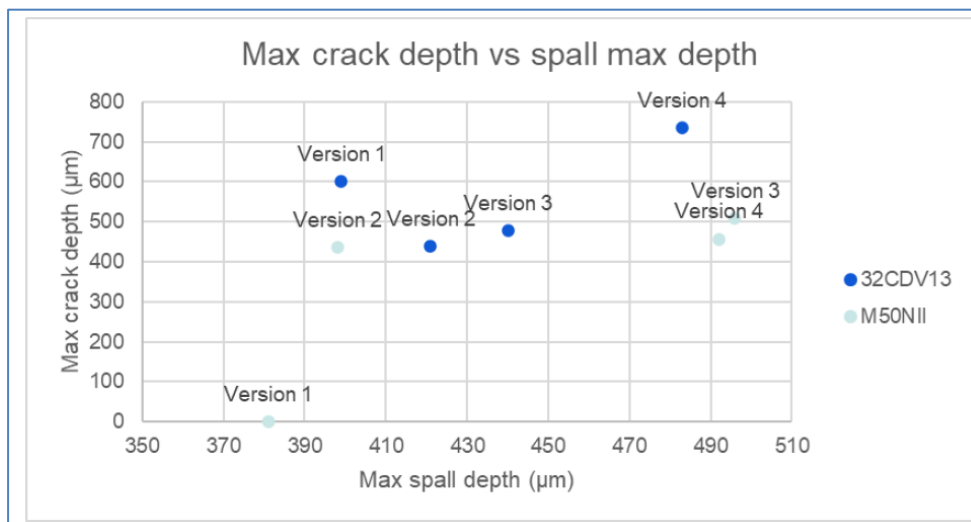


Figure 43: Relation between max. spalling depth and max. crack depth for measured outer ring specimen for phase I

5.5 Phase II

The intention of Phase II was to implement an additional body stress (complex load) on the baseline variant of the test specimens to evaluate the influence of this secondary driver on the damage and failure behavior. Therefore, the shaft specimen was drilled and machined into a hollow shaft, and the outer ring was produced with a notch design, as presented in chapter 2. In this design, body stress is introduced in the axial direction for the hollow shaft and in the circumferential direction for the outer ring, highlighting the two main differences in load conditions for these two applications.

5.5.1 Hollow shaft

For the hollow shafts, a pre-test was performed as a risk mitigation to check and validate that the additional bending moment and ovalization of the hollow shaft can initiate crack propagation with the known scratch geometry of Phase I. The intention was to maintain the same scratch geometry as that used for Phase I. Before physical testing, some investigations were performed on the simulation side to check whether crack propagation was possible or not (see chapter 6.5.1). This pre-test nevertheless demonstrated that the given load level is not sufficient to produce any crack into the depth of the material. It was only possible to reproduce the results of Phase I with classical spalling (see Figure 44). With a maximum depth of 123.5 μm , no cracking was observed. This might be due to the body stress load condition in the axial direction (as mentioned above), which is not perpendicular to the crack fronts and therefore does not lead to a crack opening. Further investigations on the impact of ovalization of the shaft on crack opening were performed by simulation (see chapter 6). The difference in simulation (crack propagation is likely) and test (no crack propagation found after testing) could be explained not only by the limited test time and test stop due to vibration signal but also by the fact that simulations were only done for the first few propagation steps to check general feasibility of propagation at this stage.

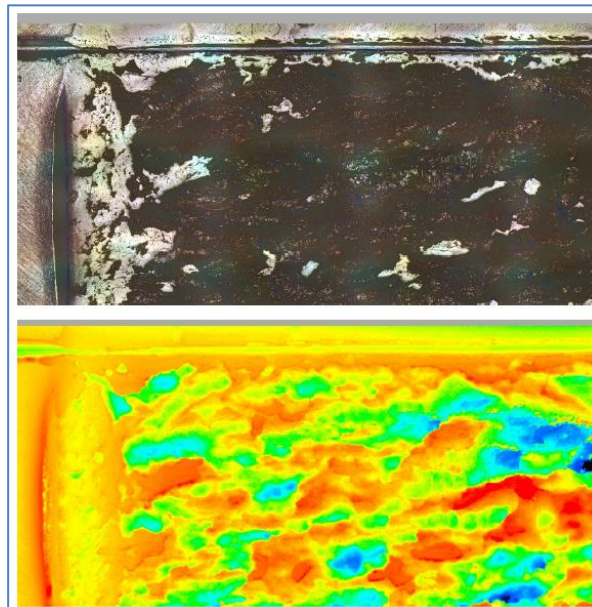


Figure 44: Classical spalling for Pre-Test of phase II shafts – V1.1

As a consequence, the pre-damage of the shafts for Phase II was modified using a laser scratch. With the help of a laser, v-shaped scratches with a depth of 0.8–1 mm were introduced and tested again. With the new pre-damage, tests at 2.4 GPa and 2.9 GPa were conducted for Phase II for both materials. No additional re-testing for the Phase I specimen with the laser scratch was performed because of time and specimen limitations. Table 32 provides an overview of the tested specimen and load levels. After testing, the specimens were cut and

checked for cracks. No further crack propagation was achieved for 2.4 GPa load level (it was not possible to clearly distinguish between potentially vaporized steel residue from the laser and a small starting crack propagation), whereas at 2.9 GPa, a starting crack propagation in the range of 200 μm could be observed for the 16NCD13 material (see Figure 45 to Figure 46) with crack branching after 50 μm . For the 32CDV13 material, the results were different. For both load levels, it was possible to generate a crack network with breakouts to the surface but with a finite crack into the depth of the material for the given run time. For the 2.4 GPa load level, crack propagation into a depth of 400 μm was measured, whereas 200 μm were measured for the higher load level of 2.9 GPa. The test for 2.9 GPa was stopped much earlier because of the vibration signal limit due to severe surface damage, which could explain the lower crack propagation depth.

Version	Material	Max. contact pressure	Test time	Load cycles	Crack growth	Test stop criterion
V1.1	16NCD13	2.4 GPa	107h 52min	115.6 M	No	Vibration signal
V1.1	16NCD13	2.4 GPa	76h 44 min	82.9 M	No	Vibration signal
V1.1	16NCD13	2.4 GPa	36h 27min	39.4 M	No	Vibration signal
V1.1	16NCD13	2.4 GPa	29h 58min	32.4 M	No	Vibration signal
V1.1	16NCD13	2.9 GPa	08h 40min	9.4 M	Yes, into depth	Vibration signal
V1.1	16NCD13	2.9 GPa	12h 14min	13.2 M	Yes, into depth	Vibration signal
V1.1	16NCD13	2.9 GPa	1h 4min	1.2 M	Yes, into depth	Vibration signal
V2.1	32CDV13	2.4 GPa	33h 08min	35.8 M	Yes, connected to surface, not in depth	Vibration signal
V2.1	32CDV13	2.4 GPa	27h 51min	30.1 M	Yes, connected to surface, not in depth	Vibration signal
V2.1	32CDV13	2.4 GPa	04h 59min	5.4 M	Yes, connected to surface, not in depth	Vibration signal
V2.1	32CDV13	2.9 GPa	1h 12min	1.3 M	No	Vibration signal
V2.1	32CDV13	2.9 GPa	34min	0.6 M	Yes, connected to surface and into depth	Vibration signal
V2.1	32CDV13	2.9 GPa	37min	0.7 M	No	Vibration signal

Table 32: Overview table of phase II results

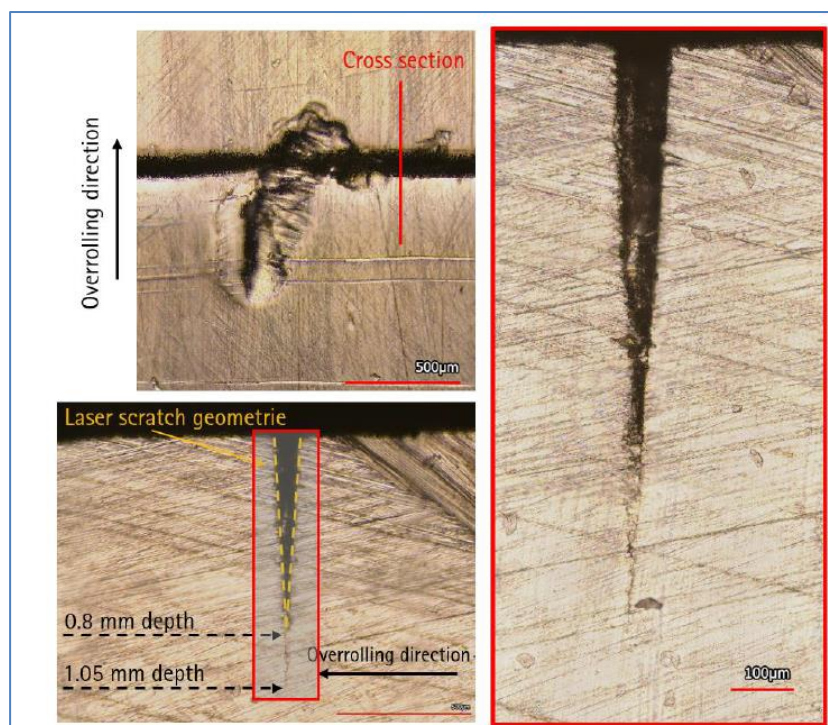


Figure 45: Cross-section of V1.1 shaft with low load level (2.4 GPa)

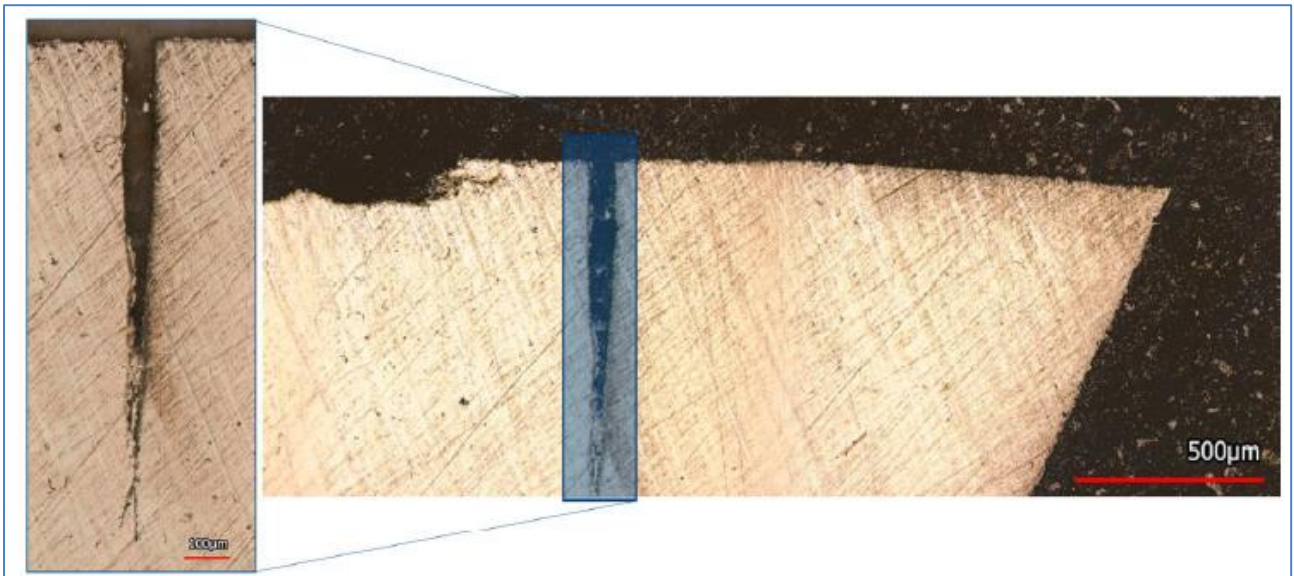


Figure 46: Cross-section of V1.1 shaft with high load level (2.9 GPa)

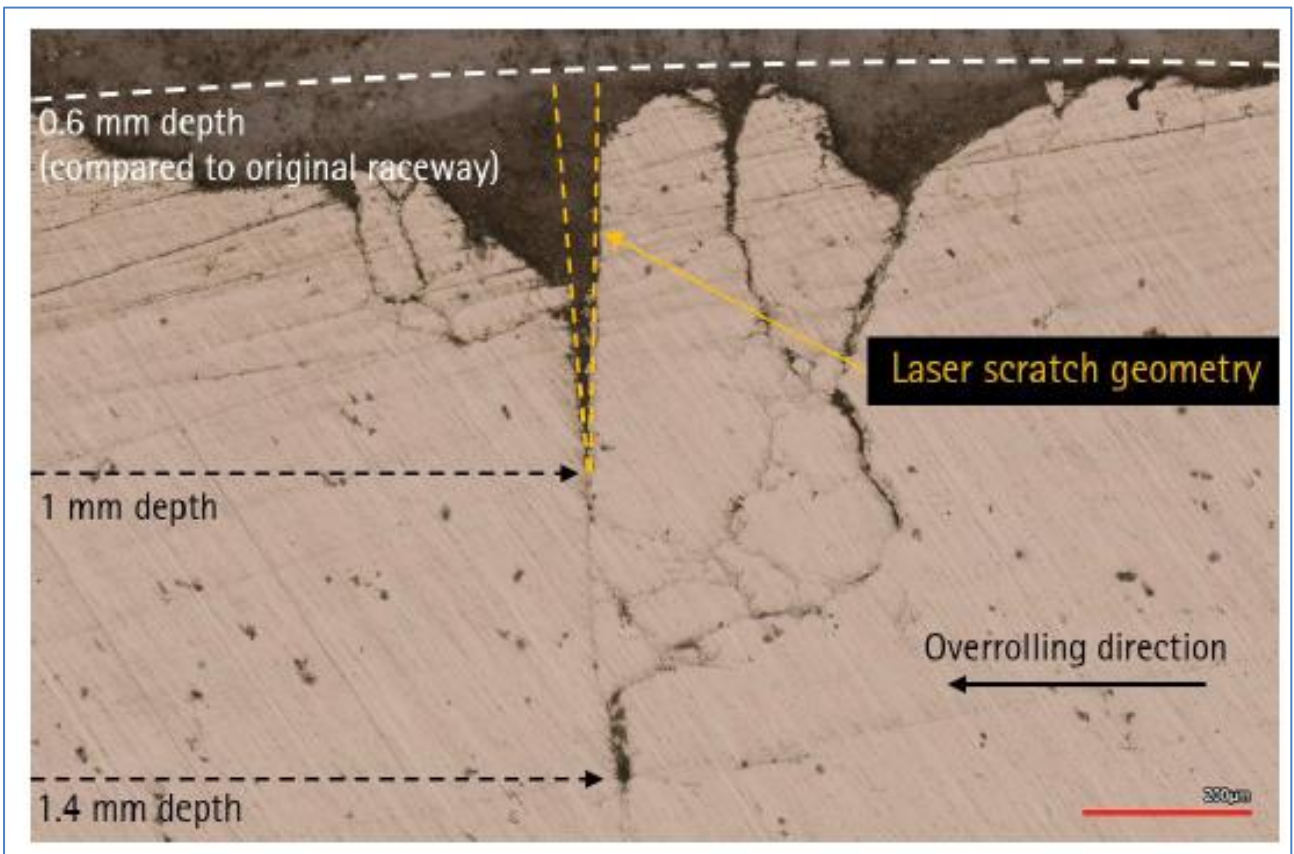


Figure 47: Cross-section V2.1 – 4 shaft for low load level (2.4 GPa)

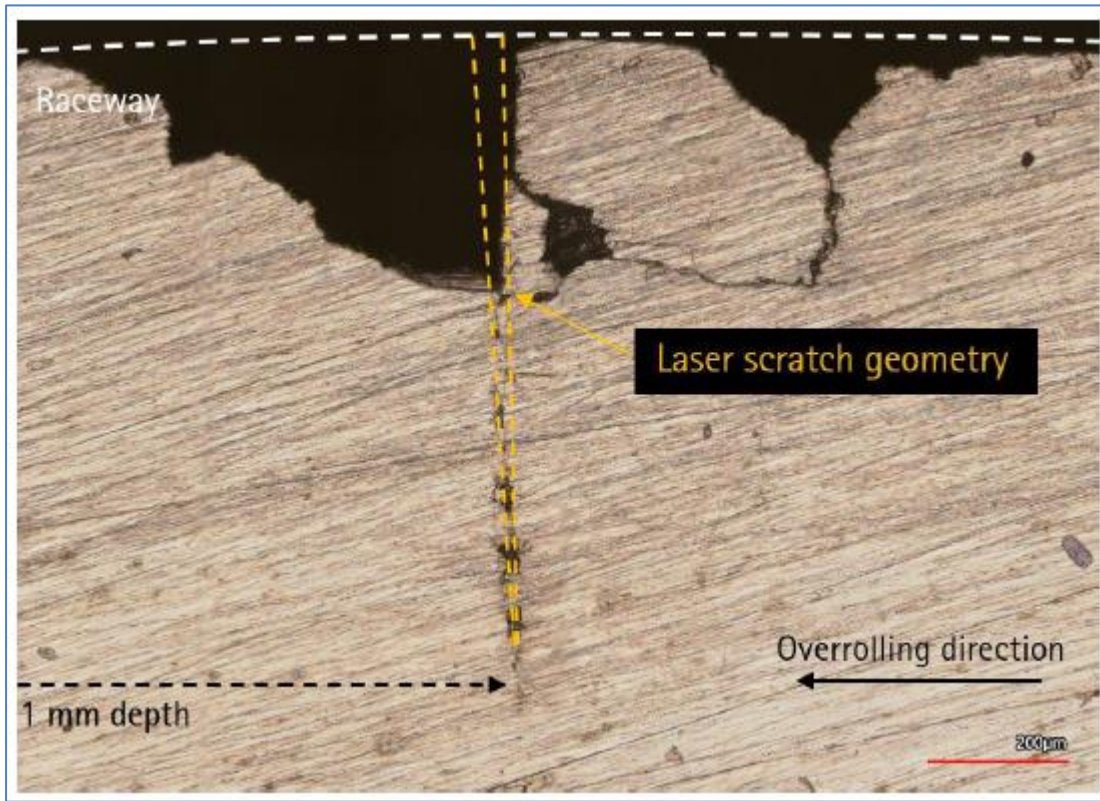


Figure 48: Cross-section V2.1 – 7 shaft for low load level (2.4 GPa)

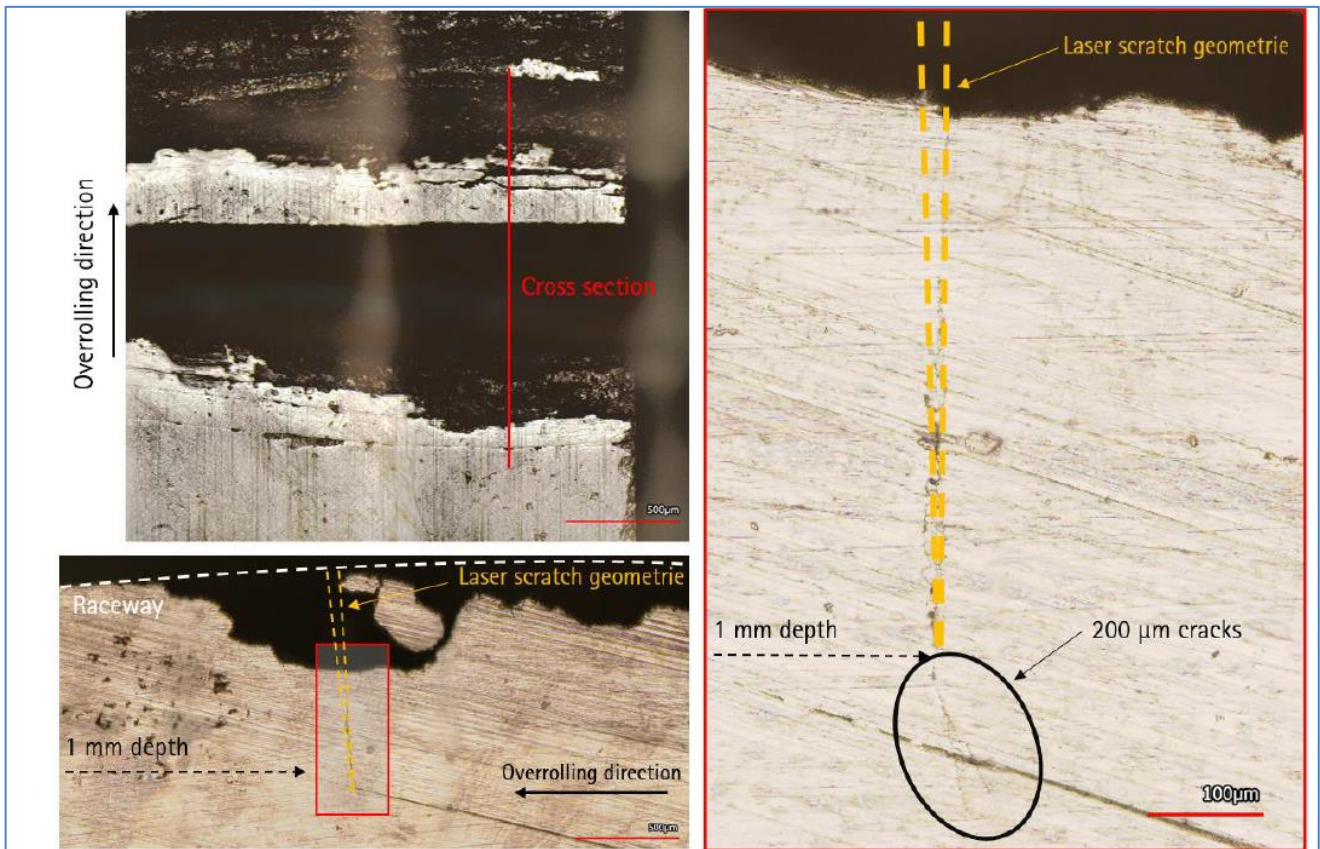


Figure 49: Cross-section V2.1 shaft for high load level (2.9 GPa)

5.5.2 Outer ring with notch

As described in chapter 2.1, two different notch designs (T102 and T104) for the outer ring specimens were prepared as risk mitigation strategy for testing. Both notch types were produced with EDM (electrical discharge machining). The T102 version includes a thinner ring thickness at the notch compared to the T104 version and is more severe with regard to the body stress introduced into the raceway. The body stress produced by the notch is in the circumferential direction (perpendicular to the crack), which led to an opening of the crack fronts.

An overview of the results for both variants is presented in Table 33. An initial pre-test for the 32CDV13 material was performed with the T102 specimen type at 2.4 GPa. The T102 design with the high contact pressure led to a very fast spall initiation and a crack through the thickness of the specimen. Therefore, phase II test campaign was initiated with the less severe design (T104).

Notch design	Material	Version	Sample quantity	Max. contact pressure	S/N	Spall initiation	Analysis
T104	M50Nil	Version 1	3	2.4 GPa	221013 221025 221026	All spalled All with through crack	Topography: 3 Crack analysis: 3
	32CDV13	Version 1	3	2.4 GPa	22503 22506 22516	All spalled No through crack	Topography: 2 Crack analysis: 3
T102	M50Nil	Version 1	3	1.8 GPa	221017 221024 221028	Spalled and severe cracks No spall - suspension time No spall - suspension time	Topography: - Crack analysis: -
	32CDV13	Version 1 Pre-Test	1	2.4 GPa	22538	Spalled Through crack	Topography: - Crack analysis: 1
	32CDV13	Version 1	1	1.8 GPa	22501	No spall - suspension time (tested at 2.4 GPa afterwards)	Topography: - Crack analysis: -
	32CDV13	Version 1	3	2.4 GPa	22501 22533 22505	Spalled / No crack No spall - suspension time No spall - suspension time	Topography: - Crack analysis: -

Table 33: Summary of results for phase II for outer ring specimens

For all tested M50Nil specimens, spall initiation with a crack through the thickness was observed. The results are summarized in Table 34 and Figure 50 through Figure 52. The topography and size of the spalled area were enlarged compared with the tests for the baseline variant without body stress. For one of the bearings, there was also a secondary crack initiation before the pre-damage scratch (in the rolling direction), potentially due to the high deformations after the first crack. All cracks through the thickness started at the area of deepest spall, while no secondary cracks were connected to the crack through. It was observed that the crack propagation direction reversed approximately at half of the raceway thickness. This could be associated with overload fracture while reaching tensile strength within the residual cross-section. The crack angle for the cracked rings was not measured, but based on the figures below, a crack angle between 50-70° can be assumed.

Version	Serial number	Spalling Depth (max) [mm]	Width [mm]	Length [mm]	Test time [Mio. cycles]
Version 1 - T104	B-221013	~0.7	14	16	2.1
Version 1 - T104	B-221025		14	19	2.9
Version 1 - T104	B-221026		14	20	2.2

Table 34: Summary of testing results for phase II – M50Nil

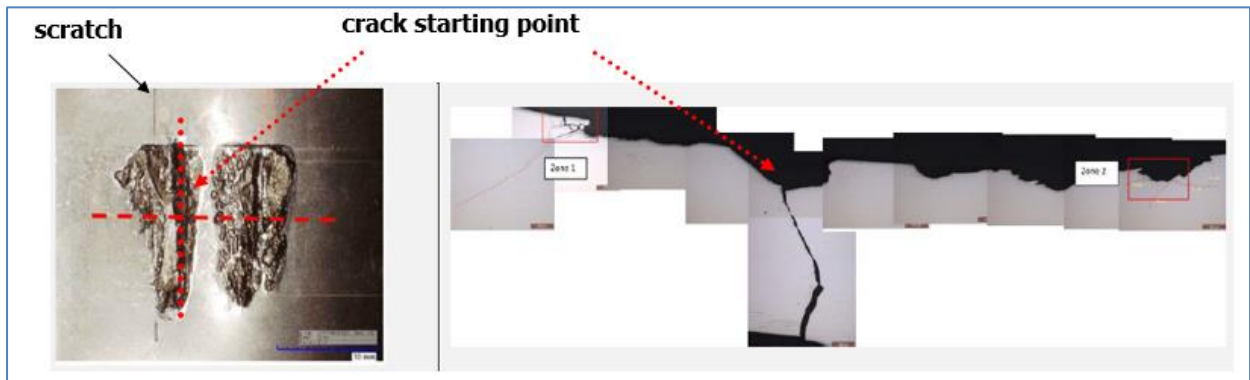


Figure 50: Cut of T104 - B-221013 specimen

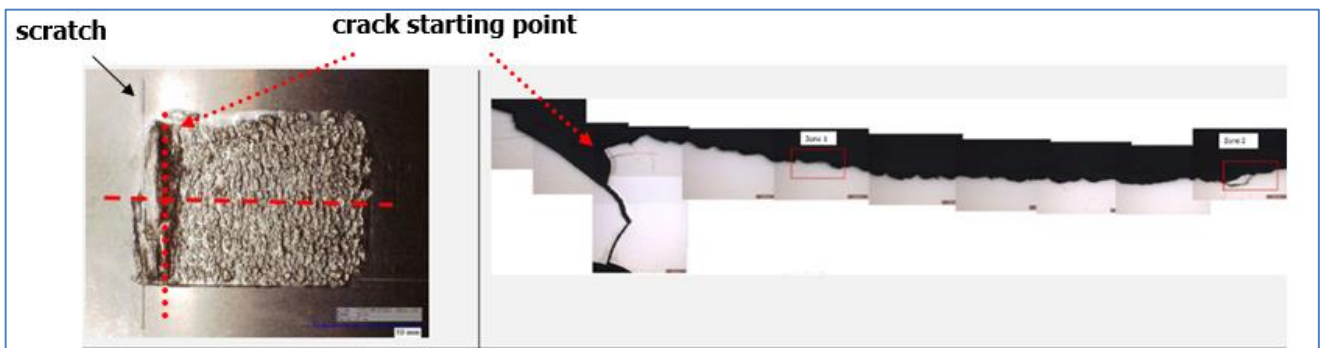


Figure 51: Cut of T104 - B-221025 specimen

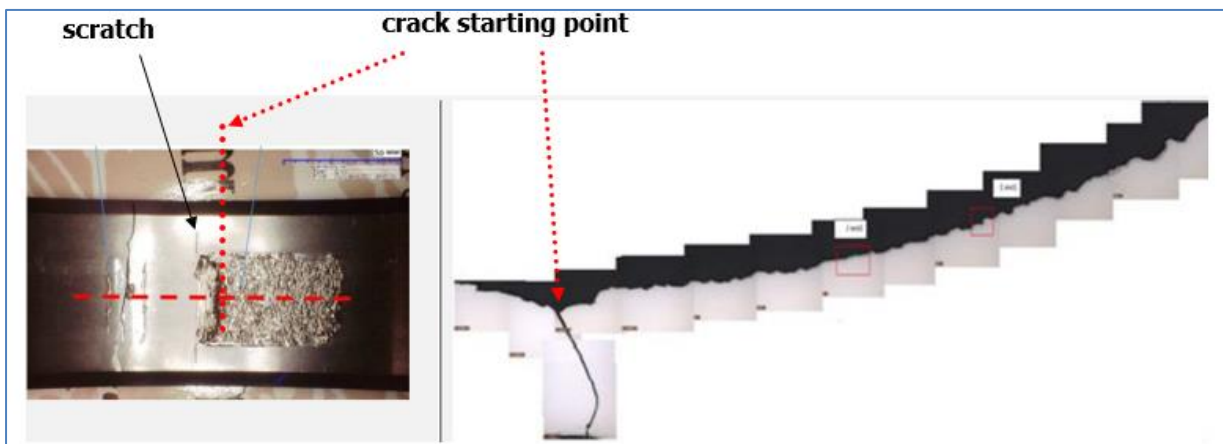


Figure 52: Cut of T104 - B-221026 specimen

For all 32CDV13 specimens, the spalling size and depth increased compared with the Phase I testing results, similar to what was observed for the M50Nil material. Nevertheless, it was not possible to produce a result with a crack through the raceway. Identical to the Phase I results, several cracks were found during the material cut, the lengths of which remained indicatively below 300 μm . The results are summarized in Table 35 and Figure 53 to Figure 55. There, cracks were found which turned their propagation direction toward the surface (see Figure 56).

Version	Serial number	Spalling depth (max) [mm]	Width [mm]	Length [mm]	Test time [Mio. cycles]
Version 1 – T104	DA-22503	~0.45	13	26	113.3
Version 1 – T104	DA-22506		13	6.2	86.6
Version 1 – T104	DA-22516		13	17	115.6

Table 35: Summary of testing results for phase II – 32CDV13

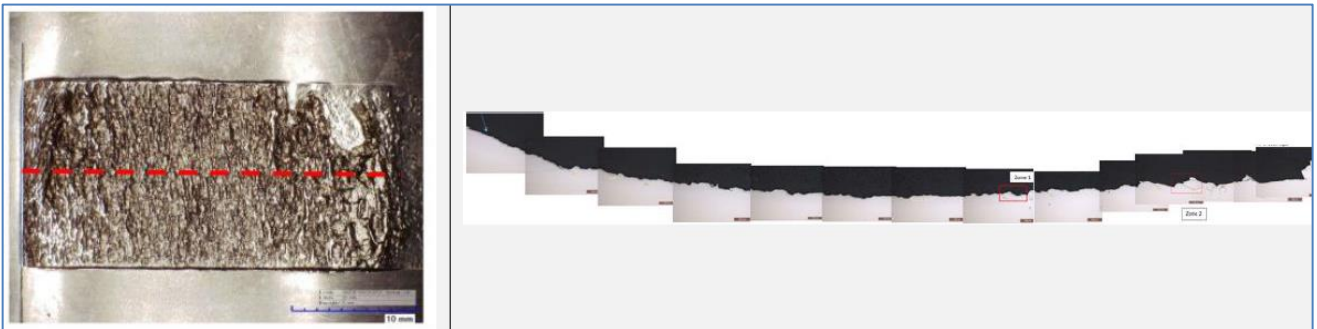


Figure 53: Cut of T104 - B-22503 specimen



Figure 54: Cut of T104 - B-22506 specimen

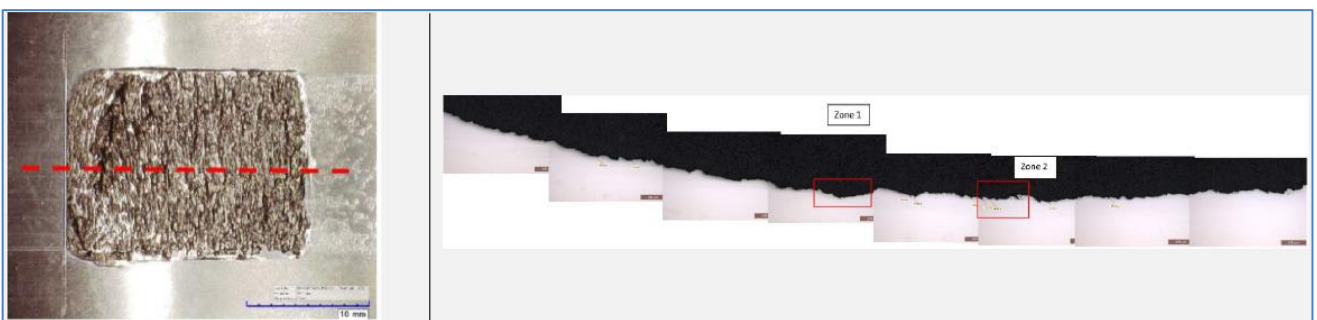


Figure 55: Cut of T104 - B-22516 specimen

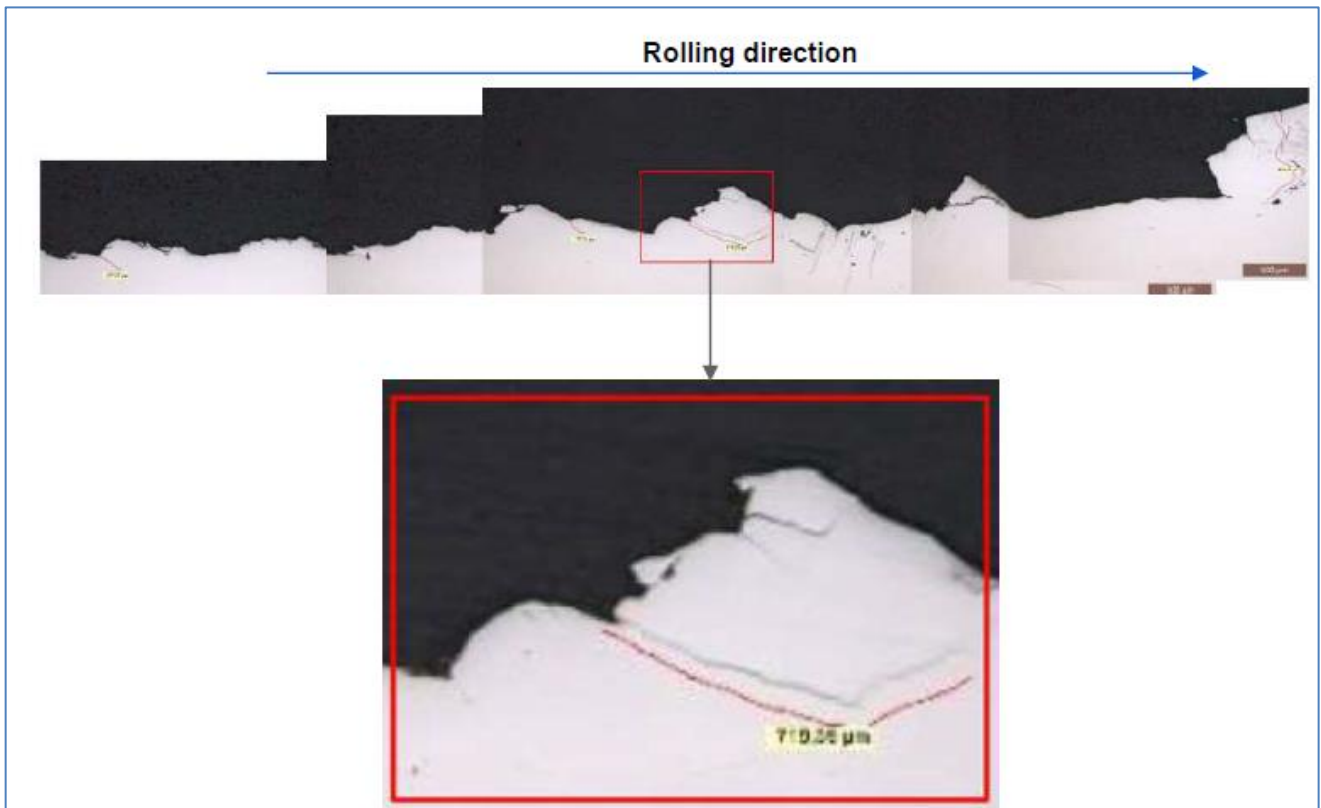


Figure 56: Material cut of 32CDV13 specimen (T104) for phase II

After testing the T104 specimen, the more severe design (T102) was tested again by starting at 1.8 GPa for the M50Ni material. It turned out that one specimen had severe cracks with a crack through, while the other two did not even show spall initiation and reached the suspension time of the test. For a deeper understanding, tests of the 32CDV12 material were also repeated at 1.8 and 2.4 GPa. While the lower load level did not show any damage until the test completion time was reached, the higher load level showed inconsistent results. One bearing test was stopped with a spall initiation without a crack through, while the other two reached the suspension time without any spall. As this was not expected and also different from the pre-test results (with severe cracks), an un-notched ring was tested under Phase I conditions, without body stress. As expected, it spalled similar to the previous Phase I results without any crack through. Therefore, a general issue (e.g. damage of test bench components which led to higher deformations or vibrations) on the test rig could be ruled out. Nevertheless, it was not possible within the scope of the project to provide a sure conclusion on this inconsistency for T102 specimens, but two hypotheses that are discussed in the frame of the overall overview and conclusion in chapter 5.6.

5.6 Test results – overview and conclusions

This chapter summarizes the previously presented results and highlights the main observations. To do so, the maximum spalling depth and the lifetime to spall initiation for the different tested versions are compared against the baseline variant to evaluate visible trends. In addition, conclusions about the test results are presented for both materials. An overall conclusion for the context of the project, and recommendations for future development projects, are highlighted in chapter 6.

Various specimens with different properties and boundary conditions were tested during the three main Phases I.1, I.2, and II for a case hardened material (16NCD13 and M50Ni1) and nitrided material (32CDV13).

During Phase I.1, the specimens were tested in pure rolling contact fatigue with the damaged raceway at three different load levels. For all materials, it was demonstrated that a certain limit exists, below which no spalling was generated for the given damage (scratch). Nevertheless, at a contact pressure of 2.4 GPa, all specimens produced a spalling failure of the raceway. By several cuts and surface topography measurements, it was shown that no crack into the depth was found, which indicates that at these conditions no crack propagation into the depth occurred. For all specimens, cracking was found to reach only a limited depth, whereas the spalling area increased with time with repetitive breakouts at the raceway surface.

During Phase I.2, parameters such as hardness depth, hardness, and residual stress profile were changed for the different material types. The main goal of this Phase was to study the influence of these parameters on the spalling depth and the tendency for crack initiation and propagation into the depth of the material. It was demonstrated for all specimens that the modified parameters did not lead to crack initiation and propagation into the depth of the material. Nevertheless, the spalling depth and time to spalling initiation were different for almost all specimen types. Identical to Phase I.1 (baseline variant), a finite depth of cracking was observed, while the spalling area increased with time with repetitive breakouts at the raceway surface. No additional testing was performed at the lower load levels of 1.5 GPa and 1.8 GPa. Because no spalling occurred for Phase I.1 at these load levels, it can be concluded that the results with the changed parameters in I.2 did not lead to a significant change in the spalling and cracking behaviour of the samples tested. Nevertheless, it is not proven whether the contact pressure threshold at which cracking initiates is shifted to a slightly higher or lower value.

For all nitrided shafts, no classical spalling was observed. Peeling of the white layer was observed, which was inspected and checked by additional material cuts. It turned out that the brittle white layer from the nitriding process was the root cause. Together with pre-damage introduced into the surface layer, it led to peeling of the white layer. Because of the peeling-off of the white layer, most of the tests were stopped when the chip detection sensor was triggered. Some further analysis was done at AH Tech (see also A.5) on the white layer problem and studies were found which show improved lifetime for undamaged contact areas of gears. Nevertheless, this was not proven by additional testing of the shaft specimen. For the nitrided outer rings, the white layer was removed (as it is typically done for bearing applications). As a result, keeping the white layer for these tests made it impossible to draw further conclusions for this material.

As a summary of Phase I, the following two figures (Figure 57 and Figure 58) highlight the maximum spalling depth for the different versions tested through Phase I. The results were checked for any trend that could be derived (e.g. spalling depth vs. hardness/hardness depth), but based on the available data, it was not possible to give a clear statement for a trend. The only thing that could be highlighted is that the specimens with the highest hardness depth for the case hardened material have the lowest spalling depth (V3 for 16NCD13 and B-Version 1 for M50Ni1). Nevertheless, all of the parameter changes within Phase I led to finite crack depth and spalling without severe cracking into the depth of the material. Besides the spalling and crack depth, no clear trend could be observed for additional parameters (e.g. on the lifetime to spall initiation or spall depth vs. residual stress), as a high scatter band is present for this parameter.

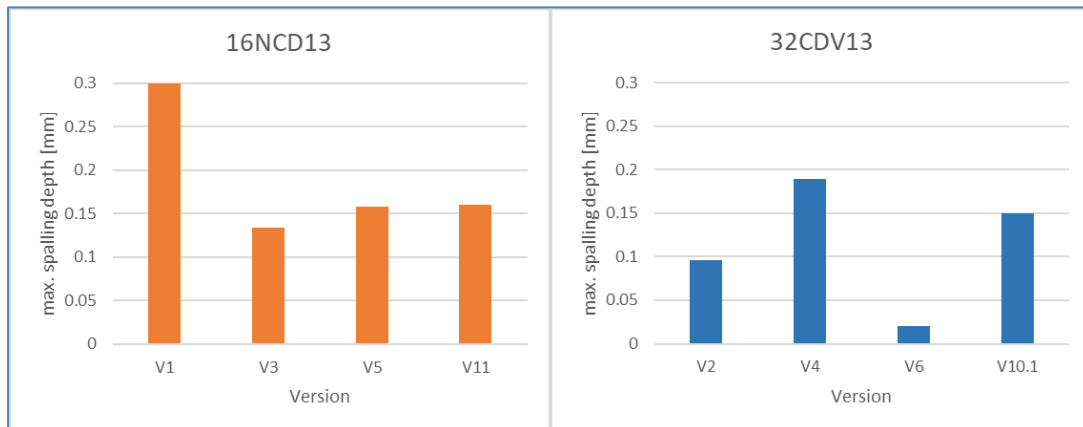


Figure 57: Comparison of max. spalling depth of all tested shafts (phase I.1 and I.2)

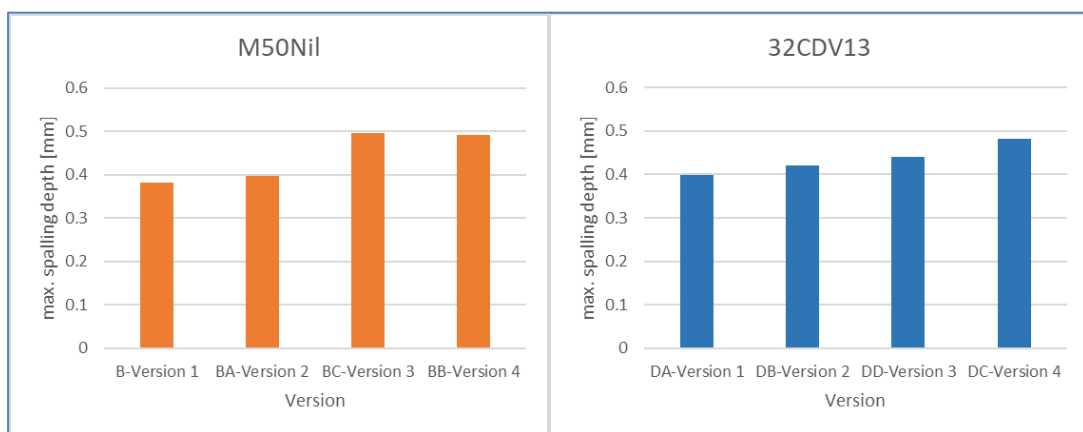


Figure 58: Comparison of max. spalling depth of all tested outer rings (phase I.1 and I.2)

For Phase II of testing, an additional body stress was introduced for the baseline specimens by modifying the geometry. The tests were performed at two different load levels to evaluate potential crack propagation into depth for different body stresses. For the shaft specimens no crack into depth was observed during initial pre-tests, whereas a more severe laser scratch led to crack propagation into the depth of the material. Probably because of the missing shoulder height of this damage, no classical spalling was observed anymore. For the nitrided material, there was also a breakout of the surface with a crack network toward the surface that could be observed. This could be explained by the presence of the brittle white layer compared with the case hardened specimens.

For the outer ring specimens, both materials were also tested at two different load levels, introduced by different notch geometries (T104 and T102). With a thicker rim of the notch for T104, the design was less severe compared to T102. For the T104 design, it turned out that all specimens with M50NiL spalled with a crack propagation through the full thickness of the specimen with deep spalling and similar characteristics, whereas the 32CDV13 specimens behaved differently by only spalling without any through-crack. Nevertheless, for both materials, the spalled area increased with the introduction of body stress compared with Phase I. The difference in results might be explained by the different fracture toughness (which is higher for 32CDV13) of the material and therefore a significant difference in crack propagation behavior.

For the T102 geometry, two contact pressure levels were tested (1.8 GPa and 2.4 GPa). The more severe geometry led to inconsistent results. As presented in Table 33, there was a high scatter band of results for both materials and load levels. The load was lowered to 1.8 GPa, but the results remained inconsistent without a clear tendency. To rule out any structural issues with the test bench, a Phase I bearing was tested to verify that

there was no general behavior drift of the test bench. No difference from Phase I results was observed. No evidence for this inconsistency in T102 specimens was obtained at this stage of the project. Nevertheless, there are two hypotheses to explain the T102 results. On the one hand, the flexibility of the T102 notch could lead to a misalignment of the bearing and a change in load distribution and contact pressure. On the other hand, initiated cracks could lead to a change in the failure mode compared to the T104 design.

As a result for Phase II, it was observed that the additional body stress led to a significant reduction in lifetime for both specimen types, whereas the 32CDV13 material for the outer ring performed better than the other tests for Phase II. This could be partially explained by the better fracture mechanics properties of the core material compared to M50Ni1 and 16NCD13. It should also be mentioned that the spalling depth was significantly increased for all specimens where spalling occurs (see Figure 59 as an example of outer ring specimens). As mentioned above, Phase II was also the only Phase where cracking through the material (into depth) was observed.

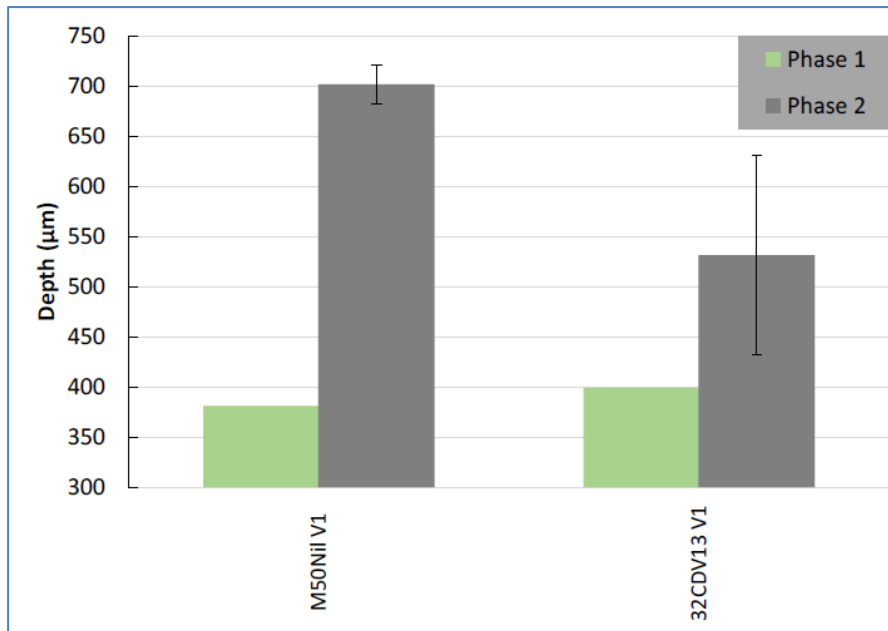


Figure 59: Comparison of max spalling depth for phase I and II for outer ring specimen

As a summary of the test campaign, the following two tables (Table 36 to Table 39) highlight the main results according to the maximum spalling depth, lifetime to spall initiation and status of cracks for both specimen types with comparisons to baseline variants.

Test results variation compared with baseline						
Phase	Specimen	Material	Change compared with baseline	Max. spalling depth [mm]	Lifetime to spall initiation (mean value) [Mio]	Crack
Phase I.1	V1	16NCD13	Baseline*	0.3	54	No Crack
Phase I.2	V3	16NCD13	Increased CHD	-55%*	-27%*	No Crack
Phase I.2	V5	16NCD13	Increased CHD with salt bath hardening	-47%*	-9%*	No Crack
Phase I.2	V11	16NCD13	Intermediate heating and surface rolling	-47%*	-20%*	No Crack
Phase II	V1.1	16NCD13	Hollow shaft, 2.4 GPa	No spalling	-14%*	Yes, into depth
Phase II	V1.1	16NCD13	Hollow shaft, 2.9 GPa	No spalling	-89%*	Yes into depth

*variation according to marked reference baseline (16NCD13 – V1)

Table 36: Overview of test results for shaft specimen for 16NCD13

Test results variation compared with baseline						
Phase	Specimen	Material	Change compared with baseline	Max. spalling depth [mm]	Lifetime to spall initiation (mean value) [Mio]	Crack
Phase I.1	V2	32CDV13	Baseline**	0.096	135	No Crack
Phase I.2	V4	32CDV13	Increased NHD	+97%**	-90%**	No Crack
Phase I.2	V6	32CDV13	Nitro carburizing process	-80%**	-26%**	No Crack
Phase I.2	V10.1	32CDV13	Intermediate heating	+56%**	-82%**	No Crack
Phase II	V2.1	32CDV13	Hollow shaft, 2.4 GPa	No classical spalling	-82%**	Yes, into depth with breakouts of surface
Phase II	V2.1	32CDV13	Hollow shaft, 2.9 GPa	No classical spalling	-98%**	Yes, into depth with breakouts of surface

**variation according to marked reference baseline (32CDV13 – V1)

Table 37: Overview of test results for shaft specimen for 32CDV13

Test results variation compared with baseline						
Phase	Specimen	Material	Change compared with baseline	Max. spalling depth [mm]	Lifetime to spall initiation (mean value) [Mio.]	Crack
Phase I.1	B-Version 1	M50Nil	Baseline*	0.381	43.8	Finite crack
Phase I.2	BA-Version 2	M50Nil	Reduced hardness depth	+4%*	-27%*	Finite crack
Phase I.2	BC-Version 3	M50Nil	Increased compressive residual stress	+30%*	-53%*	Finite crack
Phase I.2	BB-Version 4	M50Nil	Reduced surface hardness and hardness depth	+29%*	-47%*	Finite crack
Phase II	B T104-Version 1	M50Nil	Notch design – less severe	+84%*	-99%*	Crack trough thickness
Phase II	B T102-Version 1	M50Nil	Notch design – more severe	No general statement possible due to spread of results / inconsistency		

*variation according to marked reference baseline (M50Nil – V1)

Table 38: Overview of test results for outer ring specimen for M50Nil

Test results variation compared with baseline						
Phase	Specimen	Material	Change compared with baseline	Max. spalling depth [mm]	Lifetime to spall initiation (mean value) [Mio.]	Crack
Phase I.1	DA-Version 1	32CDV13	Baseline**	0.399	114.8	Finite crack
Phase I.2	DB-Version 2	32CDV13	Reduced hardness depth	+6%**	+5%**	Finite crack
Phase I.2	DD-Version 3	32CDV13	No change (slight reduction of compressive residual stress)	+10%**	+44%**	Finite crack
Phase I.2	DC-Version 4	32CDV13	Reduced surface hardness and hardness depth	+21%**	+22%**	Finite crack
Phase II	DA T104-Version 1	32CDV13	Notch design – less severe	+33%**	-12%**	Finite crack
Phase II	DA T102-Version 1	32CDV13	Notch design – more severe	No general statement possible due to spread of results / inconsistency		

**variation according to marked reference baseline (32CDV13 – V1)

Table 39: Overview of test results for outer ring specimen for 32CDV13

6. Prediction of rolling contact fatigue crack propagation

6.1 Introduction

This work deals with 2D rolling contact fatigue crack propagation under complex load conditions in case hardened components. This is not only about describing the spalling effect but also to understand the damage process and predict the crack path in the structure. To achieve this goal, three separate parts are considered as follows:

- Part I (D2-4): Development of a 2D-FE- model for simulating crack growth under rolling contact (phase I.1). This report provides detailed information on the fracture mechanical methods and approaches for stress intensity factor calculations used to simulate rolling contact fatigue in our project. In addition, fatigue crack concepts and fracture criteria under 3D mixed-mode loading are presented. There is also a summary of the main works on crack growth under rolling contact fatigue and a discussion of the reasons for selecting the methods for simulating crack growth under rolling contact for this project [6].
- Part II (D2-5): Further development of the FE-model in D2-4 to prepare phase I.2 of this project. Residual stresses are considered in the simulation of crack growth under rolling contact fatigue. The crack growth simulations were performed assuming an external crack in a semi-infinite plane under rolling contact [7].
- Part III (D2-7): The aim of this work is to predict the crack paths in the hollow shaft and the outer ring under rolling contact fatigue in Phase II. The measured residual stresses, geometry of the component and complex loads by the rolling elements were considered. These methods developed for investigating crack growth can be applied to other practically relevant problems such as rolling contact in planetary gears.

6.2 Description of the FE-model and simulation approach

In this work, linear-elastic fracture mechanics and an initial technical surface crack is assumed for the fracture mechanical investigations. Because of the large number of interactively influencing parameters, such as contact geometry, load, lubricating film, rolling velocity, coefficient of friction, material properties, inclusions, microstructure, surface treatment and impurities [14], rolling contact fatigue is a complex problem. In the works (D2-4) and (D2-5), the following important parameters are considered: contact geometry, loading, material properties, and friction at the cylinder/half-plane (ring) and crack surfaces. The crack growth simulation was carried out by the University of Paderborn [8] using the program system ADAPCRACK3D [15]. This software has been used successfully in many problem solutions, such as numerical determination of crack paths in three-dimensional structures, e.g., crack growth in a shutter ring of a hydraulic press [16], simulation of 3D structures under the influence of temperature [17] and crack propagation in additive manufactured materials and structures [18]. Using ADAPCRACK3D and FEM, the domain around the growing crack is replaced by a sub-model technique [19]. The calculations of the stress intensity factors K_I and K_{II} (SIFs) in this work were done using energy release rates determined with the modified virtual crack closure integral (MVCCI) [20]. Using the σ_1' criterion [21], the cyclic SIFs as well as the kinking angles are determined. This criterion is based on the fact that crack propagation occurs perpendicular to the maximum principal normal stress σ_1' on the crack front. The equivalent stress factor K_V depends on the three SIFs K_I , K_{II} , K_{III} and the crack kinking angle [16].

The components to be examined are represented as 3D-models with constant and equal thickness (see Figure 60 (a)). The raceways of the hollow shaft and outer ring are modeled with a constant radius in the ring body. Using the symmetric boundary conditions on the side surfaces of the rolling element and the ring, the model corresponds to an infinitely long cylindrical roller rolling over an infinitely wide ring with an infinitely wide crack. The initial crack with a defined coefficient of friction between the crack surfaces is a through edge crack. Here, the crack is perpendicular to the side surfaces of the ring. In this case, the model corresponds to a plane model with a state of plane strain. The crack grows uniformly across the width of the ring so that the stress intensity factors are constant along the crack front.

During the rollover process without slipping, a constant pressing force F and constant drive torque M act at the center of the roller, as shown in Figure 60(b). The force F depends on the radius of the rolling element R and contact pressure p and is determined so that a certain contact pressure is established on the raceway. The drive torque $M=500000 \text{ N}\mu\text{m}$ is used in all simulations. The roll path is $s=3000 \mu\text{m}$ long and is divided into 25 equal roll increments. Assuming linear elastic fracture mechanics (LEFM), a fracture mechanics evaluation is done at every roll increment (see Figure 61), with the cyclic equivalent stress intensity factor $\Delta K_V = K_{V,max} - K_{V,min}$ and crack kinking angle being important quantities in crack growth simulations. If ΔK_V is smaller than the threshold value, the crack cannot grow. If the crack propagation is stable ($\Delta K_{th} < \Delta K_V < \Delta K_C$), the crack is extended by Δa , taking into account the kinking angle. When ΔK_V has one maximum value greater than ΔK_{th} , the crack grows without branching. The crack branches when ΔK_V has two maxima.

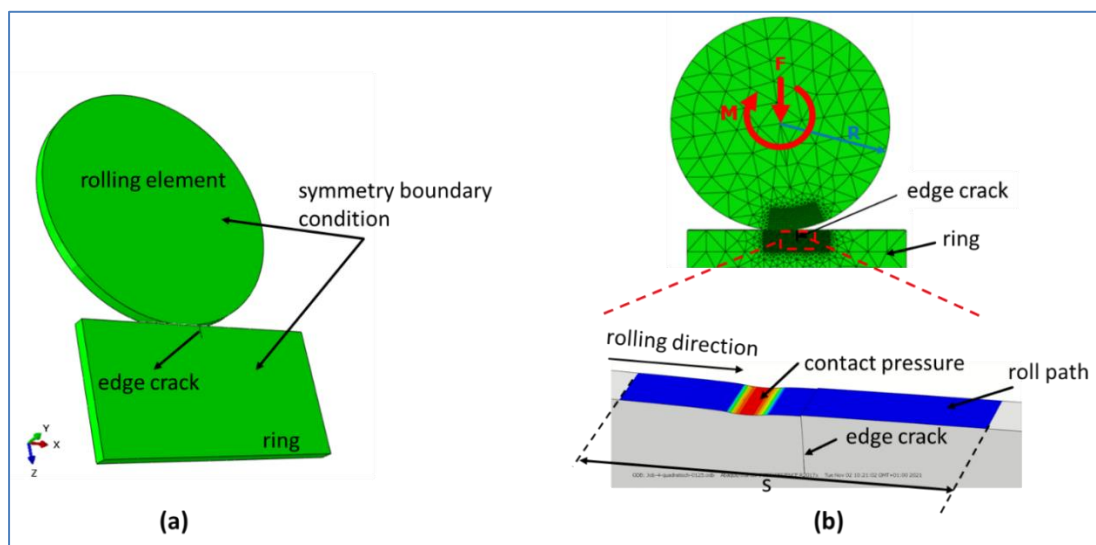


Figure 60: Model description for predicting the crack path under rolling contact fatigue, (a) 3D-model of the rolling element and the ring, (b) definition of the parameters used in crack growth simulations

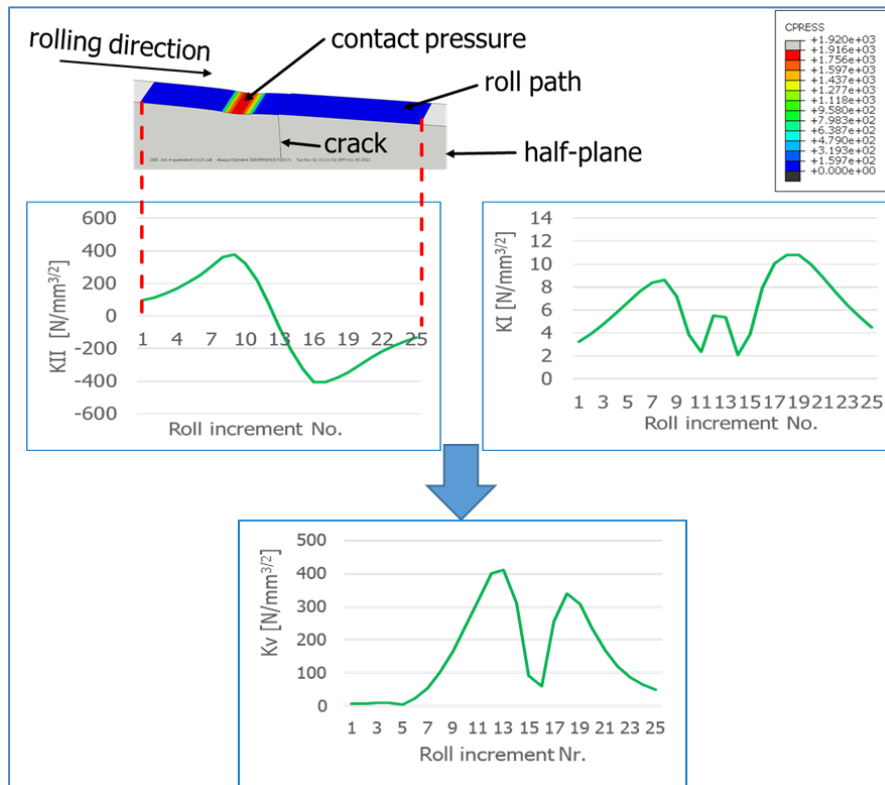


Figure 61: Example of a snapshot of the contact pressure during the rollover process und and the resulting SIFs K_I , K_{II} and K_V for one rollover process, K_V has two maxima

6.3 Parametric study to prepare Phase I.1

In this section, a basic parametric study was conducted in advance to prepare Phase I.1 testing in chapter 5.3. The crack paths were investigated assuming a semi-infinite plane with an edge crack under pure rolling contact load by varying the following parameters:

- Initial crack length (cases 1 and 2)
- Crack angle (cases 3 and 4)
- Friction coefficient: cylinder/half-plane (cases 5 and 6)
- Contact pressure (cases 7 and 8)
- Friction coefficient: crack surfaces (cases 9, 10 and 11)

The equivalent stress intensity factor ΔK_V for the growing crack is compared with the typical threshold value of approx. $150 \text{ N/mm}^{3/2}$ against fatigue crack growth in steel. This limit is represented by red line in the figures. The rolling element radius $R=10 \text{ mm}$ is used for all simulations in this chapter.

6.3.1 Influence of initial crack length on crack paths and stress intensity factors

Two initial crack lengths of 0.5 mm and 1 mm were selected to study the influence of the initial crack on the development of the crack path, see Table 40 (case 1 and case 2). These two initial cracks are typical lengths for an initial technical crack.

Parameter	unit	case number	
		1	2
Initial crack length	[mm]	0.5	1
Crack angle	[DEG]	30	30
Friction coefficient: cylinder/half-plane		0.15	0.15
Contact pressure	N/mm ²	1500	1500
Friction coefficient: crack surfaces		0.15	0.15

Table 40: Cases 1 and 2 with initial crack length of 0.5 mm and 1 mm

Figure 62 shows that K_{II} is higher for longer initial cracks and that crack growth with the short initial crack already begins in roll increment 5, whereas in case 2, it begins at roll increments 7 and 8. The positions of the cylinder in these roll increments are shown in Figure 63.

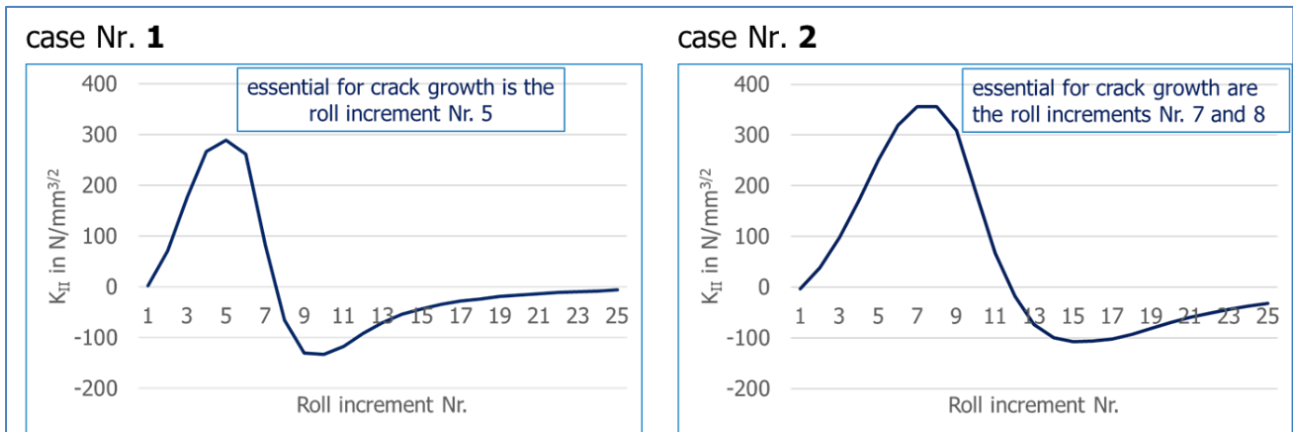


Figure 62: K_{II} -graph during the rollover process for the initial cracks; case no. 1 (left) and case no. 2 (right)

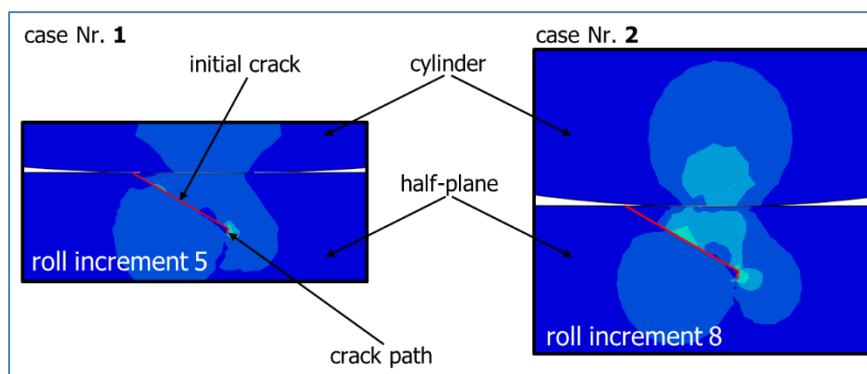


Figure 63: Positions of the cylinder at roll increments 5 and 8 for cases 1 and 2, respectively

The crack paths in both cases are similar, whereas the values of K_V are larger for the initial crack with a length of 1mm, see Figure 64. The maximum value of K_V at the initial crack increases with initial crack length. The values of K_V decreases more slowly with increasing initial crack length and crack growth and reach the threshold value for larger additional crack lengths.

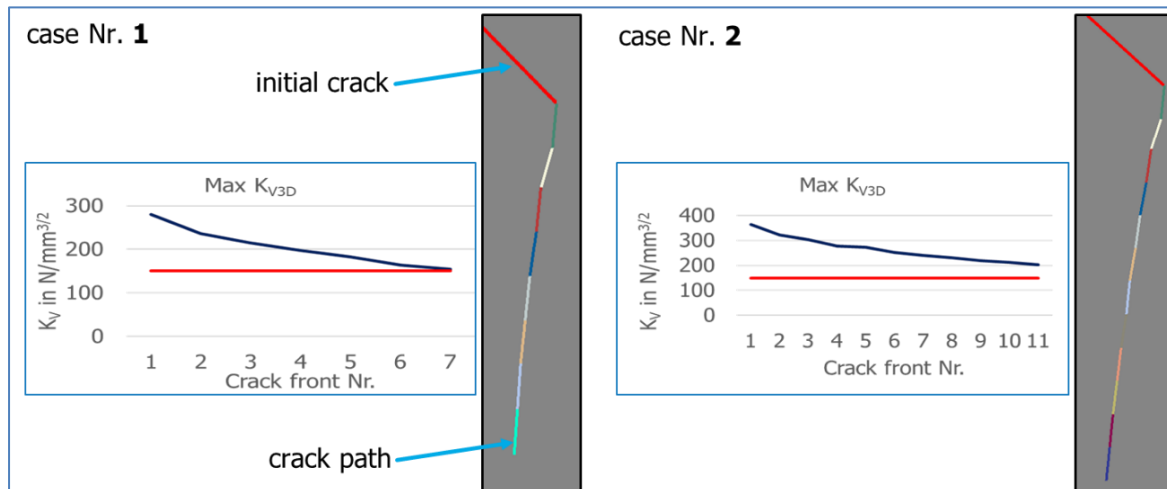


Figure 64: Crack path and its K_I during crack growth for cases 1 and 2

These investigations show that the initial crack length has no influence on the initial crack kinking angle or the basic course of the crack path with these selected parameters and boundary conditions.

6.3.2 Influence of initial crack angle on crack paths and stress intensity factors

Two initial crack angles 15° and 90° were selected to study the influence of the initial angle on the development of the crack path, see Table 41.

Parameter	unit	case number	
		3	4
Initial crack length	[mm]	0.5	0.5
Crack angle	[DEG]	15	90
Friction coefficient: cylinder/half-plane		0.15	0.15
Contact pressure	N/mm ²	1500	1500
Friction coefficient: crack surfaces		0.15	0.15

Table 41: Cases 3 and 4 of crack angles of 15° and 90°

The SIF K_{II} for the initial crack with an inclination angle of 15° (case 3) and 90° (case 4) are shown in Figure 65. The two curves show two extreme values with different signs. These are larger than the threshold, which can lead to crack branching. It can also be seen that the first extreme value of K_{II} for the crack with an inclination angle of 15° has a positive sign, whereas the first extreme value of K_{II} for the crack with an inclination angle of 90° has a negative sign. These signs indicate the direction in which the crack will grow. This means that the initial crack with an inclination angle of 15° grows downwards in roll increment 4 and upwards in roll increment 9 as shown in Figure 68. In this case, simultaneous crack growth toward the surface and into the material is possible. In contrast to case 3, the initial crack with 90° grows first to the right in roll increment 10 and then to the left in roll increment 15, see Figure 69. Here, both cracks grow simultaneously into the material.

It is also interesting to see that the cylinder in case 3 lies on the crack in the two extreme values (see Figure 66). In case 4 the cylinder is at the first extreme value before the crack and at the second extreme value after the crack (see Figure 67).

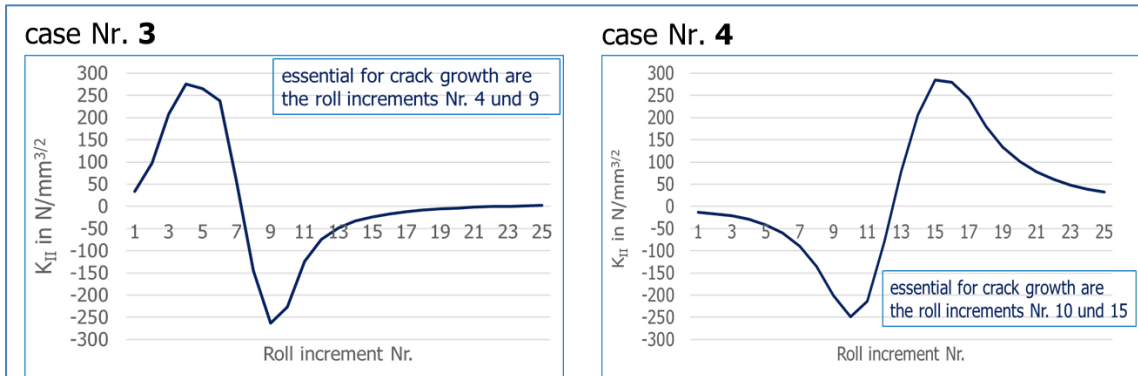


Figure 65: K_{II} -graph during the rollover process for the initial crack; for case no. 3 (left) and for case no. 4 (right)

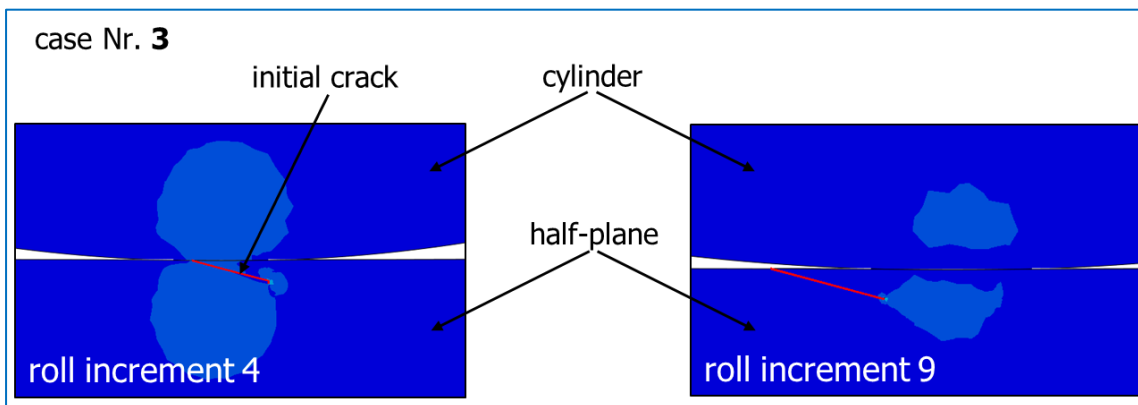


Figure 66: Positions of the cylinder at roll increments 4 and 9 for case 3

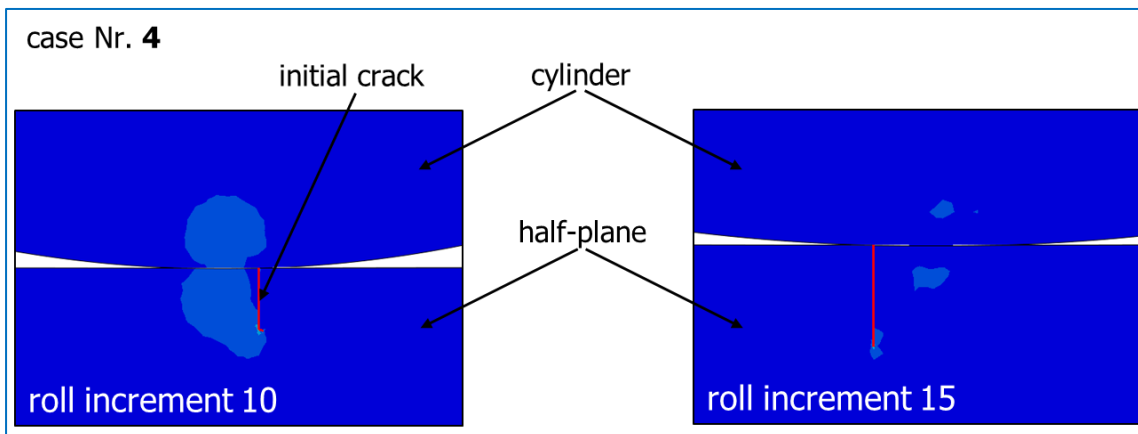


Figure 67: Positions of the cylinder at roll increments 10 and 15 for case 4

In case 3, both branched cracks show a steady decrease in K_V with crack growth, with the downward-growing crack stopping first (see Figure 68). In this case, K_V decreases only slowly for the additional crack that grows toward the surface (possibly no crack standstill). K_V in case 4 shows a similar decreasing trend for both branched cracks, with K_V being higher for the left branched crack (see Figure 69).

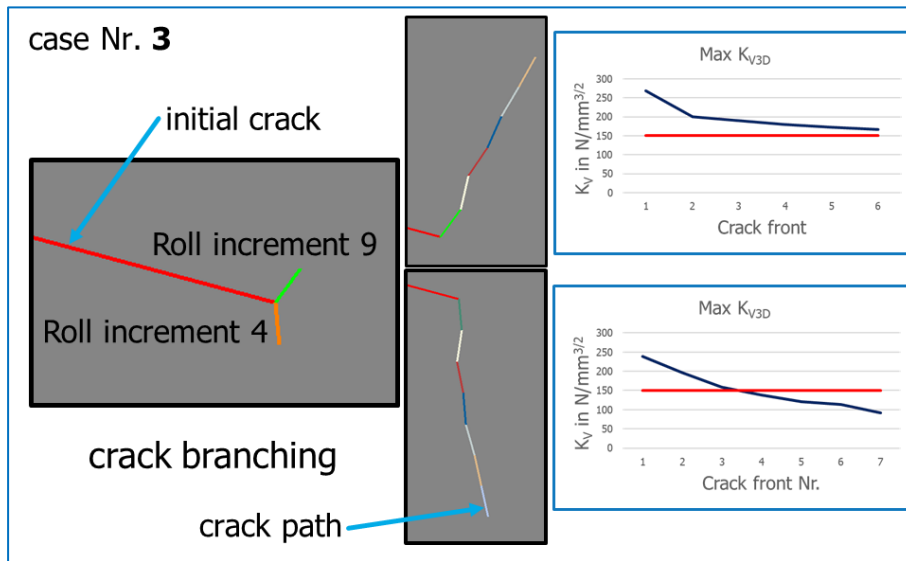


Figure 68: Case no. 3, Influence of initial crack length on crack path with a crack angle of 15 degrees

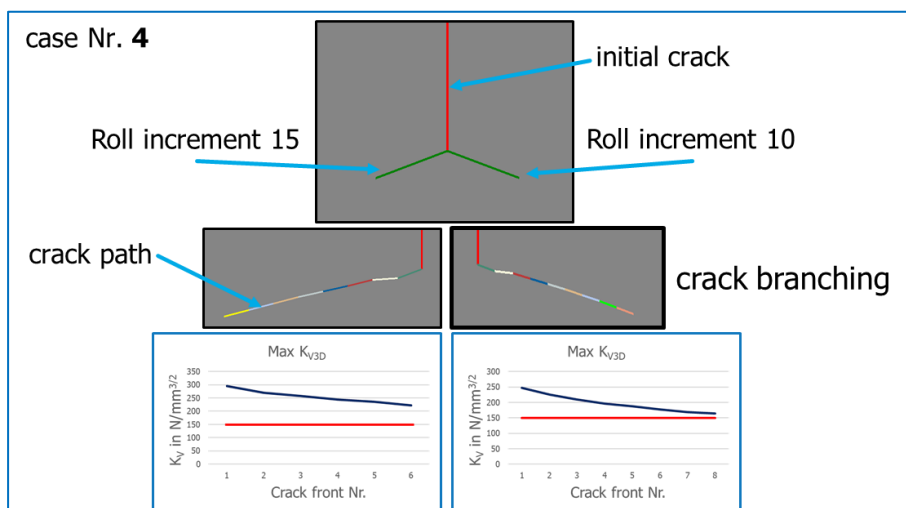


Figure 69: Case no. 4, influence of initial crack length on crack path with a crack angle of 90 degrees

These results with these selected parameters and boundary conditions show that the initial crack angle has no influence on the initial crack kinking angle. In both cases 3 and 4, the kinking angle at the first crack extension are about $\pm 70^\circ$ (Mode II controlled). The influence of crack angle on crack paths and SIFs is summarized as follows:

- Depending on the initial crack angle, two extreme values of ΔK_V are relevant to crack growth during the rollover process of the initial crack (crack branching is possible). With medium starting angles of 30° , there is only one relevant extreme value (see cases 1 and 2). The value of K_V increases slightly with increasing crack initiation angle
- Initial crack angles have major influence on the basic course of the crack path

6.3.3 Influence of friction (cylinder / half-plane) on crack paths and stress intensity factors

To investigate the influence of the friction coefficients between the cylinder and the half-plane, two extreme values were selected (see Table 42). Since the coefficient of friction in the pairing of steel on steel is generally between 0.15 and 0.2, the value 0.15 was selected in case 5. The upper limit of 0.8 in case 6 was adopted as the upper limit to clearly show the difference from the lower limit in crack development. The results for cases 5 and 6 are similar to those for case 1 except for numerical fluctuations.

Parameter	unit	case number	
		5	6
Initial crack length	[mm]	0.5	0.5
Crack angle	[DEG]	30	30
Friction coefficient: cylinder/half-plane		0.15	0.8
Contact pressure	N/mm ²	1500	1500
Friction coefficient: crack surfaces		0.15	0.15

Table 42: Cases 5 and 6 of friction coefficients of 0.15 and 0.8 (cylinder/half-plane)

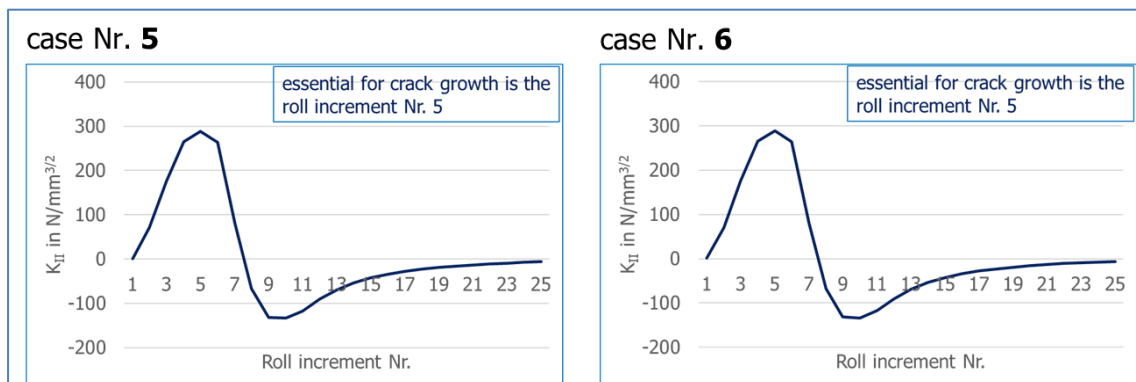


Figure 70: K_{I1} -graph during the rollover process for the initial crack in case no. 5 (left) and for case no. 6 (right)

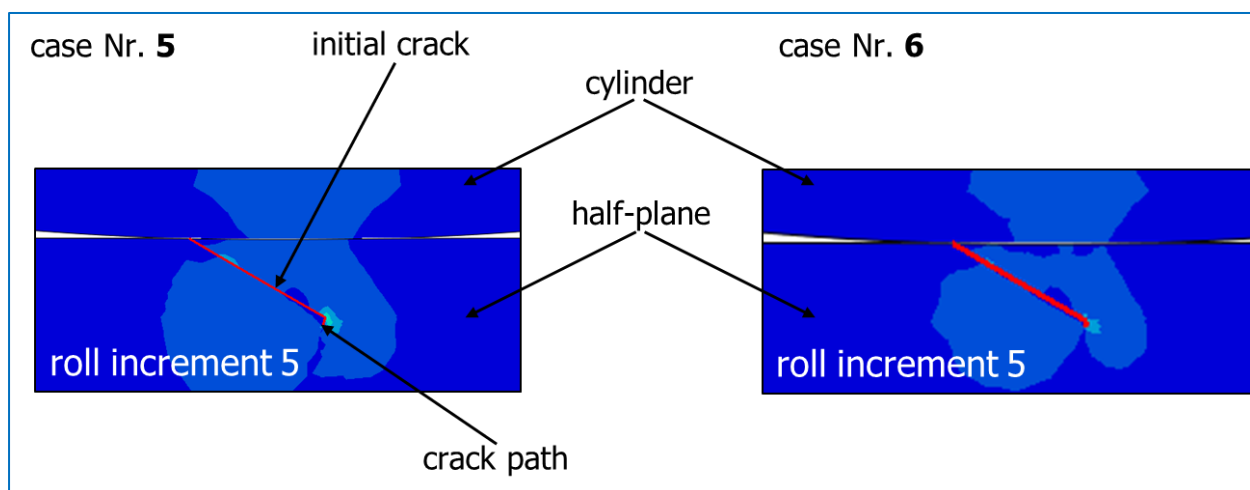


Figure 71: Positions of the cylinder at roll increment 5 for cases 1 and 2

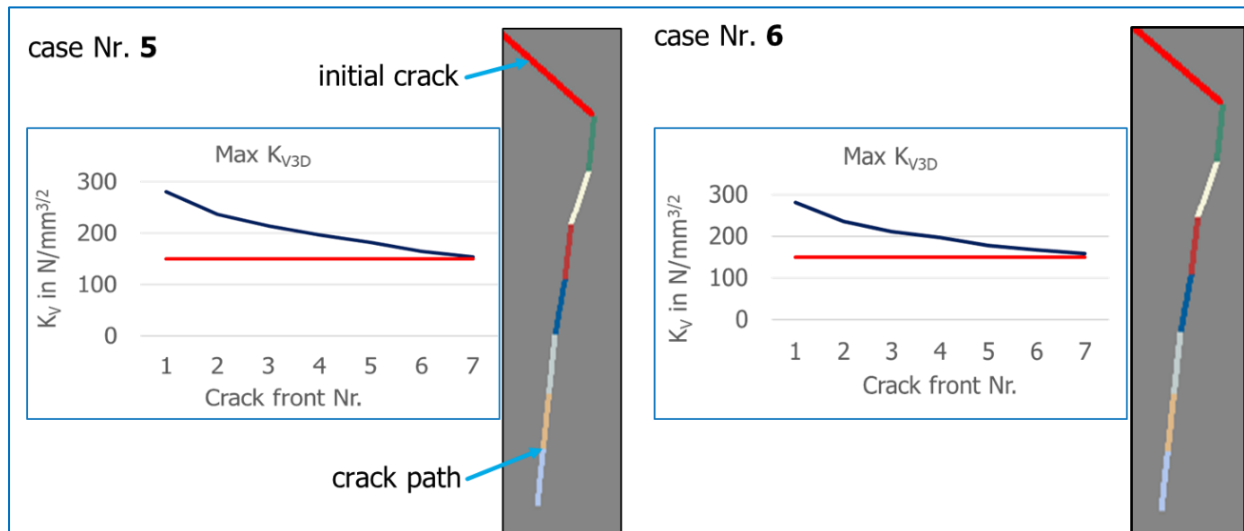


Figure 72: Crack path and its max K_V during crack growth for cases 5 and 6

These results show that the coefficient of friction between the cylinder and the half-plane does not affect the crack growth behavior as long as the contact pressure between the roll and the half-plane is sufficiently high. The cylinder does not slip because of the drive torque (no-slip condition fulfilled).

6.3.4 Influence of contact pressure on crack paths and stress intensity factors

In cases 7 and 8, the influence of the contact pressure level on the crack path was investigated, see Table 43. Two values were selected here. A value of 3000 N/mm² (case 8) was chosen to study the influence of high contact pressure on the crack path. The smallest value of 500 N/mm² was assumed to show the crack path in the limit values. Because the contact pressure of 500 N/mm² is very low, the cylinder slips. In this case, simulation of the global model is not possible. For this reason, the coefficient of friction between the cylinder and the half-plane was set to $\mu = 0.8$ in case 7 to prevent the cylinder from slipping (see Table 43).

Parameter	unit	case number	
		7	8
Initial crack length	[mm]	0.5	0.5
Crack angle	[DEG]	30	30
Friction coefficient: cylinder/half-plane		(0.15) 0.8	0.15
Contact pressure	N/mm ²	500	3000
Friction coefficient: crack surfaces		0.15	0.15

Table 43: Cases 7 and 8, influence of contact pressure on crack path. In case 7, the coefficient of friction was replaced with 0.8 to prevent the roller from slipping (contact pressure of 500 N/m² is very low)

The resulting K_{II} is very small, as shown in Figure 73 (left). In this case no crack growth is to be expected. In contrast to case 7, the contact pressure in case 8 is high, accompanied by a larger K_{II} . Here, roll increments 4 and 11 are decisive for crack growth, as shown in Figure 33 (right). It can also be seen here that the high values of K_{II} persist from 1 to 8 roll increments. In the case of a kinked crack, the loading maximum is reached at a later roll increment because the first maximum is very wide. This can lead to multiple crack branches. The position of the cylinder at roll increment 7 is shown in Figure 74.

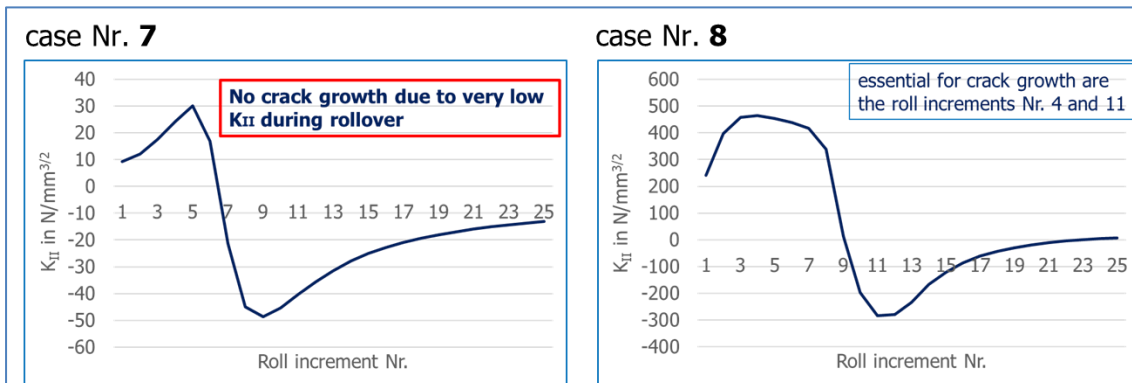


Figure 73: K_{II} -graph during the rollover process for the initial crack in case no. 7 (left) and for case no. 8 (right)

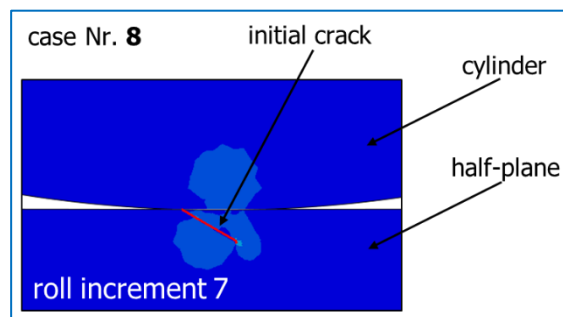


Figure 74: Positions of the cylinder at roll increment 7 for case 8

Due to high crack loading, the specified crack increment of 1% of the initial crack length is still too large, see Figure 75. This causes a strong decrease in K_{II} at the first additional crack and changes the crack kinking angles. The calculation with a crack increment of less than 1% of the initial crack length is very complex and requires considerable time. Therefore, only one side of the crack growth was simulated. Figure 75 also shows that K_{II} decreases rapidly with increasing additional crack length and reaches a standstill. No further simulations were performed because the crack path jumps too much. In the case of smaller crack increments, smoother crack paths are expected, but no fundamentally different results are expected.

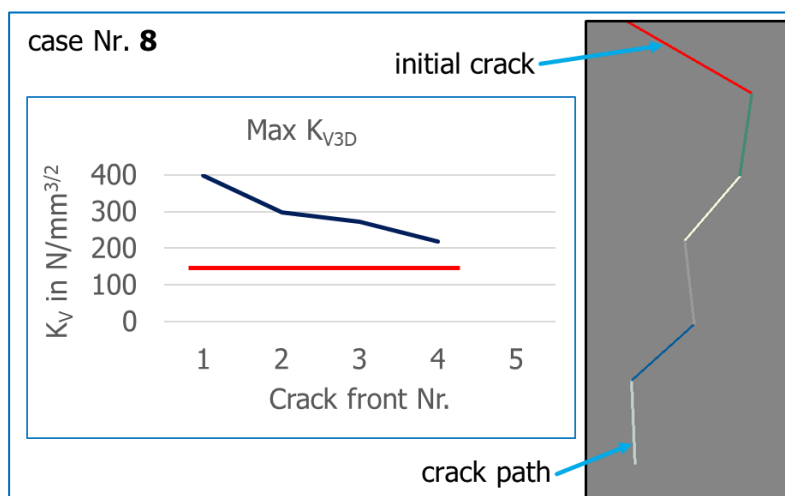


Figure 75: Crack path and its K_V during crack growth for case 8

These investigations show that a certain minimum pressure is required to cause crack growth. At very high pressure, crack growth is also possible at the second extreme value after the crack has been rolled over. This

can lead to crack branching. In the case of high crack loading K_{II} at very high pressure, K_{II} decreases rapidly with crack growth.

6.3.5 Influence of friction at crack surfaces on crack paths and stress intensity factors

The influence of the friction coefficient between the crack surfaces on the crack growth is investigated. Three values of 0, 0.45 and 0.7 were selected for the investigations, see Table 44.

Parameter	unit	case number		
		9	10	11
Initial crack length	[mm]	0.5	0.5	1
Crack angle	[DEG]	30	30	15
Friction coefficient: cylinder/half-plane		0.15	0.15	0.15
Contact pressure	N/mm ²	1500	1500	3000
Friction coefficient: crack surfaces		0.45	0.7	no

Table 44: Cases 9, 10 and 11 of friction coefficients 0.45, 0.7 and 0 (crack surfaces)

Since K_{II} is small in cases 9 and 10, no crack growth is expected (see Figure 76). In case 9, K_{II} just about reaches the threshold. In the case of crack growth, the crack will grow as shown in Figure 77 and then come to a standstill. The positions of the cylinders to the crack in roll increment 4 for case 9 and in roll increment 5 for case 10 are shown in Figure 78.

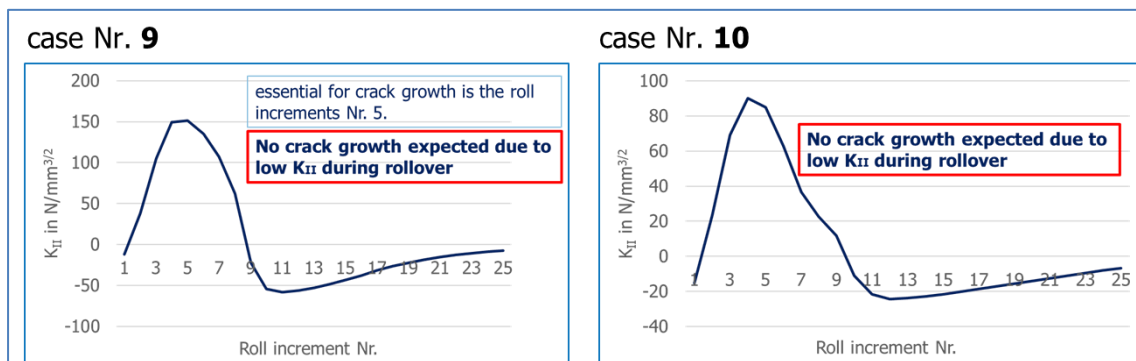


Figure 76: K_{II} -graph during the rollover process for the initial crack in case no. 9 (left) and for case no. 10 (right)

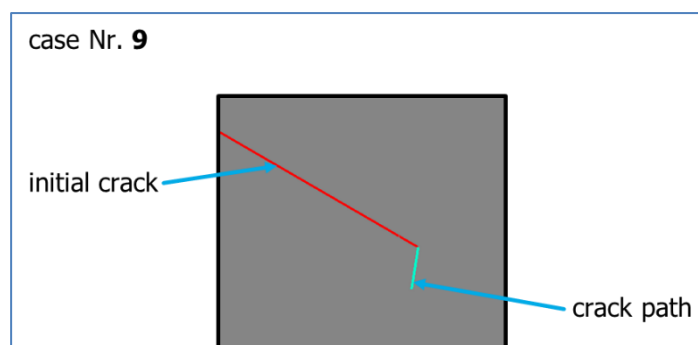


Figure 77: Crack path for case 9

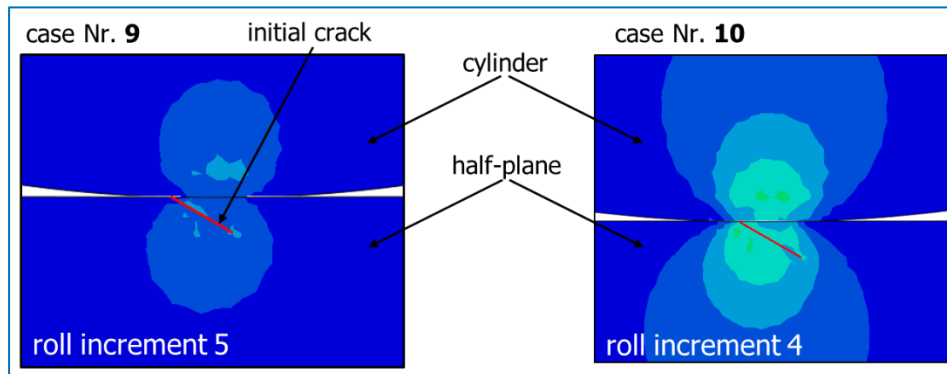


Figure 78: Positions of the cylinder at roll increments 5 and 4 for cases 9 and 10, respectively

These investigations show that with increasing crack surface friction in cases 9 and 10, the magnitude of the extreme values decreases rapidly. Crack standstill is expected with high crack flank friction.

To investigate a conservative case, the contact pressure in case 11 was increased to a very high value of 3000 MPa and the friction between the crack surfaces was neglected. The predicted crack path is shown in Figure 79.

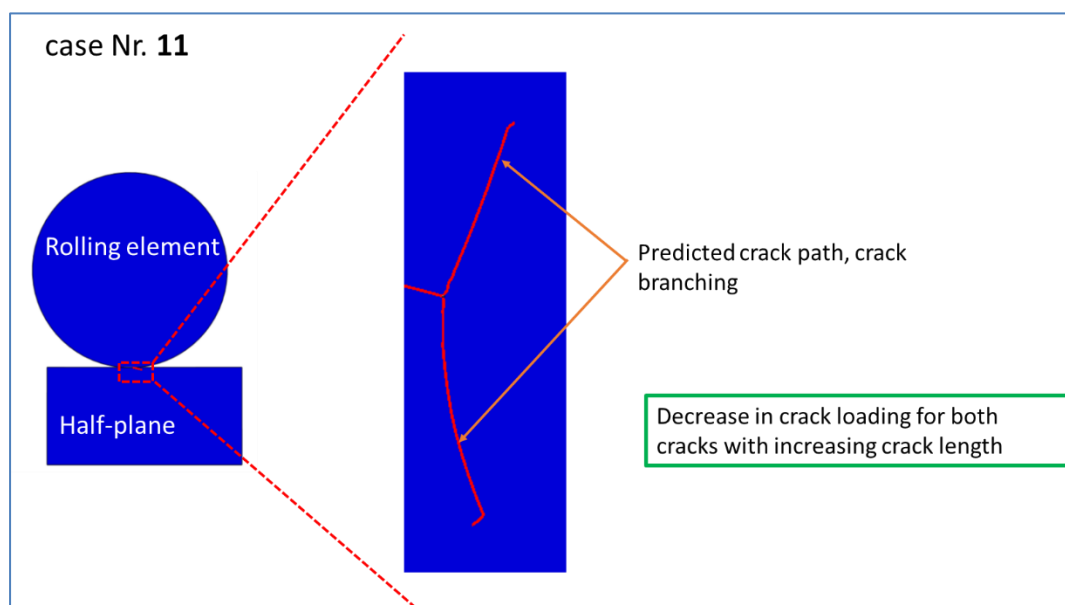


Figure 79: Predicting of crack paths for an edge crack in a semi-infinite plate under pure rolling contact fatigue

The results of the calculated K_V for the upward and downward crack branches are shown in Figure 80 and Figure 81. A continuous decrease in K_V with increasing additional crack length can be observed in both crack branches and an almost linear decrease in K_V in the downward crack branch. In this case too, a likely crack stop can be assumed at the lower crack branch.

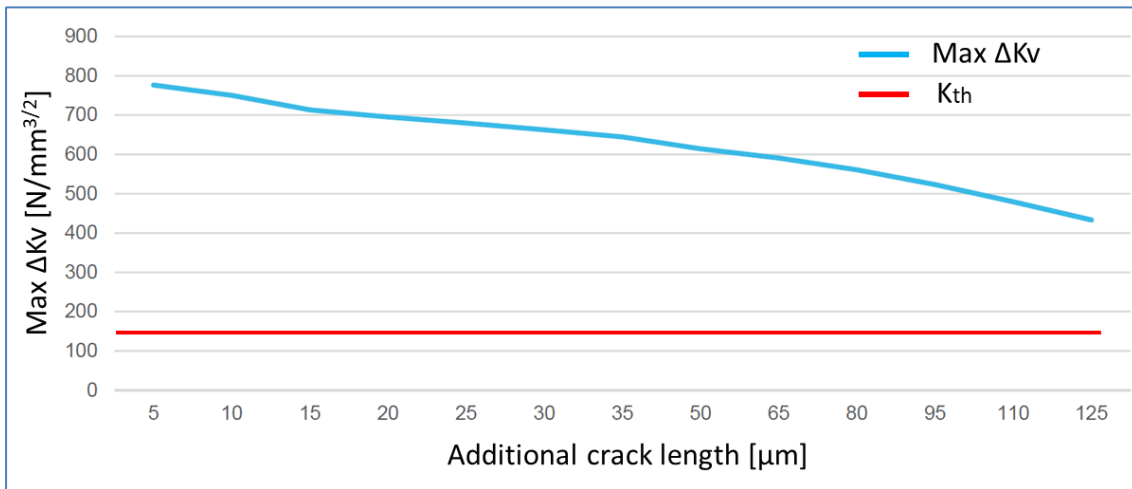


Figure 80: Results of max Kv for the upward crack branch

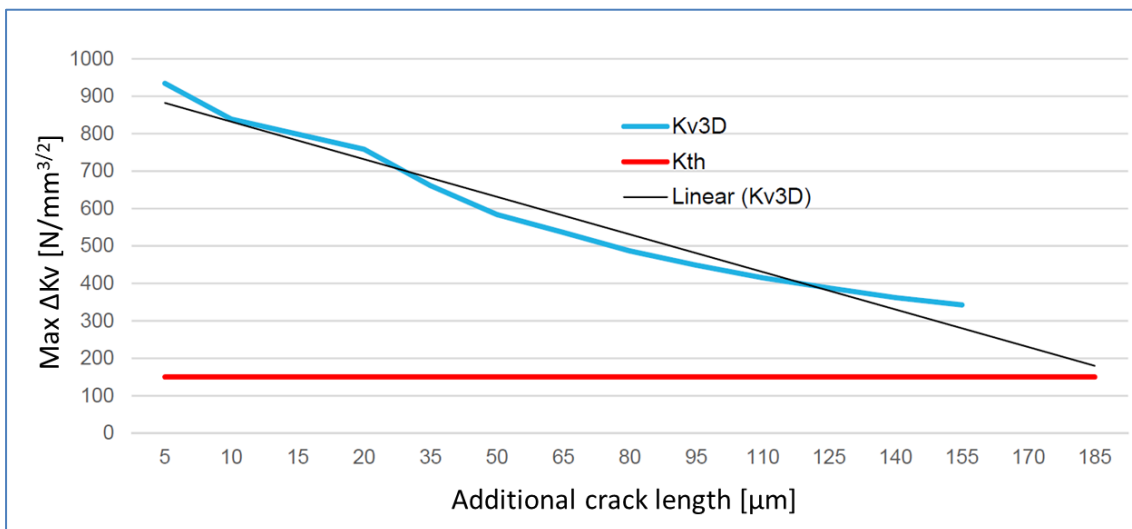


Figure 81: Results of max Kv for the downward crack branch

6.3.6 Comparison of the FE- results with the literature

Figure 82 compares of the influence of the friction coefficient between the crack faces of the determined results with the literature [23]. The three diagrams at the top describe the curves of K_{II} with different friction coefficients between the crack surfaces. These are: $\mu = 0.15, 0.45$ and 0.7 , see cases 1, 9 and 10. The diagrams below describe the calculated curves of K_{II} and those determined from the literature. In this case, the graph of K_{II} has been determined in case 3 and had the same initial crack angle of 15° as in the literature. The parameters used in the thesis [23] are as follows: initial crack length: 6 mm, initial crack angle: 15° , friction coefficient between cylinder and half-plane: 0.025, contact pressure $P_{max} = 845$ MPa. The friction coefficients used between the crack faces are $\mu = 0.01, 0.1$ and 0.5 .

The calculated K_{II} show a course similar to that in the literature, so that the values increase at the beginning and reach a maximum first. After that, the values decrease and reach a minimum.

As in the literature, cases 1, 9, 10 also show a decreasing maximum K_{II} with increasing friction coefficient values.

The graph of K_{II} in case 3 with $\mu=0.15$ is compared with the graph from the literature with $\mu=0.1$, since the two friction coefficients are not far apart and the two crack angles in case 3 and in the literature are the same. One

can see very clearly that the maximum value is greater than the minimum value in terms of amount in both curves.

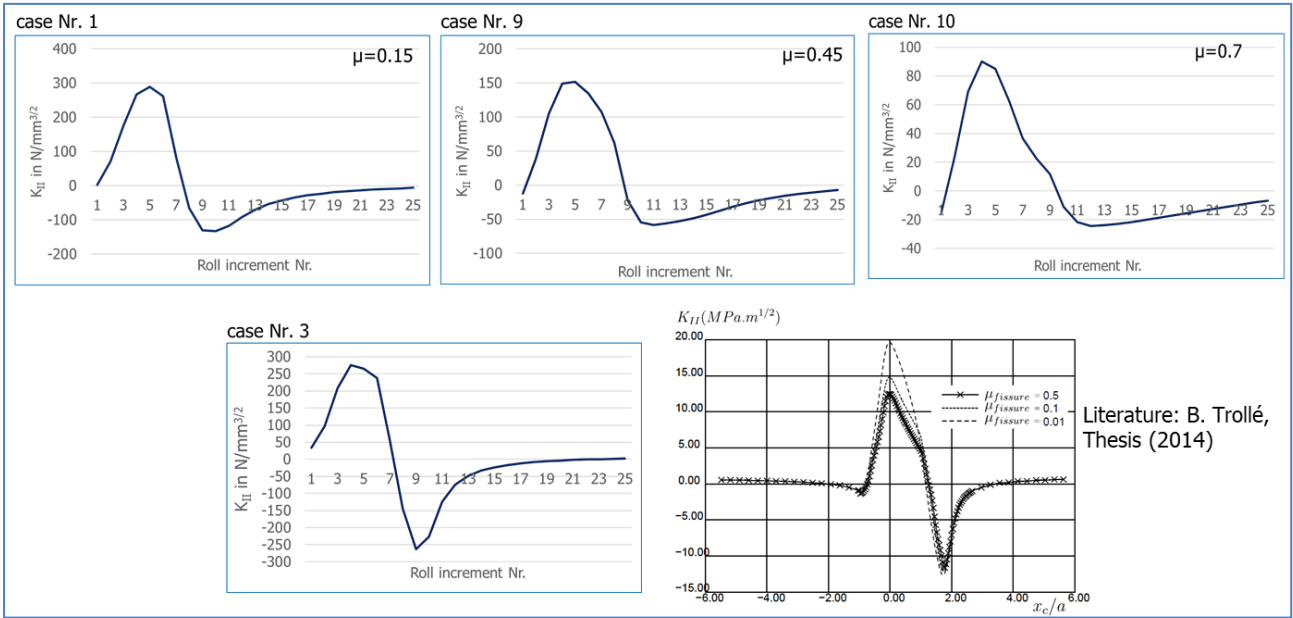


Figure 82: Comparison of the results with the literature [23], effect of the friction coefficient of crack faces μ on the calculated graph of K_{II} in cases 1, 9 and 10: the initial crack angle is different from the simulation and the literature (top); graph of K_{II} : the initial crack angle from the simulation and literature is the same (below)

Next, crack paths under rolling contact from the literature [23] were qualitatively compared with our results from case 4, see Figure 83. Cracks in a part of unknown origin [24] (see Figure 83 (right above)) were predicted in [23] (see Figure 83 (right bottom)). Crack paths for two cracks were obtained separately for each of the cracks ($l= 6 \text{ mm}$, crack angle $=15^\circ$, friction coefficient of crack faces $=0.01$, friction coefficient between cylinder and half-plane $= 0.025$) [23]. A similar path of the branched crack was predicted with our method (see Figure 83(left)).

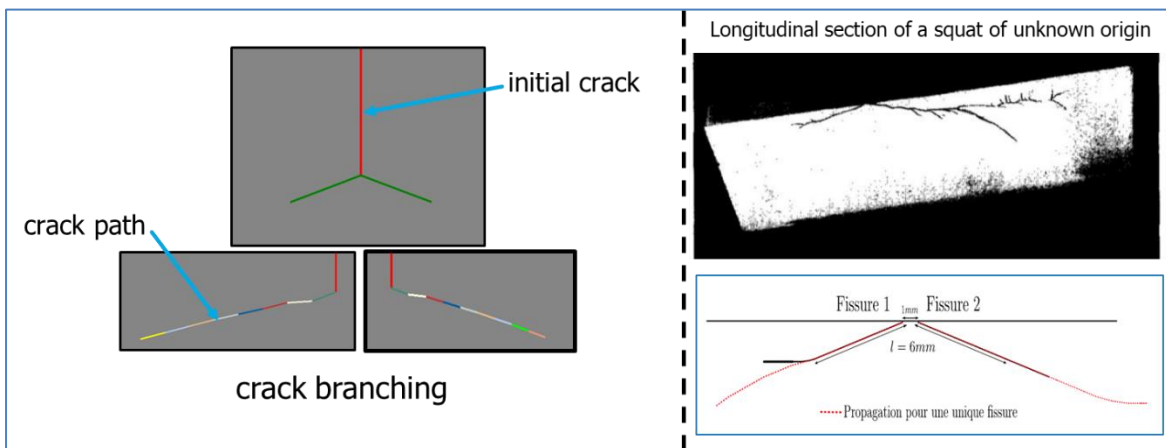


Figure 83: Comparison of the FE-results of the crack branching from case 4 (left) and the literature (right [23])

Another example from the literature can be compared qualitatively with the calculations from case 3. The crack from the literature [25] shows an initial inclination angle $20^\circ-30^\circ$, see Figure 84. During crack propagation, crack branching and deflection were observed. The result from case 3 is compared with the crack from the literature at the point where the main crack changes direction significantly. The previously formed branches were not

considered in the simulation because the initial crack length used is 0.5 mm. Our results show that the crack may branch into two cracks. According to the simulation results, the branch growing towards the surface would continue to grow, while the branch growing into the depth of the material would eventually stop growing. With the proposed FE-approach, a similar initial angle of crack branching as in the literature could be predicted. In the literature [25] it can be seen that the upper crack (main crack) continues to grow after branching, whereas in our model it does not. A possible reason for this is that the contact loads used in the literature are significantly larger than those in our model. The further path of the main crack in the literature with its subsequent crack branches cannot be simulated with the current status of our FE-approach. In the simulations, growth is considered to happen at the conditions of one single roll increment, which may affect the crack path predicted.

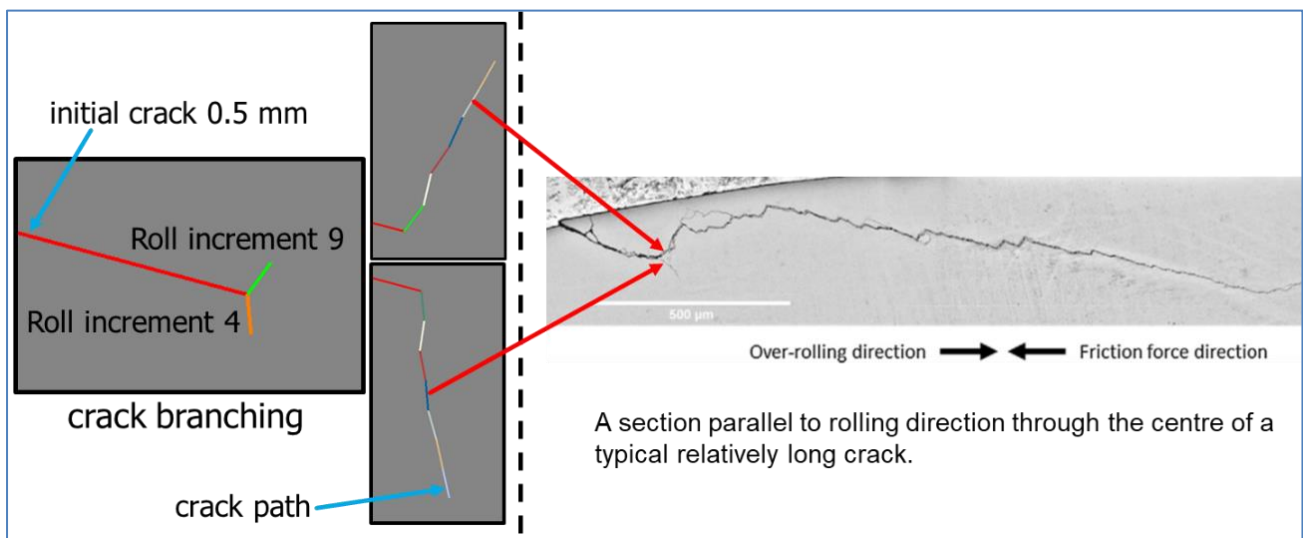


Figure 84: Comparison of the FE-results of the crack branching from case 3 (left) and the literature [25] (right)

6.3.7 Discussion of the results

Essentially, Mode II loading can be observed at the initial crack due to compressive loading between the initial crack surfaces, because only planar sliding is possible at the initial crack surfaces. In some cases, the initial crack has two extreme values with alternating Mode II loading. In this case, crack branching at about $\pm 70^\circ$ to the initial crack is possible. Crack loading decreases with increasing additional crack length. Crack stopping is expected here. Flat initial crack angles with high contact pressure and low friction at crack surfaces promote crack branching, which can lead to spalling.

6.4 Phase I.2

In preparation for Phase I.2, a parameter study was conducted to investigate the influence of residual stresses and pure rolling contact on crack growth. The aim of Phase I.2 was to investigate the maximum crack growth depth and tendency of crack propagation (into the core or back to the surface) in comparison with the basic variant of Phase I.1. To achieve this goal, the simulation model developed previously in chapter 6.3 was used as a global model. This forms the essential properties of the rolling contact and the crack surface contact. The fracture mechanics evaluation method developed in D2-4 is being evolved to ensure a reliable prediction of the crack paths and the stress intensity factor curves in the case of rolling contact, frictional crack-surface contact and residual stresses. The influence of the initial crack angle, initial crack length and residual stresses on the crack path and the graph of the stress intensity factors was investigated using a parametric study. The

simulations were performed using the parameters in Table 45. The crack paths were investigated assuming a semi-infinite plane with an edge crack under rolling contact fatigue.

Fixed parameters	
Friction coefficient: cylinder/half-plane (no slipping)	0.15
Friction coefficient: crack faces	0.15
Cylinder radius R [mm]	10
Maximum contact pressure p_0 [MPa]	1500
Material properties	
Young's modulus E [MPa]	210000
Poisson's ratio ν	0.3

Table 45: Definition of the friction coefficients, load parameters, cylinder radius, contact thickness and material properties used in the simulations

6.4.1 Implementation of residual stresses in the FE model

The graph of the residual stresses in the depth direction can be described with an exponentially damped function of the n th degree as follows [22]:

$$\sigma_{res}(z) = \left[\sum_{k=0}^{k=n} A_k z^k \right] e^{(-Bz)}, \quad (1)$$

where A_k and B are coefficients dependent on the residual stress profile and z is the coordinate in the depth direction.

The graph of "9HP" was considered in the simulations, because the curve shows the highest tensile residual stress values. This selection enables a better assessment of the influence of residual stresses on crack development.

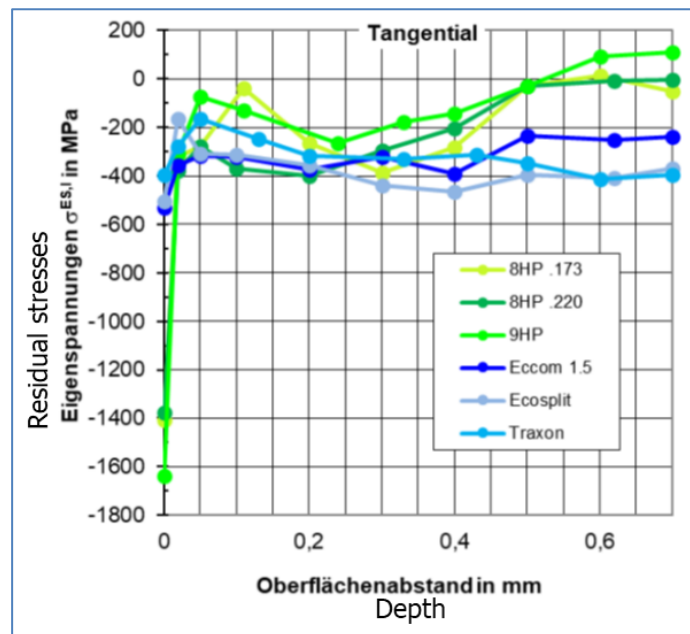


Figure 85: Residual stress curves of various planetary gears from the ZF Group

The residual stresses were modeled by thermal stresses as shown in Figure 86. Here, the temperature is specified in the model, which results in a temperature expansion. Thermal stresses that correspond to residual stresses are generated by restraints against expansion, e.g., fixed clamping. The relevant coefficients of thermal expansion are determined by control calculations and thus also by the distribution of residual stresses. The thermal expansion coefficients in the z-direction are defined as zero to avoid unwanted deformations and residual stresses in the z-direction. Using Equation 1 (see Figure 87), the temperature distribution is determined according to the following damped third-order polynomial:

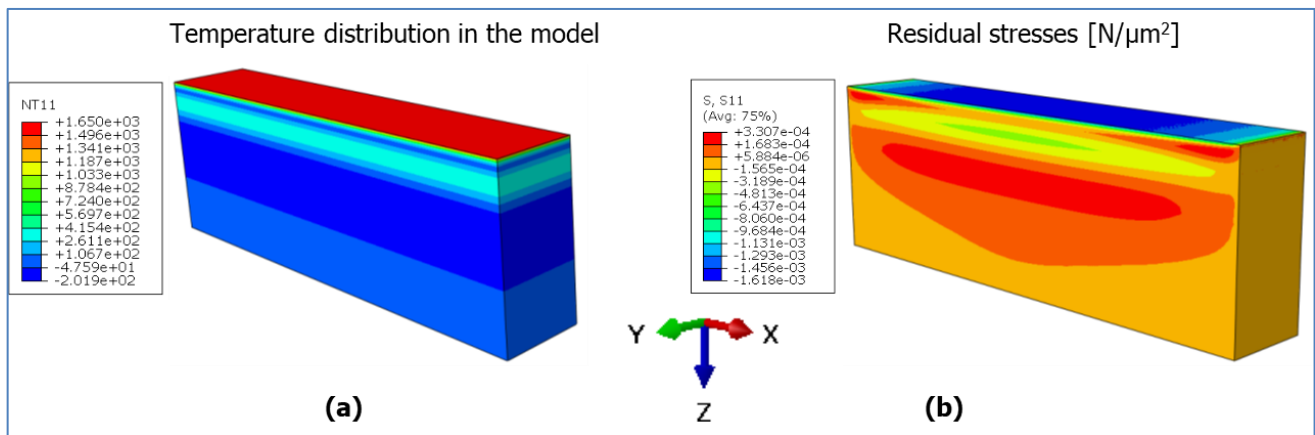


Figure 86: Modeling of residual stresses due to thermal stresses, (a) temperature distribution in the model, (b) residual stresses

$$T(z) = [1650 - 35.5 * z + 0.237 * z^2 - 0.000348 * z^3] * \exp(-0.007 * z) \quad (2)$$

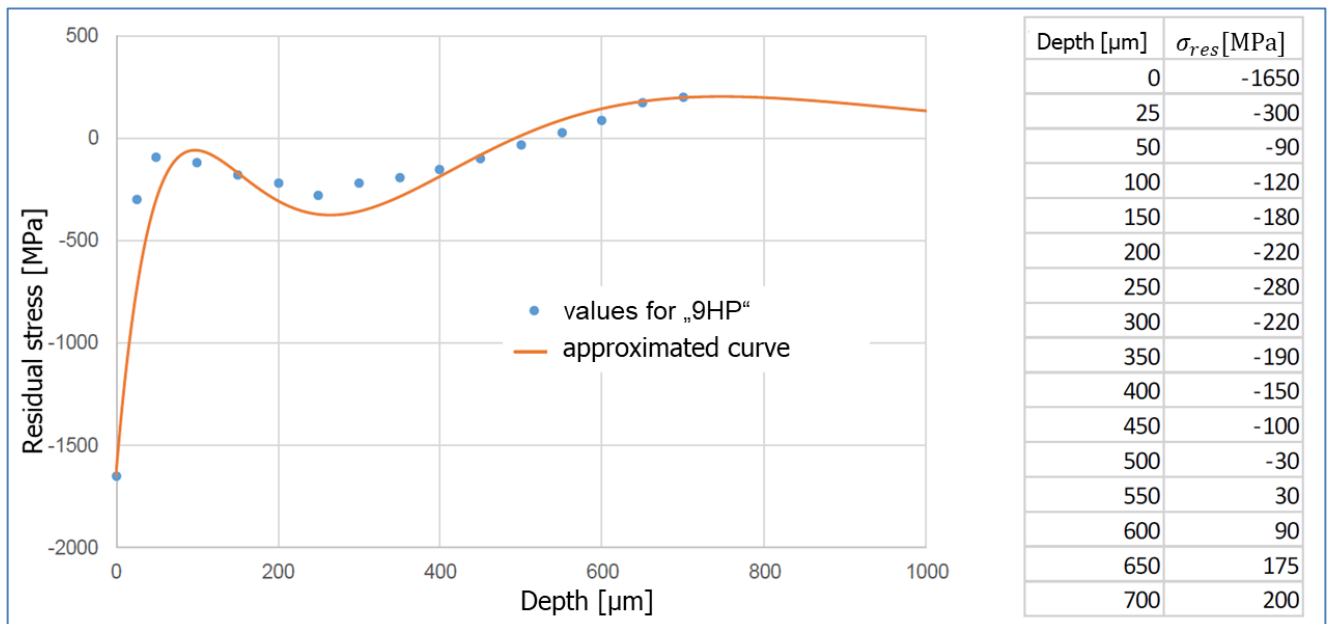


Figure 87: Approximate curve used for FE-analysis based on values from "9HP"

6.4.2 Parametric study

6.4.2.1 Influence of rolling contact and residual stresses on the crack path for different initial crack angles and different initial crack lengths

In this part, a parametric study was conducted to prepare Phase I.2. In these investigations, various initial crack lengths with different initial crack angles were investigated, see Table 46. The influence of residual stresses on crack growth under rolling contact is the subject of the investigation.

Parameter	unit	case number		
		1	2	3
Initial crack length	[mm]	0.5	0.5	0.7
Crack angle	[DEG]	15	90	90
Friction coefficient: cylinder/half-plane		0.15	0.15	0.15
Contact pressure	N/mm ²	1500	1500	1500
Friction coefficient: crack surfaces		0.15	0.15	0.15
Residual stress		yes	yes	yes

Table 46: Cases 1, 2 and 3 of initial crack lengths 0.5 mm and 0.7 mm

Results of case 1

Case 1 is considered in this study. This is an inclined initial crack with a length of 0.5 mm and an inclination of 15°, see Figure 88. The graph of the residual stresses is shown here without the effect of rolling contact.

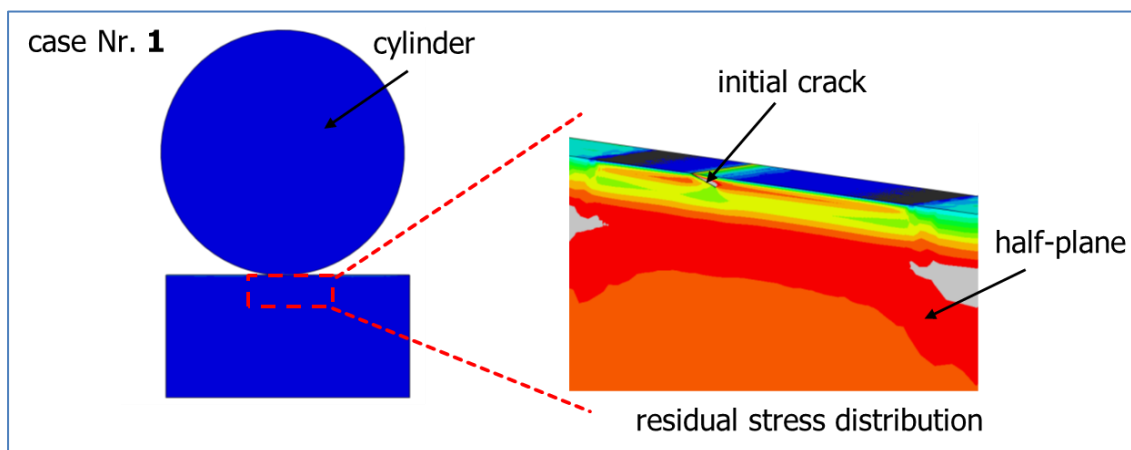


Figure 88: Simulation of rolling contact, simulation model (left), progression of residual stresses without rolling contact (right)

To illustrate the influence of the residual stresses, the graph of K_{II} at the initial crack under rolling contact was investigated, see Figure 89. The results of D2-4 (without residual stresses) are compared with those of the current case (with residual stresses). The results show a constant negative offset in the K_{II} curve due to residual stresses.

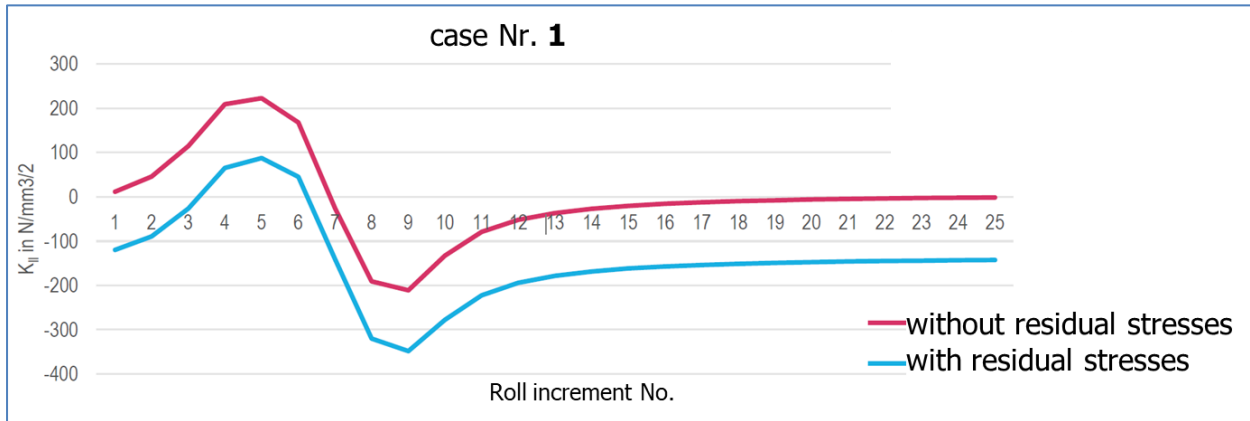


Figure 89: Influence of residual stresses on the course of the K_{I_I} at the initial crack under rolling contact

When evaluating K_V in Figure 90, there was a clear difference between cracks that were also under residual stresses. In this case, there is only one clear maximum value. That is, the crack is predicted to grow towards the surface without branching, whereas the crack without residual stresses may undergo crack branching.

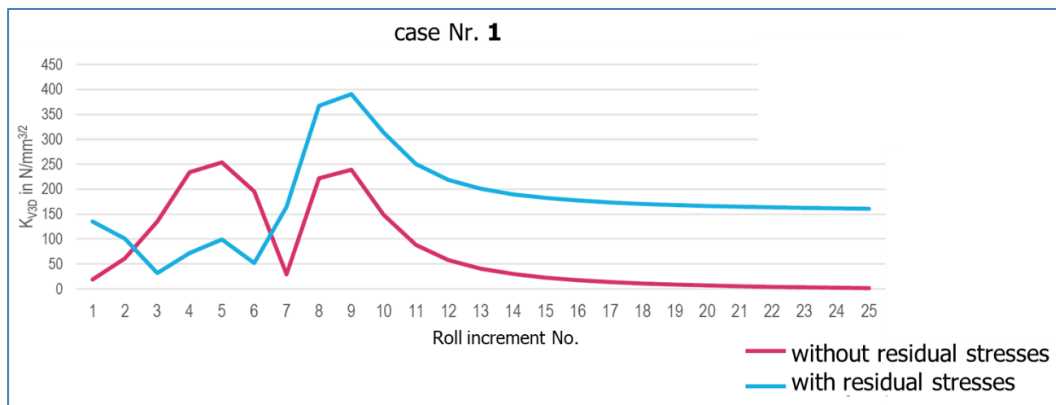


Figure 90: Influence of residual stresses on the graph of the K_V at the initial crack under rolling contact

After simulating the crack growth for case 1, the following crack path was obtained after six crack extensions, see Figure 91.

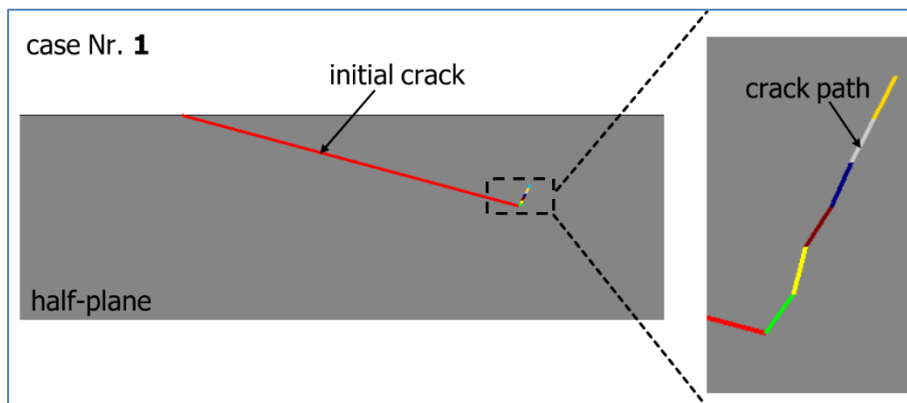


Figure 91: Crack path after 6 crack increments with $5 \mu\text{m}$ length under rolling contact

The crack path for the crack growth considering residual stresses was compared with the crack path from project D2-4 (without residual stresses), as shown in Figure 92. For this comparison, only the crack path

(without residual stresses) in the direction of the surface was considered. Here, it can be clearly seen that the residual stresses have no influence on the crack path with these selected parameters and boundary conditions.

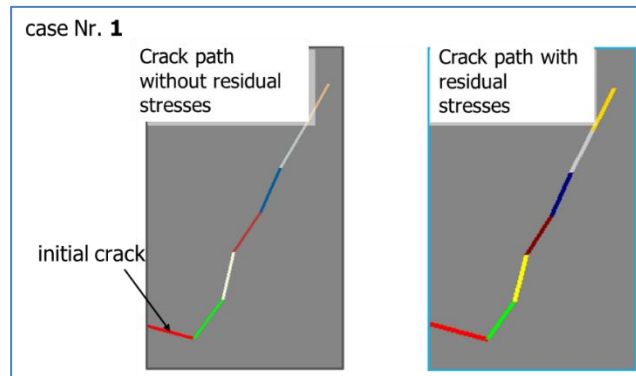


Figure 92: Comparison of the crack paths with and without residual stresses under rolling contact

Since the crack after kinking mainly grows under Mode I loading, K_I values were calculated for the two crack paths in Figure 92 and compared with each other (see Figure 93). Although the crack paths are similar up to front 6, the two graphs of the K_I differ. While the non-residual stress crack stops (K_I decreases, near $K_{th} = 150 \text{ N/mm}^{3/2}$), the crack with residual stress is able to grow (K_I is constant and much larger than K_{th}).

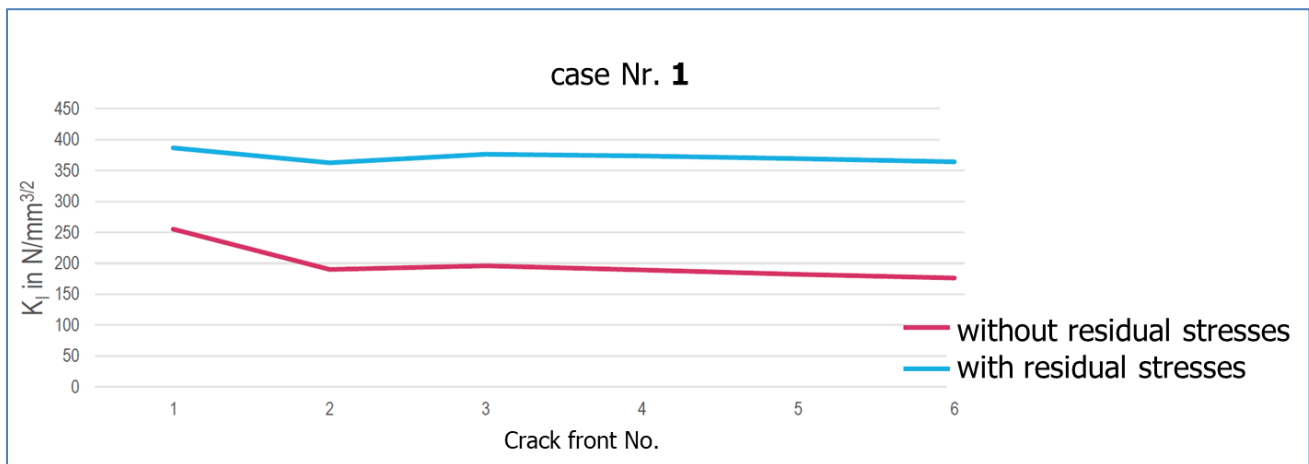


Figure 93: Influence of residual stresses on the K_I graph after kinking under rolling contact

The crack growth simulation was continued for case 1 and stopped shortly before complete spalling so that a meaningful evaluation could take place, see Figure 94. The crack growth occurred almost under Mode I loading. Near the edge, the crack extension is almost perpendicular to the surface. In this case, spalling is expected.

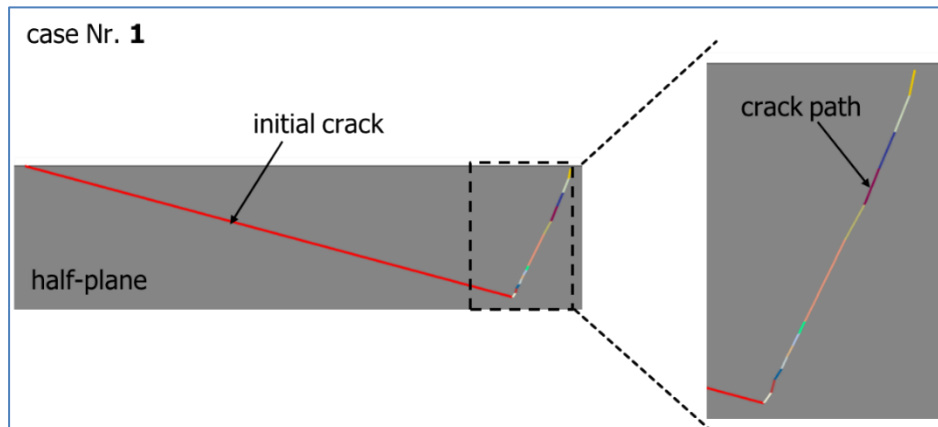


Figure 94: Crack path after 13 crack increments

It is also interesting to see how the crack opening at crack front 12 (just before spalling) behaves when rolled over, see Figure 95. Here it can be clearly seen that the crack only opened under the influence of residual stresses (without rolling contact), since the residual stresses do not act perpendicular to the crack. In rolling increment 5, the crack is closed under the influence of the rolling contact and residual stresses, with the rolling pressure playing a significant role. The crack opened in rolling increment 9, essentially due to residual stresses. The crack opened in the roll increment 25 mainly due to the residual stresses.

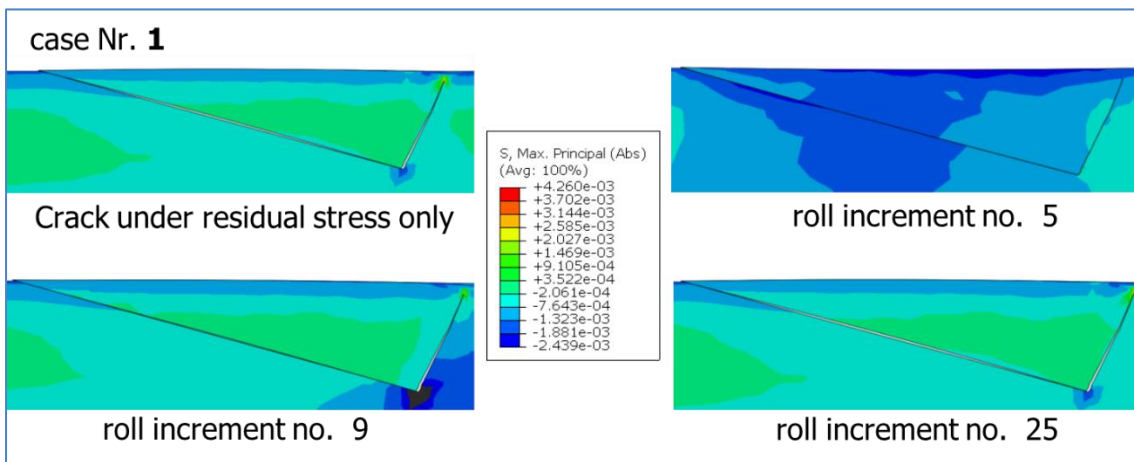


Figure 95: Crack opening at crack front 12 at different roll increments

The position of the roller in roll increments 9 and 25 is shown in Figure 96.

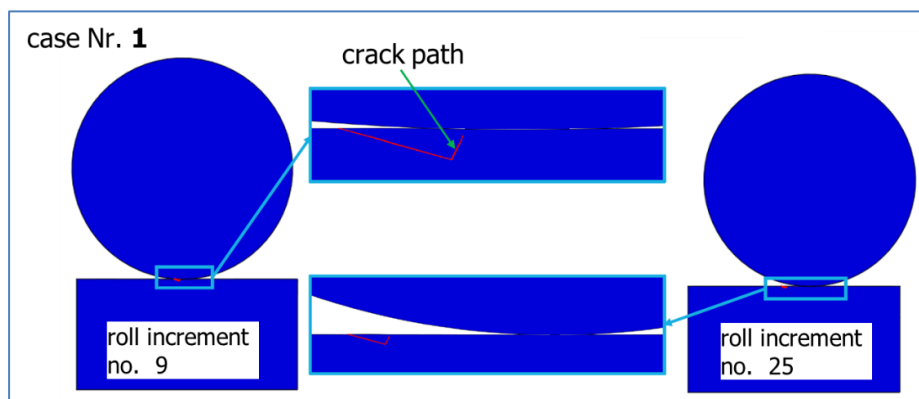


Figure 96: Roll positions at crack front 11 at different roll increments

Results of case 2

In case 2, a vertical crack with a length of 0.5 mm is investigated. Figure 97 describes the half-plane with a crack under residual stresses.

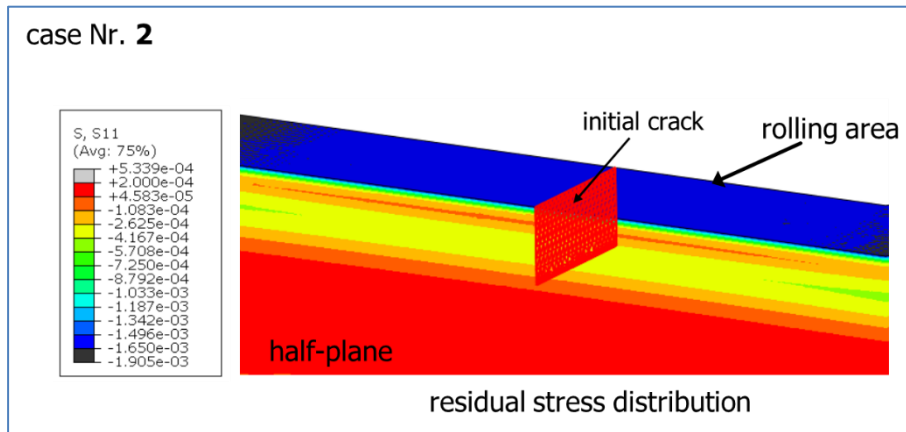


Figure 97: Residual stress distribution for half-plane with vertical crack

Compared with the crack from project D2-4, the extreme values of K_{II} were reduced by the residual stresses due to the additional pressure on the two crack surfaces (see Figure 98).

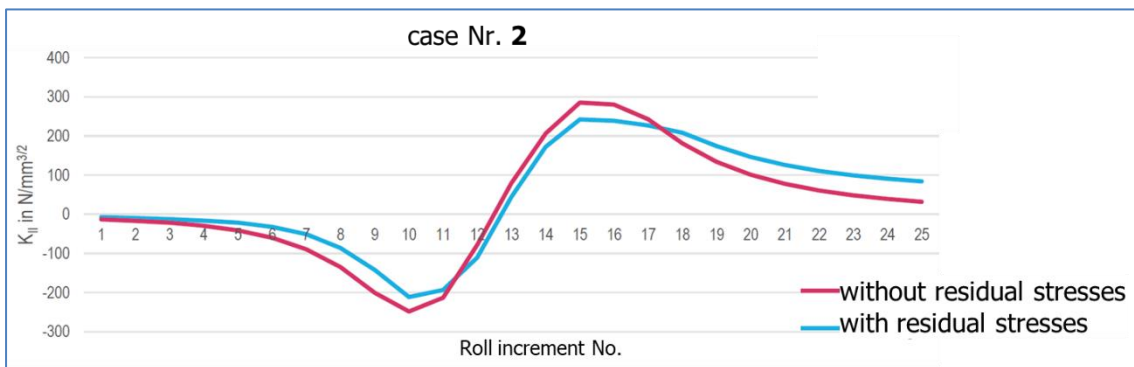


Figure 98: Influence of residual stresses on the graph of K_{II} at the initial crack under rolling contact

The values of K_V show that the two extreme values of the two cracks occur at the same point with and without the action of residual stresses, see Figure 99. That is, the crack will branch. Here, too, the extreme values of the crack under residual stresses are somewhat smaller than those of the crack without residual stresses.

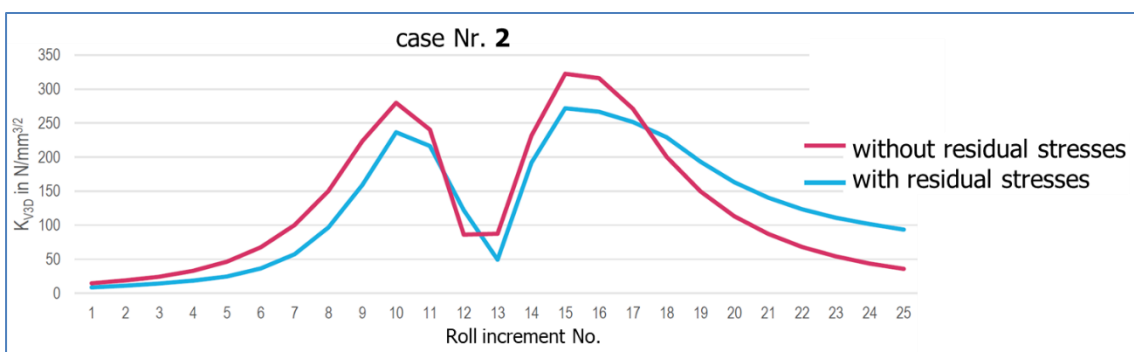


Figure 99: Influence of residual stresses on the graph of K_V at the initial crack under rolling contact

Figure 100 and Figure 101 show that the residual stresses have no significant influence on the crack path with these selected parameters and boundary conditions. On the other hand, the residual stresses reduce the values of K_V , see Figure 100 and Figure 102 below. This means that the crack under residual stresses comes to a standstill earlier than the crack without residual stresses. This is because the relative displacement of the crack edges is hindered by the additional compressive stresses. Figure 102 describes the potential crack branching in case 2.

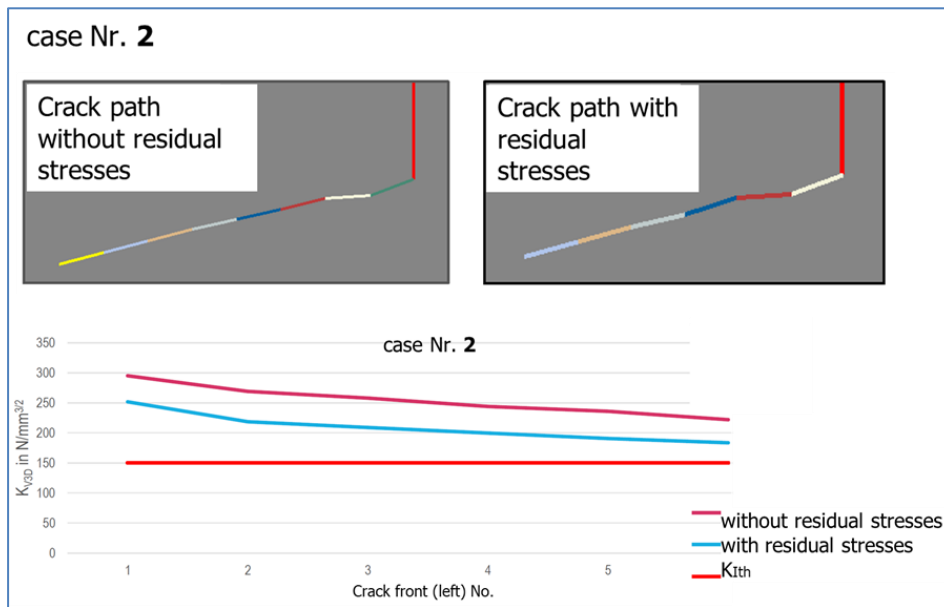


Figure 100: Comparison of left crack paths with and without residual stresses

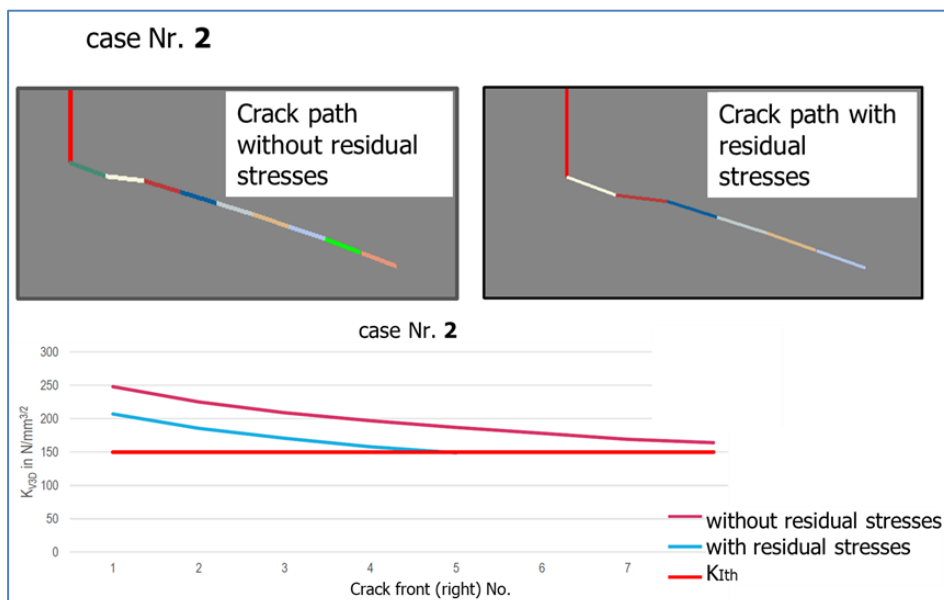


Figure 101: Comparison of right crack paths with and without residual stresses

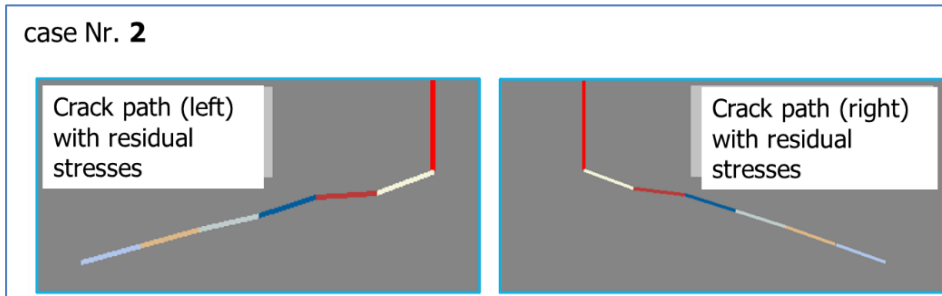


Figure 102: Crack branching. Left and right crack paths due to the rolling process and residual stresses

Results of case 3

In case 3, a vertical crack with a length of 0.7 mm was investigated (see Figure 103). In this case, the crack tip is under the maximum residual tensile stress.

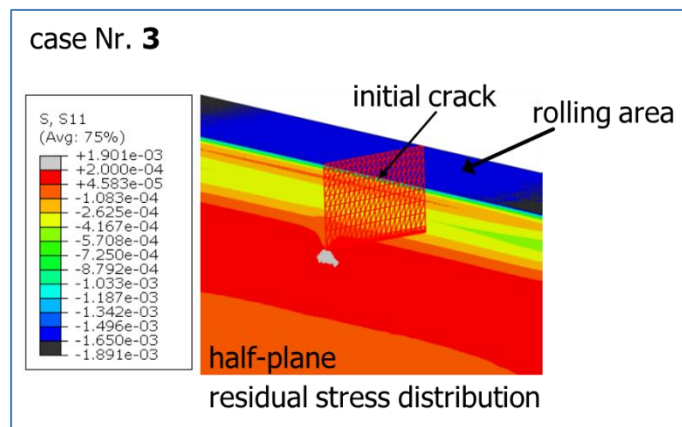


Figure 103: Residual stress distribution for the half-plane with vertical crack

To determine the influence of the initial crack length and the residual stresses on the crack loading parameters K_{II} and K_V , the results of cases 3 and 4 were compared, see Figure 104. This shows that with local tensile residual stresses at 0.7 mm, crack loading parameters increased.

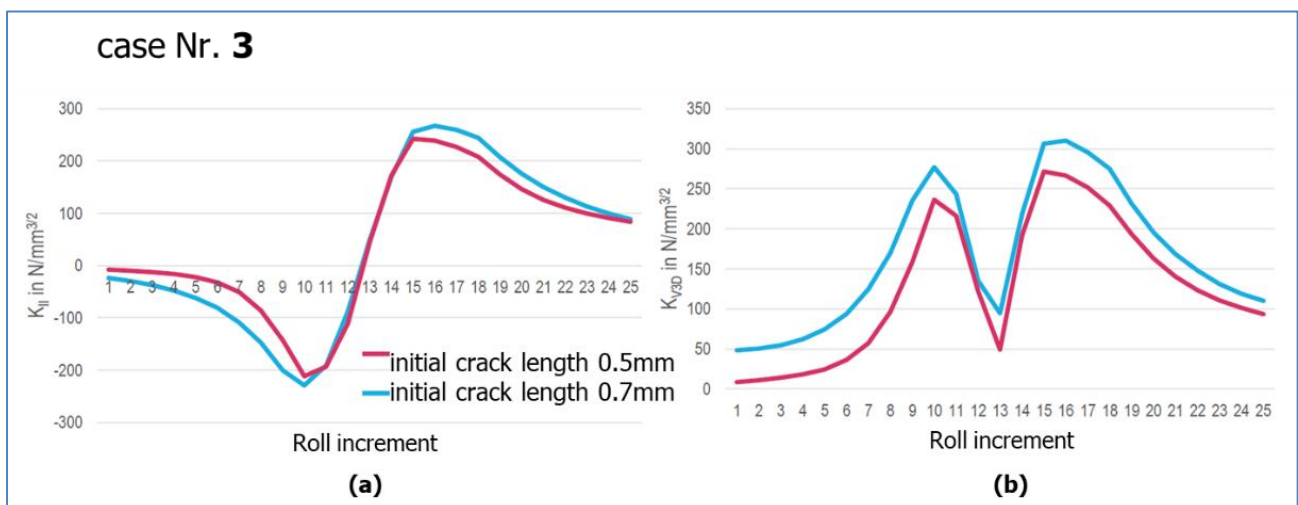


Figure 104: Influence of initial crack length and residual stresses on K_{II} and K_V

Due to the residual compressive stresses, the upper area closes (see Figure 105(a)). On the other hand, the crack is open in the lower part because of residual tensile stresses, which appear with increasing loading on the crack, (see Figure 105(b)).

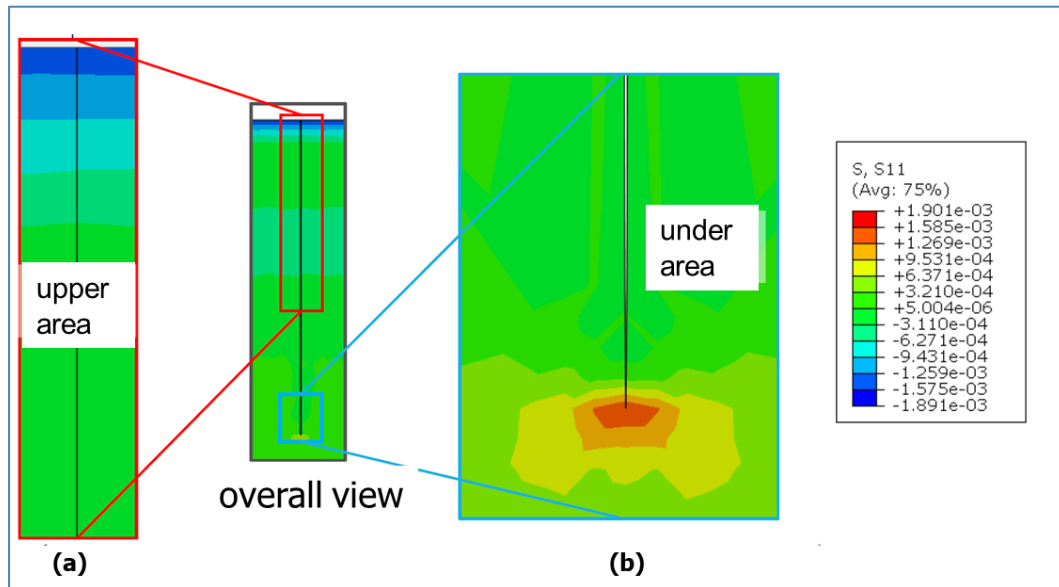


Figure 105: Influence of residual stresses on crack edge properties, crack closure (left) and crack opening (right)

Figure 106 describes the crack growth in case 3. The values of K_V decrease with increasing crack length. A crack stop is likely.

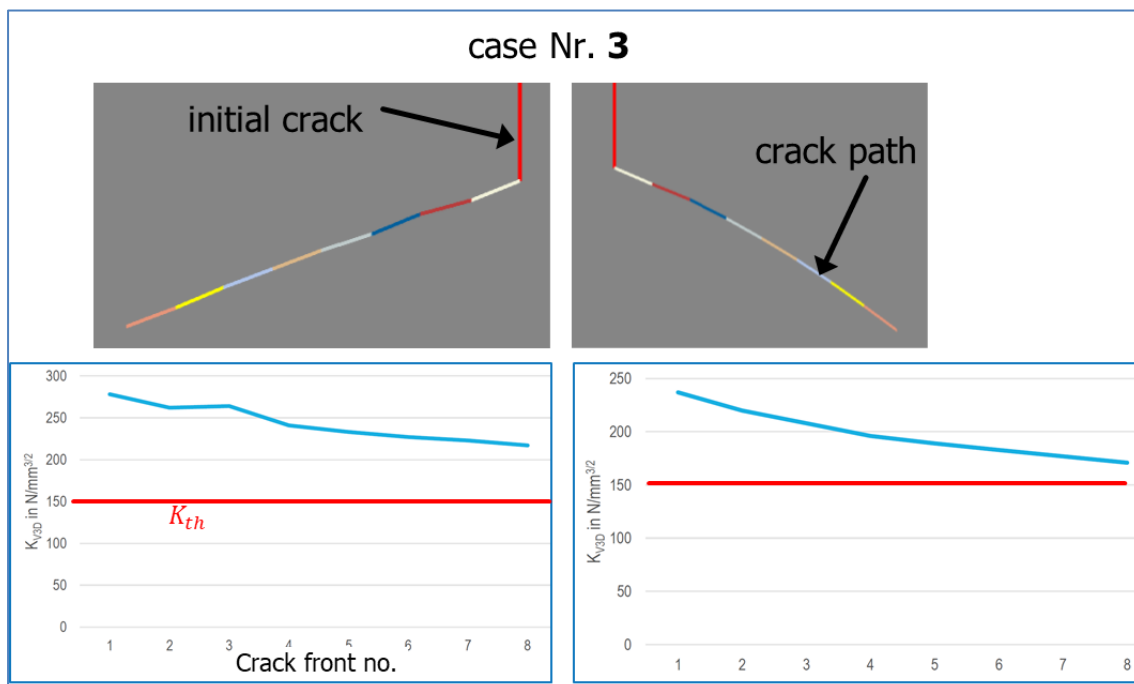


Figure 106: Crack branching, left and right crack paths and K_V due to the rolling process and residual stresses

6.4.3 Prediction of rolling contact fatigue crack propagation using the measured residual stresses from the shaft/16NCD13

A crack growth simulation was performed to prepare Phase I.2 for the shaft/16NCD13. For a conservative analysis, the friction between the crack surfaces was neglected. The selected parameters for the crack growth simulation are shown in Table 47. The residual stresses as measured were used in this simulation. The residual stresses in the shaft were modeled by thermal stresses in the FE-model (see Figure 107).

Parameters used in the simulation	
Initial crack length [mm]	0.3
Initial crack angle [DEG]	20
Residual stress	yes
Friction coefficient: cylinder/half-plane (no slipping)	0.15
Friction coefficient: crack surfaces	no
Cylinder radius R [mm]	11.97
Maximum contact pressure p_0 [MPa]	2400
Material properties/16NCD13	
Young's modulus E [MPa]	211000
Poisson's ratio ν	0.3

Table 47: Definition of the parameters and material properties used for the crack growth simulation in a semi-infinite plane under rolling contact fatigue considering the residual stresses

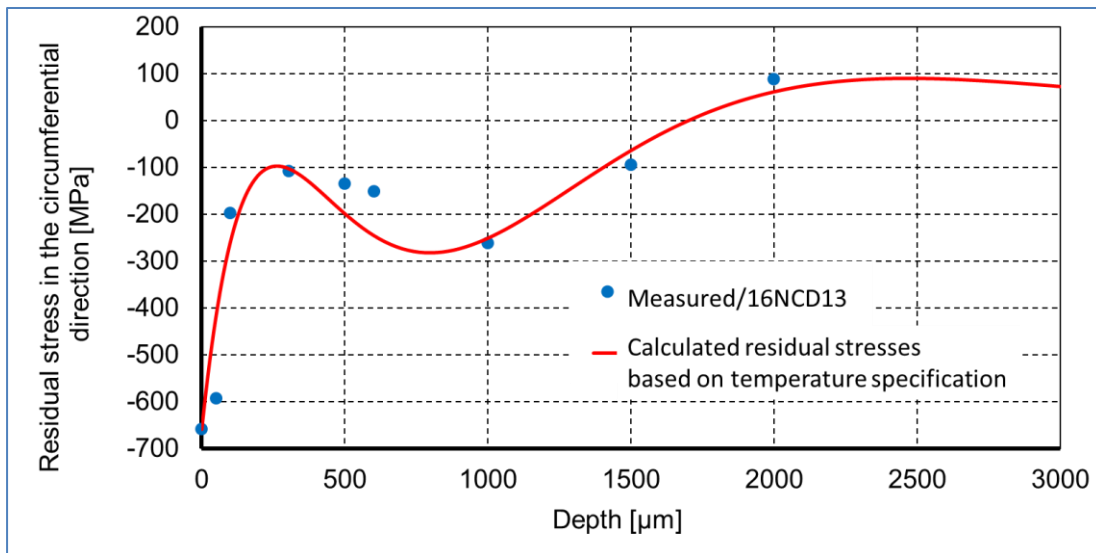


Figure 107: Description of the measured residual stress curve in the shaft/16NCD13 and the residual stress curve used to simulate crack growth under rolling contact fatigue

Results

The crack growth simulation was performed assuming an edge crack in a half plane. The crack tip is located in the compressive area of the residual stresses. The simulation showed that the initial crack may branch. After limited crack growth in the lower crack, the crack stops due to the weakening of crack loading due to the compressive residual stresses. The upper crack continues to grow toward the surface first. When close the surface, the simulation predicts that the crack may branch again, which may lead to further growth parallel to the surface (see red arrows in Figure 108). These branches can grow to the surface and cause spalling. The crack loading is near the threshold, so the crack may stop.

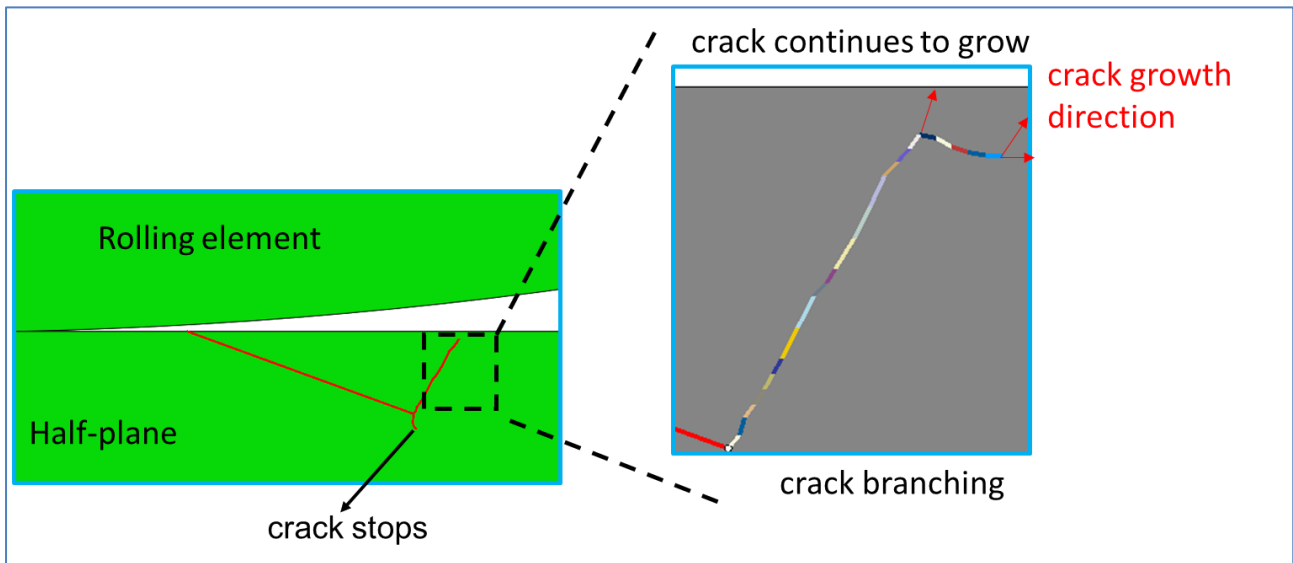


Figure 108: Prediction of crack paths for an edge crack in a semi-infinite plane under rolling contact fatigue

6.4.4 Discussion of the results

The results of cases 1, 2 and 3 show that the initial crack grew essentially under Mode II loading independent of the initial angle, initial crack length and residual stresses. Here, the crack is sharply kinked at the first crack propagation. At an initiation crack angle of 15° , the crack grew substantially to the top of the half-plane with increasing Mode I loading. In the case of long additional cracks, crack growth was driven by residual stresses. At an initial crack angle of 90° , a reduction in crack loading due to compressive residual stresses near the edge was observed for both the initial crack and the kinked additional crack. In the case of branched cracks, the crack growth was essentially under decreasing Mode I loading, and crack arrest is expected. The residual stresses do not affect the paths of the branched cracks. The crack loading has increased from 0.5 mm to 0.7 mm due to the increase in the initial crack length, because the crack tip is in the area of the residual tensile stresses.

6.5 Phase II

In this chapter the influence of an additional load (complex load) was investigated. First, a parametric study was carried out considering crack growth in a semi-infinite plane. Using the measured residual stresses, crack growth simulations were then carried out in the hollow shaft and in the outer ring.

6.5.1 Parametric study to prepare Phase II

Since in chapters 6.3 and 6.4 the cracks have demonstrated a tendency to stop when loaded only in rolling contact and residual stresses, an additional load (such as a bending load) is considered in this study. The aim here is to investigate whether an additional load can control the crack path into the core of the component. The crack paths were investigated assuming a semi-infinite plane with an edge crack under rolling contact fatigue.

6.5.1.1 Influence of rolling contact, residual stress and complex load on the crack path

When considering the bending load as a complex load, two load situations arise in the calculation model (see Figure 109). Load situation 1 describes the crack growth simulation with rolling contact. Here, the residual stresses and the additional bending load, which is defined as compressive stress, are taken into account (see

Figure 109 (a)). On the other hand, load case 2 describes the crack growth simulation without rolling contact. Here, the residual stress and the bending load, which is defined as the tensile load, as shown in Figure 109 (b). The residual stress curve used is shown in Figure 87.

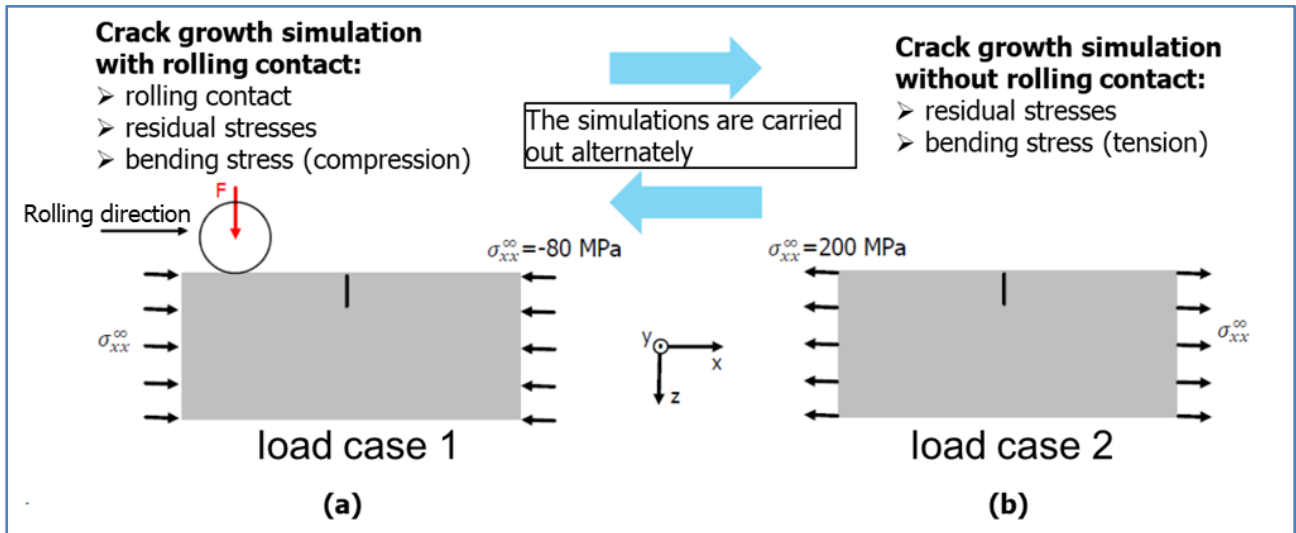


Figure 109: Crack growth simulation under additional bending load

To investigate the influence of the complex load, three cases were investigated (see Table 48). Three different initial crack lengths and two different crack angles were considered.

Parameter	unit	case number		
		4	5	6
Initial crack length	[mm]	0.5	0.7	1
Crack angle	[DEG]	15	90	90
Friction coefficient: cylinder/half-plane		0.15	0.15	0.15
Contact pressure	N/mm ²	1500	1500	1500
Friction coefficient: crack faces		0.15	0.15	0.15
Residual stress		yes	yes	yes
Complex load		yes	yes	yes

Table 48: Cases 4, 5 and 6 of initial crack lengths 0.5 mm, 0.7 mm and 1 mm

6.5.1.2 Results of case 4

Figure 110 shows a comparison of the influence of the complex load on the graph of K_{II} at the initial crack. Load 1 is described with roll increments 1-25. Load 2 occurs at roll increments 0 and 26. It can be clearly seen that a constant negative shift of K_{II} in load 1 occurs due to compressive loading. At load 2, the value of K_{II} is reduced by tensile loading.

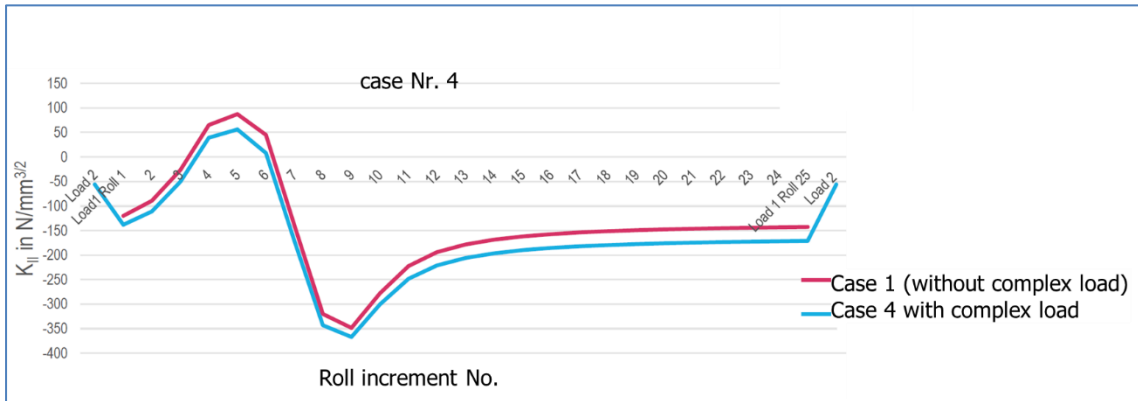


Figure 110: Influence of complex loads on the graph of the K_{II} at the initial crack

Figure 111 describes the comparison of K_V in cases 1 and 4. Here one observes a constant increase in K_V in load 1 due to additional complex load (compression). In load 2, K_V is reduced due to the complex load (tension).

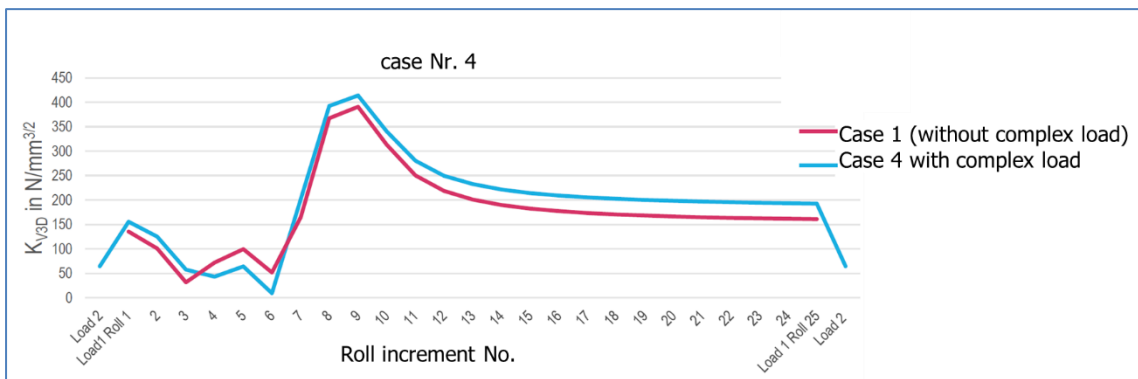


Figure 111: Influence of complex loads on the graph of K_V at the initial crack

Figure 112 compares the crack paths of cases 1 and 4. Here, the complex loads have no influence on the crack path.

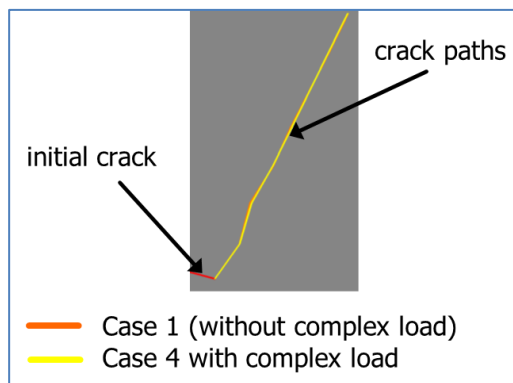


Figure 112: Comparison of crack paths after kinking for cases 1 and 3

6.5.1.3 Results of case 5

In case 5, a crack length of 0.7 mm is considered. Figure 113 describes the results of the K_{II} for cases 3 without a complex load and 5 with a complex load. The cracks in cases 3 and 5 have the same length of 0.7 mm and the same crack angle of 90° . Figure 113 shows that the complex load has no influence on K_{II} .

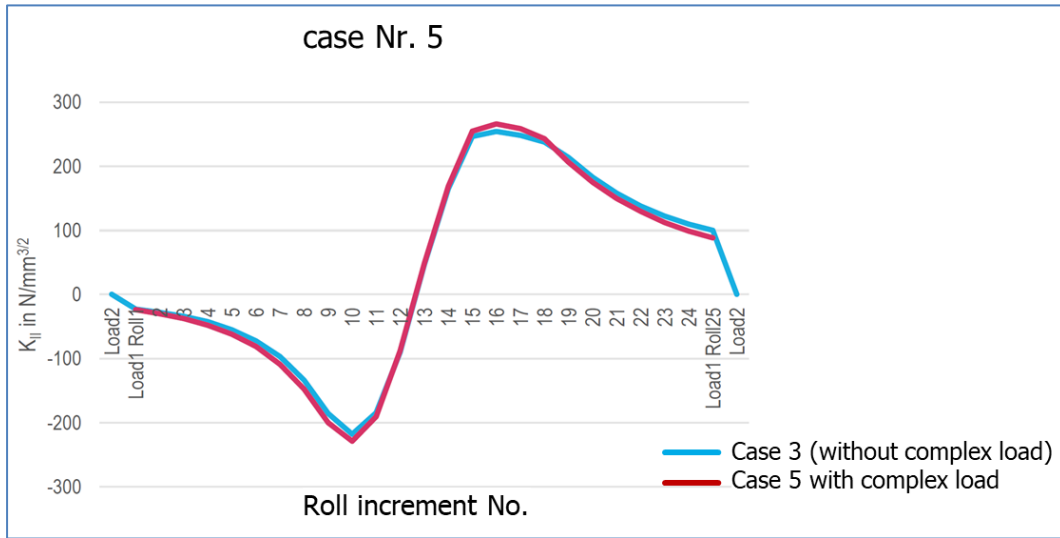


Figure 113: Influence of the load situation on the initial cracks on K_{II}

In Figure 114, the K_V curves from cases 3 and 5 were determined. Here, it can be clearly seen that K_V at load 2 is greatly increased by the additional tensile load. Compared with case 3, there is a slight reduction in K_V in case 5 at load 1 due to the additional compression. The roll positions at the maximum crack loading are shown in Figure 115.

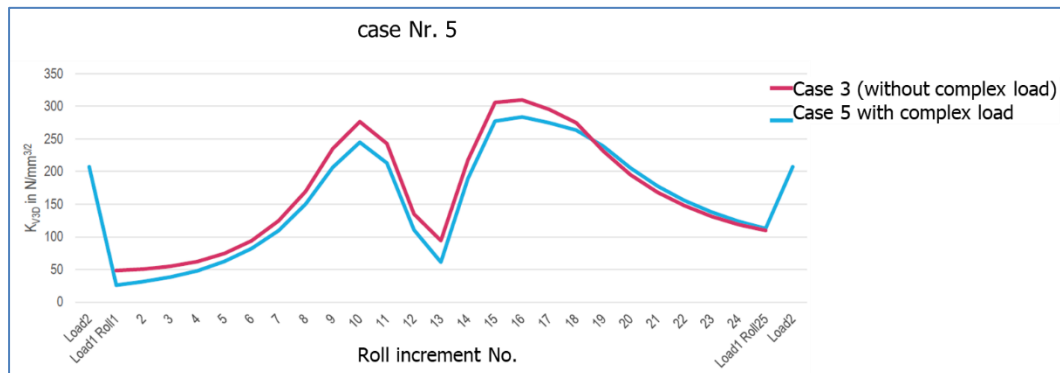


Figure 114: Influence of the load situation on the initial cracks on K_V

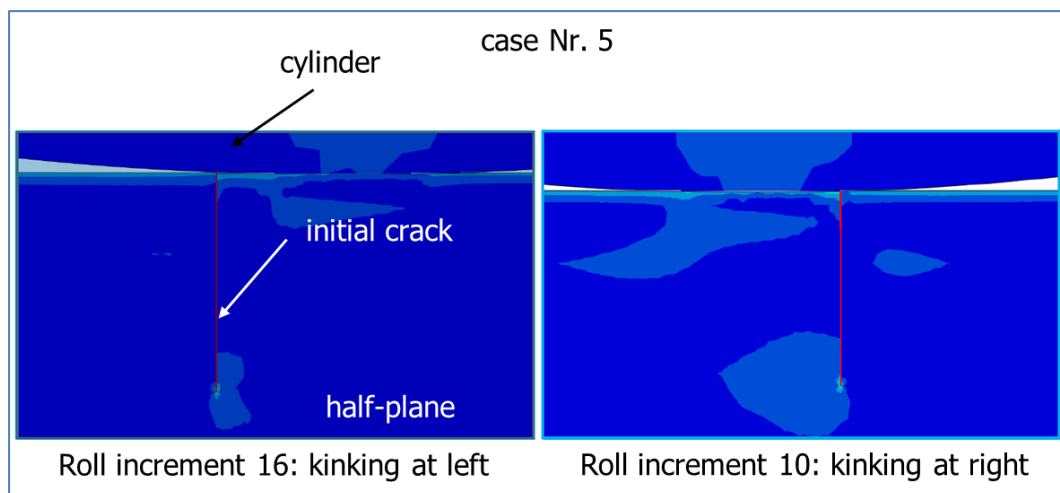


Figure 115: Roll positions (increments 10 and 16) at maximum K_V

Figure 116 describes the evolution of the crack paths and K_V in case 5 due to complex load 1 (compression) and load 2 (tension), residual stresses and rolling contact. K_V is decreasing in the left crack path due to load 1. As a result of load 2, K_V increases, with K_V being almost constant for crack fronts 9 and 10. For the right crack path, K_V is also decreasing due to load 1. Due to load 2, K_V increases and becomes larger after the third crack front than with load 1. This means that both cracks are capable of growth and are only controlled by complex load 2 (tension). It is interesting to see that the direction of crack growth has changed and is growing into the half-plane. It is to be expected that both cracks will continue to grow and not stop.

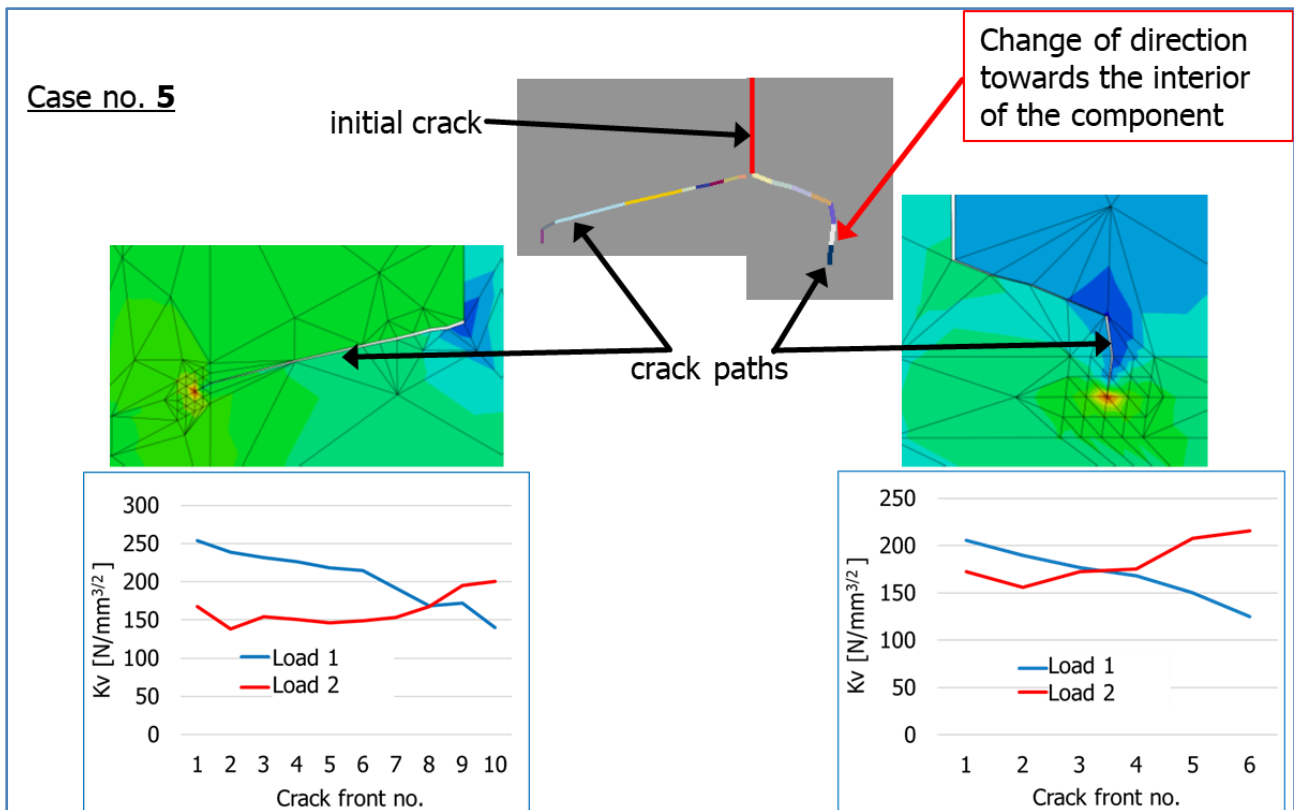


Figure 116: Comparison of the results due to load 1 and load 2, crack branching, left and right crack paths and K_V due to the rolling process, residual stresses, and complex load

6.5.1.4 Results of case 6

In this case, a longer crack of 1 mm was examined, with a further area of the crack being in the residual tensile stress field. In comparison to a crack with a length of 0.7 mm, a similar graph of K_V can be observed (see Figure 117).

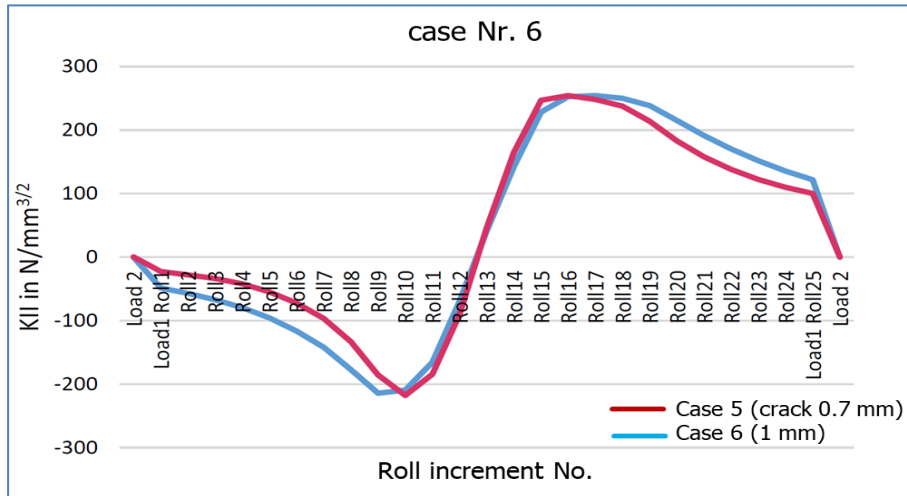


Figure 117: Influence of the load situation on the initial cracks on K_{I_I} , comparison of cases 5 and 6

Figure 118 describes the course of K_V for the initial cracks with lengths of 0.7 mm and 1 mm. Here, K_V at load 2 and the crack length of 1 mm is greatly increased due to greater initial crack length and tension. The maxima of K_V at load 1 are not decisive for crack propagation.

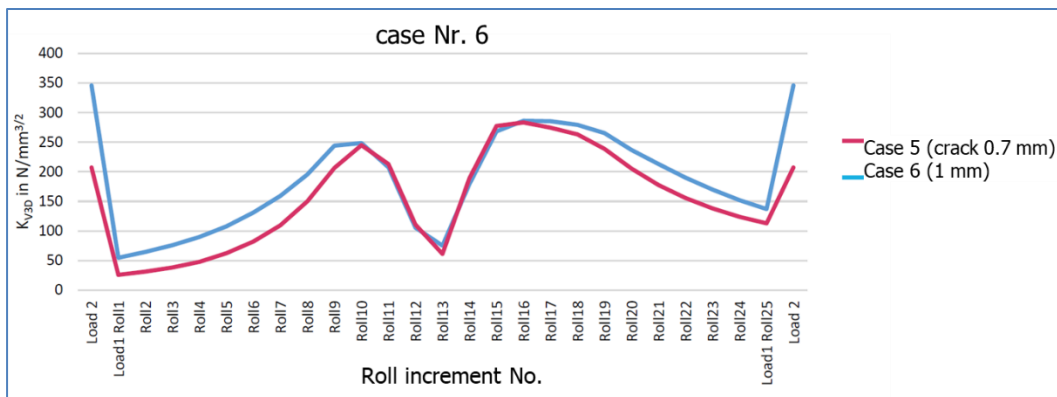


Figure 118: Influence of the load situation on the initial cracks on K_V

The influence of residual tensile stresses on the crack is shown in Figure 119. The crack is additionally loaded by tensile residual stresses.

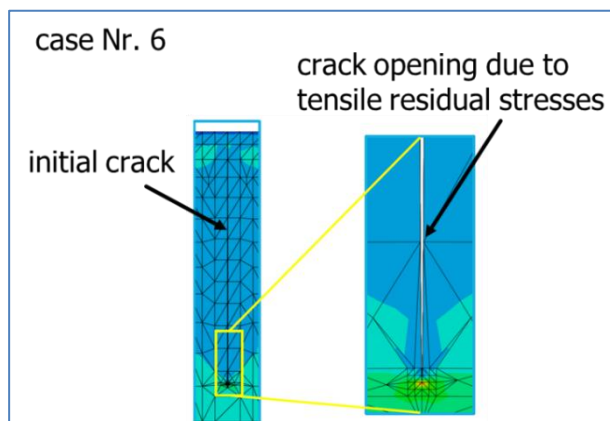


Figure 119: Crack opening of the 1 mm crack due to tensile residual stresses

In this case, the crack grows under pure Mode I loading without kinking (see Figure 120). Crack growth is accelerated with increasing crack length (no crack arrest).

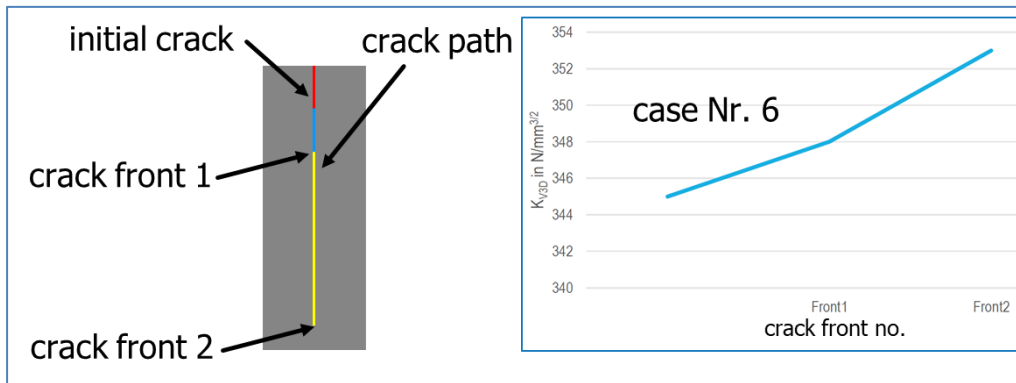


Figure 120: Crack path and value of K_V for case 6

6.5.1.5 Discussion of the results

Simulations with complex loads have shown that at the 15° crack initiation angle, Mode II loading can be seen. The K_{II} is additionally increased by pressure, resulting in a sharp kinking at the first crack propagation. In this case, the complex load has no effect on the crack path. With an initial crack angle of 90° and an initial crack length of 0.7 mm, load case 1 was initially decisive for crack growth, which is accompanied by potential crack branching as a result of alternating Mode II loading. Further crack growth occurs under Mode I loading. With increasing additional crack length, the influence of tensile stresses (see load case 2) increases. This causes the crack to kink again, growing vertically downward. Here, the crack loading increases. With an initial crack angle of 90° and an initial crack length of 1mm, the tensile stresses (load case 2) are decisive. Crack growth occurs with increasing Mode I loading.

6.5.2 Hollow shaft

6.5.2.1 Description of the FE-model

To simulate fatigue crack growth under rolling contact in the hollow shaft, the friction between the crack surfaces and between the rolling elements and the surface of the hollow shaft is considered. The coefficients of friction used, radius of the rolling element, contact pressure and material parameters are described in Table 49.

Parameters used in the simulations	
Friction coefficient: cylinder/hollow shaft (no slipping)	0.15
Friction coefficient: crack surfaces	0.15
Cylinder radius R [mm]	9
Maximum contact pressure p_0 [MPa]	2400
Inside radius [mm]	32
Outside radius [mm]	37.5
Material properties/32CDV13	
Young's modulus E [MPa]	211000
Poisson's ratio ν	0.3

Table 49: Definition of the parameters and material properties used in the crack growth simulation in the hollow shaft under rolling contact fatigue

Figure 121 (a) describes the hollow shaft model used to predict the crack path in rolling contact fatigue. A 2D model of the raceway area was used for the simulation (see Figure 121 (b)). The resulting contact pressure due to the rolling element and the rolling path of 3 mm used for the evaluations are described in Figure 121 (c). The rolling path was selected so that the influence of the rolling contact on crack development is completely covered and the maximum values that occur, such as stress intensity factors, lie within this range.

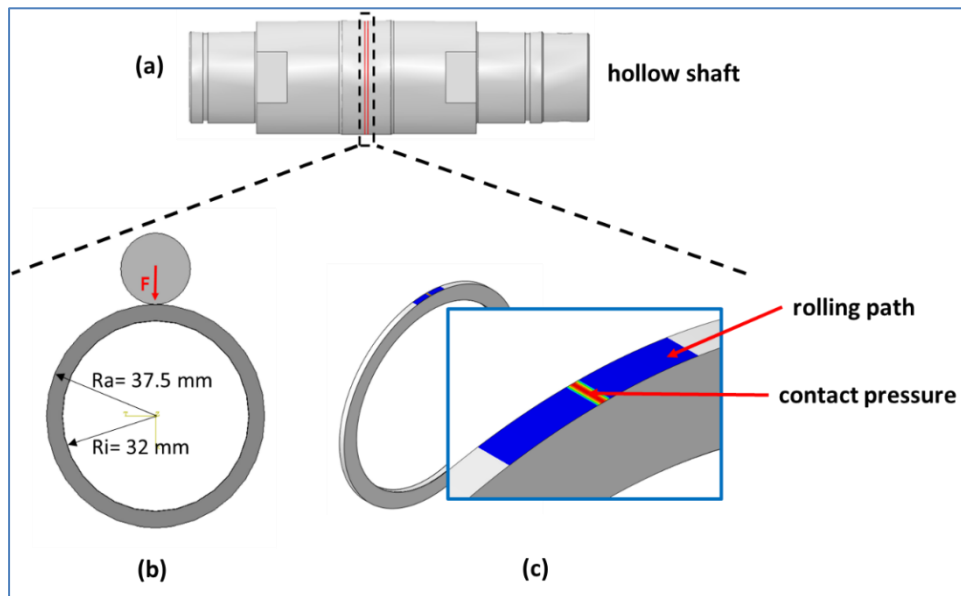


Figure 121: Model used to predict the crack path during rolling contact fatigue in the hollow shaft; (a) hollow shaft, (b) 2D-model used for the simulation, (c) area of the rolling path and the contact pressure due to rolling contact

For the 2D model of the ring, the study accounted for the fact that the hollow shaft deforms because of the contact pressure, thereby increasing the stiffness of the ring. For this reason, the stress distribution of the ring in the hollow shaft was set as a target for the 2D model, see Figure 122. To replicate the higher stiffness provided by the complete geometry of the hollow shaft, the ring model was supported by an additional ring within the actual ring (see Figure 123). A radially flexible angle segment with fixed dimensions was then determined to simulate rolling contact.

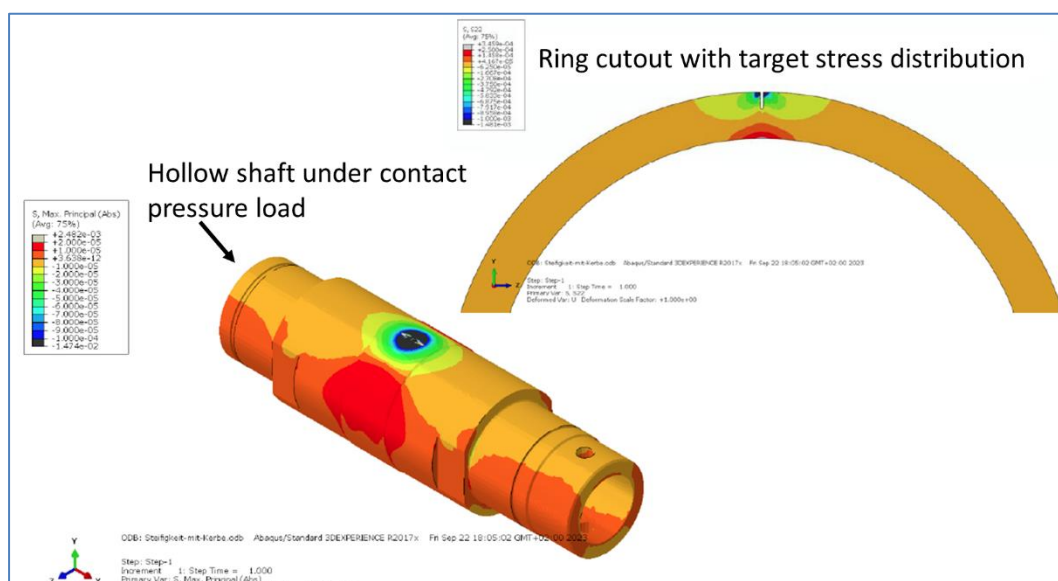


Figure 122: Calculation of the target stress distribution of the constant width ring model

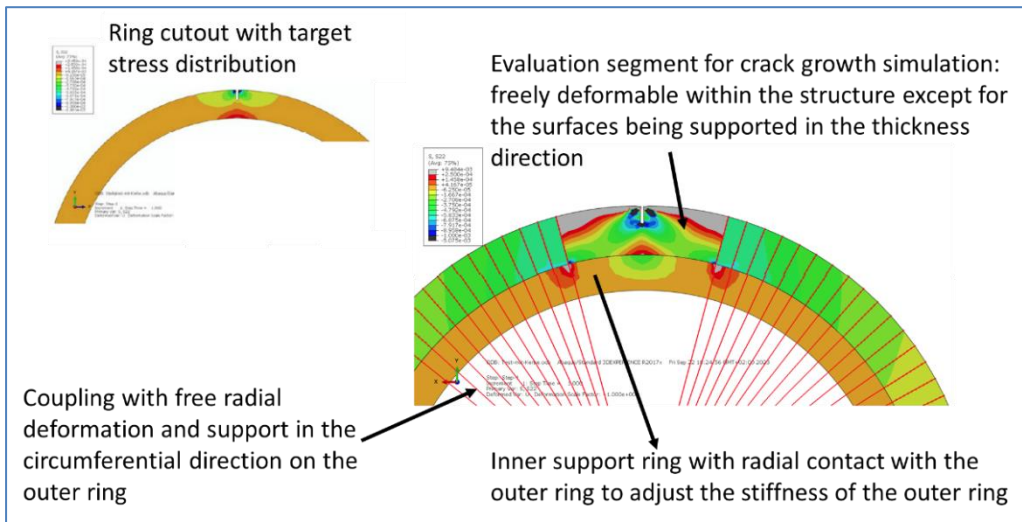


Figure 123: Description of the constant width model for the crack growth simulation

The boundary conditions and constraints used for the model in Figure 123 are shown in Figure 124. The contacts between the surfaces (inner and outer ring) and the degrees of freedom of the nodes were defined. The inner ring is supported in the Z-direction (Figure 124 (a)). A Tie-Constraint is defined between the inner and outer rings (Figure 124 (b)). The degrees of freedom of the reference point are blocked except in the Z-direction. (Figure 124 (c)). A constraint of the coupling type is defined in the outer ring (Figure 124 (d)).

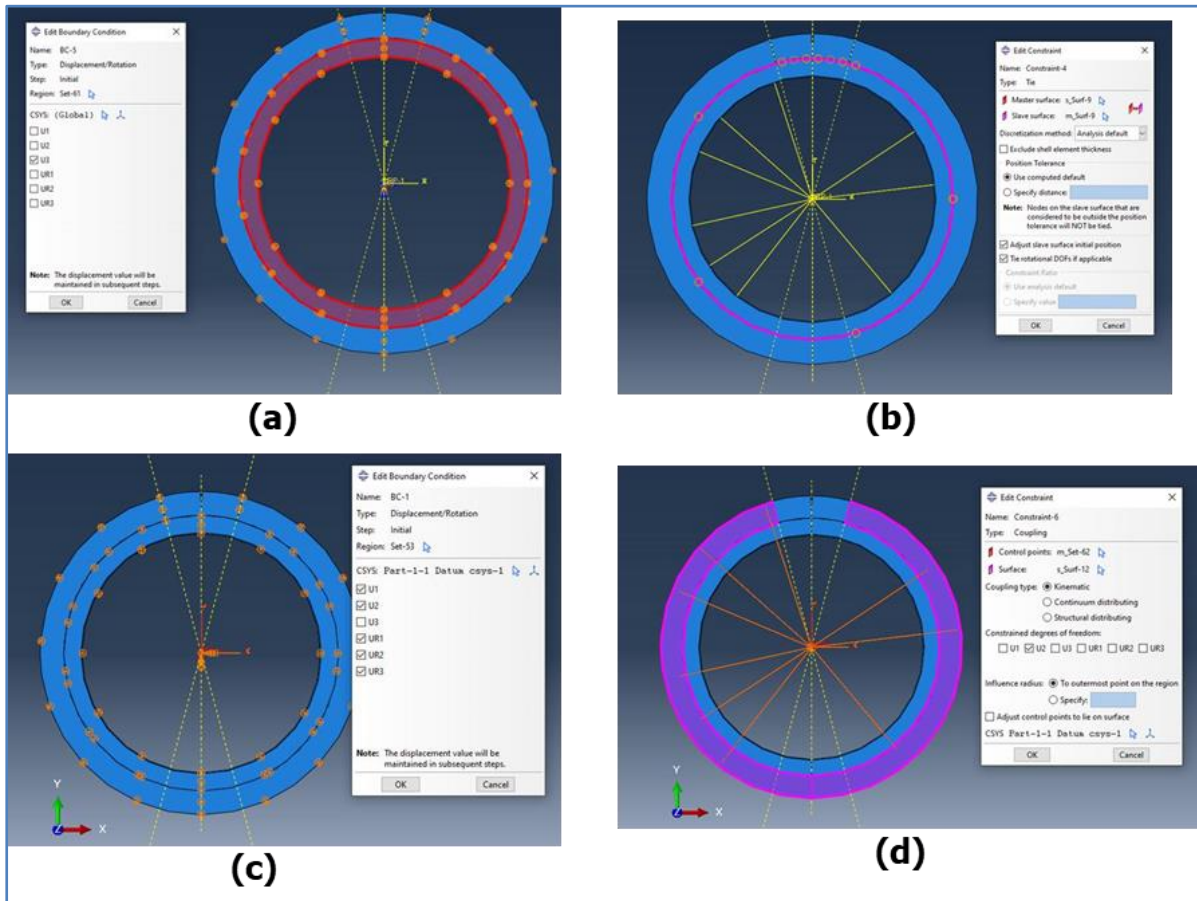


Figure 124: Kinematic boundary conditions and constraints

6.5.2.2 Implementation of residual stresses in the FE-model

The residual stresses in the hollow shaft V2.1/32CDV13 were considered in the rolling contact fatigue crack growth simulations (see Figure 125). For this purpose, the residual stresses were measured in the circumferential direction, as shown in Figure 125 (green curve). The residual stresses in the hollow shaft were modeled by thermal stresses in the FE-model. Temperatures were specified for all node rings according to the measured residual stress curve, see Figure 125 (blue curve). Because the measured residual stresses do not provide equilibrium on the FE-model used, the tensile residual stresses were calculated maintaining the measured compressive residual stresses, adjusting the residual stresses across the cross-section to ensure equilibrium is reached, see Figure 125 (red curve). The red curve was used for crack growth simulations.

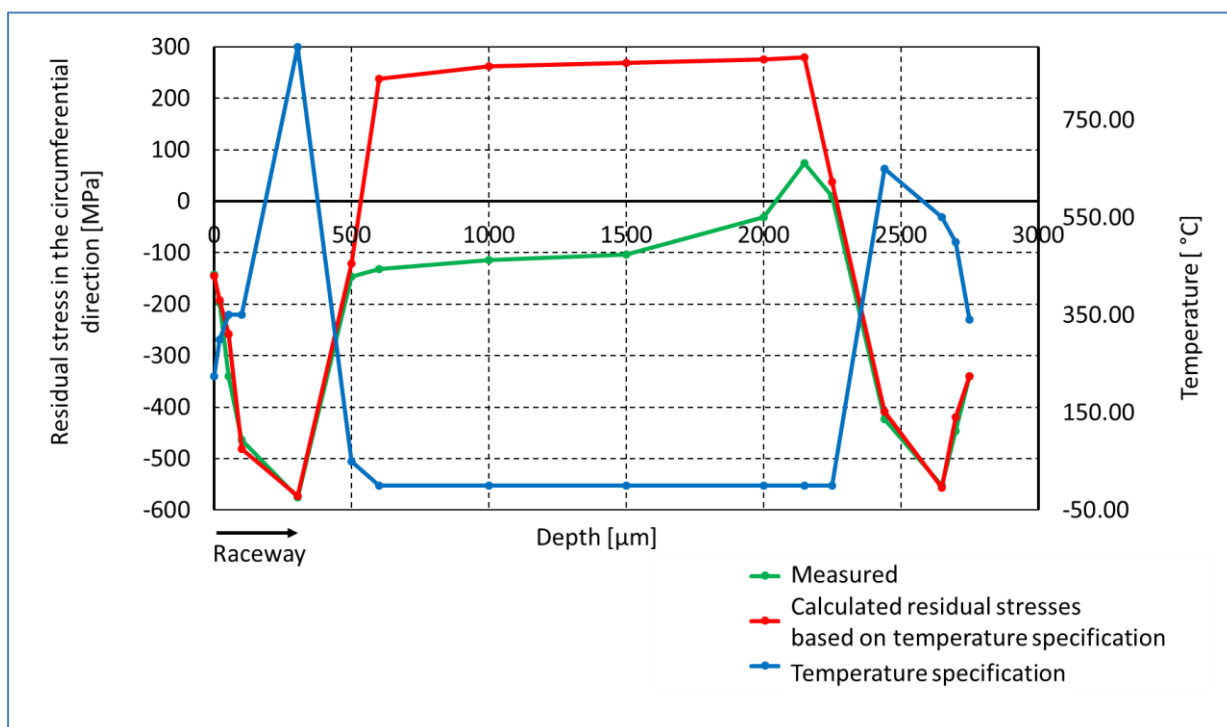


Figure 125: Description of the measured residual stress curve in the hollow shaft V2.1/32CDV13 and the residual stress curve used to simulate crack growth under rolling contact fatigue

Figure 126 (a) shows the calculation model under residual stresses, where the relevant area for the fracture mechanical evaluation is meshed much more finely (see Figure 126 (b)). Next, a notch with a length of 1 mm in the radial direction is made in the model (see Figure 126 (c)). Therefore, this length was chosen to investigate the influence of tensile residual stresses on crack growth. The compressive residual stresses near the surface push the two edges of the notch together, whereby in the notch base the edges are pulled apart because of high tensile residual stresses (see Figure 126 (d)).

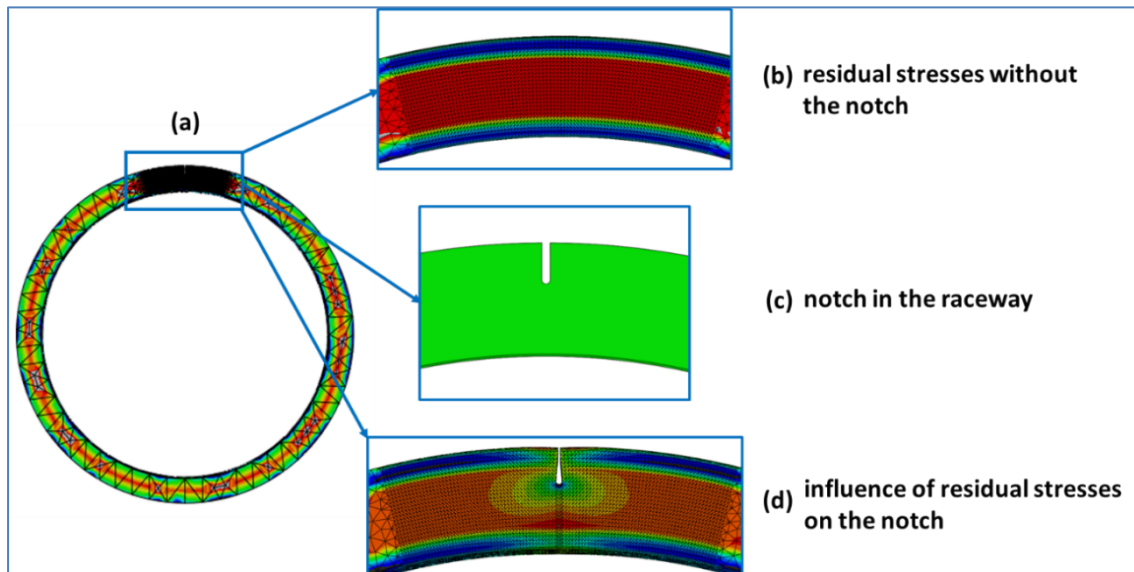


Figure 126: Modeling of residual stresses by thermal stresses, (a) distribution of residual stresses in the cross section of the raceway, (b) distribution of residual stresses in the cross section without notch, (c) adding the notch in the raceway and (d) influence of residual stresses on the notch

6.5.2.3 Crack growth simulation approach and results for rolling contact fatigue

Simulation approach

Crack growth simulations under rolling contact fatigue in the hollow shaft were carried out considering the residual stresses and complex loads. An initial crack with a length of 0.2 mm is made at the notch (see Figure 127(a)). The notch and the crack are aligned in the radial direction because the influence of the residual stresses is greatest here. The crack growth simulations were carried out in three steps, considering the following load situations. In the first step, the hollow shaft is subjected to bending due to the two rolling elements. The influence of the resulting bending stresses on the crack is then evaluated (see Figure 127(a)). In the second step, the crack loading due to the simultaneous effect of rolling contact and bending by the rolling element is analyzed (see Figure 127(b)). In the last step, the hollow shaft is once again subjected to bending load by two rolling elements (see Figure 127(c)). The bending stress was determined using the FE-model and the loads on the roller elements. This considers the bending stress amplitude independent of the superimposed stresses from rolling contact.

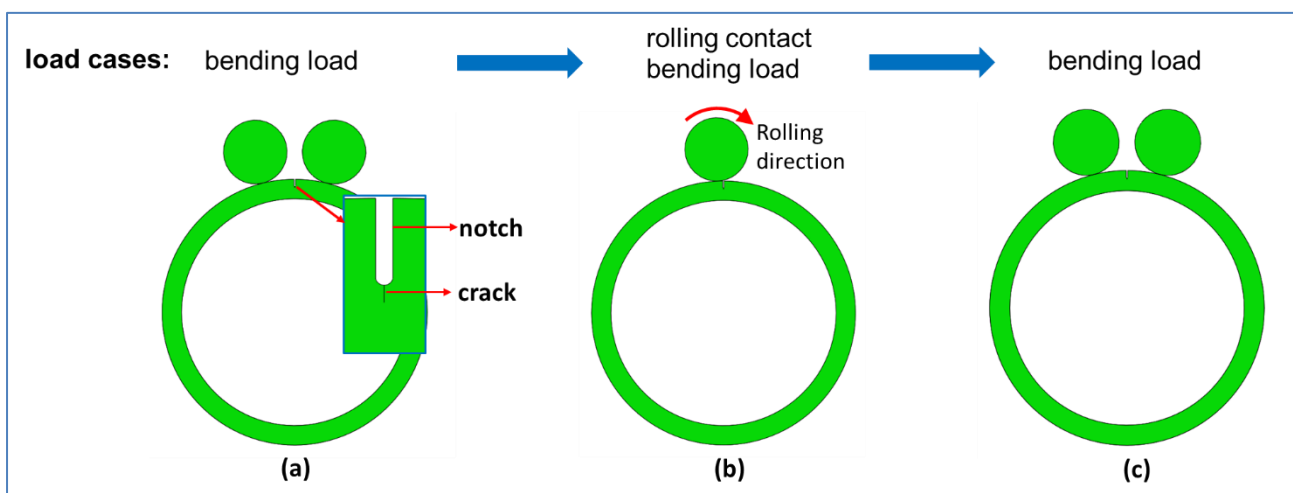


Figure 127: Crack growth simulation sequence for predicting the crack path in the hollow shaft considering the bending load and rolling contact fatigue

The simulation scheme is shown in Figure 128. The evaluation of the crack loading parameter K_V is determined for each simulation step. Once all load situations in Figure 128 are simulated, the maximum occurring ΔK_V is determined. The course of K_V considering all simulation steps in Figure 128 is shown in Figure 129. If ΔK_V is greater than the threshold value, the crack extends by $da = 5 \mu\text{m}$ and the simulations are restarted.

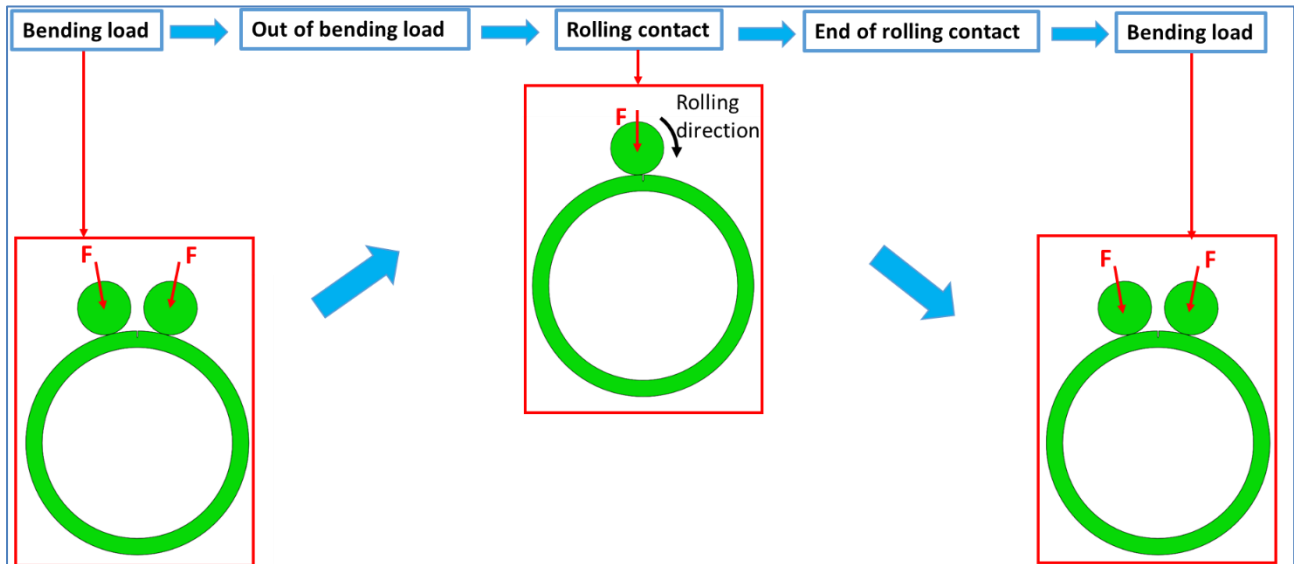


Figure 128: Scheme for simulating crack growth considering the following loading situations: bending load, rolling contact and the resulting stresses.

Results

The results of the equivalent stress intensity factor ΔK_V were used for the fracture mechanical evaluation of the crack growth simulations under rolling contact fatigue. The crack is capable of growth if ΔK_V is greater than the threshold value of $\Delta K_{th} = 150 \text{ N/mm}^{3/2}$. The courses of K_V during crack growth at the crack fronts are shown in Figure 129. The value of K_V was calculated in several steps according to Figure 128. The values of K_V are largest at the beginning because of the higher residual tensile stresses without the effect of the bending load and without rolling contact. As soon as the crack is between the two rolling elements (see Figure 127(a)), the crack front is relieved, which is accompanied by a reduction in the value of K_V . Next, K_V was investigated considering the simultaneous action of the bending load and the rolling contact (see Figure 127(b)). In this case, the crack is relieved even more, which is accompanied by a significant reduction in K_V . When the rollover process stopped, the equivalent stress intensity factor increases again. Afterwards, ΔK_V increases due to the bending load (see Figure 127(c)). The generated $\Delta K_V \approx 275 \text{ N/mm}^{3/2}$ is crucial for fatigue crack growth under rolling contact. After the first simulation with the initial crack, the crack is extended by $da = 5 \mu\text{m}$ to front 1. Simulations with the same steps were repeated for front 1 to front 8. Low alternating Mode II loading was observed at the initial crack, which was accompanied by straight crack growth without branching due to dominant Mode I loading. With increasing crack length, no significant change in Mode II loading and an increase in the mean value of Mode I loading were observed. From front 6 onwards, K_V is high, so the crack will potentially grow very quickly, see Figure 130. As a result, failure of the hollow shaft under Mode I loading is expected.

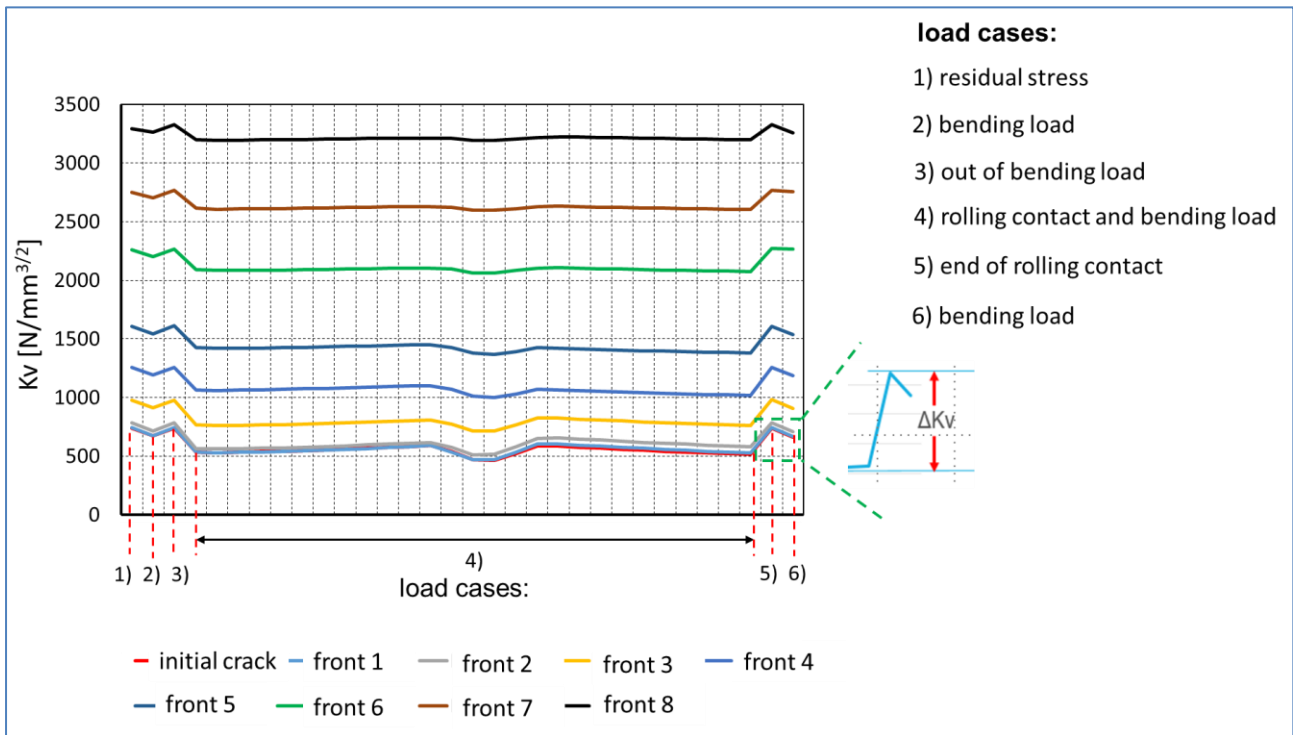


Figure 129: Graph of the equivalent stress intensity factor in rolling contact fatigue and under static load under the influence of residual stresses

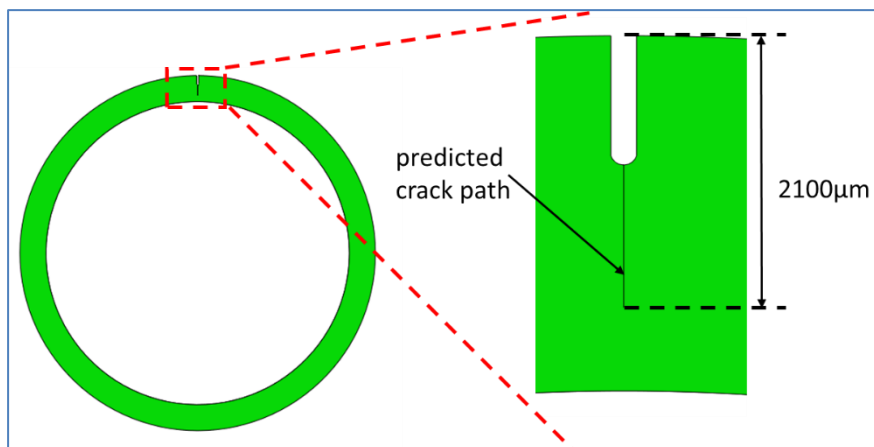


Figure 130: Prediction of the crack path under rolling contact fatigue considering residual stresses in the hollow shaft

In addition, the crack loading was determined when the crack was far from the contact pressure. For this purpose, the crack loading under the sole effect of residual stresses was compared with that under combined residual stresses and contact pressure far from the crack. The equivalent stress intensity factor due to the sole effect of residual stresses is $K_V = 736.3 \text{ N/mm}^{3/2}$. If the rolling element is far from the crack, its crack loading is unaffected.

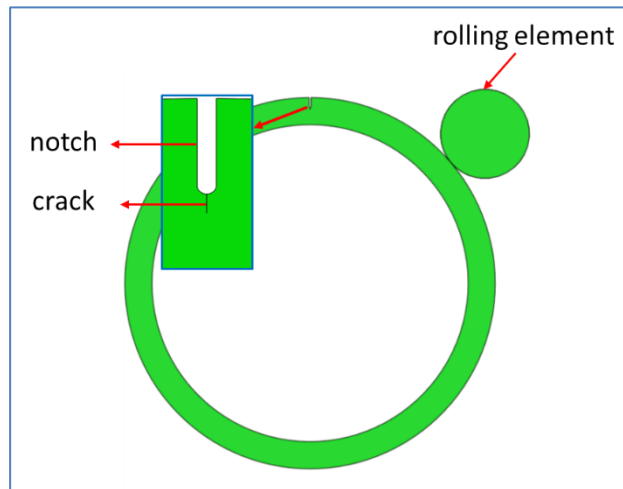


Figure 131: Roller position at a maximum circumferential stress on the outer edge of the notch

6.5.2.4 Comparison of the predicted crack path with crack propagation in the real test

The predicted crack path from the initial crack to front 8 and the crack growth in the test of V2.1/4 are shown in Figure 132. The crack in the simulation grew straight from the notch in the radial direction, as shown in Figure 132(a). A comparable crack propagation from 1 mm to 1.4 mm depth starting from the laser scratch can be observed in Figure 132(b), whereby a crack network also formed during the test.

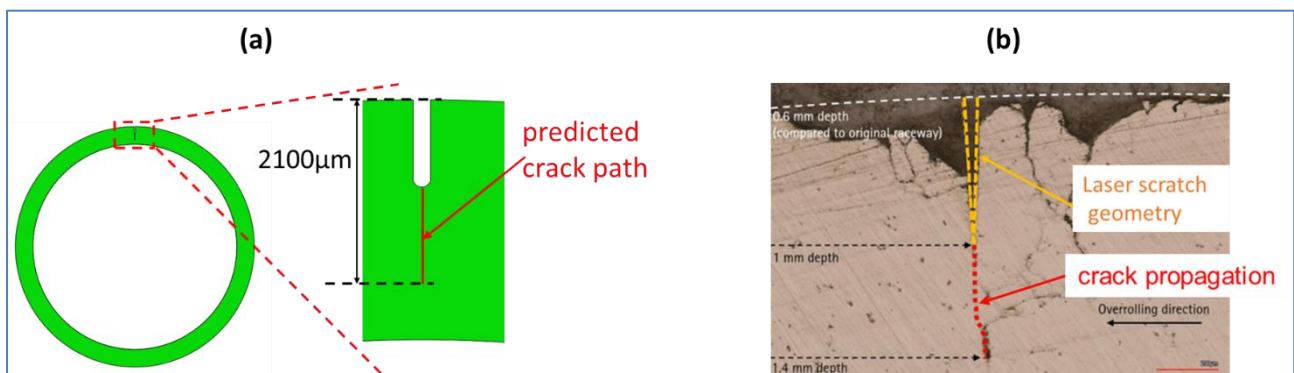


Figure 132: Comparison between the numerical and real tests, (a) prediction of the crack path under rolling contact fatigue considering the residual stresses in the hollow shaft, (b) crack propagation from 1 mm to 1.4 mm starting from the laser scratch and crack network near the surface and the scratch of shaft V2.1/4

6.5.3 Outer ring with notch

6.5.3.1 Description of the FE-model

The crack growth simulations in the outer ring are presented in this section. The outer rings with different notch designs (T102 and T104) were used. See Figure 133 (a) for T104. In the real tests it was found that the cracks do not start from the applied scratch, but from the spall. The maximum depths of the spalls are approximately 2.5 mm from the line of symmetry of the ring. Therefore, an initial crack that is offset 2.5 mm to the right of the symmetry line was selected for the simulation (see Figure 133 (b)). To realize the greatest influence of the residual stresses on the initial crack, the radial orientation of the crack was selected for the simulations. The crack environment and the contact area between the rolling element and the raceway are very finely meshed (see Figure 133 (c)). The kinematic boundary conditions used for the simulation are shown in Figure 134. For this purpose, a cylindrical coordinate system was used. Radial supports describe that displacements in the radial

direction of the selected nodes (on the red line) are not allowed, while tangential supports do not allow displacements in tangential directions.

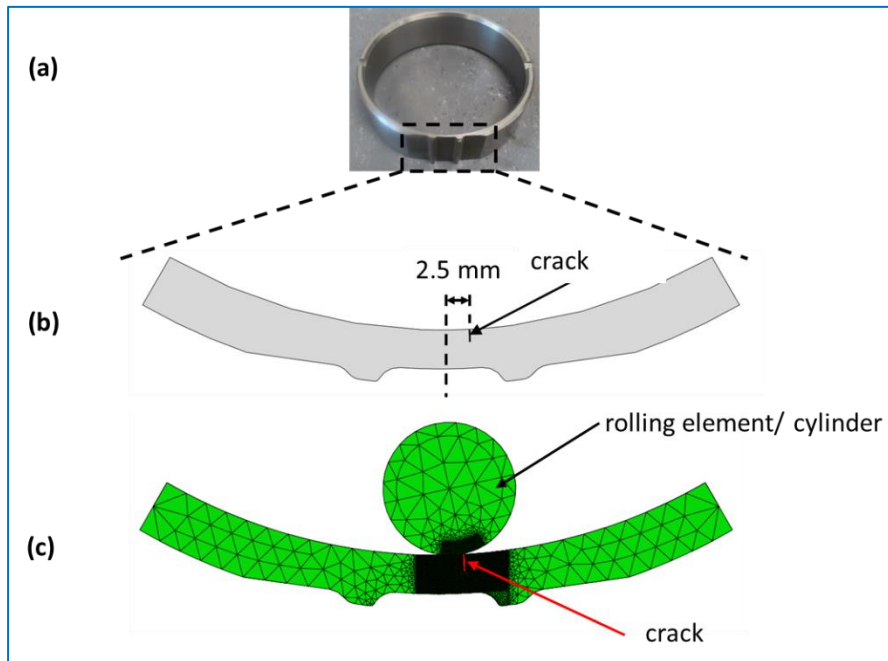


Figure 133: Model used to predict the crack path during rolling contact fatigue in the outer ring T104/ M50NiL

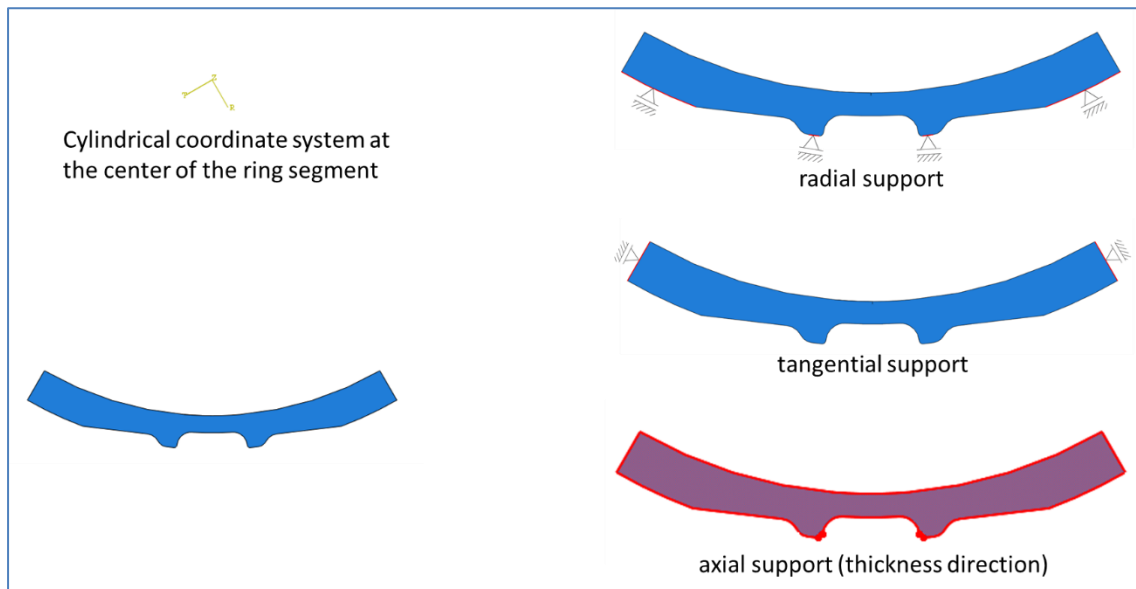


Figure 134: Kinematic boundary conditions for the ring segment

6.5.3.2 Outer ring T104

The crack growth simulations in the outer ring with the notch design T104 were carried out taking into account the friction between the crack surfaces and between the rolling element and the outer ring. The coefficients of friction, radius of the rolling element, contact pressure and material parameters used are described in Table 50.

Parameters used in the simulation	
Friction coefficient: cylinder/outer ring (no slipping)	0.15
Friction coefficient: crack surfaces	0.15
Cylinder radius R [mm]	11.97
Maximum contact pressure p_0 [MPa]	2400
Material properties/M50NiL	
Young's modulus E [MPa]	205000
Poisson's ratio ν	0.3

Table 50: Definition of the used parameters and material properties used in the crack growth simulation in the outer ring under rolling contact fatigue

Implementation of residual stresses in the FE-model

The residual stress values used in the FE-simulation were determined by measurements in the circumferential direction. The residual stresses were measured from two sides of the ring, from the raceway toward the notch and from the notch toward the raceway (see Figure 135). The graph of the measured residual stresses from the side of the raceway shows low tensile residual stress values, which suggests that the equilibrium conditions are not being met. Therefore, the two residual stress curves were connected at the point where the measured tensile residual stresses decreased from the side of the raceway. The resulting residual stress curve, which was used for the crack growth simulation, is shown in Figure 136.

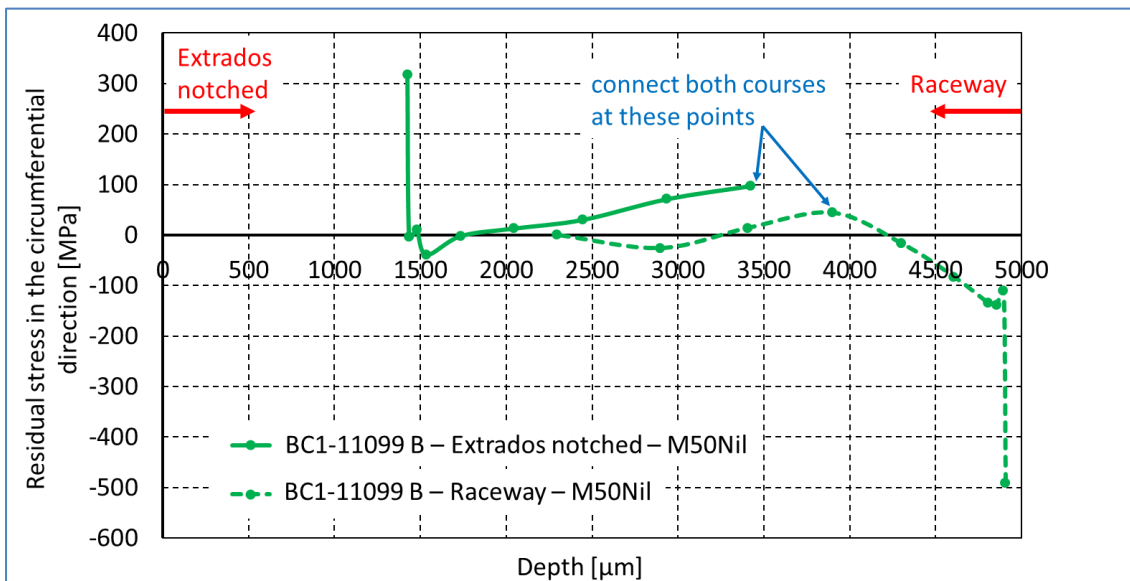


Figure 135: Measured residual stresses in the outer ring T104/M50NiL from the side of the notch and from the side of the raceway; residual stress values used for crack growth simulation

In the FE-simulations, the residual stresses in the outer ring were modeled by thermal stresses similar to those in the hollow shaft (see Figure 125). Here, the residual stresses were introduced by directly specifying the temperatures on all nodal rings in accordance with the measured residual stress curve. Figure 136 shows the measured residual stresses in the outer ring made of M50NiL/T104 and the calculated residual stresses based on the temperature distribution. The calculated residual stresses are in equilibrium and were used for the crack growth simulations.

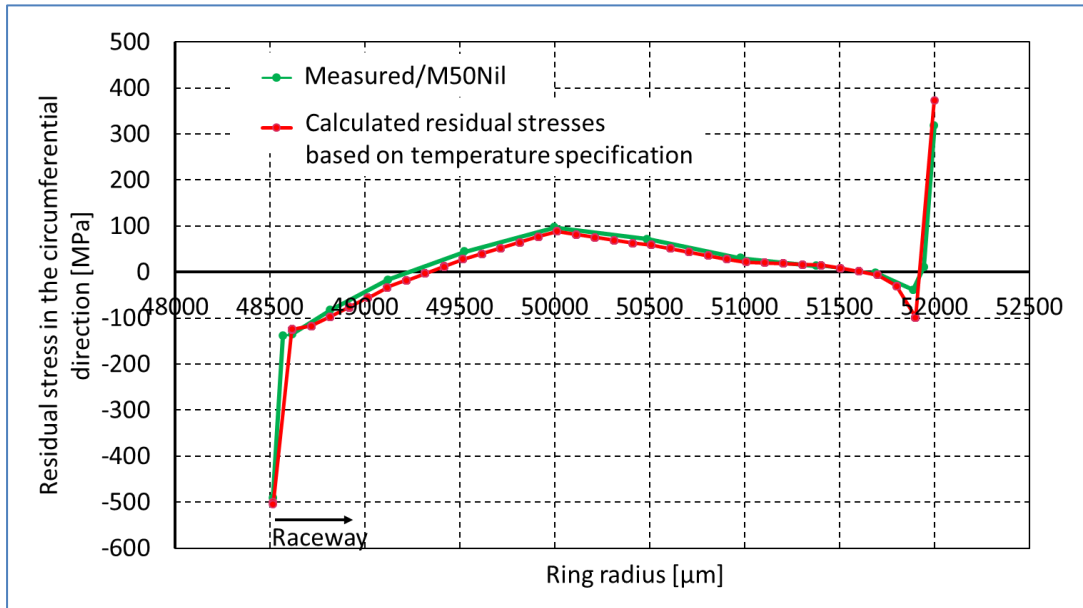


Figure 136: Description of the measured residual stress curve in the outer ring T104/M50Nil and the residual stress curve used to simulate crack growth under rolling contact fatigue

Figure 137 describes the modeling of the residual stresses by thermal stresses in the FE-model. In the relevant area for crack growth simulation, the residual stresses correspond to the measured residual stresses.

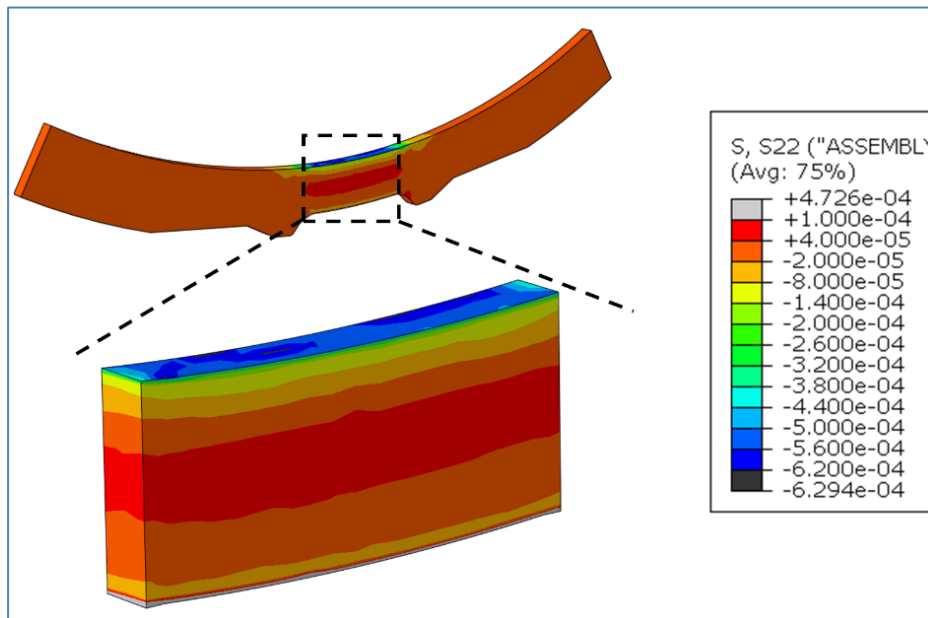


Figure 137: Modeling of the residual stresses in the circumferential direction by thermal stresses in the simulation model and in the area relevant for the crack growth simulation without a crack for outer ring design T104

Crack growth simulation approach and results for rolling contact fatigue

Simulation approach

Crack growth simulations under rolling contact fatigue were carried out in the outer ring considering the residual stresses and bending loads. These load situations were considered in the following three steps when predicting the crack path. In the first step, outer ring is subjected to bending by the two rolling elements. The influence of the resulting bending stresses on the crack is investigated in Figure 138(a). In the second step, the crack propagation due to the simultaneous effect of rolling contact and bending by the rolling element is

analyzed (see Figure 138(b)). In the last step, the outer ring is once again subjected to bending by two rolling elements (see Figure 138(c)).

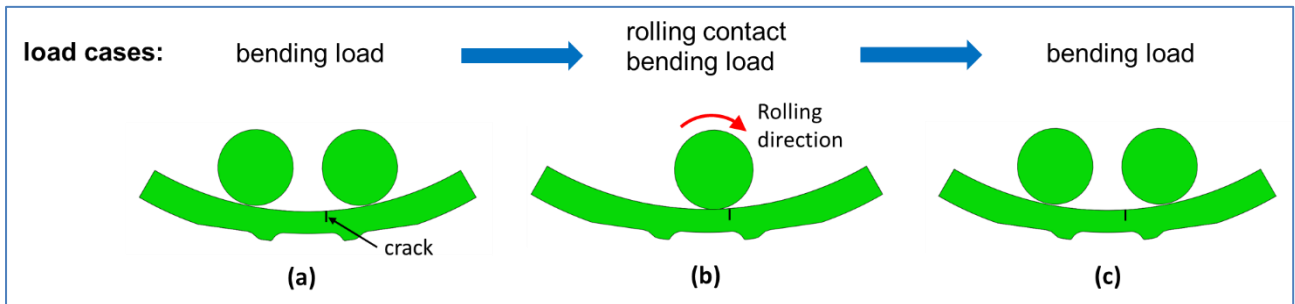


Figure 138: Crack growth simulation sequence for predicting the crack path in the outer ring considering the bending load and rolling contact fatigue

The simulation scheme is shown in Figure 139. The crack loading parameter K_V is evaluated for each simulation step. When all load situations in Figure 139 are simulated, the maximum occurring ΔK_V is determined. The course of K_V considering all simulation steps in Figure 139 is shown in Figure 140. If ΔK_V is greater than the threshold value, the crack was extended by $da=5\ \mu\text{m}$ and the simulations was restarted.

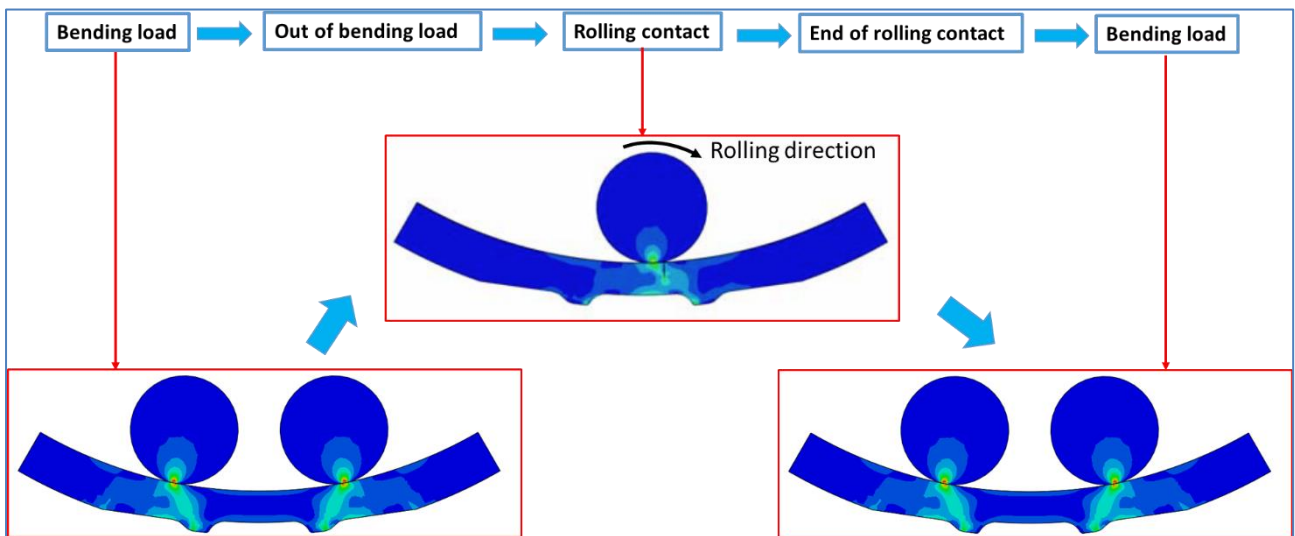


Figure 139: Scheme for simulating crack growth considering the following loading situations: bending load, rolling contact and the resulting compressive and tensile stresses.

Results

To calculate the crack path, the graph of the equivalent stress intensity factor K_V for different load cases (see Figure 140) was determined and analyzed. Figure 140 describes the graph of K_V for a simulation of a kinked crack with an initial crack length of 1mm, see Figure 141. In this crack configuration, the residual stresses have a negligible influence on K_V and therefore also a smaller influence on crack growth. On the other hand, due to bending, K_V increases above the threshold value at the location where the crack is located between the two rolling elements, see Figure 138 (a). After that, ΔK_V increases even further up to a maximum value of approx. 600 [N/mm^{3/2}]. At this point the rolling element is in front of the crack (see Figure 138 (b)). As soon as the crack is rolled over and the rolling element is after the crack, K_V decreases again. Afterwards, K_V increases due the bending and reaches a value of approximately 187 [N/mm^{3/2}] due to the load situation in Figure 138 (c). The maximum value of ΔK_V in this graph is crucial for the fracture mechanical evaluation. These steps are repeated for each crack extension.

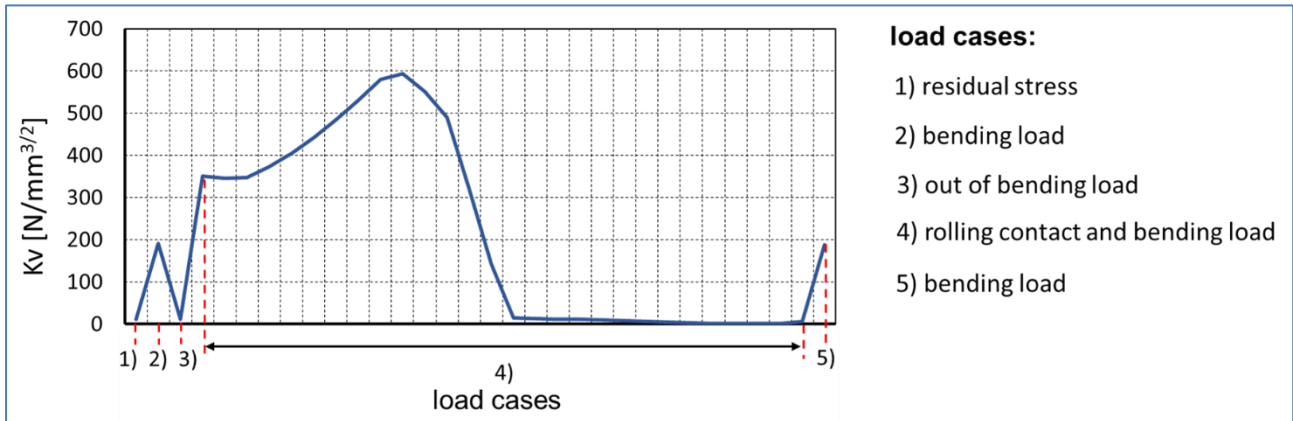


Figure 140: Course of K_v under different load situations for a kinked crack with an initial crack length of 1 mm to evaluate the crack extension by da , see Figure 141

Spalls of various depths were observed during the tests. To investigate the influence of spalling depth on the crack path, crack growth simulations were performed with initial crack lengths of 1 mm, 1.5 mm and 2 mm. The results of the crack growth simulations with initial crack lengths of 1 mm, 1.5 mm and 2 mm are shown in Figure 141. As the initial crack length increases, the first crack extension tends downward in small steps.

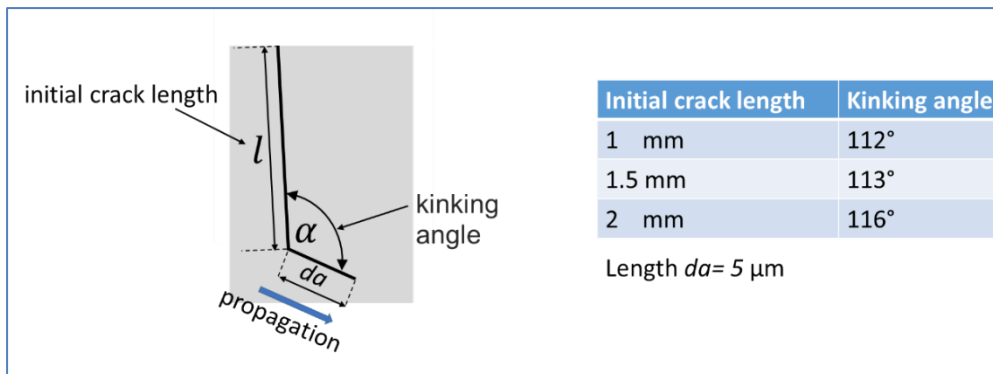


Figure 141: Influence of initial crack length on kinking angle during rolling contact fatigue in the outer ring

The predicted crack paths at initial crack lengths of 1.5 mm and 2 mm are shown in Figure 142. The crack paths are similar. In contrast to the crack paths, the calculated values of the maximum equivalent stress intensity factor ΔK_V in case of an initial crack length of 2 mm showed significantly larger values compared to the ΔK_V values with an initial crack length of 1.5 mm (see Figure 142). As an example, the position of the rolling element at maximum crack loading (Max ΔK_V) at crack front 17 (after 17 crack extensions) is shown in Figure 143. As the crack length increases, the crack grows almost straight under Mode I loading due to rolling contact before rolling over the initial crack. It was observed that the Mode II loading of the crack increases with increasing crack length due to the rolling contact after rolling over the initial crack, which is accompanied by an increasing tendency for crack growth to change direction. As the crack length increases, there is a significant decrease in the remaining ligament between the crack tip and the lower edge of the ring, which is accompanied by a significant increase in the basic loading in the remaining ligament.

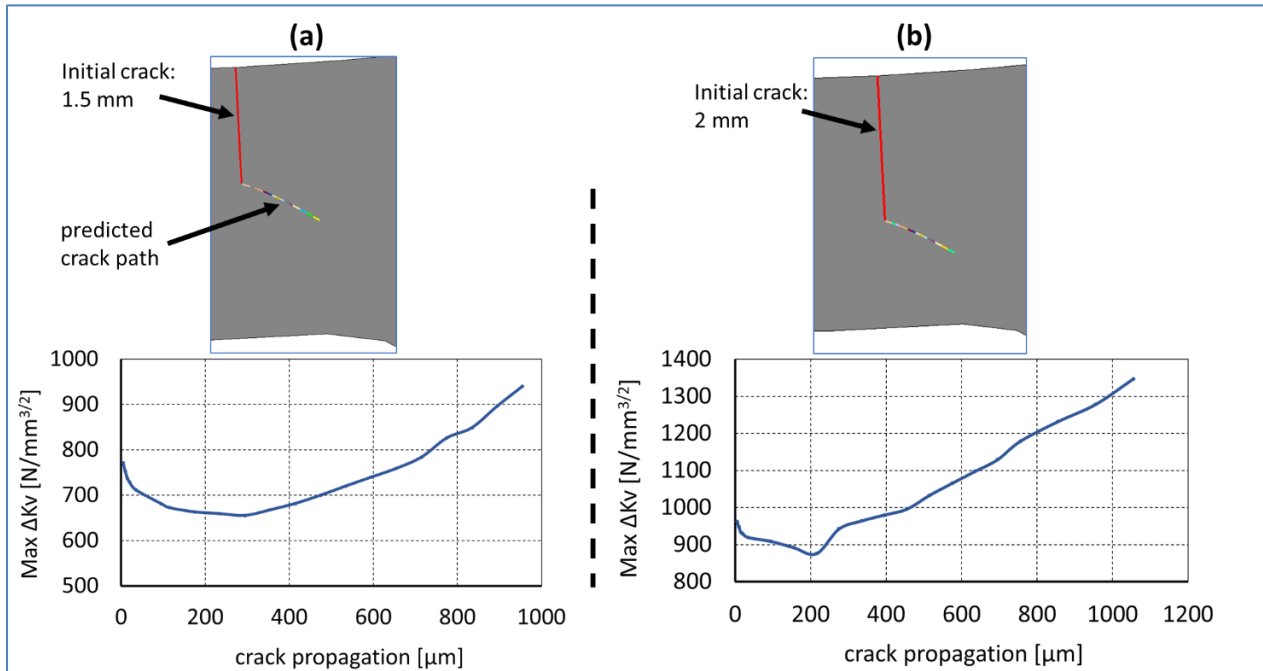


Figure 142: Predicted crack paths and associated values of maximum equivalent stress intensity factor K_V during crack growth for the initial crack lengths 1.5 mm and 2 mm

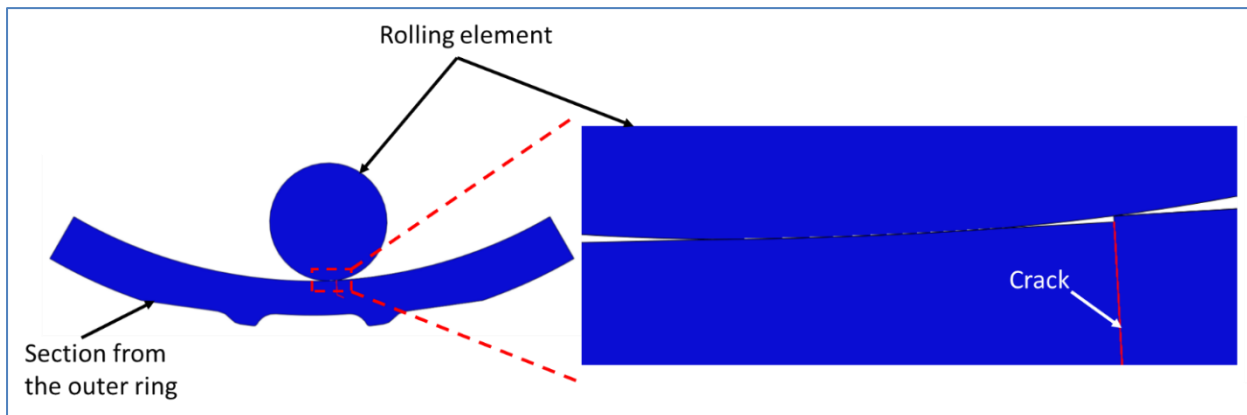


Figure 143: Roller position at maximum load with an initial crack length of 1.5 mm at crack front 17

Comparison of the predicted crack path with crack propagation in the real test

To compare the results of the crack growth simulations with the crack growth in the real tests, the crack in the real tests is divided into two regions I and II, as shown Figure 144. In the first part I the crack grows inclined inwards. After the cracks have reached a certain depth, their growth direction changes in part II.

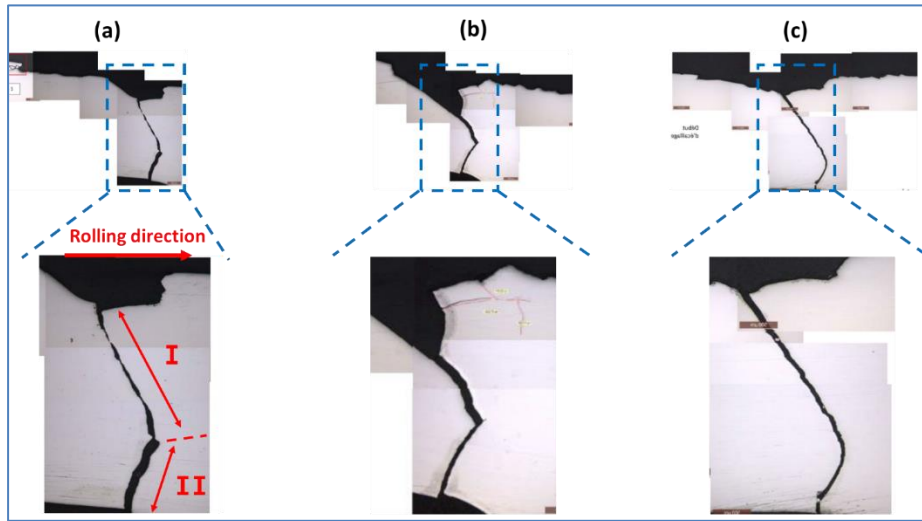


Figure 144: Crack propagation in the outer ring T104/M50Ni1 for (a) SN 221013, (b) SN 221025 and (c) SN 221026

The calculated crack path with an initial crack length of 1.5 mm was compared with the resulting crack in the outer ring made of M50Ni1, T104/SN221025. The predicted crack path agrees very well with the crack path in the real test in part I, see Figure 145. In this case, the equivalent stress intensity factor shows high values, so that the fracture toughness of the material is reached quickly after further crack growth (see Figure 142). Unstable crack growth in part II is expected.

To determine the direction of further crack growth in part II, the maximum principal stresses are evaluated (see Figure 146). This shows that there is a high base loading in the remaining cross-section. This loading situation can lead to the complete fracture of the remaining cross-section due to strength failure. In this case, sharp kinking of the crack is very likely. The quantitatively expected direction of further crack growth in area II is shown in Figure 146.

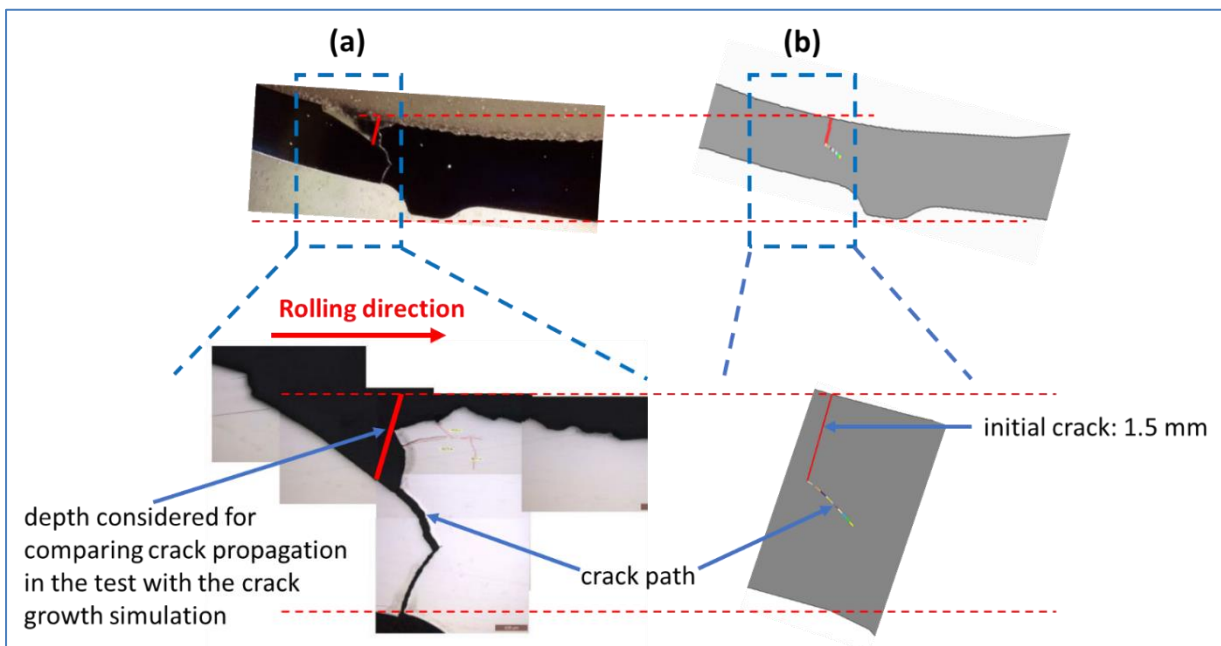


Figure 145: Schematic representation of the comparison between crack propagation in the test and the crack growth simulation, (a) crack propagation during the test of "M50Ni1 Version 1 T104 S/N221025", (b) crack path prediction by the crack growth simulation

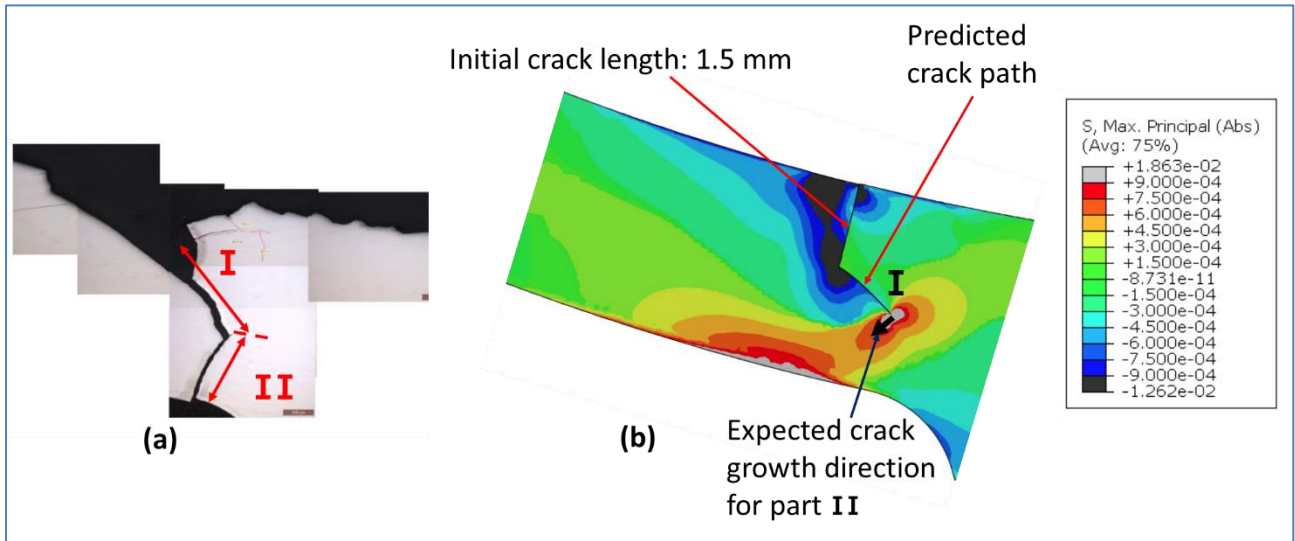


Figure 146: Representation of the maximum principal stresses in the remaining cross-section to estimate the direction of further crack growth, (a) crack propagation during the test of "M50Nil Version 1 T104 S/N221025, (b) maximum principal stresses in the remaining cross section and the estimated direction of further crack growth

Comparison between predicted crack paths of materials M50Nil and 32CDV13

A crack propagation simulation was also carried out for the outer ring application with the 32CDV13 material for the T104 geometry. The approach of the crack propagation simulation and the implementation of the residual stresses in the FE-model was performed in the same way as for the application with the M50Nil material. The measured and calculated residual stress values are shown in Figure 147.

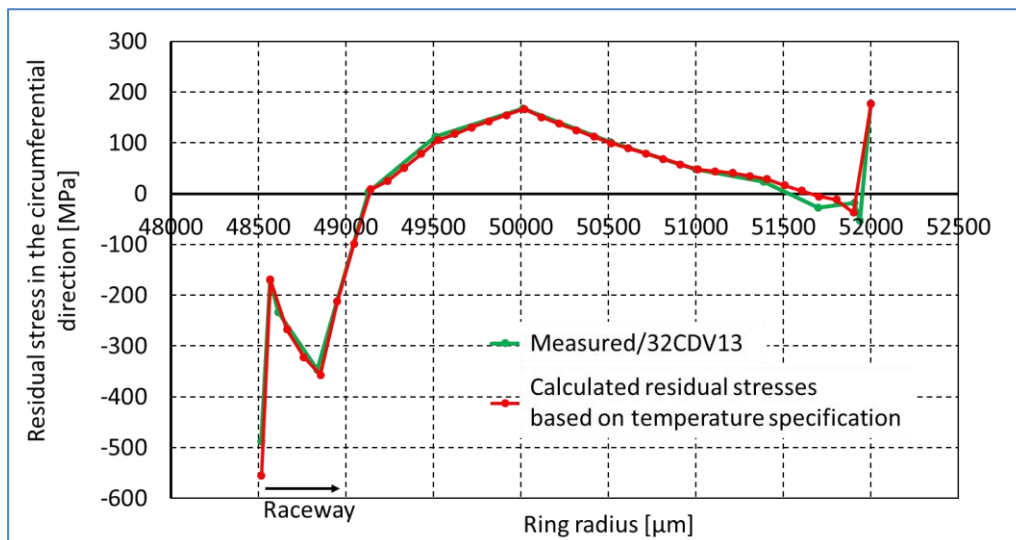


Figure 147: Description of the measured residual stress curve in the outer ring T104/32CDV13 and the residual stress curve used to simulate crack growth under rolling contact fatigue

The crack paths in the two outer rings made of M50Nil and 32CDV13 are similar (see Figure 148).

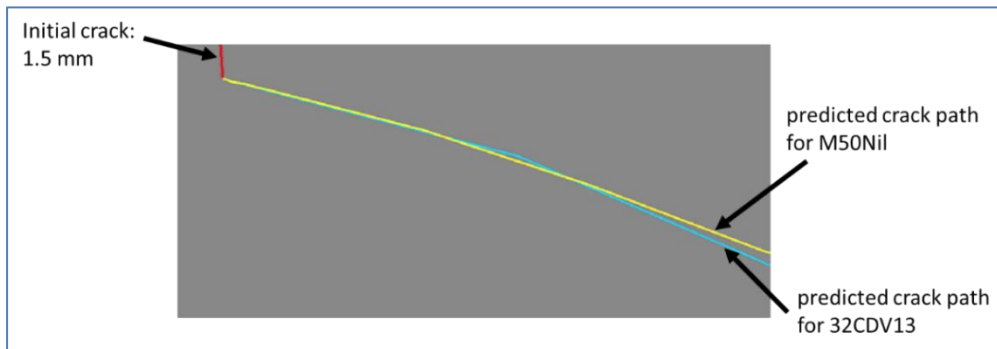


Figure 148: Predicted crack paths for the outer rings T104 made of M50NiL and 32CDV13 under the same boundary conditions

6.5.3.3 Outer ring T102

The simulation with the T102 design was conducted in preparation for Phase II. For this first investigation, the residual stress curve on the side of the raceway was used. The crack growth simulation procedure for the outer ring with notch design T102 (M50NiL) is similar to that of variant T104. The parameters used for the simulation are shown in Table 51. The residual stresses in the outer ring were modeled using thermal stresses. The measured residual stresses on the side of the raceway were used (see Figure 149). In contrast to the initial crack in the outer ring T104, a shorter initial crack of 0.3 mm was selected for the outer ring T102 in order to investigate the influence of the initial crack length on the crack path. The initial crack of 0.3 mm is in the range of compressive residual stresses.

Parameters used in the simulation	
Initial crack length [mm]	0.3
Initial crack angle	Radial direction
Residual stress	yes
Bending loads	yes
Friction coefficient: cylinder/outer ring (no slipping)	0.15
Friction coefficient: crack surfaces	0.15
Cylinder radius R [mm]	11.97
Maximum contact pressure p_0 [MPa]	2400
Material properties/M50NiL	
Young's modulus E [MPa]	205000
Poisson's ratio ν	0.3

Table 51: Definition of the parameters and material properties used for the crack growth simulation in outer ring T102/ M50NiL under rolling contact fatigue considering residual stresses

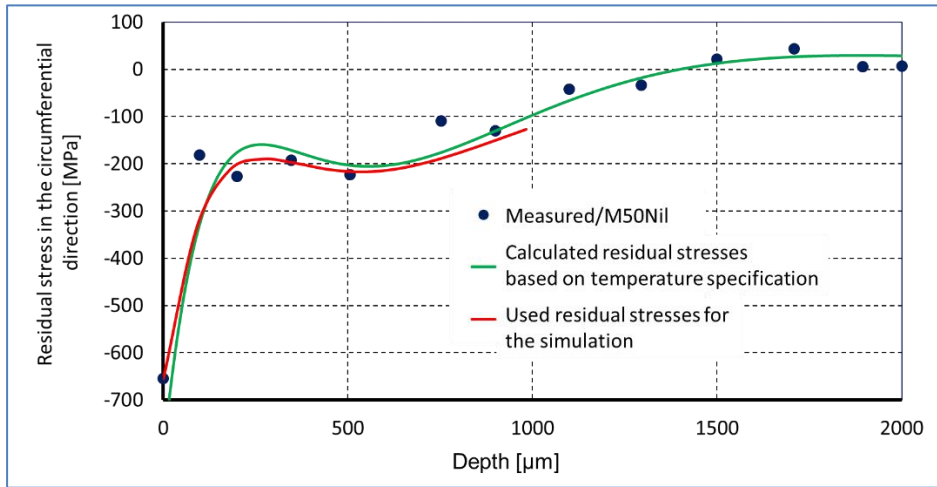


Figure 149: Description of the measured residual stress curve in the outer ring (T102/M50NiI) and the residual stress curve used to simulate crack growth under rolling contact fatigue

Figure 150 describes the modeling of the residual stresses by thermal stresses in the FE-model. In the relevant area for crack growth simulation, the residual stresses correspond to the measured residual stresses.

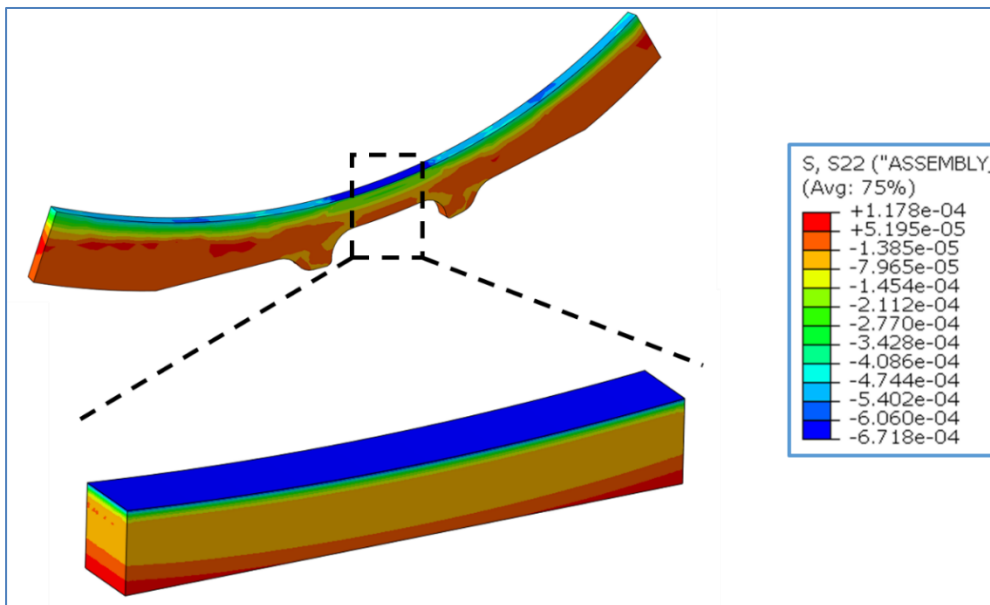


Figure 150: Modeling of the residual stresses in the circumferential direction by thermal stresses in the simulation model and in the area relevant for the crack growth simulation without a crack for outer ring design T102

Results

Figure 151 describes the global simulation model and the predicted crack paths using the parameters in Table 51. The initial crack branches. The crack branches grow parallel to the surface. The crack loading on the left side decreases continuously as the crack grows, although a crack stop can be expected when the threshold value is reached (see Figure 152(a)). The crack on the right side grows initially and then stops after three extension segments at front 3, as shown in Figure 152(b). As the left crack grows, the crack loading on the right crack slowly increases again, although this increase does not cause further growth of the right crack branch. For this reason, crack arrest of the right crack is also expected.

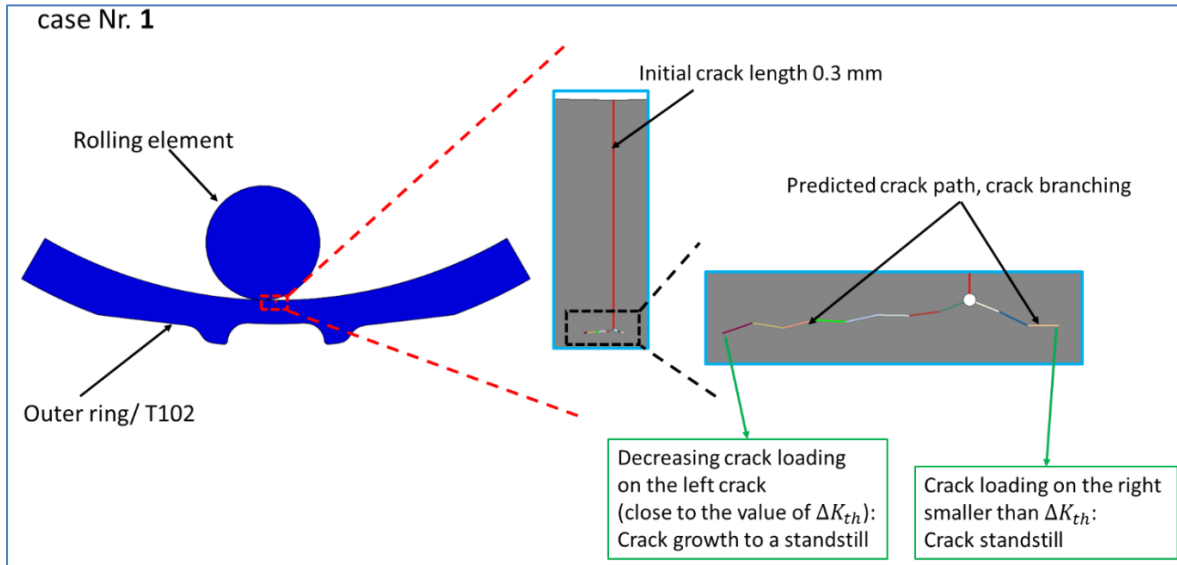


Figure 151: Predicting of crack paths in the outer ring (T102/M50Ni) for case 1 (initial crack length of 0.3 mm) under rolling contact fatigue

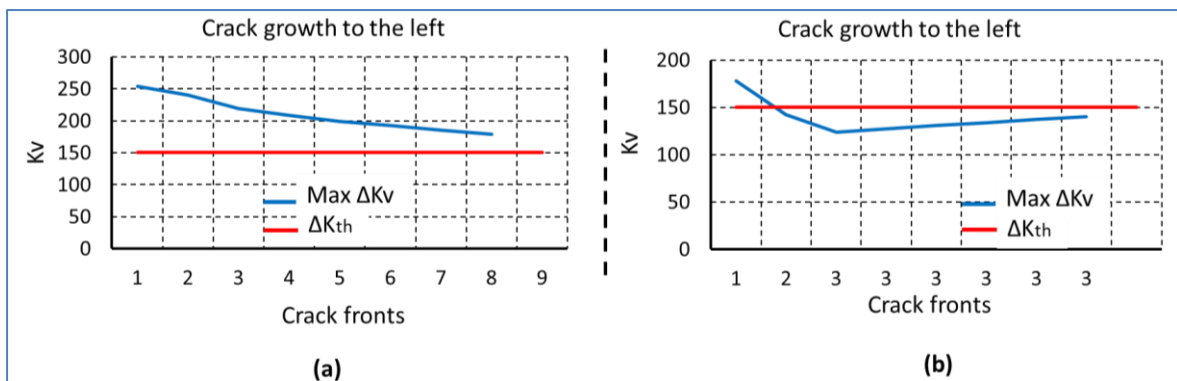


Figure 152: Graph of Max Kv during crack growth, (a) left crack path and (b) right crack path (see Figure 151)

6.6 Simulation conclusion

The aim of this study was to understand the damage process and to predict crack paths in the hollow shaft and outer ring under rolling contact fatigue. Here, 2D-crack growth simulations were performed under LEFM assumptions. For this purpose, the induced crack loading due to overrolling was analyzed and evaluated in detail for each simulation step of crack propagation. This enabled a better understanding of crack propagation in the structure due to rolling contact fatigue. These simulations were performed by [8] using the FE-program ABAQUS and the crack propagation simulation program ADAPCRACK3D. The developed methods in this project for crack growth investigation can be applied to other relevant problems such as rolling contact in planetary gears. Due to the extensive project, three separate parts are considered as follows:

Parametric study to prepare Phase I.1

First, crack growth simulations were carried out under pure rolling contact fatigue. The aim of this study was to investigate whether crack growth under pure rolling contact fatigue stops at a finite depth or not. Using a basic parametric study, the following influencing quantities were taken into account: crack angle, crack length/crack depth, contact pressure and coefficient of friction between the crack surfaces. In the crack growth simulations, the crack was extended by a length da if the crack was capable of growth ($\Delta K_V > \Delta K_{th}$). The length da is chosen to be as small as possible and is adjusted in the simulations so that the crack path can be

calculated most accurately. Calculating the crack extension is possible, but time-consuming. The calculation of the service life can also be implemented in the simulation model.

From this study, it is evident that Mode II loading occurs essentially at the initial crack due to the compressive loading between the initial crack surfaces. With alternating Mode II loading at the initial crack, crack branching was possible. Flat initial crack angles, high contact pressure and low crack surface friction promote crack branching, which can lead to spalling. This study has also shown that the crack loading decreases with increasing additional crack length. Here, crack stopping is to be expected.

Phase I.2

In the second part (Phase I.2), crack paths were predicted considering pure rolling contact fatigue and residual stresses. The aim of Phase I.2 was to investigate the maximum crack growth depth and tendency of crack propagation (into the core or back to the surface) in comparison to the basic variant of Phase I.1. The residual stresses were modeled by thermal stresses. In this part, a parametric study was carried out in preparation for Phase I.2. In these investigations, various initial crack lengths with different initial crack angles were investigated.

The results of this study showed that the initial crack grew essentially under Mode II loading independent of the initial angle, initial crack length and residual stresses. Here, the crack was sharply kinked at the first crack propagation. At the initiation crack angle of 15°, the crack grew substantially to the surface with increasing Mode I loading. In the case of long additional cracks, the crack growth was driven by the residual stresses. At the initial crack angle of 90°, a reduction in crack loading due to compressive residual stresses near the edge was observed for both the initial crack and the kinked additional crack. In the case of branched cracks, the crack growth was essentially under decreasing Mode I loading, whereby crack arrest was expected. The residual stresses do not affect the paths of the branched cracks. The crack loading has increased from 0.5mm to 0.7mm due to the increase in the initial crack length, because the crack tip was in the area of the residual tensile stresses.

Phase II

In the third part (Phase II), both the residual stresses and complex loads (bending loads) were considered. To predict crack paths under rolling contact and body stress loading conditions, the measured residual stresses in the hollow shaft and in the outer ring were used. For this purpose, the residual stresses were measured from both the inner and outer diameters to realize accurate measurements. The measured residual stresses in the hollow shaft showed high compressive residual stresses on the side of the raceway and on the inner diameter. Relatively lower residual tensile stresses were measured in the middle area. When implementing this residual stress curve in the FE-simulation, it was found that these residual stresses were not in equilibrium. With the assumption that the compressive residual stresses on both surfaces are representative, the tensile residual stresses were determined so that the equilibrium condition of the residual stresses was fulfilled. In the crack growth simulations, the residual stresses in the circumferential direction were considered because they influence crack growth in the hollow shaft. Residual compressive stresses act to close the crack. On the other hand, tensile residual stresses open the crack, which is accompanied by a possible increase in crack loading. The residual stresses in the FE simulations were modeled using thermal stresses.

The measured residual stresses in the outer ring were measured both from the side of the raceway and from the side of the introduced notch. In this case, the measured residual stresses could be used for crack growth simulation without need of adjustments to ensure equilibrium. The residual stresses combined with body stress were considered in the FE-simulations.

The crack growth simulations also considered complex loads in the form of bending loads. On the hollow shaft, a notch was made in the axial direction. In this case, the induced axial stresses had no significant influence on crack loading. On the other hand, the circumferential stresses due to the ovalization of the hollow shaft were considered (see Figure 123). In the case of the outer ring, the bending load influenced on the crack when the crack was between the rolling elements and when the crack is rolled over by the rolling element.

Simulation results

The results of the crack growth simulations showed good agreement with some results of the tests. Here, crack paths in the hollow shaft and in the outer ring were predicted and compared with the cracks that developed in the same parts. The prediction of the crack path after spalling in the outer ring agreed very well with the crack paths in the tests. Both the course of the crack path and its location in the real tests were successfully predicted. During the tests, crack networks and short crack growth in the radial direction occurred on the hollow shaft with a notch. The crack growth simulation in the hollow shaft also showed crack growth in the radial direction without crack branching. It was predicted that the crack would continue to grow due to high tensile residual stresses until total failure of the hollow shaft. The cracks only grew slightly deeper in the real tests. The resulting crack networks on the surface next to the notch were probably due to the influence of the white layer. This assumption requires further study.

In the future, these FE-models could be expanded into 3D. The presented numerical results from the parametric study and the results from Phase I and Phase II only apply to the investigated cases with the corresponding geometries of the components and cracks, the boundary conditions and the prevailing residual stresses. For this reason, new problems with other residual stress curves or other crack parameters such as crack angle and crack length should be examined and evaluated separately.

7. Summary and conclusion

The main focus of the work for D2-7 was the detailed description of test and simulation activities that were done by taking into account the main objectives for tasks 3, 4, and 5 ([1],[2]). This includes an evaluation of the tested parameters with interpretations of all observations made during testing, as well as validation and correlation of the simulations performed within the test campaign. The test campaign was divided into three main Phases:

- Phase I.1: Pure RCF for different load levels
- Phase I.2: Pure RCF by varying key parameters
- Phase II: RCF with additional body stress (complex load)

These different Phases were created to validate the hypotheses which were defined and presented during D2-2 as a fundamental baseline for this research project [4]:

1. In the case of a pure rolling contact load, the initiation of a crack with a finite depth may occur.
 - Crack growth ends at a finite depth
 - A crack typically leads to spalling damage
 - Crack growth toward the surface is known for pure RCF. Crack growth into the material is known in combination with a second driver (body stress)
2. Without a complex load situation present, such as for example, in a planetary gear, there will be no further crack growth under a single load of the rolling contact.
3. Crack propagation into the material is only possible under the complex load situation (body stress) and must be considered in this case.

Test campaign

Phase I.1 was used to study the influence of different load levels on the initiation of spalling and cracks under pure RCF for a pre-damaged raceway. The results demonstrated that a limit exists for both materials, below which no spalling could be introduced for the given pre-damage, whereas the load level of 2.4 GPa repeatably produced spalling. Identical observations were made for Phase I.2, where parameters such as hardness depth, hardness, and residual stress were varied. Within the three load levels that were tested, the limit for no spall initiation remained between 1.8 GPa and 2.4 GPa, whereas it was again only possible to initiate spalling at a load level of 2.4 GPa. A more detailed limit could not be identified because only three load levels were tested. Nevertheless, a clear trend for both materials and applications was not observed; it was only the case that specimens with the highest case hardening depth had the lowest spalling depth for the case hardened material. Finally, all the tests for Phase I.1 and I.2 validated the hypothesis that crack growth ends at a finite depth and pure rolling contact typically results in classical spalling damage for the single load condition without further crack growth through the material.

During Phase II, a complex load (second driver) was introduced by modification of the specimens, thus introducing additional deformations. The tests showed for the outer ring application that the second driver led to severe cracks through the material. It was also shown that for the same load level, no cracks through the material occurred for the nitrided material, which could be explained by a higher crack growth threshold value. For the shaft application, it was only possible at a higher load level (2.9 GPa) to introduce further crack growth but still without any crack through the material. Cracks that were perpendicular to the raceway (as implemented during test campaign) were less critical to the bending moment because bending stress acts in the axial direction, which does not promote crack propagation. In addition, the ovalization of the shaft, which produces stress loading in the circumferential direction (perpendicular to the scratch of the test campaign), is

too small to promote crack propagation. Finally, it was not further investigated during the test campaign whether circumferential cracks (in the rolling direction) are more severe according to bending load stress loading. Further testing with cracks in the rolling direction should be carried out to prove this hypothesis.

Nevertheless, the test results proved that deeper crack propagation into the depth of the material with a crack through the complete thickness was mainly driven by the second driver (additional body stress), and the potential for this type of failure can be significantly reduced by reduction or elimination of such a second driver.

Because the setup and load conditions were different for both tested applications (shaft and outer ring), it is difficult to compare the results in detail. Nevertheless, it is possible to highlight that both applications showed a limit for no spall initiation between 1.8 GPa and 2.4 GPa, and no major influence of hardness, NHD, CHD, or residual stress was observed during Phase I of testing, only a small variation in spalling depth. The trend of higher case hardening depth producing shallower spalling could be observed for both applications. To illuminate further trends, additional testing is recommended to achieve statistical significance. A comparison for the nitrided material is difficult due to the issues with the white layer for the shaft application.

Simulations

A verification of the above mentioned facts was generated by the simulations described in frame of D2-7. The simulation model developed within the scope of this project validated the test results and the hypothesis that additional body stress is required to promote a crack through the material. In particular, for the outer ring application, it was also possible to predict the crack path with a crack through by considering the present crack initiation based on the maximum spalling depth. The assumption of an initial crack in the simulation is mandatory because the model is based on fracture-mechanics principles which are not predictive enough to judge spall initiation or short crack growth. Nevertheless, the simulations were also capable of showing crack propagation parallel to the surface under specific circumstances depending on the assumptions made (see example in chapter 6.5.1).

For the shaft application, some deviations were observed between the simulation and test results, although the simulation was based on some worst-case load conditions. Nevertheless, the simulation results were always on the conservative side (meaning that crack propagation or crack through is more likely) in that they used maximum tensile residual stresses from the measurement/simulation and maximum initial crack length. Moreover, sensitivity analyses (e.g., for the crack angle) were done to permit use of the most severe crack condition.

Supported by the simulations, it is therefore possible to lend support to the second and third hypotheses given above.

The simulation model and its complexity were reduced to 2D and fixed crack extensions in order to significantly reduce calculation time for the frame of the project. However, this can be changed, if required, to allow for estimations on 3D cracking or residual lifetime based on da/dN curves.

The test campaign, as well as the simulations made during the GIFT research project, demonstrated that body stress is the main factor influencing the likelihood of a crack through the material, whereas the other parameters simulated and tested within this research project showed some degree of influence on crack propagation, but did not lead to a crack through. Therefore, it is necessary to study each case separately in detail, especially for those cases where additional body stress could not be avoided or where parameters differ significantly from those used within this project. This might be the case for residual stress profiles, which could differ from the values of this research project because of differences in manufacturing steps.

Classification of the project in the context of future developments

As an overall conclusion within the framework of the project, it is worth mentioning that no fixed limits for the given parameters, load conditions, or body stresses could be presented for carry-over to other applications. Potential applications may include planetary gears, integrated or non-integrated bearings, and gears or integrated raceways on housings, liners, and shafts (this list does not claim to be exhaustive).

Limits that may be derived from the test campaign and simulation (e.g. maximum allowable pressure level or body stress) could be different for other applications due to geometrical effects or manufacturing influences (e.g., influence on fracture mechanics properties of the material). Nevertheless, it is possible to use the general approach in any number of other applications using the flow chart presented below (see Figure 153).

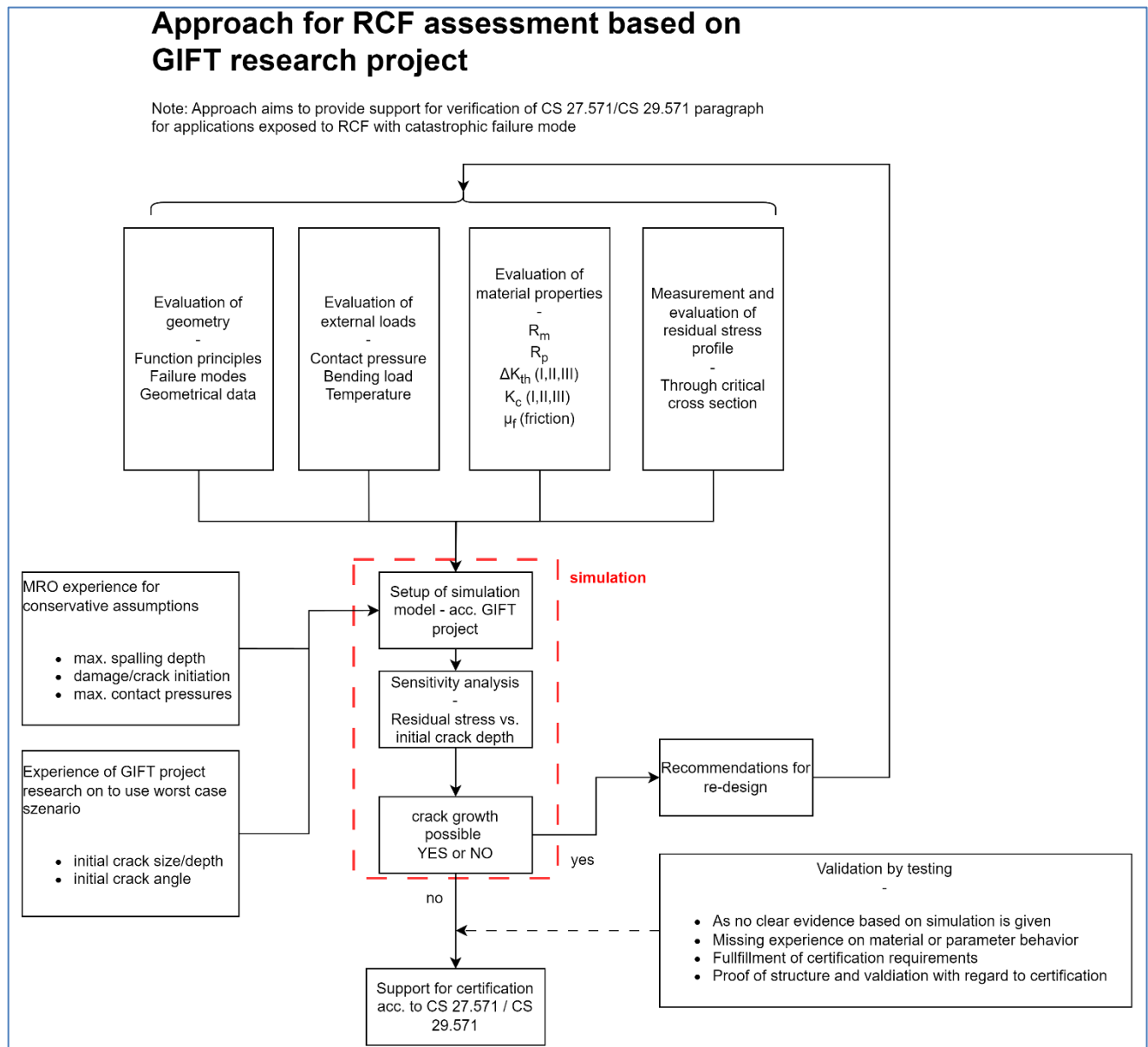


Figure 153: Potential use of experience from research project within other applications

As a starting point and baseline, four main pillars can be mentioned. These are: the evaluation of the geometry, external load, material properties, and residual stress profile (see Figure 153 for more details on information needed). Moreover, additional information should be derived from available MRO data to ensure that the

simulation is conservative. This could be done by additional output of MRO data, which is currently not considered as generic MRO data (e.g., maximum spalling depth or information on subsurface cracks).

A general experience on the sensitivity of the initial crack depth/angle to key parameters has been gained from the current research project and could be used in conjunction with MRO data to build the simulation model properly (e.g., maximum spalling depth in a range of 0.3-0.5 mm vs. critical crack depth based on the residual stress profile for the tested applications). Detailed knowledge on these pillars is mandatory for further evaluation and must be integrated for any new application, which might also entail the use of further simulation model details (e.g., 2D vs. 3D). Nevertheless, model optimization is recommended due to time consuming simulation and could be supported by additional testing as well. After some sensitivity analysis within the simulation, a statement of potential critical crack growth can be made, which could lead to recommendations for re-design. If critical crack propagation can be excluded by simulation, additional testing can be used in conclusion to validate the results and support certification according to CS 27.571/CS 29.571. Additional testing could be necessary for several reasons (see also details in Figure 153).

As demonstrated by Figure 153, the simulations developed herein (see chapter 6) and the experience won from testing (see chapter 5) are not limited to the applications of this research project. They can be transferred to support future development activities and provide recommendations for more sustainable design solutions to avoid critical crack propagation. With the information gained from this research project, it was possible to provide a guideline for future development of components subject to RCF and featuring a catastrophic failure mode.

8. References

References for which the revision status is not provided refer to the last completely signed and therefore approved version.

- [1] EASA, Procurement Document “Integrity improvement of rotorcraft main gear box (MGB)”, EASA.2019.HVP.17, 09/2019
- [2] EASA/ZFL, Contract “Direct service contract for H2020 Project: Integrity improvement of rotorcraft main gear box (MGB), EASA.2019.C15, 16/06/2020
- [3] D2-1: S. Hilleke, Technical Note “Review of the state-of-the-art design criteria for reliability and flaw tolerance in integrated bearing races and list of relevant design parameters identified”, 01 June 2021
- [4] D2-2: S. Hilleke, Technical Note “Detailed analysis methodology”, 10 November 2021
- [5] D2-3: W. Riesen, “Initial Test Plan”, 02 December 2021
- [6] D2-4: R. Boukellif, “Design parameters limitations for reliability and flaw tolerance”, 22 March 2023
- [7] D2-5: R. Boukellif, “Critical threats and crack development”, 12 July 2023
- [8] G. Kullmer, B. Schramm, T. D. Joy, “Simulation Reports from: (May, 2022), (December, 2022), (June, 2023), (December, 2023)”, Paderborn University
- [9] D2-6: W. Riesen, Test Instruction “Final Test Plan”, 26 May 2023
- [10] TR 230126: K. Agode / F. Gervais, “ Test Report”, Issue B, SKF, 2023
- [11] IMKT, “Evaluation of test results at the IMKT for the project EASA-GIFT-MGB”, Issue 5, 2023
- [12] IWT Bremen / Gear Research Center (FZG), “Optimized compound layer design for highly loaded nitrided gears”, 2023
- [13] FVA 386 III, “Verbindungsschichtdesign für tragfähigkeitsoptimierte Zahnflanken”, 2023
- [14] D. Hannes, “On fatigue crack growth modelling of surface initiated rolling contact fatigue using the asperity point load mechanism”, Doctoral Thesis no. 85, Department of Solid Mechanics, School of Engineering Sciences KTH Royal Institute of Technology, Stockholm, Sweden (2014)
- [15] M. Fulland, M. Schöllmann, H. A. Richard, “ADAPCRACK3D - Development of the program for the simulation of three-dimensional crack propagation processes”, taken from: S.N. Atluri, F.W. Brust (Eds.): Advances in Computational Engineering & Sciences, Vol. I, Tech Science Press, Palmdale, USA (2000), 948-953
- [16] M. Fulland, H.A.Richard, “Numerical Determination of Crack Paths in Three-Dimensional Structures with the Program System ADAPCRACK3D”, Institute of Applied Mechanics, University of Paderborn, Pohlweg 47-49, 33098 Paderborn, Germany
- [17] T .D. Joy, J.-P. Brüggemann, G. Kullmer, “Crack growth simulation with Adapcrack3D in 3D structures under the influence of temperature”, Procedia Structural Integrity 13, (2018), 328-333
- [18] A. Riemer, H. A. Richard, “Crack Propagation in Additive Manufactured Materials and Structures”, Procedia Structural Integrity 2 (2016), 1229-1236
- [19] M. Schöllmann, M. Fulland, H. Richard, “Development of a new software for adaptive crack growth simulations in 3d structures”, Engineering Fracture Mechanics, 70(2) (2003), 249–268
- [20] E.F. Rybicki and M.F. Kanninen, “A finite element calculation of stress intensity factors by a modified crack closure integral”, Engineering Fracture Mechanics, 9 (1977), 931-938
- [21] M. Schöllmann, H.A. Richard, G. Kullmer et al., “A new criterion for the prediction of crack development in multiaxially loaded structures”, International Journal of Fracture 117 (2002), 129-141

- [22] T. Manns, "Analyse oberflächennaher Eigenspannungszustände mittels komplementärer Beugungsverfahren", Forschungsberichte aus dem Institut für Werkstofftechnik, Metallische Werkstoffe der Universität Kassel, Band 11, Herausgeber: B. Scholtes, 2011
- [23] B. Trollé, "Simulation multi-échelles de la propagation des fissures de fatigue dans les rails", Thèse (2014).
- [24] D. CANNON and H. PRADIER, "Rail rolling contact fatigue Research by the European Rail Research Institute Wear", vol. 191, 1996, 1-13.
- [25] P. Rycerz, A. Olver, A. Kadiric, "Propagation of surface initiated rolling contact fatigue cracks in bearing steel", International Journal of Fatigue 97 (2017), 29-38

Bibliography

Project reports

- D1-1: W. Riesen, "Review of the state-of-the-art rotorcraft gearbox configuration and component designs", 02 December 2021
- D1-2: W. Riesen, "Description and supporting evaluation of architecture and individual component design proposals, as well as determination of component/ sub-system design solutions", 04. May 2023
- D1-3: W. Riesen, "Stream 1: Summary and conclusion report", 6. October 2023
- D2-1: S. Hilleke, "Review of the state-of-the-art design criteria for reliability and flaw tolerance in integrated bearing races and list of relevant design parameters identified", 01 June 2021
- D2-2: S. Hilleke, "Detailed analysis methodology", 10 November 2021
- D2-3: W. Riesen, "Initial Test Plan", 02 December 2021
- D2-4: R. Boukellif, "Design parameters limitations for reliability and flaw tolerance", 22 March 2023
- D2-5: R. Boukellif, "Critical threats and crack development", 12 July 2023
- D2-6: W. Riesen, "Final Test Plan", 26 May 2023

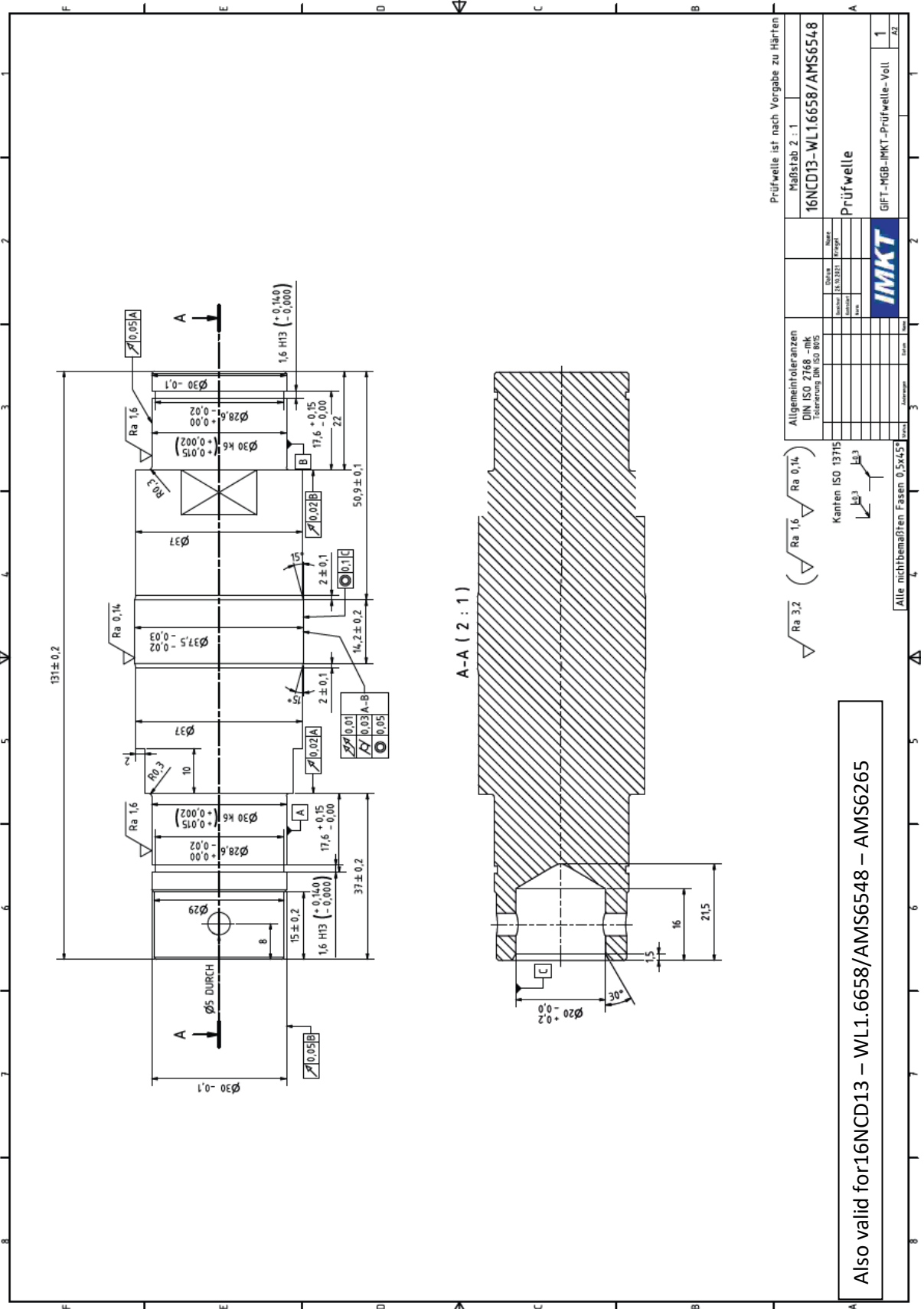


Figure 163: Detailed view of solid shaft specimen for test bench '2' (Phase I, valid for both materials)

Prüfwelle ist nach Vorgabe zu Härten		Maßstab 2 : 1	
Allgemeintoleranzen DIN ISO 2768 -mk Toleranzung DIN ISO 8015		16NCD13-WL1.6658/AMS6548	
Kanten ISO 13715 Kanten Ra 3.2 (Ra 1.6 Ra 0.14) Kanten Ra 0.05 (Ra 0.02 Ra 0.01)		Prüfwelle	
Alle nichtbenannten Fasen 0,5x45°		GIFT-MGB-IMKT-Prüfwelle-Voll	
IMKT		1	
Dateiname: 15.10.2017_Erzeugt		2	
Datei: 15.10.2017_Erzeugt		3	
Gezeichnet: 15.10.2017		4	
Geprüft: 15.10.2017		5	
Freigegeben: 15.10.2017		6	
Abgegeben: 15.10.2017		7	
Bearbeitet: 15.10.2017		8	

Also valid for 16NCD13 – WL1.6658/AMS6548 – AMS6265



RNU 206 ECP

- Popular item
- SKF Explorer

Cylindrical roller bearings, single row,
without an inner ring

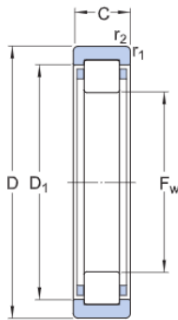
Bearing data

[Tolerances](#),
Normal, P6,
[Radial internal clearance](#),
table

Bearing interfaces

[Seat tolerances for standard conditions](#),
[Tolerances and resultant fit table](#)

Technical specification



DIMENSIONS

F_w	37.5 mm	Diameter under rollers
D	62 mm	Outside diameter
C	16 mm	Width
D1	≈52.08 mm	Shoulder diameter outer ring
$r_{1,2}$	min.1 mm	Corner radius

CALCULATION DATA

Basic dynamic load rating	C	44 kN
Basic static load rating	C_0	36.5 kN
Fatigue load limit	P_u	4.5 kN
Reference speed		13 000 r/min
Limiting speed		14 000 r/min
Calculation factor	k_r	0.15
Limiting value	e	0.2
Axial load factor	Y	0.6

Figure 164: Detailed information of bearing specimen predesign for test bench '2'

A.3 Complex load introduction for outer ring

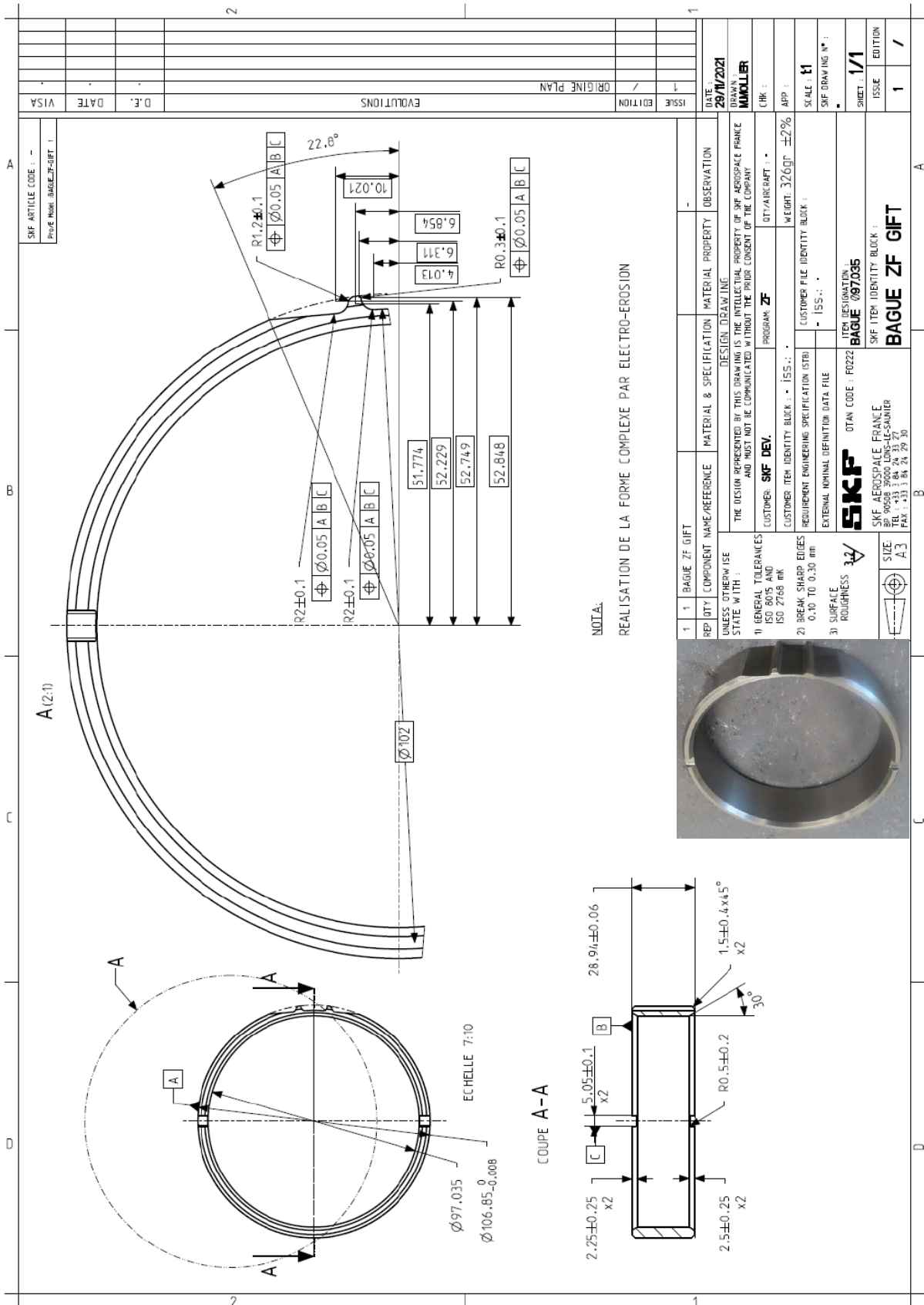


Figure 165: Phase II test specimen for test bench '1' (outer ring with notch - Version T102 C)

A.4 Complex load introduction for shaft

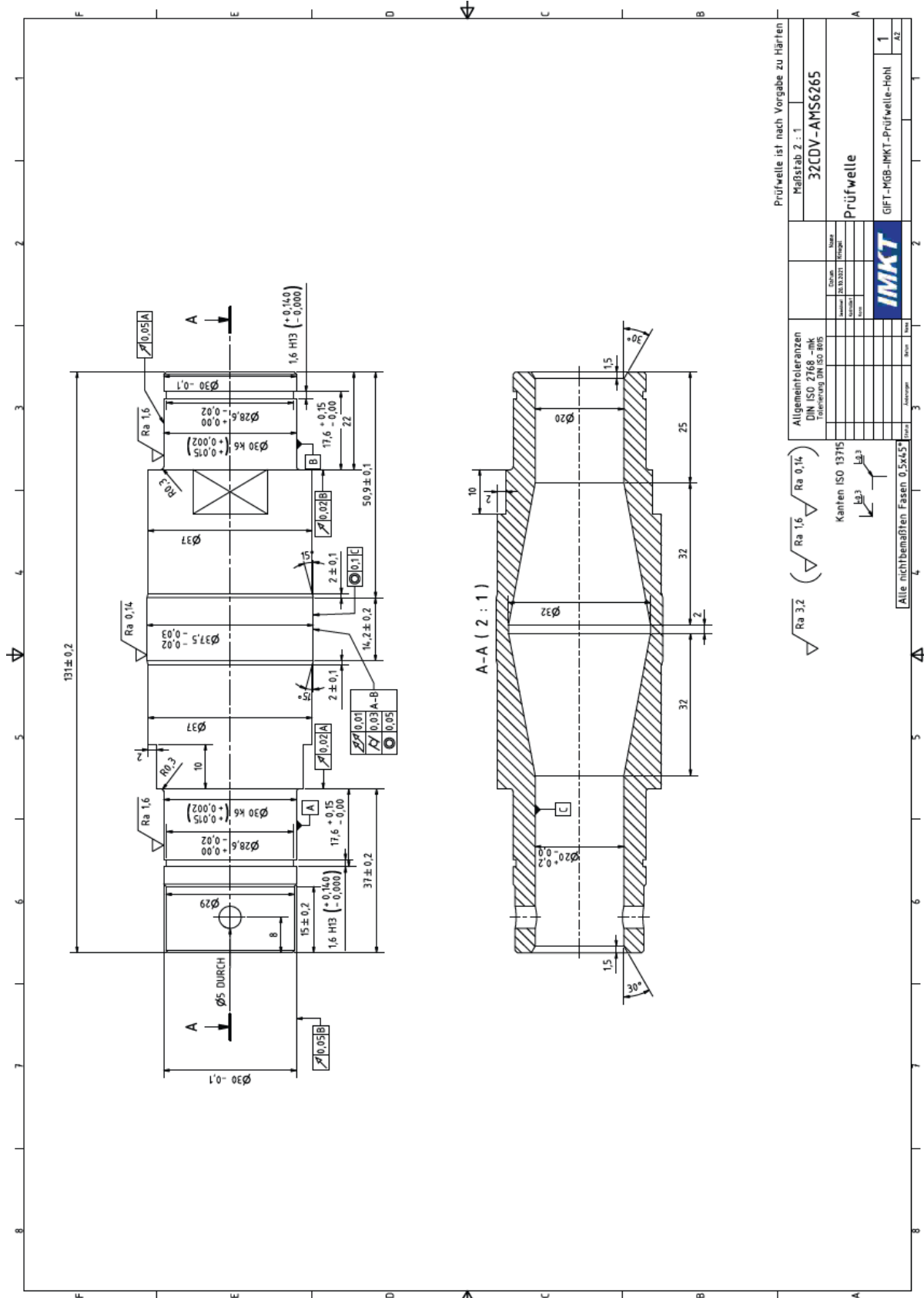


Figure 166: Phase II test specimen for test bench '2' (hollow shaft)

A.5 White layer evaluation

As described in chapter 5, the brittle white layer led to some uncommon peeling of the surface layer for the nitrided shafts. This issue was not observed for the ring application. Based on a root cause analysis and metallographic investigations, it turned out that the peeling of the surface layer occurred due to the brittle white layer (which was not removed for the shaft application) in conjunction with the introduced damage. The white layer was not removed due to prior experience and knowledge on gear and teeth applications (see [12] and [13]), as the white layer can be used to improve carrying load capacity, especially in contacts. Although it was known that pre-damage could decrease this capacity, this severe peeling of the surface layer was not expected.

In the aviation industry it is typically a pre-defined requirement in bearing applications to remove the complete white layer, or at least a minimum of 8 μm of the surface layer before finishing the surface. For other aviation applications, there is no precise specification or requirement available at AH Tech defining the removal (or non-removal) the white layer. It is more or less dependent on the component and application. For some parts known to AH Tech, the removal of the white layer was required by means of a chemical surface treatment. Nevertheless, there are parts at AH Tech typically produced with a white layer for nitro carburizing processes when specific corrosion or wear properties are required. Based on this fact and the research topics within [12] and [13], the white layer was not removed for the nitrided shafts in the GIFT research project.

Due to presence of the white layer, the nitrided shaft samples were ultimately not adequate for the purpose of the tests. As a result, it was impossible to conclude whether or not spalling would have occurred if the white layer had been removed.



European Union Aviation Safety Agency

Konrad-Adenauer-Ufer 3
50668 Cologne
Germany

Project website <https://www.easa.europa.eu/research-projects/integrity-improvement-rotorcraft-main-gear-box-mgb>

Tel. +49 221 89990- 000
Mail research@easa.europa.eu
Web www.easa.europa.eu

An Agency of the European Union

